

**TOWARDS QUANTUM NANOMECHANICS WITH
A TRAPPED DIAMOND CRYSTAL COUPLED TO
AN ELECTRONIC SPIN QUBIT**

by

Peng Ji

B.S in Physics, Capital Normal University, 2009

M.S in Physics, University of Pittsburgh, 2013

Submitted to the Graduate Faculty of
the Kenneth P. Dietrich School of Arts and Sciences in partial
fulfillment

of the requirements for the degree of

Doctor of Philosophy

University of Pittsburgh

2018

UNIVERSITY OF PITTSBURGH
KENNETH P. DIETRICH SCHOOL OF ARTS AND SCIENCES

This dissertation was presented

by

Peng Ji

It was defended on

March 20, 2018

and approved by

M. V. Gurudev Dutt, Associate Professor, Department of Physics and Astronomy

Brian R. D'Urso, Assistant Professor, Department of Physics, Montana State University

David Pekker, Assistant Professor, Department of Physics and Astronomy

Adam K Leibovich, Professor, Department of Physics and Astronomy

Daniel G. Cole, Associate Professor, Department of Mechanical Engineering and Materials

Science

Dissertation Director: M. V. Gurudev Dutt, Associate Professor, Department of Physics

and Astronomy

TOWARDS QUANTUM NANOMECHANICS WITH A TRAPPED DIAMOND CRYSTAL COUPLED TO AN ELECTRONIC SPIN QUBIT

Peng Ji, PhD

University of Pittsburgh, 2018

Trapping of a nanodiamond/microdiamond containing Nitrogen-Vacancy centers in vacuum is an ideal platform to develop a hybrid mechanical system. In such a system, the coupling between the Nitrogen-Vacancy centers and the mechanical motion of a trapped diamond provides pathways for generating a quantum superposition state of the mechanical motion with long coherence time. In this work, I demonstrate our preliminary data in detection of Nitrogen-Vacancy spin signals from trapped diamonds using optical and magneto-gravitational trapping technologies. I compared the advantages and drawbacks of both techniques and improvements need to be made. I also explored the charge dynamics of Nitrogen-Vacancy centers in diamonds under near-IR laser illumination and first demonstrate a low energy (0.95~1.18 eV or 1050 to 1300 nm) Multi-photon Photoluminescence Excitation (PLE) spectrum of NV centers in a sub-millimeter diamond crystal.

Keywords: Nitrogen Vacancy, diamond, mechanical oscillator, coupling, spin, charge dynamics, multi-photon, PLE.

TABLE OF CONTENTS

1.0 INTRODUCTION	1
1.1 Quantum Behavior	1
1.2 Quantum Mechanical Oscillator	2
1.3 Hybrid Mechanical System	3
1.3.1 Superconducting Qubit Coupled to A Mechanical Resonator	4
1.3.2 Solid State Qubit Coupled to A Mechanical Resonator	5
1.3.3 Atoms, Ions, Cavity Photons Coupled to A Mechanical Resonator	7
1.3.4 General Hamiltonian of A Hybrid Mechanical System	8
1.3.5 Evaluate A Hybrid Mechanical System	9
1.4 Works in This Dissertation	9
1.4.1 Developing A Quantum Hybrid Mechanical System with A Trapped Diamond and A Spin Qubit	10
1.4.1.1 Motivation And Hypothesis	10
1.4.1.2 Advantages of A Trapped Diamond System	10
1.4.1.3 Approach	10
1.4.1.4 To The Field	11
1.4.2 Charge Dynamics of NV Centers Under Near-IR Laser Illumination	12
1.4.2.1 Hypothesis	12
1.4.2.2 Novel Regime	12
1.4.3 Multi-Photon Photoluminescence Excitation of NV centers	12
1.4.3.1 Hypothesis	12
1.4.3.2 Novel Regime	13

1.5	Outline of This Dissertation	13
1.6	Appendix	14
1.6.1	Appendix: Parameters from Several Published Cavity Optomechanics Experiments	14
1.6.2	Gravitational Effect on Quantum Mechanics	16
1.6.2.1	Gravity Induced Decoherence	16
1.6.2.2	Schrödinger-Newton (SN) Equation	18
1.6.3	Abbreviations In This Dissertation	18
2.0	BACKGROUND	20
2.1	Nitrogen Vacancy (NV) in Diamond	20
2.1.1	Crystalline Structure of NV Centers in Diamond	20
2.1.2	The Electronic Structure of NV Center	20
2.1.3	NV ⁻ Spin Properties	23
2.1.4	Two-Level Model for NV ⁻ Ground Spin State and ODMR Spectrum	26
2.1.5	Preparing Superposition between $ +1\rangle$ and $ -1\rangle$ Spin State	30
2.2	A Scheme to Create Large Quantum Superposition State	31
3.0	OPTICAL TRAPPING OF NANODIAMONDS	34
3.1	Introduction	34
3.2	Principles of Optical Trapping	35
3.2.1	Forces on A Trapped Particle	35
3.2.2	Simulation of the Trapping Force	41
3.3	Loading Nanodiamonds	43
3.3.1	Nebulizing Nanodiamonds Suspended in Solvent	43
3.4	Optical Trapping of Diamond in Air	44
3.4.1	Experimental Setup	44
3.4.2	Photoluminescence Spectrum from NV Centers in Trapped Diamonds	46
3.4.3	Spin Detection from NV Centers in Trapped Diamonds	46
3.4.4	Temperature Measurement Using NV Centers in Trapped Diamonds	48
3.5	Optical Trapping of Diamond in Vacuum	49
3.5.1	Our Results	49

3.5.2	Estimation of the Temperature in High Vacuum	49
3.5.3	Review of Peer’s Work at the Same Time	51
3.5.4	Key Parameters to Develop Optical Trapping of Diamond System	51
3.6	Conclusion	54
3.7	Appendix	54
3.7.1	Appendix: Justification of Thermal Dissipation Model	54
3.7.2	Appendix: Trapping Diamond with Graphene	55
4.0	MAGNETO-GRAVITATIONAL TRAPPING OF MICRODIAMONDS	59
4.1	Introduction	59
4.2	Magnetic Field Distribution at the Trap Region	60
4.2.1	Coordinates and Origin	60
4.2.2	Magnetic Field and Potential Energy in the Trap	61
4.3	Experimental Setup	65
4.3.1	Optical Setup	65
4.3.2	Microdiamond Samples and Loading Method	68
4.4	Results from CNW Diamond Sample	69
4.4.1	Probing the Spin Signals in the Magneto-Gravitational Trap	69
4.4.2	Electro-Static Force Assisted Magneto-Gravitational Trap	70
4.4.3	Motion Properties of A Trapped Diamond in Vacuum	73
4.4.3.1	Thermalized Motion of the Trapped Diamond	74
4.4.3.2	Power Spectrum of the Motion	74
4.4.3.3	Cooling of the Diamond in Vacuum	76
4.4.3.4	Linearity of the PSD Signal	78
4.4.3.5	Cooling Results	79
4.4.4	Procedure to Look for ODMR Signal from A Trapped Diamond	80
4.4.5	Possible ODMR Signal from A Trapped CNW Diamond	81
4.4.6	Limitation of Current Technique	84
4.5	Results from Adamas Diamond Sample	86
4.5.1	Photoluminescence and Spectrum from A Trapped Diamond	86
4.5.2	Probing Method Result	86

4.5.3	Statistic of ODMR Contrast over Samples	87
4.5.4	Thermal Detection from a Trapped Diamond in Vacuum	87
4.5.5	Thermal Dependence of ODMR Signals outside the Trap	90
4.5.6	Analysis Conclusion	91
4.6	Conclusion and Future Directions	91
4.7	Appendix	95
4.7.1	Appendix: Parameters in Simulations	95
4.7.2	Appendix: ODMR Contrast Model	96
4.7.3	Appendix: Thermal Distribution and Power Spectrum	98
4.7.4	Appendix: Vacuum System and Measurement	101
4.7.5	Appendix: Q Factor Measurement in High Vacuum	103
4.7.6	Appendix: Cooling of The Motion on Transverse Direction	105
4.7.7	Appendix: Possible Improvements of Optics for A Single NV photo- luminescence Collection	106
4.7.8	Appendix: Preliminary Result in a Electromagneto-Gravitational Trap	107
4.7.9	Appendix: Designs of Trap, Ultrasonicator and Feedback Circuits . .	108
4.7.10	Appendix: Other Instruments in the Experiment	112
5.0	CHARGE STATE DYNAMICS OF NITROGEN-VACANCY CEN- TERS IN DIAMOND UNDER 1064 NM LASER EXCITATION	117
5.1	Introduction	117
5.2	Experiment	118
5.2.1	Diamond Samples	118
5.2.2	Improving Thermal Contact and Drift	119
5.3	Results and Discussion	121
5.3.1	Steady State Photochromism with IR Excitation	121
5.3.2	Time Resolved Photoluminescence	123
5.3.3	Theoretical Model	125
5.3.4	Fast Modulation of Photoluminescence from Both Charge States . .	130
5.3.5	Optically Detected Magnetic Resonance (ODMR) Signal under 1064 nm Laser Illumination	131

5.3.6	Conclusion	135
6.0	MULTIPLE-PHOTON PHOTOLUMINESCENCE EXCITATION OF NV CENTERS IN DIAMOND	136
6.1	Introduction	136
6.2	Background	137
6.3	Experimental Setup	140
6.4	Results	142
6.4.1	Power Dependence	142
6.4.2	Spectrum and Lifetime	142
6.5	Analysis	147
6.6	Conclusion	151
7.0	CONCLUSION	153
7.1	Developing A Quantum Hybrid Mechanical System with A Trapped Diamond and A Spin Qubit	153
7.1.1	Hypothesis	153
7.1.2	Accomplishment	153
7.1.3	Conclusion	154
7.1.4	Outlook	154
7.2	Charge Dynamics of NV Centers Under Near-IR Laser Illumination	155
7.2.1	Hypothesis	155
7.2.2	Accomplishment	156
7.2.3	Conclusion	156
7.2.4	Outlook	156
7.3	Multi-Photon Photoluminescence Excitation of NV centers	157
7.3.1	Hypothesis	157
7.3.2	Accomplishment	157
7.3.3	Conclusion	157
7.3.4	Outlook	158
7.4	Publications	158
	BIBLIOGRAPHY	159

LIST OF TABLES

1	Parameters and calculations from published experimental cavity optomechanics results. To keep consistent the symbols defined in this dissertation, we have redefined some symbols from the original papers. Also we may refer to some undefined symbols and relations which will be introduced in the latter sections (e.g. section 1.3.5 and 3.5.4). Briefly, ω_m is the mechanical angular frequency; Γ_0 is the natural damping angular frequency; κ is the decay angular frequency of a cavity; λ is the coupling strength (angular frequency) for a single photon; T is the environmental temperature and C is the cooperativity. Q is the dimensionless mechanical energy dissipation factor.	17
2	List of abbreviations used more than once in this dissertation	19
3	Mean free path of air at 295 K	55
4	Mean free path of air in pressure ranged from 0.2 to 0.9 mBar, as the measured range in reference [1]. And the calculated temperatures are based on our model and the parameters from [2]. The temperature is calibrated for 0.9 mBar and same parameters are used to predict temperature for the rest of the pressures down to 0.2 mBar.	56
5	List of other instruments used in our experiment	116

LIST OF FIGURES

1	<p>(a) A superconducting qubit coupled to a 6.175 GHz mechanical oscillator experimentally realized by O’Connell et al. The mechanical dissipation factor is $Q=260$, and coupling strength is 124 MHz. See reference [3] for details. (b) A high-frequency bulk acoustic wave resonator (~ 6.65 GHz) is strongly coupled to a superconducting qubit. Their Q factor is calculated as 7.1×10^5, and the coupling strength is 300 kHz [4]. Figures are reprinted with permissions from References [3, 4]</p>	4
2	<p>(a) The motion of a cantilever with a magnetic tip is coupled to a single electron spin polarization through the gradient magnetic field gradient from the tip [5]. Figure is reprinted with permission from Reference [5] (b) Setup depicting the proposed coupling scheme [6] between a single NV spin and a mechanical oscillator through a strong magnetic gradient (black curves). Such a scheme can result in ground state cooling and can be used to prepare non-classical quantum states.</p>	6
3	<p>(a) The simplest cavity optomechanics setup consists of a traditional optical cavity with an oscillating end mirror [7]. (b) An 1D photonic crystal silicon nano-beam. The fundamental optical resonance of the structure occurs at a frequency 195 THz ($\lambda = 1,537$nm) is coupled to the mechanical resonance (breathing mode) occurs at 3.68 GHz by radiation pressure in reference [8]. Figures is reprinted with permission from Reference [8].</p>	8

4	(a)NV crystalline structure in diamond lattice (black circles represent carbons; white for vacancy and brown for nitrogen). (b)NV symmetry(C_{3v}) in the diamond lattice.	21
5	(a)Orbital electron configurations for ground state NV^0 and excited state NV^{0*} in diamond band gap (b)Corresponding NV^0 electronic structure. The curved arrow indicates the phonon relaxation process from the vibronic continuum to the excited state.	21
6	(a)Orbital electron configurations for ground state NV^- and excited state NV^{-*} in diamond band gap (b)Corresponding NV^- electronic structure. The curved arrow indicates the phonon relaxation process from the vibronic continuum to the excited state.	22
7	Photoluminescence spectrum from NV centers in nanodiamond excited by 532 nm laser under 16 K temperature	23
8	The optical readout and initialization mechanism of NV^- ground spin states (a)Schematic of optical transitions for NV^- center. Solid lines indicate radiative transitions and dashed lines are non-radiative transitions (b)Spin contrast between $ m_s = -1\rangle$ and $ m_s = 0\rangle$ as a function of time [9].	24
9	(a)A NV^- center in an arbitrary DC magnetic field, the NV axis is defined as \hat{z} direction. (b)Simulation of the frequency splitting as a function of the magnitude of magnetic field, θ is assumed as 45° . The dashed line ignores the transverse component of magnetic field. (c)The ZFS frequency $D = 2.87$ GHz and the frequency splitting between $ +1\rangle$ and $ -1\rangle$ is $2\gamma B_z$ due to the external magnetic field. (d)The optically detected magnetic resonance (ODMR) signal from an aligned NV^- center respect to \mathbf{B} field ($\theta = 0$). $\mathbf{B} = B_z \hat{z} \approx 29.5$ G \hat{z} estimated from the frequency splitting.	27

10	(a)2-level model for NV^- ground spin state. δ is the detuning; Ω is the Rabi frequency; Γ_1 is the intrinsic relaxation rate of the population from a spin-lattice interaction; Γ_2^* is dephasing rate of the coherence; Γ_p is the pumping laser induced population polarization rate to ground spin state $ 0\rangle$. Γ_c is the pumping laser induced decoherence rate. (b)Simulation of an ODMR signal follows equation (2.6), where $\alpha = 1.0, \beta = 0.7, \Gamma_1 = 2\pi \times 1.0 \times 10^3, \Gamma_2^* = 2\pi \times 2.0 \times 10^5, \Gamma_p = 2\pi \times 5.0 \times 10^6, \Gamma_c = \Gamma_p/2, \Omega = 5.0 \times 10^7$. All rates are typical values [10] from a bulk diamond sample and in unit of rad/s.	29
11	The scheme to prepare superposition between $ +1\rangle$ and $ -1\rangle$ spin state. (a)Two impulsive microwave with different frequencies can be used to drive $ 0\rangle$ to $ \pm 1\rangle$ separately. δ_{\pm} are the detuning and Ω_{\pm} are the Rabi frequencies (b)The three eigenstates solved by Hamiltonian (2.10), which are the superpositions of $ 0\rangle$ and $ \pm 1\rangle$	31
12	The scheme in reference [11] to create a large quantum superposition motion state. The quantum system is initialized to $ 0\rangle_m \otimes 0\rangle$ for motional phonon and spin state.	33
13	Illustration of depicting nano-particle in Raleigh scattering regime. Laser propagates along z direction.	36
14	(a)The field profile for a tightly focused Gaussian beam by an 0.9 NA objective and directions of gradient and scattering force(b)Axial Force (F_x) for a 100 nm sized diamond(c)Potential energy along x direction for a 100 nm sized diamond(d)Transverse Force (F_y) for a 100 nm sized diamond(e)Potential energy along y direction for a 100 nm sized diamond	40
15	(a)Axial Force (F_x) for a 50nm sized diamond(b)Axial potential energy for a 50nm sized diamond	41
16	Calculations of trapping frequencies on different directions for a 50nm diamond using 0.1 W trapping laser power.	42
17	Diagram of depicting the loading procedure. The nanodiamonds(blue dots) fly against the light propagation direction and get trapped at the laser focus (dark blue dot).	42

18	Confocal integrated optical trapping system. The 0.9 NA objective is placed in the chamber. 1064nm trapping laser and green excitation laser are focused by the objective. An achromatic lens group is used to correct the color aberration between the green laser and the trapping laser. Photoluminescence from NV centers in the trapped diamond is also collected by the objective and detected by a single photon counting module (SPCM) or a spectrometer. A 30 μm wire is placed close to the focus of trapping, which delivers the microwave to the trapped diamond for an ODMR experiment. Two cameras are used to collect the scattering image of the trapped diamond.	45
19	Photos of the chamber and nebulizing tube system used in optical trapping .	46
20	(a)Photo of an optically trapped nanodiamond in atmosphere pressure by 0.9 NA objective lens in the chamber. (b)The Photoluminescence image of the NV centers in the trapped diamond. The optics are optimized for 1064 nm laser focus, the effective NA of green illumination and photoluminescence collection path is smaller than 0.9, which explains the larger size of the diamond on the image compared to the diffraction limit of 0.9 NA.	47
21	(a)The Photoluminescence spectrum from NV centers detected from a trapped diamond. The fingerprint is the zero-phonon-line of 637 nm. (b)Detected ODMR signal from NV centers in the trapped diamond without an external magnetic field.	47
22	(a)The detected ODMR signal splits when a magnet is placed close to it. (b)Magnet moved closer to the trapped diamond.	48

23	(a)Key parameters in the cat state creation scheme in Chapter 2 for current optical trapping, the threshold for $C = 1$ can be achieved when the pressure lowers down to 10^{-5} torr. We did not bring in a magnetic tip yet to our current experiment. The choice of G_m is based on a moderate selection in reference [11]. (b)Cooperativity as a function of Q and magnetic field gradient for optical trapping. The pressure and gradient range for calculations are based on the experimental results from references [12, 13]. Due to the current trapping limitation by heating problem, we are sitting at red spot in the figure. Decrease the pressure and increase the magnetic gradient will enhance the cooperativity. High quality nanodiamond sample is required to get a higher Q factor. For cooperativity calculation $T_2=100 \mu s$, $N=10$, $s=1$, $T=300$ K.	53
24	(a)Thermal conductivity from Figure 4 in reference [2]. We use the fit parameters in this figure and equation (10) in their paper to calculate the thermal conductivity from 0.2 to 0.9 mBar pressure as in reference [1]. (b)The measured internal temperature of a Paul trapped diamond using the ODMR technique from NV centers in the diamond. The measured pressures ranged from 0.2 to 0.9 mBar (Figure 3(b) in reference [1]). Figures are reprinted with permissions from References [2, 1]	56
25	The schematic of our laser trapping technique on the TEM grid	57
26	Geometry of our experimental Magneto-Gravitational trap. (a)Outline of the trap (b)X-Y plane projection (c)Y-Z plane projection.	60
27	Magnitude of the B-field distribution in our magneto-gravitational(MG) trap. We set a upper limit threshold of 0.5 T (or 1 T) on the color map for a better contrast (a)X-Y plane, $z=0$. (b)Y-Z plane, $x=0$	61

28	Comparison of the magnetic potential energy U_B and the total potential energy $U = U_B + U_g$ of a $15 \mu m$ diamond in the trapping region. Black lines are equal potential energy boundaries for different colors. (a) U_B on the X-Y plane, $z=0$, shows an enclosed energy minimum on this plane (b) U_B on the Y-Z plane, $x=0$, shows no enclosed energy minimum on this plane (c) U on the X-Y plane, $z=0$, shows an enclosed energy minimum on this plane also shows an enclosed energy minimum on this plane close to the bottom pole pieces. (d) U on the Y-Z plane, $x=0$, also shows an enclosed energy minimum on this plane close to the bottom pole pieces.	62
29	B-field components and total potential energy of a $15 \mu m$ diamond in the Magneto-Gravitational (MG) trap. (a)(b)B-field and potential energy along a vertical (\hat{y}) cross line through the origin. (c)(d)B-field and potential energy along a transverse (\hat{x}) cross line through the origin. (e)(f)B-field and potential energy along an axial (\hat{z}) cross line through the origin.	64
30	Optical setup for MG trapping experiments. The trap is placed in a vacuum chamber, and an objective lens is placed outside to collect the PI and scattering light from the trapped diamond. The green laser illuminates along with the axial direction. The photoluminescence is collected along the transverse direction and conducted to a Single Photon Counting Module (SPCM) or a Spectrometer. The rotating mirror is for scanning the photoluminescence image of the trapped diamond in free space. The scattering of the green laser can be monitored on camera 1 and camera 2 toward transverse and axial directions. The scattering laser spot is also projected on a Position Sensitive Detector (PSD), which mainly tells the position of the diamond on axial and vertical directions in our experiment. The position signal will be displayed on a computer and processed to control the feedback laser force from a 980nm diode laser.	66

31	(a)PSD chip from Hamamatsu model s5980. Black lines are fake color 30 μm gaps in between the four elements. (b)The principle of position detection: Photo-current induced by the scattered laser beam (light green color) tells the positions of the trapped diamond. $(I_A+I_B)-(I_C+I_D)$ tells the vertical position of the diamond respect to the equilibrium position. $(I_A + I_C) - (I_B + I_D)$ tells the axial position of the diamond respect to the equilibrium position. $(I_A+I_B+I_C+I_D)$ should tell the transverse position of the diamond respect to the equilibrium position when the diamond is in and out of the focus. External circuits are used to convert the current to voltage signals.	67
32	A diagram of depicting the procedure of loading diamonds into a magneto-gravitational trap.	68
33	(a)Probe coated with diamonds is inserted into the trapping region. The black strip is the copper deposited kapton film which delivers the MW to the trapping region. (b)The best ODMR we observed from a selected diamond on the probe with same illumination method for a trapped diamond.	70
34	(a)The ultrasonicator is biased with -20 V voltage to negatively charge diamonds on it before spraying (b)The Enlarged MG trap levitating a negatively charged diamond with the help of electrostatic force from biased pole pieces.	71
35	Electric field distribution in the trap region when a 15 V voltage is applied on top pole pieces and the bottom ones are grounded (a)The field vector along the axial direction through the origin (b)The numerical result of the E_z component of electric filed along axial direction in (a) with a linear fit.	72
36	Thermalized motions of the trapped diamond at 2.0×10^{-2} torr vacuum (a)The occurrence histogram and Gaussian fit (red) of axial position (b)The linear fit(red line) of axial position on the log scale (c)The occurrence histogram and the Gaussian fit (red) of vertical motion (d)The linear fit (red line) on the log scale of vertical motion.	75

37	The power spectrum from the motion of a trapped diamond before and after the cooling is applied in linear scale (a)Thermalized motion on axial(\hat{z}) direction 2.0×10^{-2} torr vacuum (b)Cooled motion on axial(\hat{z}) direction 1.0×10^{-5} torr vacuum (c)Thermalized motion on vertical(\hat{y}) direction 2.0×10^{-2} torr vacuum (d)Cooled motion on vertical(\hat{y}) direction 1.0×10^{-5} torr vacuum	77
38	PSD time domain harmonic amplitude linearity calibration, the error is too small to be seen. (a)PSD signal versus galvo amplitude at fixed laser power (b)PSD signal versus laser power at fixed galvo amplitude	79
39	The photoluminescence image from the CNW diamond in the trap(a)not cooled (b)cooled	80
40	(a)Step 1: label the probe tip on cameras (b)Step2: move the diamond to overlap the marker on the cameras. High voltages V1 and V2 are on top pole pieces. The bottom pole pieces are grounded. The diamond is negatively charged.	82
41	(a)Signal at position ($z=0,y=0$) on camera 1 (b)Signal at position ($5\mu m,-18\mu m$) on camera 1 (c)Signal at position ($2\mu m,0\mu m$) on camera 1 (d)The scattering(SC) signal from a non-florescence diamond compared to the photoluminescence signal from the CNW diamond in (a).	83
42	(a)Identify NV centers in trapped diamond with optical spectrum (b)PL image for NVs in a trapped Adamas $15 \mu m$ diamond with cooling under 10^{-5} torr vacuum.	86
43	Statistic of ODMR contrast outside the trap from 20 Adamas $15 \mu m$ and 20 CNW diamonds. The x axis indicate the area under the (normalized) ODMR spectrum.	88
44	(a)The temperature dependent DWF from 10 different diamonds (10 sampling for each) with error bar (b)The mean DWF on log scale shows its linearity.	89
45	(a) Temperature on a trapped diamond detected at ambient pressure at different green laser powers. (b)With or without cooling IR laser, the temperature of the same trapped diamond is measured under 10^{-5} torr vacuum at different green laser powers.	89

46	The temperature dependence ODMR signal when the magnetic field is zero outside the trap (a)A CNW sample (b)An Adamas 15 μm sample	91
47	(a)Key parameters in the cat state creation scheme above for the MG trapping [14] and the Enlarged MG trapping with current parameters (b)Cooperativity as a function of Q and magnetic field gradient for MG trapping (c)for Enlarged MG trapping. For cooperativity calculation in (b)(c), $T_2=100 \mu s$, $N=10$, $s=1$, $T=300$ K. The magnetic gradient range used for calculation is based on a possible gap size in a MG trap. Current experiments stay on the red spots on the figures.	92
48	The magnetization curve of soft ferromagnetic material Hiperco 50A.	94
49	Seven-level model as in reference [15] (a)A single NV with non-aligned magnetic field (b)The seven levels when magnetic field is 0. The transition rates between levels can be written as k'_{ij} . Solid lines are radiative decays while dashed lines are non-radiative decays. (c)The new seven levels when the magnetic field is not 0. The transition rates between levels can be written as k_{ij} . Solid lines are radiative decays while dashed lines are non-radiative decays.	96
50	(a)Vacuum chamber, ion gauge and electronic feed through for a MG trapping experiment. (b)The pump cart with a turbo and connected to a mechanical pump in the pump room. The mechanical pump can generate a 10^{-2} torr vacuum while the turbo will create a 10^{-5} torr vacuum in the chamber measured from the ion gauge in (a).	101
51	Left: the frequency drift over time. Time lapses with the scan number, which indicates a frequency decrease over time. Right: fitted resonance peak, $Q \approx 846$	102
52	Left: the post-processing shifted frequency map over time. Time lapses with the scan number. Right: fitted resonance peak, $Q \approx 10532$	102
53	A random frequency diffusion behavior exists	103
54	A E field gradient decrease can be seen from a simulation when a diamond drops downwards by 10 μm along \hat{y} direction.	104

55	(a)Oscillation frequency peaks detected from a trapped diamond by the PSD (b)Cooling applied for all three peaks. Solid lines corresponds to designed different channels: axial(green), vertical(red), transverse(blue).	105
56	(a)The electromagnet trap, coils are covered under the Teflon(white) (b)A trapped particle in the electromagnet trap. (c)A probe with diamond on it has been inserted into the trapping region to explore the ODMR signal at different currents.	108
57	The ODMR detected from CNW diamond sample on the probe in a random location in the Electromagneto-Gravitational trap with different current in the coils. The splitting of ODMR signals at 0 A indicates a non-zero magnetic field at the location of NV centers	109
58	The designed parameters of the Hiperco 50A pole pieces. First row: top pole piece geometry. Second row: bottom pole piece geometry.	110
59	The geometry and driven circuit of for the ultrasonic horn (a)Parameters (b)Photo of the built one in our lab (c)Circuit drawing modified from reference [16] as in our experiment (d)Photo of our built circuit.	111
60	The diagram of the feedback loop. A,B,C,D correspond to the four elements of the position sensing detector in Figure 31. V-I-V indicates a voltage to current to voltage conversion.	112
61	Design of PSD photo currents amplification circuit and the soldered one in our experiment.	113
62	The photo of Arduino Due board and related shield plugging on it. We build the shield based on Dr.D’Urso’s design.There are four set of Arduino used in our experiments. One for displaying the read-in 3 voltages (x,y,z) from the PSD circuit and transfer the values to computer from a serial port. Another three are for processing the PSD circuit voltages and output modulated signals(phase and amplitude) to the feedback circuit.	114
63	(a)Drawing of the feedback circuit diagram modified from [16] as used in our experiment. (b)Photo of our soldered circuit with a fan forced air onto the circuit.	115

64	<p>(a) Experimental confocal microscope integrated with 1064 nm CW laser. 532 nm laser, photoluminescence from NV centers and 1064 nm laser are separated by two dichroic beam splitters (DBS1 and DBS2). A moving lens (ML) in 1064 nm laser path helps to correct the chromatic aberration of the high NA Objective (Obj). Scanning mirror (SCM) helps to obtain 2D photoluminescence image. Samples are indium soldered on the cold finger made of copper (Cu), and microwaves are delivered with antenna (MW) to the sample. Notch 532 nm (NF) and different long pass (LP) and short pass (SP) filters are applied for different collection windows (650 nm LP and 800 nm SP for NV⁻ or 582/75 nm bandpass filter for NV⁰). The photoluminescence was coupled into a single mode fiber (SM fiber) and received by Single Photon Counting Module (SPCM) or a spectrometer (SPEC) (b) Optical image of indium soldered bulk diamond on a copper plate (yellow), the indium solder (silver) can be seen through the bulk diamond, which is 3.5*3.5mm for its dimension (c) SEM image of 100 nm commercial nanodiamond deposited on a silicon chip.</p>	120
65	<p>(a) Photochromism behavior of NV centers in bulk diamond at room temperature 295K under 1064 nm laser illumination (120 s exposure). ZPL of NV⁰ and NV⁻ are observed at 575 nm and 638nm; strong Raman peak is observed at 572.8 nm (b) Photochromism behavior of NV centers in 100 nm diamond nanocrystal at 16K under 1064 nm laser illumination (30 s exposure). ZPL of NV⁰ and NV⁻ are observed at 575 nm and 637nm; no obvious Raman peak is observed at 572.8 nm. Shaded ranges indicate NV⁰ (yellow) and NV⁻ (red) photoluminescence collection window, shared with (a) and (b).</p>	122
66	<p>Confocal images of ensemble of NV centers in bulk diamond sample at room temperature under 0.25mW Green excitation (a) NV⁻ photoluminescence data (b) NV⁰ photoluminescence data (c) Time trace of the NV⁻ photoluminescence counts, under IR gating (10 mW), normalized to when IR is off (d) Time trace of the NV⁰ photoluminescence counts, under IR gating (10 mW), normalized to when IR is off.</p>	124

67	(a) Photoluminescence versus time (Savitzky-Golay filter applied [17]) while fast switching on and off 1064 nm laser applied by AOMs; inner figure: Zoom in of the “slow effect” (b) Optical pulsed sequence used in the experiments for result (a)	125
68	The theoretical model for NV charge state flipping. Left: our postulated model that NV^0 is excited first by 532 nm laser (green arrow), then it captures an electron promoted by 1064 nm laser from the valence band (pink arrow). This two-step procedure converts NV^0 to NV^- . Right: accepted photo-ionization two-step procedure induced by 532 nm laser (green arrows indicate the two steps), which converts NV^- to NV^0 [18] through the conduction band.	127
69	Dependence of the charge-flipping rate $r = r^{-/0} + r^{0/-}$ on the 1064 nm laser power. Green laser excitation is fixed at 0.3 mW.	128
70	(a) Photoluminescence versus time (SavitzkyGolay filter applied [17]) under fast modulation to examine the rapid quenching behavior; inner figure: Zoom in of the fast edges of photoluminescence counts (b) Optical pulse sequence used for the results in (a)	129
71	ODMR signals comparison with IR and no IR for (a) NV^- charge state (b) NV^0 charge state	132
72	(a) Spin dependence of NV^0 photoluminescence counts (SavitzkyGolay filter applied [17], normalized to steady state) through charge state flipping after switching on 1064 nm laser (i) Zoom in of photoluminescence contrast (ii) Exponentially fit of the photoluminescence contrast decay time (b) Corresponding pulsed sequence: start with green laser initialization pulse for 2300 ns, followed with a 2.87GHz π pulse to flip the spin after green was off. A green detection pulse was applied 100 ns after the Pi pulse, and IR gating pulse was 50 ns after that.	134

73	(a) Multiphoton excitation (Green, Red, Pink arrows) and emission processes (Orange arrow) of a defect. The yellow continuum indicates ground and excited state related vibronic band. The black curved arrow represents the phonon relaxation process. (b) Intermediate state (dash line) model for a Two-Photon excitation process.	139
74	An OPA system served as a tunable light source, providing 200 ps excitation pulses at 250 kHz repetition rate. The “signal and “idler outputs of the OPA were directed onto the sample optical path using dichroic beam splitters (DBS1 and DBS2). Additional bandpass filters and longpass filters were placed along the “signal and idler paths respectively to get rid of any light leaking from the OPAs pump source (800 nm). Laser paths for the different wavelength regions were blocked or opened as needed in the experiments. The photoluminescence can be directed unto a spectrometer or a Single Photon Counting Module (SPCM) for lifetime measurements.	141
75	Power dependence of NV^0 and NV^- fluorescence intensities at (a) 535nm and (b) 1276nm excitation wavelengths. The solid lines are power-law fits with n as the power parameter.	143
76	Fluorescence of NV diamond at various pump powers for (a) 1060 nm excitation, (b) 1210 nm excitation and their corresponding NV^- to NV^0 ratio (c).	144
77	(a) Representative PLE spectra of NV centers at 1050 nm, 1090 nm, 1150, and 1280 nm. The fluorescence spectra are normalized to maximum intensity. (b) Integrated intensity of NV^0 (550-620 nm) and NV^- (750-800 nm) from spectra, e.g. Figure 77(a), versus excitation wavelength. The ratio between NV^- and NV^0 intensities is also shown in the graph.	145

78	(a) Fluorescence comparison of single-photon excitation (510 nm and 550 nm) with multi-photon excitation (1060 nm). In graph (b), the NV^- fluorescence is taken at two wavelength windows for comparison. The fluorescence decay at 1 mW pump power is fitted with a bi-exponential function. The longer lifetime or slower decay component is plotted for various excitation wavelength. The shorter lifetime or faster decay component is consistent at 6.9 ± 1.7 ns. Representative decay plots and bi-exponential fits for (c) NV^0 and (d) NV^- fluorescence comparing shorter, 1060 nm, versus longer, 1276 nm, excitation wavelength are also shown above.	146
79	Two-photon absorption cross section calculated based on our PLE data . . .	148
80	A two-photon, three-photon excitation of NV^- and NV^0 respectively leaving them in their excited states (*). An excited negatively charged state NV^{-*} could absorb another photon to raise the electron out to the conduction band. If an NV^- state absorbs three photons with a total energy of 2.60 eV, it is converted into the excited state of NV^0 . A direct three-photon absorption of an NV^0 electron from the ground state will leave it in its excited state (NV^{0*}) if the total photon energy is greater than or equal to 2.16 eV.	150

1.0 INTRODUCTION

1.1 QUANTUM BEHAVIOR

Macroscopic quantum mechanics is a research topic where scientists try to observe the quantum behavior directly from a macroscopic object. Since last century, quantum mechanics has demonstrated its power to govern the microscopic world. For example, the distribution of silver atoms in a Stern-Gerlach apparatus can only be explained by two discrete spin-z projections; the electron interference pattern always shows up even when the intensity of the electron beam is reduced to single electron level in a double slits interference experiment. Classical physics cannot explain these phenomena. However, quantum behavior can only be detected indirectly in the macroscopic world through collective microscopic quantum behaviors such as the photoelectric effect and the superconductivity of a solid state material at low temperature. The absence of a direct observation of quantum behavior from a macroscopic object (e.g. Superpositions of the position states of a large particle, Schrödinger's cat) prevents scientists from verifying many proposed modifications to existing quantum theory, such as the gravity-induced state collapse model. The observation of macroscopic quantum behavior could also be a bridge to reconcile quantum theory and general relativity, which describes space time in a large scale structure. Therefore, fundamental physics study would ideally extend the direct observation of quantum behavior to the macroscopic world. Developing a system that can prepare robust quantum states for a macroscopic object becomes a possible task with the development of laser and cryogenic technology.

1.2 QUANTUM MECHANICAL OSCILLATOR

A simple harmonic oscillator (SHO) is one of the simplest mechanical systems to be used as a macroscopic object. Other complicated mechanical systems can also be approximated as a SHO for a small displacement away from a stable equilibrium point. Also, a harmonic oscillator is one of the analytically solvable quantum systems, where physicists have a complete theory of its energy levels and quantum states. Generating simple harmonic oscillators at the nanometer and micron scale gradually enlarges the dimensions of the mechanical system so that their quantum behavior can be observed experimentally.

One of the basic assumptions of quantum mechanics is that a system can be fully described by its state $|\Phi\rangle$, and the value of a physical quantity \hat{O} refers to an ensemble-averaging of the physical quantity $\langle\Phi|\hat{O}|\Phi\rangle$ on its state. Therefore, if physicists can prepare a non-classical state, such as the eigenstates of the quantum system, we can compare the observation with quantum theory. A quantum SHO can be described using discrete energies in the form of $E_n = (n + \frac{1}{2})\hbar\omega_m$, where $n = 0, 1, 2, 3, \dots$ is the phonon number of the eigenstate; and ω_m is the frequency of the mechanical oscillator. We can see the ground state energy is $\frac{1}{2}\hbar\omega_m$ and the separation between levels is $\hbar\omega_m$.

In a thermal bath with temperature T , a one-dimensional SHO has an average energy value of $k_B T$ based on the equipartition theorem. T is also the temperature characterizing the motion of a SHO in equilibrium with the bath. Under this condition, the average phonon number can be calculated as

$$\bar{n} = \frac{k_B T}{\hbar\omega_m} - \frac{1}{2} \quad (1.1)$$

When $k_B T \gg \hbar\omega_m$ (e.g. room temperature), the average phonon number is large and the SHO will be in a thermal state of the temperature. The possibility of taking a certain phonon number state follows Boltzmann distribution and there is no coherence between each number state; the mechanical behavior is classical in a thermal state. The average energy of a mechanical oscillator must be reduced to the order of $\hbar\omega_m$ to generate nearly pure quantum states. Here, the chance to fall into a high phonon energy state becomes low and the phonon state distribution becomes the Bose-Einstein distribution. Ideally, we would

like $\bar{n} \ll 1$, where the oscillator has a high possibility of staying in its ground state. When a SHO is in a pure quantum state, we can attempt to research its coherent property and time evolution results.

Based on the equipartition theorem, the average energy of an oscillator is proportional to the motion temperature of the oscillator. Therefore, the process of reducing the energy of the oscillator is also called the “cooling” of the motion. There are two types of cooling methods. One method is cooling the oscillator by reducing the environmental temperature T_0 ($T = T_0$ in equilibrium). This method is called passive cooling and usually requires thermal contact between the oscillator and the environment. A dilution refrigerator is commonly used, and can achieve temperatures in tens of millikelvin. Consequently, if we choose environmental cooling to bring a SHO to its ground state by satisfying the condition $k_B T < \hbar \omega_m$, we can get a lower limit of the SHO resonance frequency $f_m > \frac{k_B T}{h}$. Substituting 50 mK into the inequality, the lower limit of the SHO resonance is on the order of 1 GHz. Therefore, a high frequency mechanical oscillator is necessary to reach the ground state. The second type of cooling method is active, which usually takes advantage of the interaction between the mechanical oscillator and other quantum systems, such as cavity photons and spins. This method does not require thermal contact. The center of mass motion temperature T_{CM} can be cooled with an electromagnetic field even at room temperature. The oscillator, the environment and the active damping form a dynamic equilibrium, where $T = T_{CM} \neq T_0$ (Center of mass motion is decoupled from the internal degrees of freedom [19]). The active cooling method is less demanding in experimental conditions and requires a hybrid mechanical system.

1.3 HYBRID MECHANICAL SYSTEM

A hybrid mechanical system usually consists of a mechanical oscillator coupled to one or multiple well studied microscopic quantum systems, such as a spin of a defect center in a solid or a quantum dot. Operations on the microscopic quantum system can result in a cooling effect of the motion of the mechanical oscillator due to coupling. The coupling also

provides a method to prepare and detect non-classical states of the mechanical oscillator. The prepared non-classical mechanical state for a macroscopic object can be used to verify quantum theories proposed for macroscopic objects, such as the gravity-induced decoherence model, etc (see Appendix 1.6.2 for details). Another application is sensing the change of properties between the coupled systems. The change in the coupled microscopic quantum system can result in the change of the motion of the mechanical oscillator and vice versa. There have been many theoretical proposals and experimental implementations in the last decades on developing hybrid mechanical systems. I will enumerate several examples based on different microscopic quantum systems.

1.3.1 Superconducting Qubit Coupled to A Mechanical Resonator

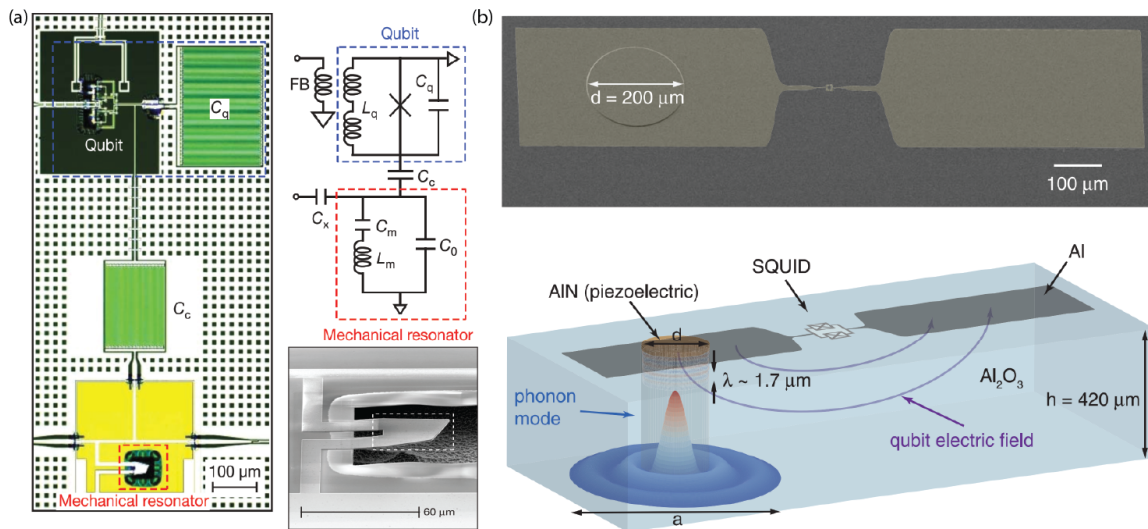


Figure 1: (a) A superconducting qubit coupled to a 6.175 GHz mechanical oscillator experimentally realized by O’Connell et al. The mechanical dissipation factor is $Q=260$, and coupling strength is 124 MHz. See reference [3] for details. (b) A high-frequency bulk acoustic wave resonator (~ 6.65 GHz) is strongly coupled to a superconducting qubit. Their Q factor is calculated as 7.1×10^5 , and the coupling strength is 300 kHz [4]. Figures are reprinted with permissions from References [3, 4]

The most famous hybrid mechanical system is the coupling of a superconducting phase

qubit to a mechanical oscillator experimentally realized by O’Connell et al in 2010 [3] (Figure 1(a)). The oscillator has a high resonance frequency of 6.175 GHz. The high frequency allowed them to use the environmental cooling technique with a dilution refrigerator to reduce the oscillator’s energy to its ground state. In their report, they first showed that they succeeded in creating a mechanical superposition state by manipulating the quantum state of the coupled superconducting qubit. However, the coherence time of these operations are limited by the coherence time of the superconducting qubit, which ranges from nanoseconds to microseconds. The most recent hybrid mechanical system using a superconducting qubit is experimentally realized by Chu et al in 2017 [4] (Figure 1(b)). In their report, a high-frequency bulk acoustic wave resonator is strongly coupled to a superconducting qubit, where the coherence time of the system is measured to be on the order of 10 microseconds.

1.3.2 Solid State Qubit Coupled to A Mechanical Resonator

A traditional solid-state quantum system (single electron spin, defect spins, etc) coupled to a mechanical oscillator was first used as a sensor in 2004 by D.Rugar et al [5] (Figure 2(a)). The motion of the cantilever with a magnetic tip is coupled to a single electron spin polarization through the gradient magnetic field from the tip. This technique is well known as Magnetic Resonance Force microscopy (MRFM). The change of the spin polarization of an electron spin induced by microwave driving can be detected from the oscillation of the cantilever. Similarly, O.Arcizet and Kolkowitz et al couple a Nitrogen-Vacancy (NV) center spin in diamond with a nanowire or a cantilever resonator to detect its vibration [20, 21]. Towards the direction of ground state cooling and coupling to generate non-classical states, Rabl et al [6] proposed a scheme such that the optical driving of a single NV spin in a bulk diamond results in the cooling of a nearby mechanical resonator through strong magnetic gradient coupling (Figure 2(b)). Similarly, a ground state cooling scheme has been proposed utilizing the coupling between either a defect center or a quantum dot, and the deformation potential of the host material [22]. Solid state qubits can have much longer coherence time, up to several milliseconds, compared to the superconducting qubit. However, reported mechanical oscillators coupled to a solid state qubit such as a cantilever suffers from the clamping loss

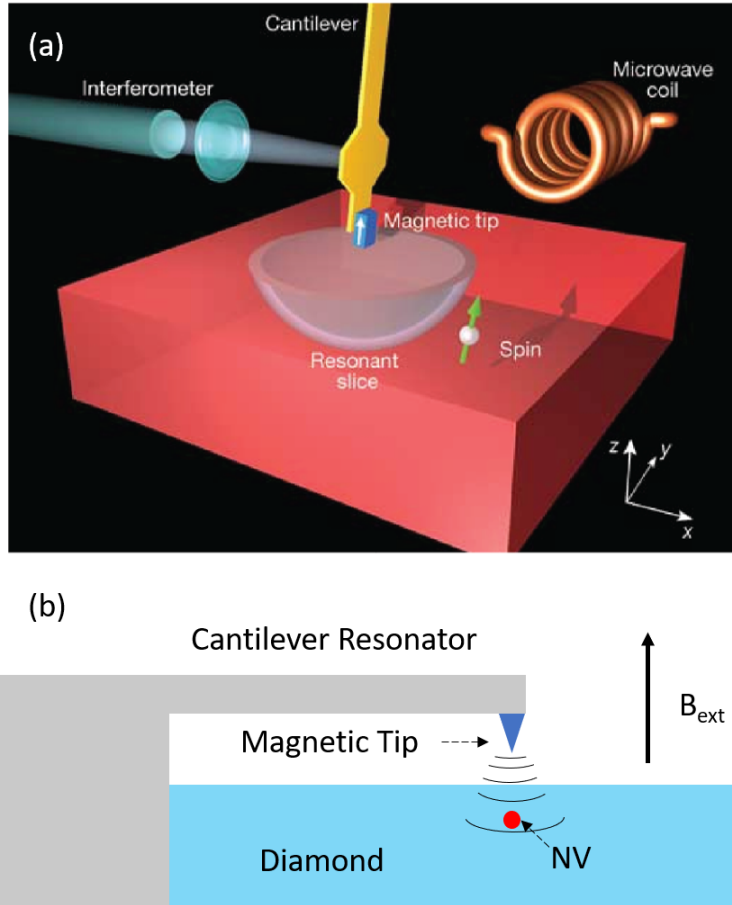


Figure 2: (a) The motion of a cantilever with a magnetic tip is coupled to a single electron spin polarization through the gradient magnetic field gradient from the tip [5]. Figure is reprinted with permission from Reference [5] (b) Setup depicting the proposed coupling scheme [6] between a single NV spin and a mechanical oscillator through a strong magnetic gradient (black curves). Such a scheme can result in ground state cooling and can be used to prepare non-classical quantum states.

from the mounting stage, which limits the Q factor of the mechanical system.

1.3.3 Atoms, Ions, Cavity Photons Coupled to A Mechanical Resonator

Atomic systems have even longer coherence time up to several seconds and therefore are good candidates for coupling. Trapped atoms and ions move as micro-mechanical oscillators. Hunger et al [23] first demonstrated experimentally a direct mechanical coupling between a trapped atomic Bose-Einstein condensate (BEC) to a nearby cantilever through attractive surface force. However, the coupling strength was tiny ($\sim 10^{-2}$ Hz) due to the large mass of the cantilever. The spins of trapped atoms have also been theoretically proposed [24], and experimentally implemented [25] to couple to a nano-cantilever with a magnetic tip through the magnetic field gradient from the tip.

Optomechanical coupling is a popular method to pair atomic systems to a mechanical resonator. Camerer et al realized remote coupling between cold atoms in on vacuum chamber and the oscillation of a membrane in another [26]. The oscillation of the membrane influences the position of the optical lattice and thus couples to the atomic motion [26]. The coupling between the membrane's motion and the atomic motion can be enhanced with a cavity. The system is placed in a high fineness optical cavity where the injected two lasers are oppositely detuned in frequency from the two cavity-resonances [27, 28, 29]. The coupling strength is then determined by the absolute value of the detuning as well as the properties of the cavity.

With the help of an optical cavity, whether it is an indirect coupling between a mechanical oscillator and the atoms through the cavity photons, or a direct coupling between the cavity photons and a mechanical oscillator, research in this field is referred to as “cavity optomechanics”. More experiments have been implemented in directly coupling cavity photons and mechanical modes. The simplest setup consists of a traditional optical cavity with an oscillating end mirror as shown in Figure 3(a). The displacement of the mirror changes the optical resonance of the cavity, which couples the cavity mode to the mechanical mode of the mirror [7]. A non-traditional nano-beam photonic crystal cavity mode has also been coupled to the mechanical mode of the nano-beam [8] (Figure 3(b)). Because there have been many cavity optomechanics experiments in recent years, we listed the parameters from

several representative works and calculated the relevant values in Appendix 1.6.1.

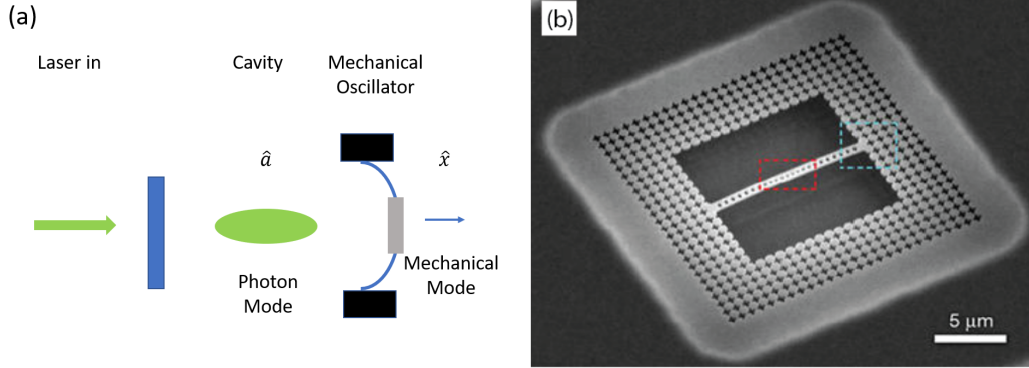


Figure 3: (a)The simplest cavity optomechanics setup consists of a traditional optical cavity with an oscillating end mirror [7]. (b)An 1D photonic crystal silicon nano-beam. The fundamental optical resonance of the structure occurs at a frequency 195 THz ($= 1,537\text{nm}$) is coupled to the mechanical resonance(breathing mode) occurs at 3.68 GHz by radiation pressure in reference [8]. Figures is reprinted with permission from Reference [8].

1.3.4 General Hamiltonian of A Hybrid Mechanical System

The general Hamiltonian for a hybrid mechanical system can be applied to the examples above and written as:

$$H = H_q + H_m + H_c \quad (1.2)$$

where H_q is the Hamiltonian of the microscopic quantum system; $H_m = \hbar\omega_m a_m^\dagger a_m$ is the Hamiltonian of the mechanical oscillator, neglecting the constant zero point energy; H_c is the coupling term between the two systems. The coupling Hamiltonian takes specific forms for different hybrid systems. For example, when a defect spin in a solid couples to the mechanical motion of the cantilever in reference [6], $H_c = \lambda S_z (a_m^\dagger + a_m)$, where S_z is spin z matrix and λ is the coupling strength. It is clear that λ should be in a unit of rad/s, as an angular frequency. The coupling is through the magnetic gradient, so λ is proportional to the magnetic gradient ∇B_z . Another example is the coupling between the atomic motion

to the membrane's motion in reference [30]. The coupling is between the positions of two oscillators and therefore $H_c = \hbar\lambda(a_m^\dagger + a_m)(b_m^\dagger + b_m)$. The coupling is indirect through photons, so the coupling strength is proportional to the product of the coupling strengths for both atom-field coupling and membrane-field coupling, etc.

1.3.5 Evaluate A Hybrid Mechanical System

The evaluation of a hybrid mechanical system depends on the purpose of a specific experiment. For example, if the mechanical motion is used to detect a spin state through coupling, the coupling strength has to be larger than the decoherence rate Γ_s of the spin state, $\lambda > \frac{1}{T_2}$, where T_2 is the spin state coherence time. For ground state cooling and creating non-classical mechanical quantum states, the coupling must be larger than the mechanical damping rate (environment-induced jump rate between different vibrational states) Γ_{th} of the oscillator as well [30, 31, 32, 33], $\lambda > \Gamma_{th}$. Cooperativity is defined in atomic-mechanical coupling scheme and can be generalized to evaluate any hybrid mechanical system. If the microscopic quantum system decoherence rate is Γ_q and the mechanical oscillator decay rate is Γ_{th} , the cooperativity $C = \frac{\lambda^2}{\Gamma_q\Gamma_{th}} > 1$ is a necessary condition to enter the quantum regime [34, 28]. When $C \gg 1$, the system allows more operations on a created non-classical state before losing its coherence, meaning the system is in a strong coupling regime. Developing a strongly coupled hybrid mechanical system has become a major topic in recent years. Chu et al in 2017 [4] reported $C = 260$ in their superconducting qubit-acoustic coupling experiment. $C = 245$ can be calculated from the spin-mechanical coupling proposal by Rabl et al [6], assuming coherence time $T_2 = 1$ ms for a single nitrogen-vacancy center in a bulk diamond. In the proposed atomic-mechanical coupling scheme [30], $C \sim 100$ can be achieved from their parameters.

1.4 WORKS IN THIS DISSERTATION

There are three projects presented in this dissertation:

1.4.1 Developing A Quantum Hybrid Mechanical System with A Trapped Diamond and A Spin Qubit

1.4.1.1 Motivation And Hypothesis The long-term motivation is to experimentally create non-classical mechanical states of a trapped microdiamond by coupling it to a spin qubit (NV center) in the diamond. The created non-classical mechanical state, for example, can be used to test quantum theories on a large object (compared to an atom or a molecule, etc.), where the gravity's influence is not negligible. As a first step toward this goal, this dissertation demonstrates the engineering and evaluation of such a diamond trapping system with experimental data. The initial hypothesis is that the optical trapping (or Magneto-Gravitational trapping) of a diamond with NV centers is a suitable platform to develop the quantum hybrid mechanical system described before.

1.4.1.2 Advantages of A Trapped Diamond System Existing quantum hybrid mechanical systems suffer from various problems in preparing non-classical motional states. For example, the superconducting qubit system is limited by the short coherence time of the qubit, while the solid system with a mechanical oscillator such as a cantilever has a low Q factor due to serious clamping loss from the mechanical contact. While the effective strength can be boosted by the use of more atoms, ions, or photons, the atomic, ion and cavity photon systems are each limited by their respective fundamental coupling strengths, which limit the observation of a non-linear quantum effect [7]. Compared to existing systems, a diamond trapping system is free of clamping loss and the NV center has a much longer coherence time compared to the superconducting qubit. Based on our calculation, a single NV center is sufficient to give large cooperativity, where we can easily enter the quantum regime. Moreover, with an active cooling mechanism and the coupling mechanism proposed in references [6, 11], the system can be operated at room temperature, which makes the experimental condition less demanding.

1.4.1.3 Approach We plan to develop the quantum hybrid mechanical system using the optical trapping technique at first. Theoretically, optical trapping of a diamond has been

proposed as a promising platform to realize the ultimate goal of creating non-classical states [11]. Compared to existing quantum hybrid mechanical systems, the diamond trapping system is expected to have better or more balanced parameters based on our calculation and simulation. For example, we should achieve high cooperativity at room temperature operation (Section 3.5.4). Technically, optical trapping of a diamond has been achieved under ambient condition [35]. The novel approach in this work is to place the system in a high vacuum environment and explore the spin signal from NV centers in the trapped diamond. No one had tried these experiments before we began this project and they are important steps towards the ultimate goal of creating non-classical states.

Through the course of experimentation, we found the trapping laser heating problem on the optical trapping platform. We changed our approach by using the newly developed Magneto-Gravitational trapping technique. Theoretically, although the Magneto-Gravitational trapping cannot give as high cooperativity as the optical trapping technique, it is still possible to enter the strong coupling regime (Section 4.6). Technically, the passive nature of the trap perfectly avoids the heating problem incurred by the optical trapping platform. The novel approach in our experiments is to detect the spin signal from a trapped diamond in a high vacuum. We also attempt to measure the internal temperature of a trapped diamond. Although the pumping laser and cooling laser have much lower powers compared to the optical trapping laser, they may still heat up the trapped diamond in a high vacuum.

1.4.1.4 To The Field These experiments are the pioneering works in developing a better quantum hybrid mechanical system. If these experiments succeed, the system can be used for quantum sensing purposes or to create a non-classical state with improved parameters. The created quantum states can be used to study a variety of quantum effects on massive objects beyond atoms and molecules. These studies may lead to better understanding of quantum theory in our daily life. Even the unsuccessful trials provide valuable knowledge to the field, and offer guidance on what others can avoid or improve upon in the future.

1.4.2 Charge Dynamics of NV Centers Under Near-IR Laser Illumination

1.4.2.1 Hypothesis Because I used a 1064 nm laser to optically levitate diamonds, it is important to understand how trapping laser affect the properties of NV centers in the diamond. I observed the intensity of NV photoluminescence changes when the continuous wave (CW) near-IR laser is on or off. We hypothesize that the intensity change is due to the charge state flipping from neutral charge state NV centers (NV^0) to negatively charged NV centers (NV^-). We also suspect the charge state dynamic depends on the NV^- spin states.

1.4.2.2 Novel Regime Previous experiments examined photophysics of NV centers under visible light illuminations. No one had simultaneously used a CW IR laser with a 532 nm pump laser on NV centers. The absence of illuminating NV with IR wavelengths is primarily due to a CW IR laser energy being below the resonance of both NV center charge states. So no interesting effects were expected. We used photoluminescence spectroscopy and optically detected magnetic resonance (ODMR) techniques to examine our hypothesis. If our hypothesis is correct, we will bring a better understanding of NV energy level structure in between the conduction band and the valence band of the diamond. We also provide a method to manipulate the NV charge state populations. If the charge state is spin dependent, our findings may result in a way to achieve single-shot measurements of NV^- spin states through reading the NV charge state populations.

1.4.3 Multi-Photon Photoluminescence Excitation of NV centers

1.4.3.1 Hypothesis In cooperation with David Snoke's group at the University of Pittsburgh (UPitt), we studied the photoluminescence excitation (PLE) efficiency of NV centers in the multi-photon regime. We attempt to excite the NV centers in a piece of bulk diamond using wavelengths from 1050 nm to 1300 nm (or 0.95 to 1.18 eV in energy). Our hypothesis proposes the photoluminescence emission efficiency is excitation wavelength dependent. We also expect to see photoluminescence peaks at multi-photon resonances corresponding to the zero-phonon lines of NV centers (575 nm for NV^0 and 638 nm for NV^-).

1.4.3.2 Novel Regime Previous experiments have examined the multi-photon PLE spectrum of NV centers up to 1040 nm. No one has yet reported the PLE measurement across the two-photon resonances of NV centers at 1150 nm and 1276 nm for NV^0 and NV^- charge states. However, for example, the excitation of NV^- on resonance at 1276 nm is significant to quantum computation and information using NV centers. Photons from NV^- zero phonon line contain more information than photons from the NV phonon sideband. The single-photon excitation laser cannot be eliminated from the photons emitted at same wavelength while the two-photon equivalent excitation can easily be separated with the emitted photons at 638 nm. Bio-applications of NV centers in nanodiamonds also require lower photon energy excitation to reduce damage to living cells. With our research, it is possible to provide an excitation wavelength with relatively high photoluminescence emission.

1.5 OUTLINE OF THIS DISSERTATION

The structure of the dissertation is as follows:

Chapter 1 introduces the big picture: developing a hybrid mechanical system, the primary motivation of our work in this dissertation.

Chapter 2 introduces the relevant NV theories and techniques and a theoretical scheme to generate a motional “Cat State” in reference [11].

Chapter 3 describes our effort in developing an optically trapped diamond with NV centers as a hybrid mechanical system. We demonstrate detection of spin signals from a trapped diamond and raise the issue of the heating problem of optical trapping in vacuum.

Chapter 4 details our effort in developing a magneto-gravitationally trapped diamond with NV centers as a hybrid mechanical system. I explore the possibility of detecting NV spin signals in a strong magnetic gradient field and measure the internal temperature of a diamond crystal in a high vacuum under laser illuminations.

Chapter 5 discusses the near-IR laser-induced charge dynamics of NV centers in diamonds. We point out this dynamic is spin dependent.

Chapter 6 analyzes multi-photon photoluminescence excitation(PLE) measurements from

an ensemble of NV centers.

Chapter 7 is the conclusion and suggestions for future work.

The appendices detail the derivation of equations and list instruments used in our experiments. If there is an applicable appendix, it is located at the end of each chapter.

1.6 APPENDIX

1.6.1 Appendix: Parameters from Several Published Cavity Optomechanics Experiments

Several experiments coupling the cavity mode to different mechanical resonators are described below and relevant parameters are listed in Table 1:

- Reference [36] couples a microwave sapphire resonator transducer to a 1 KHz niobium membrane acoustic oscillator. The transducer consists of two sapphire mushrooms with a $100 \mu\text{m}$ gap between them. The system is enclosed in a superconducting niobium cavity. One mushroom is attached to a niobium membrane serving as the mechanical oscillator while the other is attached to the bottom of the cavity.
- Reference [37] shows the coupling between the cavity field to a micromirror serving as one end mirror of the cavity. The mirror is coated on the surface of a silicon doubly-clamped beam and is used as an end mirror of a single-ended Fabry-Perot cavity. They used a particular vibration mode of the micromirror, which is about 814 kHz.
- Reference [38] reports a strong coupling between the cavity mode and a membrane resonator. Different from a reflective optomechanical coupling mechanism, where the cavity mode is detuned with the oscillation of one end mirror, a membrane resonator (50nm in thickness) is placed in a rigid cavity. The vibration of the membrane alters the cavity mode, which is called dispersive coupling. The reported lowest flexural resonance of the membrane is about 134 kHz.
- Reference [39] demonstrates the coupling between the cavity mode and the collective motion of a trapped macroscopic ensemble of ultracold atoms in the cavity. The atoms

serve as the mechanical oscillator, and their motion can be directly cooled to the ground state. The axial trap frequency of each optical lattice reported in their paper is about 42 KHz.

- Reference [40] is another experiment using the reflective coupling mechanism. A micromirror serves as one end mirror of the cavity, and its motion has been coupled to the cavity photons. The micromirror oscillates at a resonance frequency of 947 kHz. The introduction is their improvement to the effective coupling strength to the strong coupling regime by increasing the mean cavity photon number, while the fundamental single photon coupling strength remains low.
- Reference [8] demonstrates a novel cavity, which is a one-dimensional photonic crystal made of a patterned silicon nanobeam. The optical mode in this novel cavity is coupled to the acoustic resonance (breathing mode) of the nanobeam by radiation pressure. The acoustic mode is the mechanical resonator and possesses a much higher resonance frequency of 3.68 GHz compared to traditional micromechanical resonators.
- Reference [41] reports the fabrication and measurement on a cavity electromechanical system. A 100 nm thick aluminum membrane is suspended 50 nm above another aluminum layer, forming a parallel-plate capacitor which is shunted by a 12-nH inductor. At 15 mK, this combination is a superconducting microwave cavity, and the aluminum membrane serves as the mechanical oscillator which alters the resonance of the cavity due to vibration. The geometry and tension on the membrane yield a resonance frequency of 10.56 MHz for the vibration mode, which has been successfully cooled to its ground state.
- Reference [42] shows the fabrication of a "trampoline" resonator as one end mirror of an optical cavity. The resonator has a resonance frequency of 9.714 kHz. They reported larger mass (~ 100 ng) and higher Q factor for this resonator which results in higher coupling efficiency than previous Fabry-Perot-type optomechanical systems.
- Reference [43] reports an optomechanical system in the form of a spoke-anchored toroidal optical microcavity. The optical whispering gallery mode is coupled to the mechanical radial breathing mode via radiation pressure. The mechanical breathing mode has a resonance frequency of 78 MHz. The paper exhibits for the first time in an optical

experiment that the effective coupling strength can exceed both optical and mechanical decay rates.

1.6.2 Gravitational Effect on Quantum Mechanics

General Relativity (GR) describes the large-scale structures well while quantum mechanics (QM) succeeds in microscopic world [44]. It is well accepted that there are contradictions between GR and QM [45, 44]. Serious efforts had been made to reconcile the two theories since last century, and so far they have not been unified. With this in mind, trying to observe quantum superposition of a macroscopic object should help to understand the transition from QM to GR. One experimental approach physicists follow to test QM on a macroscopic object is to create a non-classical quantum state initially, let it evolve for a finite amount of time and measure its final state to compare with the theoretical prediction using QM. Therefore, developing a platform where the motional superposition states of a macroscopic particle can be easily created has a profound impact on the field. As the size of a particle increases to the macroscopic regime, the gravitational force on the particle becomes important. There are many theoretical predictions of gravitational effects on a quantum state and the modification on the existing quantum theory. I will introduce gravity-induced decoherence (or state collapse model) and the Schrödinger-Newton (SN) Equation as two famous hypotheses, which in principle can be tested on our diamond trapping platform if we create superposition position states for the diamond.

1.6.2.1 Gravity Induced Decoherence Physicists (Penrose and Diosi, etc.) have suspected the gravity may destroy a macroscopic quantum superposition state. Based on the state collapse model, suppose a particle is in a superposition state $|\psi\rangle = |\psi_1\rangle + |\psi_2\rangle$, where ψ_1 and ψ_2 have different mass distribution $\delta\rho$. The difference tends to destroy the coherence between the superposition at a time scale of [45]:

$$\tau \sim \frac{\hbar}{E_G} \tag{1.3}$$

Ref	$\omega_m/2\pi$ (Hz)	$\Gamma_0/2\pi$ (Hz)	Q	$\kappa/2\pi$ (Hz)	$\lambda/2\pi$ (Hz)	T (K)	C
[36]	10^3	2.5×10^{-6}	4.1×10^7	275	1.2×10^{-3}	4.2	2.4×10^{-11}
[37]	8.14×10^5	81	1.0×10^4	1×10^6	1.2	300	2.3×10^{-15}
[38]	1.3×10^5	0.12	1.2×10^6	5×10^5	5×10^1	0.3	8.7×10^{-7}
[39]	4.2×10^4	1×10^3	4.0×10^1	6.6×10^5	6×10^5	N/A	N/A
[40]	9.5×10^5	1.4×10^2	6.6×10^3	2×10^5	3.9	0.3	8.3×10^{-11}
[8]	3.9×10^9	3.9×10^4	1.0×10^5	5×10^8	9×10^5	20	3.9×10^{-4}
[41]	1.1×10^7	32	3.2×10^5	2×10^5	2×10^2	0.015	2.2×10^{-4}
[42]	9.7×10^3	1.3×10^{-2}	9.3×10^5	4.7×10^5	2.2×10^1	0.3	1.2×10^{-7}
[43]	7.8×10^7	3.4×10^3	2.3×10^4	7.1×10^6	3.4×10^3	0.65	2.8×10^{-6}

Table 1: Parameters and calculations from published experimental cavity optomechanics results. To keep consistent the symbols defined in this dissertation, we have redefined some symbols from the original papers. Also we may refer to some undefined symbols and relations which will be introduced in the latter sections (e.g. section 1.3.5 and 3.5.4). Briefly, ω_m is the mechanical angular frequency; Γ_0 is the natural damping angular frequency; κ is the decay angular frequency of a cavity; λ is the coupling strength (angular frequency) for a single photon; T is the environmental temperature and C is the cooperativity. Q is the dimensionless mechanical energy dissipation factor.

$$E_G = G \int d^3\mathbf{x} d^3\mathbf{x}' \frac{\delta\rho(\mathbf{x})\delta\rho(\mathbf{x}')}{|\mathbf{x} - \mathbf{x}'|} \quad (1.4)$$

where E_G is called the self-gravitational field of the difference in mass distributions. E_G is scaled with the dimension of the particle [46]. For an atomic superposition, this decay is long and easy to detect. For a macroscopic superposition, the decay is too fast, and the state collapses to a classical one before detection. To observe gravity induced decoherence, a rapid detection as well as a “quiet” environment is required: other environmental sources causing decoherence should not dominate. From this aspect, our diamond trapping system could be operated under an ultra-high vacuum so that the trapped diamond is well isolated from the environment. Therefore, our system is ideal to test gravity induced decoherence.

1.6.2.2 Schrödinger-Newton (SN) Equation Another consequence of gravity in QM theory proposed by Diosi in 1984 is a gravitational self-interacting energy term should be added to the right-hand side of the Schrödinger equation [47]:

$$i\hbar \frac{\partial}{\partial t} \Psi(\mathbf{x}, t) = \left(-\frac{\hbar^2}{2M} \nabla^2 + V_{ext} + V_g(\Psi) \right) \Psi(\mathbf{x}, t) \quad (1.5)$$

where $V_g(\Psi)$, the self-gravitational potential is a function of the state, which makes the Schrödinger equation nonlinear. This modified equation is called the Schrödinger-Newton (SN) Equation. The theory can also be tested by checking the final state of a time evolution. Another experiment to test this equation has also been proposed on a Paul trap platform [48], where the parameters (diamond size, trapping frequencies) can be fulfilled easily by the Magneto-Gravitational trapping technique.

1.6.3 Abbreviations In This Dissertation

#	Full Name	Abbreviation
1	Nitrogen-Vacancy	NV
2	Negative charge state of Nitrogen-Vacancy	NV ⁻
3	Neutral charge state of Nitrogen-Vacancy	NV ⁰
4	Photoluminescence	PL

5	Photoluminescence Excitation	PLE
6	Optical Detected Magnetic Resonance	ODMR
7	Single Photon Counting Module	SPCM
8	Zero-Phonon Line	ZPL
9	Phonon Side Band	PSB
10	Magneto-Gravitational	MG
11	Position Sensing Detector	PSD
12	Acousto-Optic Modulator	AOM
13	Nanodiamond (Microdiamond)	ND (MD)
14	Continuous Wave	CW
15	Optical Parametric Amplifier	OPA
16	Multi-Photon	MP
17	Microwave	MW
18	Near Infrared (Infrared)	NIR (IR)
19	Columbus Nanoworks	CNW (A company name)
20	Debye Waller Factor	DWF
21	Proportional Integral Derivative	PID

Table 2: List of abbreviations used more than once in this dissertation

2.0 BACKGROUND

2.1 NITROGEN VACANCY (NV) IN DIAMOND

2.1.1 Crystalline Structure of NV Centers in Diamond

The nitrogen-vacancy center is a point defect center in the diamond lattice. It consists of a nitrogen atom and a vacancy replacing the original two adjacent carbon atoms in the diamond lattice (Figure 4(a)). NV center exhibits C_{3v} symmetry (Figure 4(b)), and there are four possible orientations for an NV center in the diamond lattice. These centers can be created in a chemical vapor deposition (CVD) procedure or a high-pressure, high-temperature (HPHT) diamond synthesis process [49, 50]. Higher concentration of NV centers can be obtained by radiation, ion implantation and annealing on the synthesized diamond. The nanodiamond can be synthesized by the controlled detonation of TNT-like explosives in a closed vessel or milling from the large diamond crystal [51]. The second method will give mono-crystalline nanodiamonds usually with higher purity compared with the first method. However, the grinding procedure will introduce defects on the boundary and affect NV properties close to the surface.

2.1.2 The Electronic Structure of NV Center

Three electrons from Nitrogen pair with electrons from adjacent three carbons while two electrons from Nitrogen stay unpaired. These two electrons and three electrons from the carbons adjacent to the vacancy contribute to the electronic energy level for neutral NV

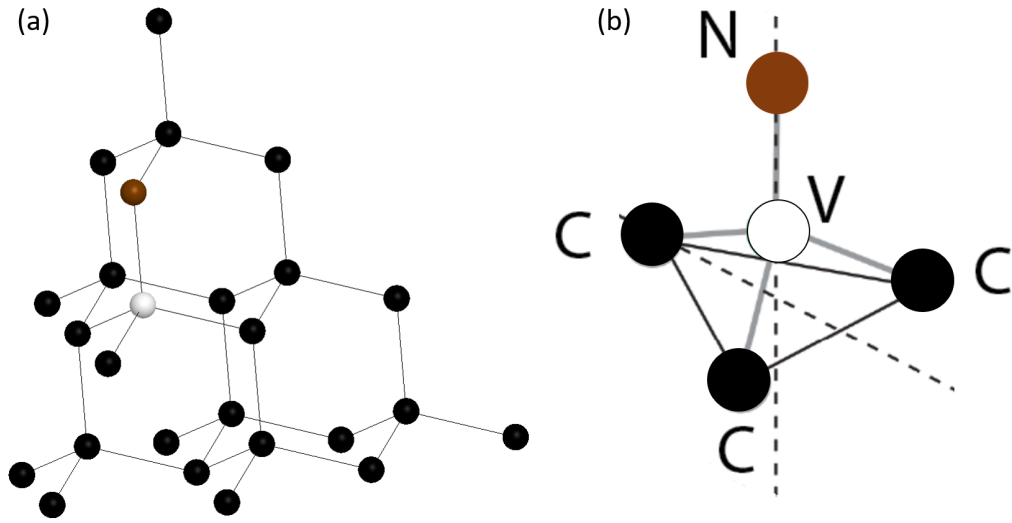


Figure 4: (a) NV crystalline structure in diamond lattice (black circles represent carbons; white for vacancy and brown for nitrogen). (b) NV symmetry (C_{3v}) in the diamond lattice.

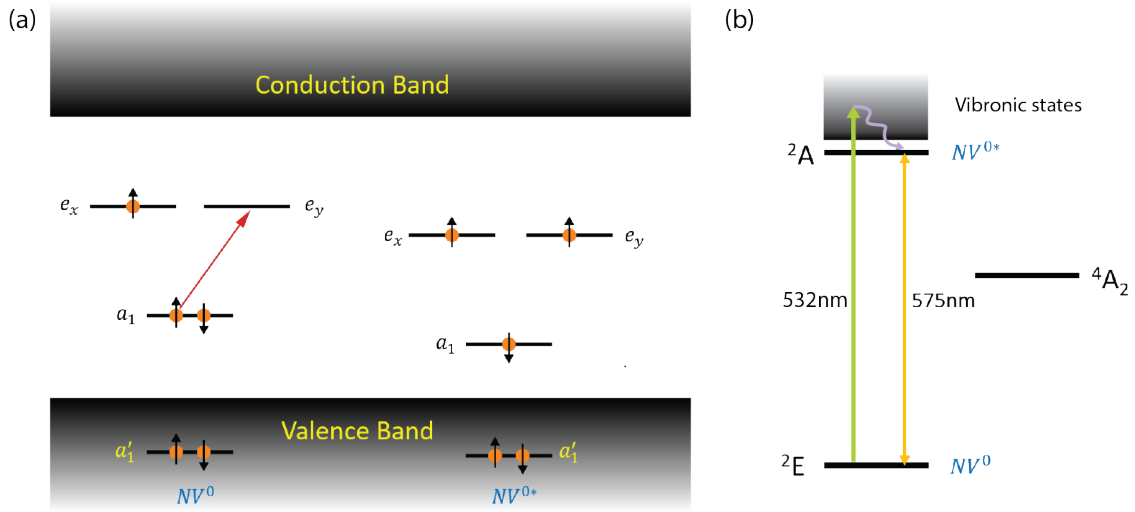


Figure 5: (a) Orbital electron configurations for ground state NV^0 and excited state NV^{0*} in diamond band gap (b) Corresponding NV^0 electronic structure. The curved arrow indicates the phonon relaxation process from the vibronic continuum to the excited state.

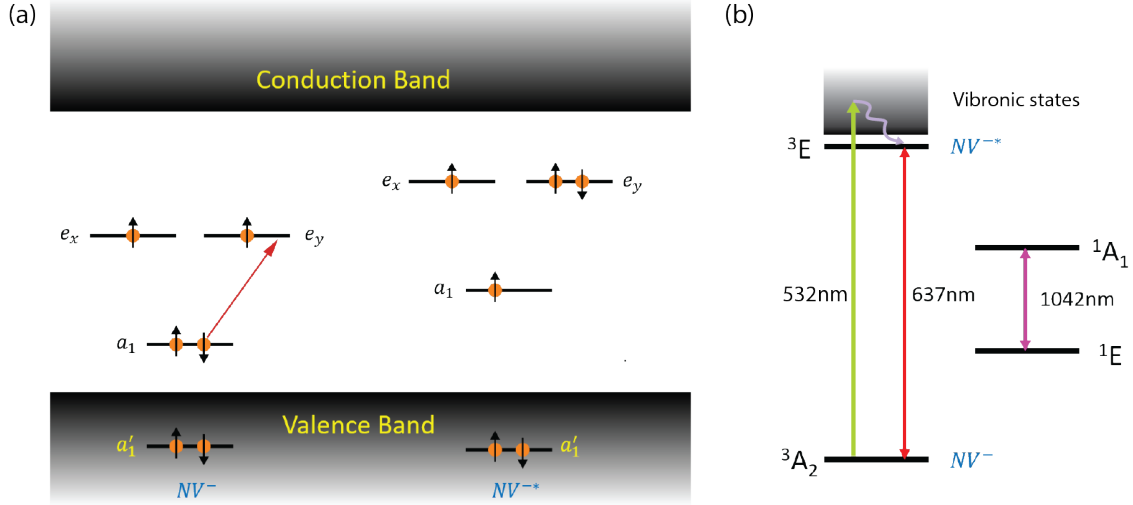


Figure 6: (a)Orbital electron configurations for ground state NV^- and excited state NV^{-*} in diamond band gap (b)Corresponding NV^- electronic structure. The curved arrow indicates the phonon relaxation process from the vibronic continuum to the excited state.

center(NV^0). If the NV^0 capture another electron from the vicinity, the charge state converts to negatively charged NV centers (NV^-). The six electrons together contribute to the electronic energy levels of an NV^- center. The molecular defect orbitals of NV center have been shown in Figure 5(a) and Figure 6(a). These molecular orbitals (MO) (a'_1, a_1, e_x, e_y) can be expressed as linear combinations of sp^3 orbitals of the nearest neighbor nitrogen and carbon atoms to the vacancy [52]. The different occupations of (a'_1, a_1, e_x, e_y) by the (five) six electrons give the electronic structures for NV center in Figure 5(b) and Figure 6(b). MO (a'_1) is usually negligible because it is in the valence band and filled up with electrons for all observable NV electronic levels. MO (e_x, e_y) are degenerate in energy [53]. The electronic structure of a neutral charge state defect NV^0 is signified at 575 nm zero-phonon-line (ZPL) on NV emission spectrum (Figure 7). The excitation from its ground state (2E) to the excited state (2A) is due to an electron transition from MO a_1 to e by absorbing a photon(or photons) [54]. The energy gap between the doublets (${}^2E, {}^2A$) and quartet state (4A_2) are currently unclear. In addition to the discrete electronic levels, there is a continuum at higher

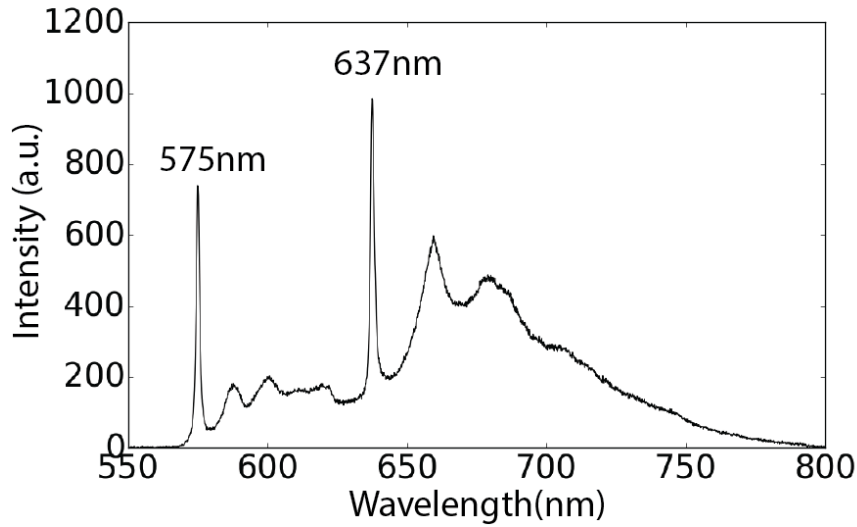


Figure 7: Photoluminescence spectrum from NV centers in nanodiamond excited by 532 nm laser under 16 K temperature

frequencies respect to the excited state in Figure 5(b), which allows off-resonance excitation through the vibronic continuum (such as using 532 nm excitation in Figure 5(b)), the phonon relaxation brings the NV^0 quickly to its excited state.

The electronic structure of a negatively charged defect NV^- is signified at 637 nm zero-phonon-line (ZPL) on NV emission spectrum under low temperature (Figure 7). The excitation from its ground state (3A_2) to the excited state (3E) is also related to an electron transition from MO a_1 to e by absorbing a photon(or photons) [54]. The energy gap between the triplets ($^3A_2, ^3E$) and singlets ($^1A_1, ^1E$) are currently unknown. Similar to NV^0 case, vibronic continuum and phonon relaxation also exist for NV^- center. An additional radiative transition between 1A_1 and 1E is also observed at 1042 nm (Figure 6(b)).

2.1.3 NV^- Spin Properties

NV^- is of the most interest in the NV centers related research. Unlike NV^0 , the triplet NV^- ground state has a detectable magnetic resonance. When there is no external magnetic

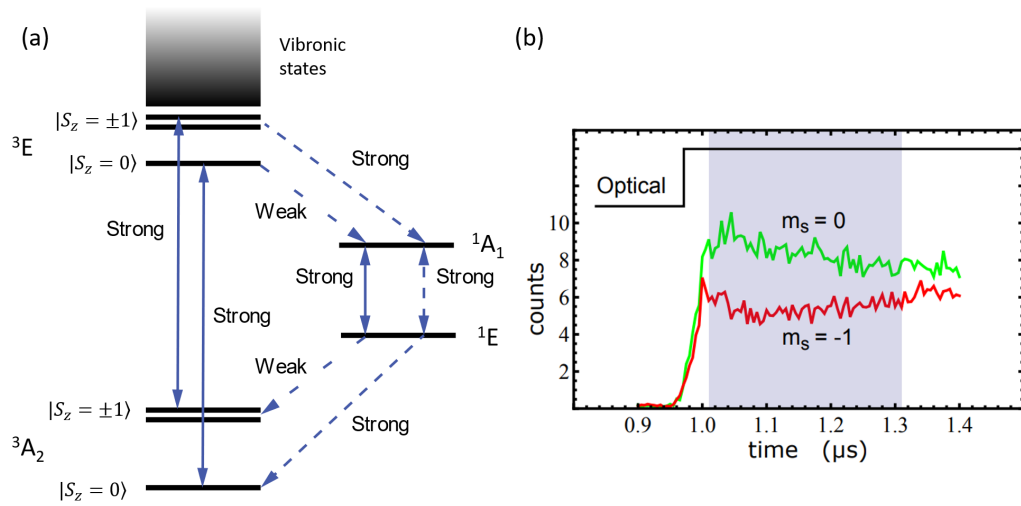


Figure 8: The optical readout and initialization mechanism of NV⁻ ground spin states (a)Schematic of optical transitions for NV⁻center. Solid lines indicate radiative transitions and dashed lines are non-radiative transitions (b)Spin contrast between $|m_s = -1\rangle$ and $|m_s = 0\rangle$ as a function of time [9].

field, the spin-spin interaction results in a zero-field splitting (ZFS) between $|m_s = \pm 1\rangle$ and $|m_s = 0\rangle$ spin states at 2.87 GHz. This ZFS together with the 637 nm ZPL are the fingerprints of NV^- center in diamond. The spin states of NV^- can be read out through optical pumping. The stronger non-radiative relaxations from $|\pm 1\rangle$ (on 3E) to 1A_1 and from 1E to $|0\rangle$ (on 3A_2) result in a 20% to 40% less emission from $|\pm 1\rangle$ spin states (Figure 8(a)). The relaxation time measured from 1E to 3A_2 is in the order of ~ 300 ns. This time duration is much longer compared to other NV^- intrinsic transition times. Therefore, it enables a spin contrast read out by measuring emission intensity within a ~ 300 ns time window after the excitation laser turned on (Figure 8(b) shows the contrast between $|0\rangle$ and $|-1\rangle$ for example). Microseconds later, the $|\pm 1\rangle$ and $|0\rangle$ will reach the same amount of emissions, where the NV^- center is polarized to $|0\rangle$ (See Figure 2(a) in Reference [55] for details). The lower emission intensity after polarization for $|0\rangle$ spin state results from the equilibrium between direct triple-triplet transition and triple-singlet-triplet transition. This polarization mechanism serves as the important initialization step in quantum computation and NV magnetic field sensing application.

Neglecting the interaction with nuclear spins from the environment, the NV^- ground state spin Hamiltonian with an arbitrary local DC magnetic field can be written as:

$$H = hD\sigma_z^2 + hE(\sigma_x^2 - \sigma_y^2) + g\mu_B\mathbf{B} \cdot \mathbf{S} \quad (2.1)$$

where D is the ZFS frequency 2.870 GHz under room temperature; E is the strain field splitting frequency; 100 kHz is a typical value of E for a bulk diamond and 5 MHz for a diamond nanocrystal [56]; $\sigma_x, \sigma_y, \sigma_z$ are the dimensionless spin matrices for a spin-1 system; $h = 6.626 \times 10^{-34}$ m²kg/s is the Planck constant; $g \approx 2$ is the Lande factor; $\mu_B = 9.274 \times 10^{-24}$ J/T is the Bohr magneton; \mathbf{B} is the DC magnetic field and \mathbf{S} is the spin operator. The magnetic field can break into two orthogonal parts B_z and $B_\perp = \sqrt{B_x^2 + B_y^2}$, where we define the NV axis as the \hat{z} direction. The angle between magnetic field \mathbf{B} and \hat{z} is θ (Figure 9(a)). With weak field approximation $B_\perp \ll B_z$, the eigen-frequencies of (2.1) can be solved as:

$$f_{0,\pm} = \frac{E_{0,\pm}}{h} = 0, D \pm \sqrt{(\gamma B_z)^2 + E^2} \quad (2.2)$$

where $\gamma = g\mu_B/h \approx 2.8$ MHz/Gauss. Figure 9(b) simulate the difference of the these eigenfrequencies when the B_\perp exists (solid lines) and the case in (2.2) where B_\perp is ignored (dashed lines). When $E \ll D$ is also satisfied, the frequency splitting between $|+1\rangle$ and $|-1\rangle$ is $2\gamma B_z$ (Figure 9(c)). Because of the polarization mechanism and the spin contrast between $|\pm 1\rangle$ and $|0\rangle$, under a continuous wave (CW) illumination of 532 nm laser and microwave (MW) sweeping across the energy splitting of NV^- ground state, photoluminescence (PL) dips can be observed on the spectrum (Figure 9(d)) due to the population transferring from $|0\rangle$ to $|\pm 1\rangle$. Therefore, this technique is named as optically detected magnetic resonance (ODMR) method. For a single NV^- which is well aligned with the magnetic field, B_z can be estimated as 29.5 G in strength from the frequency splitting in Figure 9(d).

2.1.4 Two-Level Model for NV^- Ground Spin State and ODMR Spectrum

When microwave drives between $|0\rangle$ and one of $|\pm 1\rangle$ spin states, while the other one is not populated, the NV^- ground spin state can be simplified as a two-level spin qubit. The spin Hamiltonian takes the form $H_s = S_z\omega_0$, where S_z is the spin z operator; ω_0 is the resonance angular frequency between the two levels. When the microwave is applied, its Hamiltonian also needs to be taken into consideration. Assuming microwave is polarized along \hat{x} , $H_{MW} = h\gamma B_{MW}\sigma_x\cos(\omega t + \phi_p)$, where B_{MW} is the amplitude of microwave; ω and ϕ_p are the angular frequency and the initial phase of the microwave; $\sigma_x, \sigma_y, \sigma_z$ are the Pauli matrices for a spin-1/2 system. The microwave Hamiltonian is time-dependent. To make it time independent, a standard method is using rotating frame with the same angular frequency ω and applying rotating wave approximation to the Hamiltonian. The Hamiltonian in rotating frame is given by:

$$\tilde{H} = -\frac{1}{2}\hbar\delta\sigma_z + \frac{1}{2}\hbar\Omega(\sigma_x\cos(\phi_p) + \sigma_y\sin(\phi_p)) \quad (2.3)$$

where $\delta = \omega - \omega_0$ is the detuning from resonance frequency and $\Omega = \frac{1}{2}\gamma B_{MW}$ is the Rabi frequency of driving. δ, Ω, ϕ_p are the three free parameters one can manipulate, where the system quantum state $|\psi\rangle$ evolves as $e^{-\frac{i}{\hbar}\tilde{H}t}|\psi\rangle$ for time duration t . Pulsed sequences can be created to prepare any quantum superposition state of $|0\rangle$ and $|1\rangle$.

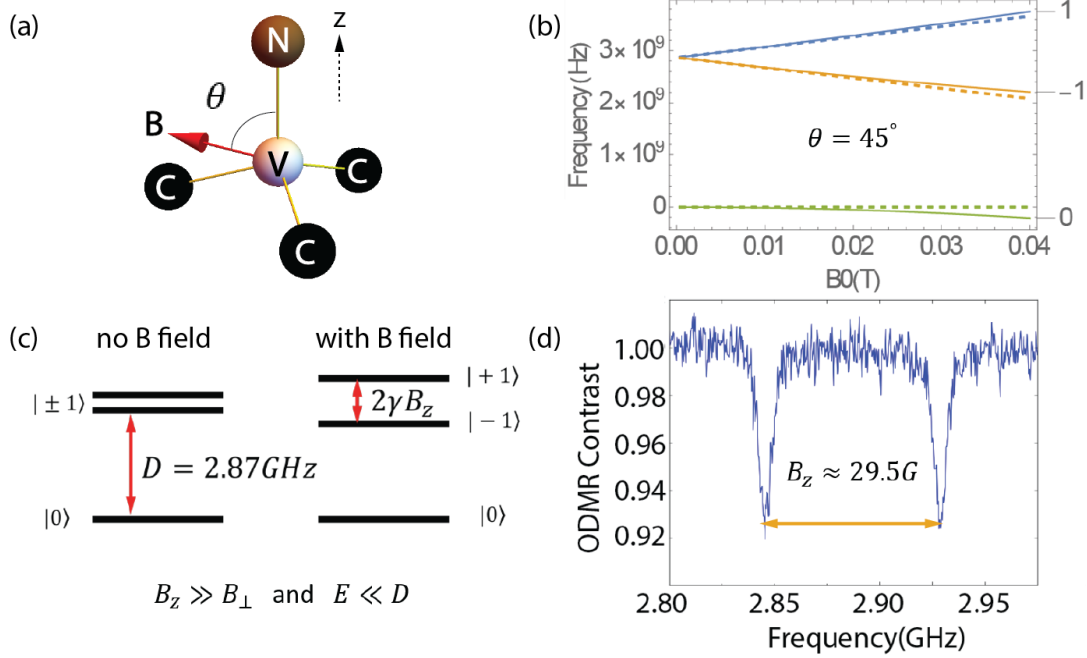


Figure 9: (a) A NV^- center in an arbitrary DC magnetic field, the NV axis is defined as \hat{z} direction. (b) Simulation of the frequency splitting as a function of the magnitude of magnetic field, θ is assumed as 45° . The dashed line ignores the transverse component of magnetic field. (c) The ZFS frequency $D = 2.87$ GHz and the frequency splitting between $|+1\rangle$ and $|-1\rangle$ is $2\gamma B_z$ due to the external magnetic field. (d) The optically detected magnetic resonance (ODMR) signal from an aligned NV^- center respect to \mathbf{B} field ($\theta = 0$). $\mathbf{B} = B_z \hat{z} \approx 29.5$ G \hat{z} estimated from the frequency splitting.

NV center is not alone in the diamond lattice. The complexity of its environment is an important source for the decoherence of the prepared NV^- spin state. Following previous works [10, 57], to calculate the ODMR spectrum, we need to solve a Master equation where the interaction between an NV^- and the environment with optical pumping is considered:

$$\frac{d\tilde{\rho}}{dt} = \frac{1}{i\hbar}[\tilde{H}, \tilde{\rho}] + \left(\frac{d\tilde{\rho}}{dt}\right)_{relax} \quad (2.4)$$

where $\tilde{\rho}$ is the density matrix in rotating frame to describe the two-level system; \tilde{H} is Hamiltonian in (2.3). The first term describes an isolated quantum system while the second term is from the relaxation due to the interaction with the environment. Here we use several relaxation rates to describe this procedure in Figure 10(a). Γ_1 is the intrinsic relaxation rate of the population $\tilde{\rho}_{ii}$ from a spin-lattice interaction, where $i = 0, 1$. Γ_2^* is dephasing rate of the coherence $\tilde{\rho}_{ij}$, where $i \neq j$. Γ_p is the pumping laser-induced population polarization rate to ground spin state $|0\rangle$. Γ_c is the pumping laser-induced decoherence rate, which is limited by the lifetime of NV^- . Solving for the density matrix by (2.4), we evaluate the ODMR spectrum with a measurement operator:

$$M = \alpha|0\rangle\langle 0| + \beta|1\rangle\langle 1| \quad (2.5)$$

where α, β are the photoluminescence emission rates from the two spin states. The ODMR spectrum can be obtained by $Tr(\tilde{\rho}M)$. Finally, the ODMR signal can be written as:

$$S(f) = S(\infty)\left[1 - \frac{C(\Delta\nu/2)^2}{(f - f_r)^2 + (\Delta\nu/2)^2}\right] \quad (2.6)$$

where the resonance frequency f_r is magnetic field dependent as introduced in (2.2); $S(\infty)$ is the photoluminescence level when microwave is far detuned:

$$S(\infty) = \frac{\beta\Gamma_1 + \alpha(\Gamma_1 + \Gamma_p)}{2\Gamma_1 + \Gamma_p} \quad (2.7)$$

The ODMR contrast C is given by:

$$C = \frac{1}{2} \frac{(\alpha - \beta)\Gamma_p}{(\alpha + \beta)\Gamma_1 + \alpha\Gamma_p} \frac{\Omega^2}{\Omega^2 + \Gamma_2(2\Gamma_1 + \Gamma_p)} \quad (2.8)$$

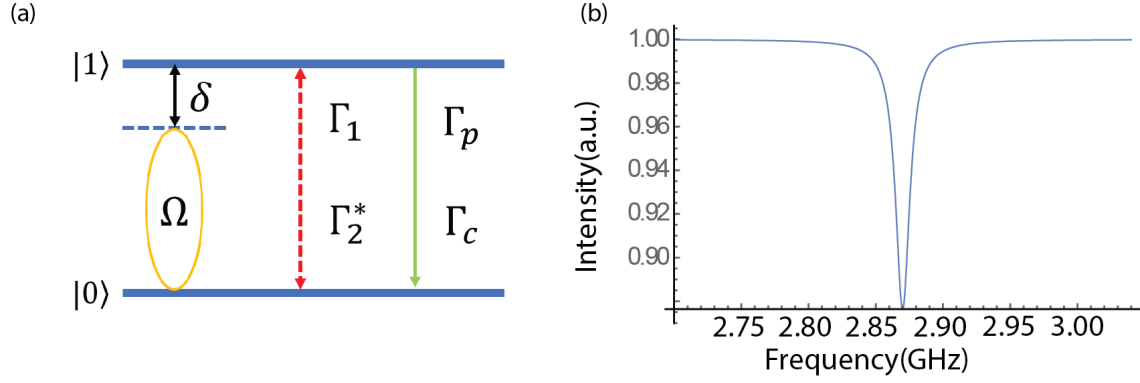


Figure 10: (a) 2-level model for NV^- ground spin state. δ is the detuning; Ω is the Rabi frequency; Γ_1 is the intrinsic relaxation rate of the population from a spin-lattice interaction; Γ_2^* is dephasing rate of the coherence; Γ_p is the pumping laser induced population polarization rate to ground spin state $|0\rangle$. Γ_c is the pumping laser induced decoherence rate. (b) Simulation of an ODMR signal follows equation (2.6), where $\alpha = 1.0$, $\beta = 0.7$, $\Gamma_1 = 2\pi \times 1.0 \times 10^3$, $\Gamma_2^* = 2\pi \times 2.0 \times 10^5$, $\Gamma_p = 2\pi \times 5.0 \times 10^6$, $\Gamma_c = \Gamma_p/2$, $\Omega = 5.0 \times 10^7$. All rates are typical values [10] from a bulk diamond sample and in unit of rad/s.

where $\Gamma_2 = \Gamma_2^* + \Gamma_c$. The linewidth is given by:

$$\Delta\nu = \frac{1}{\pi} \sqrt{\Gamma_2^2 + \frac{\Omega^2 \Gamma_2}{2\Gamma_1 + \Gamma_p}} \quad (2.9)$$

It is clear from equation (2.6) that an ODMR signal follows a Lorentz line shape. Considering the energy splitting induced by strain field and external magnetic field, as well as the possible four orientations of the defects in an ensemble of NVs sample, there are at most eight dips exist simultaneously on the ODMR spectrum. Although the condition that microwave only drives between two states is not always satisfied (the $|\pm 1\rangle$ state are not far away separated), the simplest assumption to fit a multi-dip ODMR spectrum is still a combination of multiple single-Lorentz line shape. This fitting method also seems to be used in references [58, 59, 55]. Therefore, we will also use multi-Lorentz line shape to fit our ODMR spectrum from ensemble of NV centers and validate the assumption from fitting parameters.

2.1.5 Preparing Superposition between $|+1\rangle$ and $|-1\rangle$ Spin State

We can also prepare the superposition state between $|+1\rangle$ and $|-1\rangle$ spin state. The similar rotating frame Hamiltonian can be written for a spin-1 system as [6]:

$$\tilde{H} = \sum_{i=\pm 1} -\hbar\delta_i|i\rangle\langle i| + \frac{1}{2}\hbar\Omega_i(|0\rangle\langle i| + |i\rangle\langle 0|) \quad (2.10)$$

In a simple case, we restrict to the symmetric conditions where we let $B_z = 0$, and use one microwave with the same detuning $\delta_i \equiv \delta$ and Rabi frequency $\Omega_i \equiv \Omega$ for both transitions in Figure 11. Hamiltonian (2.10) couples the $|0\rangle$ state to a bright superposition $|b\rangle = (|-1\rangle + |+1\rangle)/\sqrt{2}$, while the dark superposition $|d\rangle = (|-1\rangle - |+1\rangle)/\sqrt{2}$ remains decoupled. The eigenstates solved from (2.10) are $|d\rangle$, $|g\rangle = \cos(\phi)|0\rangle - \sin(\phi)|b\rangle$, $|e\rangle = \cos(\phi)|b\rangle + \sin(\phi)|0\rangle$, with $\tan(2\phi) = -\sqrt{2}\Omega/\delta$. The eigenvalues are $\omega_d = -\delta$, $\omega_e = (-\delta + \sqrt{\delta^2 + 2\Omega^2})/2$, $\omega_g = (-\delta - \sqrt{\delta^2 + 2\Omega^2})/2$. The parameter δ and Ω can be chosen, then time evolution with the Hamiltonian can bring a initial state to a desired superposition state.

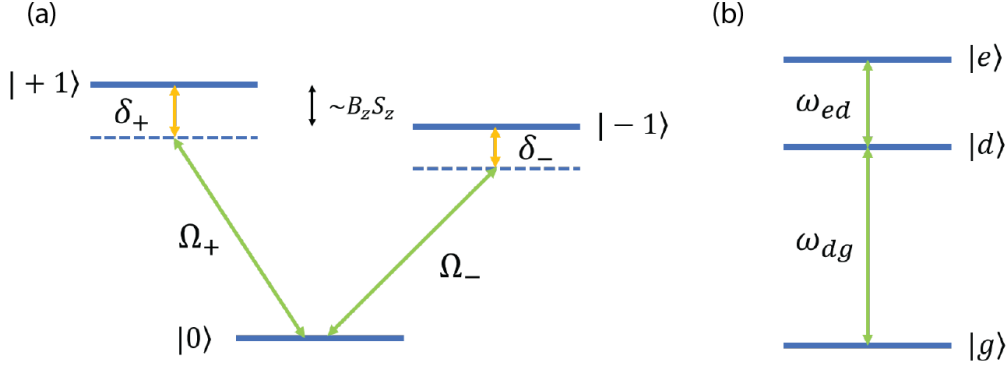


Figure 11: The scheme to prepare superposition between $|+1\rangle$ and $|-1\rangle$ spin state. (a) Two impulsive microwave with different frequencies can be used to drive $|0\rangle$ to $|\pm 1\rangle$ separately. δ_{\pm} are the detuning and Ω_{\pm} are the Rabi frequencies (b) The three eigenstates solved by Hamiltonian (2.10), which are the superpositions of $|0\rangle$ and $|\pm 1\rangle$.

2.2 A SCHEME TO CREATE LARGE QUANTUM SUPERPOSITION STATE

In quantum optics, a cat state is defined as the coherent superposition of two coherent states with opposite phase:

$$|cat\rangle \propto |+\alpha\rangle + |-\alpha\rangle \quad (2.11)$$

With the NV^- spin state manipulation mechanism, a scheme for coupling the NV^- spin in a trapped diamond to the motion of the diamond has been proposed through a strong gradient magnetic field. The scheme for creating a large quantum superposition state (or a cat state) for the mechanical motion of the trapped diamond has also been proposed theoretically [6, 11]. In this section, I will introduce a simplified version of the large superposition state creation mechanism described in reference [11].

The oscillatory motion of a trapped diamond in a harmonic potential well and the spin of an NV center in the trapped diamond are both initialized to the ground state(Figure 12):

$$|0\rangle_m \otimes |0\rangle \quad (2.12)$$

where $|0\rangle_m$ indicates the motion state with $n = 0$ and $|0\rangle$ denotes the spin-0 ground state for a NV center. The motion of the trapped diamond and the spin of the NV center are coupled through a gradient magnetic field (B in Figure 9(a) now is a z dependent B field along the NV axis). Without microwave driving, the effective Hamiltonian for the coupled system can be written as:

$$H = H_{NV} + \hbar\omega_m a_m^\dagger a_m + \lambda S_z (a_m^\dagger + a_m) \quad (2.13)$$

where ω_m is the angular frequency of the particle's oscillation in one dimension; a_m^\dagger, a_m are the creation and annihilation operators of the motional phonon mode, where $a_m^\dagger a_m = n$, the phonon number in this mode; S_z is the spin z operator for the NV ground state spin; λ characterizes the coupling strength of the system:

$$\lambda = g\mu_B G_m a_0 / \hbar \quad (2.14)$$

where g is lande factor; μ_B is Bohr magneton; G_m is the magnetic gradient along the oscillation dimension; $a_0 = \sqrt{\hbar/2m\omega_m}$ is the zero point amplitude of the trapped diamond's oscillation; m is the mass of the trapped diamond. Now suddenly flip the spin state to the superposition state $(|+1\rangle + |-1\rangle)/\sqrt{2}$ with impulsive microwave, the initial state of the system is changed to:

$$|\Phi(t = 0)\rangle = |0\rangle_m \otimes (|+1\rangle + |-1\rangle)/\sqrt{2} \quad (2.15)$$

then the time evolution under the effective Hamiltonian (2.13) will bring the system to an entangled cat state just like a Stern—Gerlach experiment :

$$|\Phi(t = \frac{\pi}{\omega_m})\rangle = (|+1\rangle|+D_m/2\rangle + |-1\rangle|-D_m/2\rangle)/\sqrt{2} \quad (2.16)$$

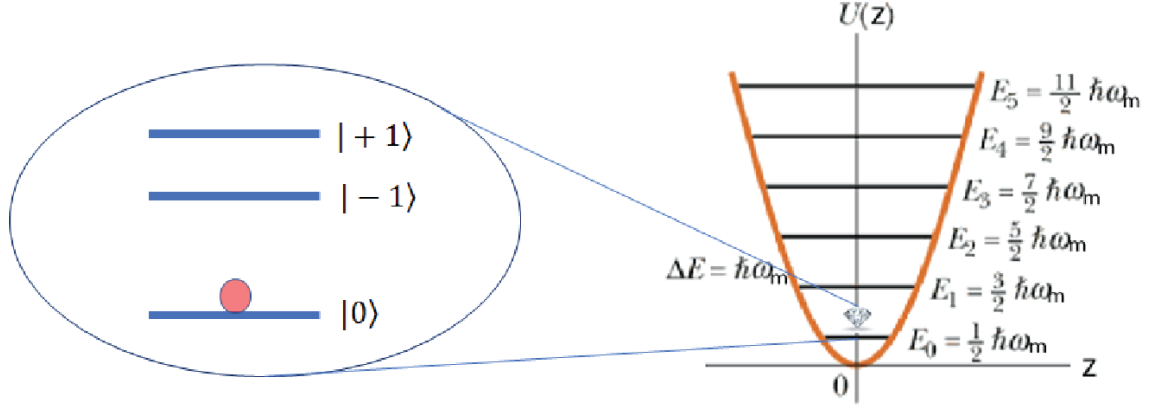


Figure 12: The scheme in reference [11] to create a large quantum superposition motion state. The quantum system is initialized to $|0\rangle_m \otimes |0\rangle$ for motional phonon and spin state.

where $|\pm D_m/2\rangle$ are the displaced states (coherent states) at half of the oscillation period:

$$|\pm D_m/2\rangle = (-1)^{a_m^\dagger a_m} e^{S_z D_m (a_m^\dagger - a_m)/4a_0} |0\rangle_m \quad (2.17)$$

where $D_m = 8\lambda a_0/\omega_m = 4g\mu_B G_m/(m\omega_m^2)$ is the maximum displacement at the half period of the oscillation (Figure 3 in reference [11]). Spin projection $S_z = \pm 1$ corresponds to the opposite signs of the displacement. To disentangle the spin and the motion state, impulsive microwaves at different frequencies can be applied to $|\pm 1\rangle$ to flip them to $|0\rangle$ state without interacting each other (spin 1 and -1 are in different magnetic field due to the displacement). Finally we obtain a standard cat state for the oscillatory motion of the trapped diamond as:

$$|\Phi\rangle = (|+D_m/2\rangle + |-D_m/2\rangle)/\sqrt{2} \quad (2.18)$$

3.0 OPTICAL TRAPPING OF NANODIAMONDS

In this project, we use a single laser beam for trapping diamond crystals with a dimension of 100 nm under atmospheric pressure or vacuum. Simulations indicate a trapped nanodiamond will become a high frequency, high Q harmonic oscillator in an ultra-high vacuum environment. The nanodiamonds (NDs) we used in experiments have built-in NV centers, which have been proved to be a robust quantum spin system at room temperature. Following the theoretical proposal in [11], we try to build up the experimental setup towards creating superposition for the mechanical motion state of a nano-sized diamond. Progress has been made in successfully trapping NDs and pumping down to the 10^{-1} torr environmental pressure. The Optically Detected Magnetic Resonance (ODMR) has been observed from the NV centers in these trapped NDs. However, the heating and burning of these NDs when we pump out to higher vacuum indicates much cleaner diamond crystals are needed than the commercially available ones nowadays.

3.1 INTRODUCTION

During the last decade, several types of systems have been proposed and created to study the quantum behavior of macroscopic objects. A major drawback of using smaller mechanical systems which increases their frequency is that the quality factor Q decreases. The associated decoherence of quantum states then limits the time for performing operations with these states [60]. An optically trapped nano-particle has been theoretically [19, 61] and experimentally [62, 63] studied as a novel mechanical oscillator. The Q factor of such an oscillator can range from 10^7 to 10^{12} depending on the vacuum, which is much higher than

other solid state systems. On the other hand, it is a key challenge to couple isolated NV centers if they are over 20 nm away from each other due to their atomic-scale size and localized wave functions. If the trapped particle is a nano-diamond containing NV centers, we can couple the spins of NV center with the mechanical motion of the diamond. The mechanical phonon mode will serve as a messenger among NV center quantum network and therefore solve the problem of long-distance coupling between NV centers. Hence, this project can potentially lead to the quantum interface between spin qubits and phonon mode as a part of a quantum network.

3.2 PRINCIPLES OF OPTICAL TRAPPING

3.2.1 Forces on A Trapped Particle

Qualitatively, a dielectric particle whose refractive index is larger than its surrounding's can be lifted and confined in the space with a focused single laser beam. There are three forces acting on the particle: scattering force, gradient force and gravity. The scattering force tends to push the trapped particle along the laser propagating direction, while the gradient force pulls the particle towards the highest intensity spot of the laser beam. In the case of a Gaussian beam, the highest intensity region is the center of laser focus. If the technique needs gravity to balance the scattering force, it is called optical levitation. This method is often used for large particle (tens of microns) where the gradient force in any direction is insufficient to balance gravity. The laser can only propagate upwards in this experimental setup. On the other hand, when the particle is small (tens or hundreds of nanometers), the magnitude of gradient force can exceed scattering force and gravity. In this case, the gradient force confines a particle in all three directions, and this technique is called optical trapping. Optical trapping setup allows the laser to propagate in all possible directions in experiments. Arthur Ashkin first realized the optical levitation of a 20 micron sized glass bead in the air in 1971, and the first optical trapping of a dielectric particle in the air was demonstrated in 1997 [64, 65]. If we treat the trapped particle as a small spring, for small displacement (~ 150 nm)

around the equilibrium point [66], the restoring force is proportional to the displacement, and the spring constant is called “stiffness”. Compared with optical trapping, the optically levitated particle usually has much smaller stiffness and therefore smaller intrinsic trapping frequency (~ 20 Hz) [67].

Quantitatively, the forces on a trapped particle are usually studied in two regimes based on scales of particle size and trapping laser wavelength. When the wavelength used to trap is far smaller than the particle size ($\lambda \ll d$), it is known as Mie scattering regime and the forces can be calculated with ray optics. In this regime, a trapped spherical particle can be treated as a micro-lens, and the optical rays will be refracted after they go through the particle. From the change of linear momentum of the optical rays, one can calculate the net restoring force on the particle. However, the geometrical optics poorly describes the light field in the vicinity of laser focus as well as it neglects physical optics phenomena such as diffraction and interference. The accuracy of ray optics calculation is limited to a particle that is at least 20 times larger than the wavelength of trapping laser [68, 69].

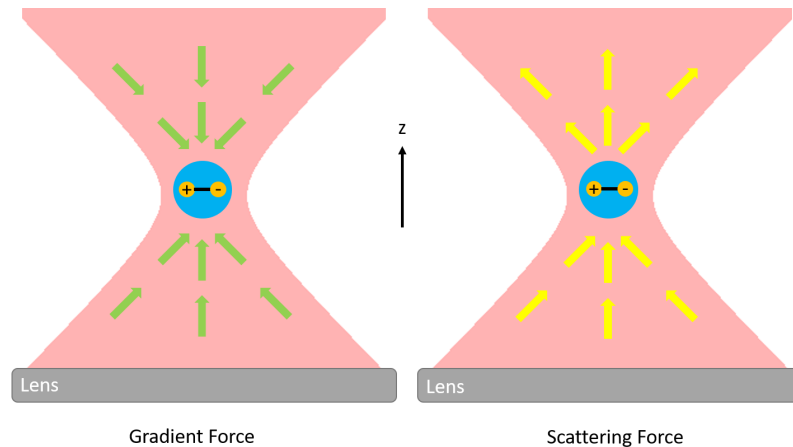


Figure 13: Illustration of depicting nano-particle in Rayleigh scattering regime. Laser propagates along z direction.

When the wavelength is much greater than the particle size ($\lambda \gg d$), it is known as Rayleigh scattering regime and the forces can be calculated by treating the particle as an electric dipole (Figure 13). This case is the situation in our experiments, and the gradient force is

shown analytically below. When a dielectric particle is polarized in the electric field. The induced dipole can be written as [70]:

$$\mathbf{p}(\mathbf{r}, t)_{dipole} = 4\pi n_{med}^2 \varepsilon_0 r^3 \left(\frac{n_r^2 - 1}{n_r^2 + 2} \right) \mathbf{E}(\mathbf{r}, t) \quad (3.1)$$

where the relative refractive index of the particle is the ratio of particle index over media index, $n_r = n_{part}/n_{med}$. ε_0 is vacuum permittivity, r is the radius of the particle. Due to the nature of a dipole (opposite charge separated by an infinitesimal distance), the Coulomb force can be written to the first order of electric field as:

$$\mathbf{F}_{dipole}(\mathbf{r}, t) = (\mathbf{p}_{dipole}(\mathbf{r}, t) \cdot \nabla) \mathbf{E}(\mathbf{r}, t) \quad (3.2)$$

In a uniform field, this expression yields zero. In a non-uniform, time-varying field, the time averaging of the gradient force on a dipole can be written as [70]:

$$\mathbf{F}_{grad}(\mathbf{r}) = \pi n_{med}^2 \varepsilon_0 r^3 \left(\frac{n_r^2 - 1}{n_r^2 + 2} \right) \nabla |\mathbf{E}(\mathbf{r})|^2 \quad (3.3)$$

where the period averaging $\langle \mathbf{E}^2(\mathbf{r}, t) \rangle_T = \frac{1}{2} |\mathbf{E}(\mathbf{r})|^2$. Meanwhile, the scattering force is given by the product of time averaging Poynting vector $\langle \mathbf{S}(\mathbf{r}, t) \rangle_T$ and scattering cross-section σ [71]:

$$\mathbf{F}_{scat}(\mathbf{r}) = \frac{n_{med} \sigma \langle \mathbf{S}(\mathbf{r}, t) \rangle_T}{c} \quad (3.4)$$

where the scattering cross-section $\sigma = \frac{8}{3} \pi k^4 r^6 \left(\frac{n_r^2 - 1}{n_r^2 + 2} \right)^2$, c is the speed of light, k is the wavenumber. Furthermore, the intensity of the laser beam is related to the time averaging Poynting vector and electric field strength by:

$$I(\mathbf{r}) \hat{z} = \langle \mathbf{S}(\mathbf{r}, t) \rangle_T = \frac{n_{med} \varepsilon_0 c}{2} |\mathbf{E}(\mathbf{r})|^2 \hat{z} \quad (3.5)$$

where \hat{z} is laser propagation direction. In our project, we are trapping diamond in air or vacuum, so if substitute equation (3.5) into (3.4)(3.3), we get:

$$\mathbf{F}_{scat}(\mathbf{r}) = \frac{128 \pi^5 r^6}{3 \lambda^4 c} \left(\frac{n_r^2 - 1}{n_r^2 + 2} \right) I(\mathbf{r}) \hat{z} \quad (3.6)$$

$$\mathbf{F}_{grad}(\mathbf{r}) = \frac{2 \pi r^3}{c} \left(\frac{n_r^2 - 1}{n_r^2 + 2} \right) \nabla I(\mathbf{r}) \quad (3.7)$$

where λ is vacuum wavelength of laser beam [72]. It is clear from equation (3.6)(3.7) that the scattering force decreases much faster than the gradient force as the size of particle decreases. Below some point, the gradient force will dominate and form three-dimensional optical trapping. Furthermore, if we apply a paraxial approximation to the Gaussian beam used for trapping, the magnitude of gradient forces on axial(\hat{z}) and transverse direction is related to the numerical aperture (NA) of the focused laser beam [62]:

$$F_{grad-axial} \propto \frac{NA^6}{\lambda^4} P \quad (3.8)$$

$$F_{grad-trans} \propto \frac{NA^4}{\lambda^4} P \quad (3.9)$$

where P is the power of the trapping laser. When the effective aperture of an objective lens is filled with a laser beam, NA of the lens equals the NA of the laser beam. From equation (3.8)(3.9), we can see for a small particle, using an objective lens with a high numerical aperture(NA) and increasing trapping laser power will both enhance the stiffness of optical trapping. Integrating equation (3.7), we can further obtain the expression of the trapping potential energy:

$$U(\mathbf{r}) = -\frac{2\pi r^3}{c} \left(\frac{n_r^2 - 1}{n_r^2 + 2} \right) I(\mathbf{r}) + Const \quad (3.10)$$

where $Const$ is an integration constant. From above discussion, it seems that smaller size makes the trapping easier. However, this is not the case. Under equilibrium condition, the particle will have $\frac{1}{2}k_B T$ average energy for each of its motion freedom based on the equipartition theorem. T is the environmental temperature if the particle is thermalized with surrounding air molecule through collisions. If active damping force is applied to the particle and reach equilibrium, $T = T_{CM}$ represents the center of mass motion of the particle. The total energy in a thermal equilibrium condition follows the Boltzmann distribution. Therefore, for a one-dimensional oscillator(or one direction of a three-dimensional oscillator which is completely disentangled with the others), the average kinetic energy $\frac{1}{2}k_B T$ will not reduce with decreasing size of the particle, but the depth of trapping potential well will be smaller from equation (3.10). Therefore, there is a possibility that the instantaneous kinetic energy of the trapped particle exceeds the depth of the potential well and jump out of trap due to its thermal motion (Brownian).

It is notable that the paraxial approximation in equation (3.8)(3.9) will only work better when the lens $NA \ll 1$. This is not the case when we trap a particle in air or vacuum. Also, we did not discuss the case when $\lambda \approx d$. Therefore, we need a more precise method to describe the field around laser focus, and numerical method is a better choice. One rigorous method to describe the field around the particle is **Generalized Lorentz-Mie Theory**. In this method, the field is treated as in a scattering problem. The incident field \mathbf{E}_{inc} and the scattering field \mathbf{E}_{scat} can be written as [73, 72]:

$$\mathbf{E}_{inc}(\mathbf{r}) = \sum_{n=1}^{\infty} \sum_{m=-n}^n a_{nm} \mathbf{M}_{nm}^{(2)}(k\mathbf{r}) + b_{nm} \mathbf{N}_{nm}^{(2)}(k\mathbf{r}) \quad (3.11)$$

$$\mathbf{E}_{scat}(\mathbf{r}) = \sum_{n=1}^{\infty} \sum_{m=-n}^n p_{nm} \mathbf{M}_{nm}^{(1)}(k\mathbf{r}) + q_{nm} \mathbf{N}_{nm}^{(1)}(k\mathbf{r}) \quad (3.12)$$

where $\mathbf{M}_{nm}^{(1)}, \mathbf{N}_{nm}^{(1)}$ are outgoing TE and TM vector spherical wavefunctions (VSWFs); $\mathbf{M}_{nm}^{(2)}, \mathbf{N}_{nm}^{(2)}$ are incoming TE and TM vector spherical wavefunctions. With the coefficients $a_{nm}, b_{nm}, p_{nm}, q_{nm}$ for each mode, one can compute the net force on the trapped particle.

Finite Difference Time Domain (FDTD) 3D full vector simulation of electromagnetic field gives another way to rigorously solve the field around the trapped particle. The Maxwell stress tensor then is used to compute the net force on the particle based on the field distribution [74]:

$$\mathbf{T} = \varepsilon_0 \varepsilon \mathbf{E} \mathbf{E} + \mu_0 \mu \mathbf{H} \mathbf{H} - \frac{1}{2} (\varepsilon_0 \varepsilon E^2 + \mu_0 \mu H^2) \mathbf{1} \quad (3.13)$$

$$\mathbf{F} = \oint_{\partial V} \langle \mathbf{T} \cdot \mathbf{n} \rangle dS \quad (3.14)$$

where $\mathbf{1}$ is the unit dyad, ε and μ are the permittivity and permeability. $\langle \dots \rangle$ is the time averaging and \mathbf{n} is the normal vector of the enclosed surface ∂V . With the above two rigorous numerical methods, the net force on the particle can be solved directly. So it is not necessary to distinguish scattering force and gradient force. The latter method is used for the simulation in the next section.

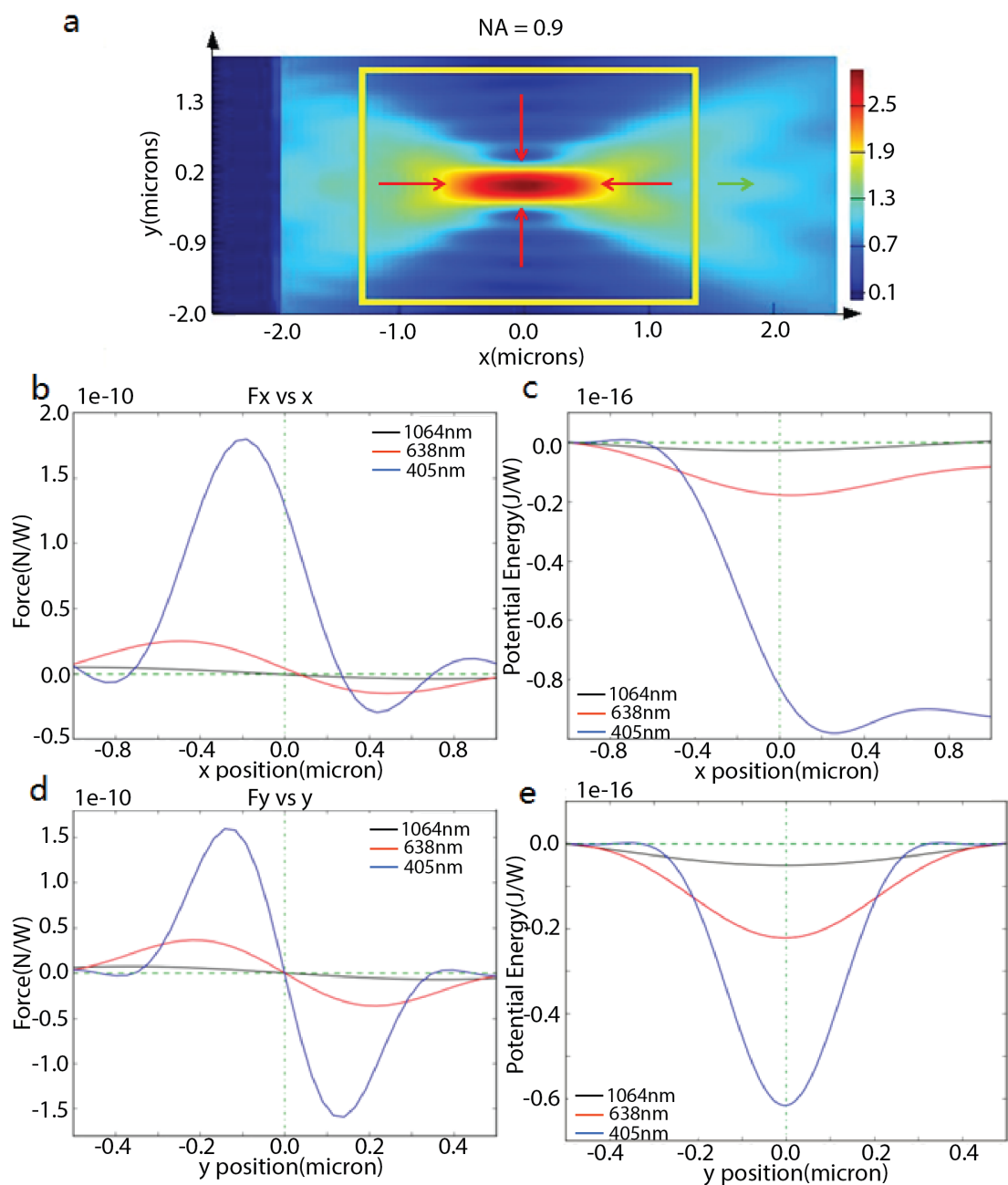


Figure 14: (a)The field profile for a tightly focused Gaussian beam by an 0.9 NA objective and directions of gradient and scattering force(b)Axial Force (F_x) for a 100 nm sized diamond(c)Potential energy along x direction for a 100 nm sized diamond(d)Transverse Force (F_y) for a 100 nm sized diamond(e)Potential energy along y direction for a 100 nm sized diamond

3.2.2 Simulation of the Trapping Force

Here I used a commercial FDTD software (FDTD Solutions from Lumerical co.) to do the following simulations. The net force on a spherically shaped diamond when it has a small

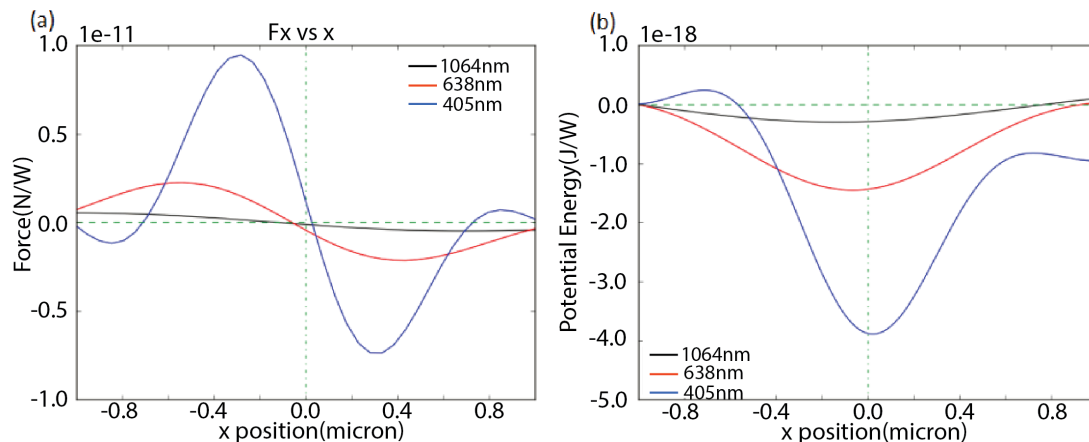


Figure 15: (a) Axial Force (F_x) for a 50nm sized diamond (b) Axial potential energy for a 50nm sized diamond

displacement around the beam waist at $x = 0$ is computed. The beam is launched along x-direction (polarized along y) in the simulation and focused with a 0.9 NA objective, as in our experiment. Figure 14 shows the simulation results of the force along the axial direction and transverse direction of the incident beam. The size of nanodiamond used in simulation is 100 nm.

The trapping force produced by a 405 nm laser is an order of magnitude higher than that of a 1064 nm laser. However, the shorter the wavelength is, the smaller the trapping volume is. Compared to 638 nm laser, the effective trapping region of the 405 nm laser is reduced nearly by a factor of 2 on both axial and transverse direction, resulting a factor of 8 decrease in the trapping volume. The ratio between particle size and trapping wavelength $\Lambda = r/\lambda$, is another key parameter. The larger the Λ is, the bigger the influence comes from the scattering force, which agrees with the equation (3.6). More importantly, the larger Λ is, the more asymmetric the trap is on the axial direction, such as the potential energy curve of 405 nm in Figure 14(c). It is clear the asymmetry of the axial trapping further decreases

the trapping volume, which may end up with lower trapping efficiency. The 50 nm particle simulation brings back the symmetry on axial direction in Figure 15. Therefore, the selection of this ratio is important to increase the trapping efficiency, which we experimentally proved it in the next section. The transverse direction is always symmetric due to the symmetry of the system. Meanwhile, we also calculated the trapping frequencies for each wavelength. The transverse frequencies are larger than the axial frequencies and they are typically hundreds of kHz. Figure 16 shows calculation results in the table.

λ (nm)	Trap freq. (x) (kHz)	Trap freq. (y, z) (kHz)
1064	100.3	203.6
637	274.2	587.8
405	665.1	1487.1

Figure 16: Calculations of trapping frequencies on different directions for a 50nm diamond using 0.1 W trapping laser power.

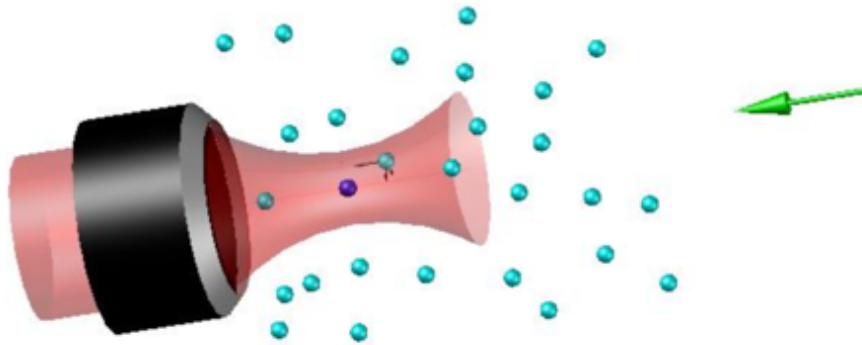


Figure 17: Diagram of depicting the loading procedure. The nanodiamonds(blue dots) fly against the light propagation direction and get trapped at the laser focus (dark blue dot).

3.3 LOADING NANODIAMONDS

3.3.1 Nebulizing Nanodiamonds Suspended in Solvent

This loading procedure is operated in air. The vibration of the piezo in a commercial nebulizer(MABIS 40-370-000) will create liquid droplets in micron size. The size of the droplet depends on the shaking amplitude and frequency. The nebulizer we used in our experiment can generate droplets in 5~10 μm and gives enough initial kinetic energy for the droplet to fly out of the nebulizer through the tubing on the nebulizer. Here, we just simply replace the pure water(or medicine) with a regular solvent such as ethanol or IPA. 100 nm nanodiamonds(1 mg/mL, 500NV on average in each diamond, Adamas Nanotechnology) are mixed into the solvent, and the solution was ultrasonicated for over 1 hour to break the agglomeration of these nanocrystals. The dilution we chose was 1:100. Droplets carrying one or several diamonds fly to laser trapping region with a certain amount of kinetic energy. They will collide with air molecules and slow down when they arrive at the trapping region. The solvent evaporates fast enough that only the solids left on the way to trap. When a diamond falls into the trap and does not have enough kinetic energy to escape, it will be trapped (Figure 17). The wavelength of the trapping laser was 637 nm and 532 nm at first. However, after hundreds of attempts, we found it is difficult to trap with these parameters. Based on our simulation before, we believe the asymmetry of the potential well on the laser propagation direction is responsible for the escape of a trapped diamond. The solution we finally found is to increase the wavelength of the trapping laser and decrease the size of the diamond, which agrees our simulation results. In the following experiment, we use 1064 nm laser as the trapping laser while we reduce the diamond size to 40 nm(15NV, Adamas Nanotechnology). With these new parameters, we can successfully trap diamond over 50 percent of attempts, and they can stay trapped for days.

3.4 OPTICAL TRAPPING OF DIAMOND IN AIR

3.4.1 Experimental Setup

We first tried optical trapping of diamond in the air. The trapping laser is optimized at 1064 nm. The trapping laser is integrated with a home-made confocal microscope, which enables us to scan and collect the photoluminescence emitted from the NV centers in the trapped ND. The setup diagram is shown in Figure 18 and photos in Figure 19. With this setup, we successfully trapped 40 nm ND (~ 15 NV in each ND on average) efficiently in the air (Figure 20), where the trapping lifetimes are at least hours before we interrupt them.

Stability is a key feature of an optical trap, which significantly affects the average photoluminescence (PL) level and the quality of the ODMR signal when there is a non-uniform magnetic field. Two major optimizations were made to stabilize the trapped ND in the air. As we know, most objectives cannot be corrected for 1064 nm (trapping laser), 532 nm (pumping laser) and 600~800 nm photoluminescence simultaneously. Especially for 1064 nm and 532 nm, the experimentally measured chromatic aberration is in the order of microns. To trap the diamond and collect the photoluminescence from the trapped ND, it is necessary to compromise one laser to the other. If we choose to converge the trapping laser a little bit before injecting into the objective by a long focal length converging lens, we find the trapping becomes less stable. This is because the objective is designed for a collimated incident beam. The angled incidence beam will cause a lower effective NA when the beam is focused. So does the stiffness of the trap. Therefore, we choose to sacrifice a little bit quality of the confocal microscopy by diverging the green laser (as well as the photoluminescence collection path) to match the trapping position using an achromatic lens combination (Figure 18). In this way, we maximize the trapping ability of the high NA objective.

Another instability source is from the wire to deliver microwave. To deliver the microwave close to the trapped ND, a suspended 30 μm gold plated tungsten wire is positioned near the trap after an ND is captured. However, we find the suspended wire is oscillating while the microwave is delivering, which induces oscillations to the ND through the air. We believe

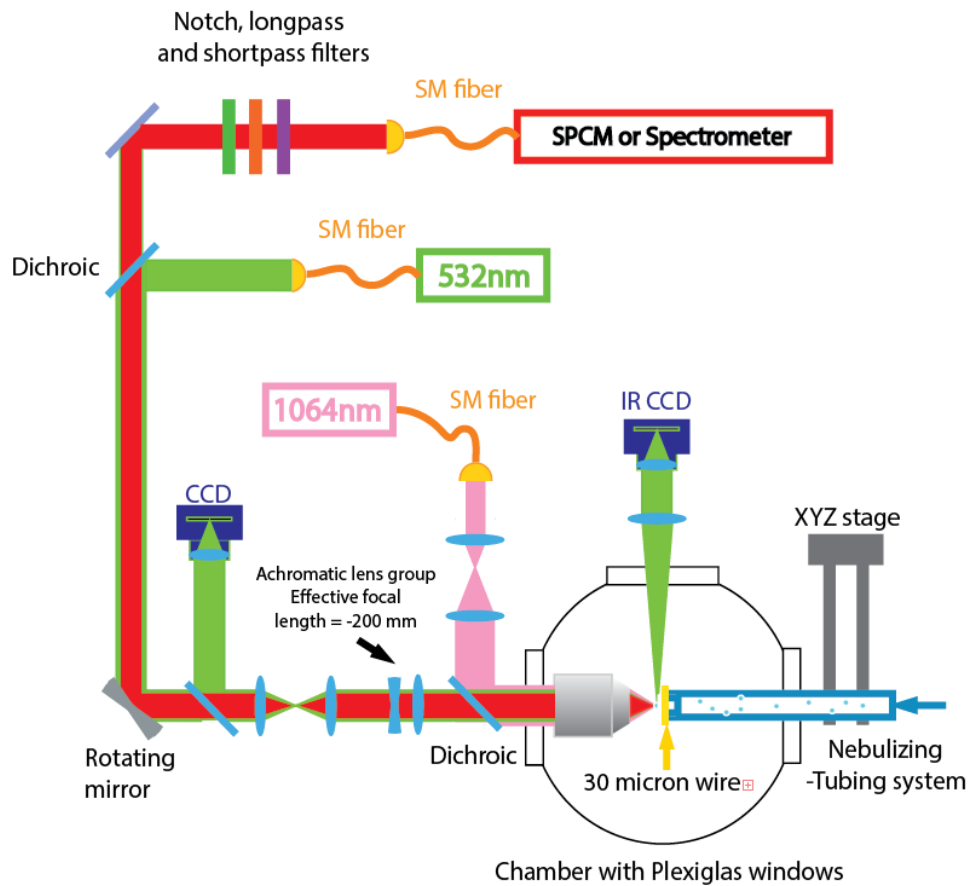


Figure 18: Confocal integrated optical trapping system. The 0.9 NA objective is placed in the chamber. 1064nm trapping laser and green excitation laser are focused by the objective. An achromatic lens group is used to correct the color aberration between the green laser and the trapping laser. Photoluminescence from NV centers in the trapped diamond is also collected by the objective and detected by a single photon counting module (SPCM) or a spectrometer. A 30 μm wire is placed close to the focus of trapping, which delivers the microwave to the trapped diamond for an ODMR experiment. Two cameras are used to collect the scattering image of the trapped diamond.

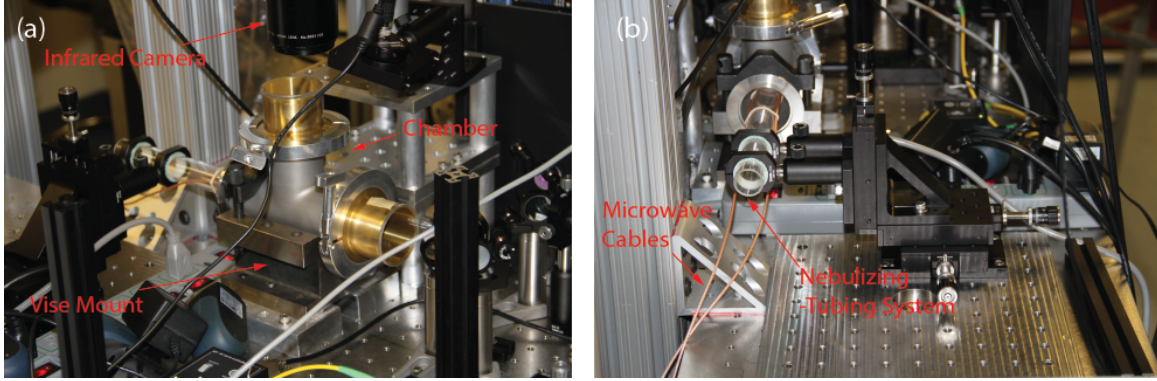


Figure 19: Photos of the chamber and nebulizing tube system used in optical trapping

the thermal expansion of the wire takes credit for the wire's oscillation. So the modification we made was attaching the wire to one edge of a thin cover slip (~ 0.17 mm thick) and adhere them together, which limited the oscillation of the wire.

3.4.2 Photoluminescence Spectrum from NV Centers in Trapped Diamonds

With the improvements above, we stabilized the trapped ND in the air and obtained the NV photoluminescence spectrum in Figure 21(a) from a trapped diamond. A ZPL emission peak at about 637 nm can be seen clearly on the NV photoluminescence spectrum, which is the fingerprint of NV centers in diamond.

3.4.3 Spin Detection from NV Centers in Trapped Diamonds

With the gold plated tungsten wire delivering microwave to the trapped diamond, we successfully observed the ODMR signal from NV centers in the trapped diamond (Figure 21(b)). More importantly, the stability now allows us to split Zero-Field ODMR signal by introducing a DC magnetic field close to the trapped ND (Figure 22). The split corresponds to the Zeeman splitting of spin 1 and -1 ground spin states as introduced in Chapter 2.

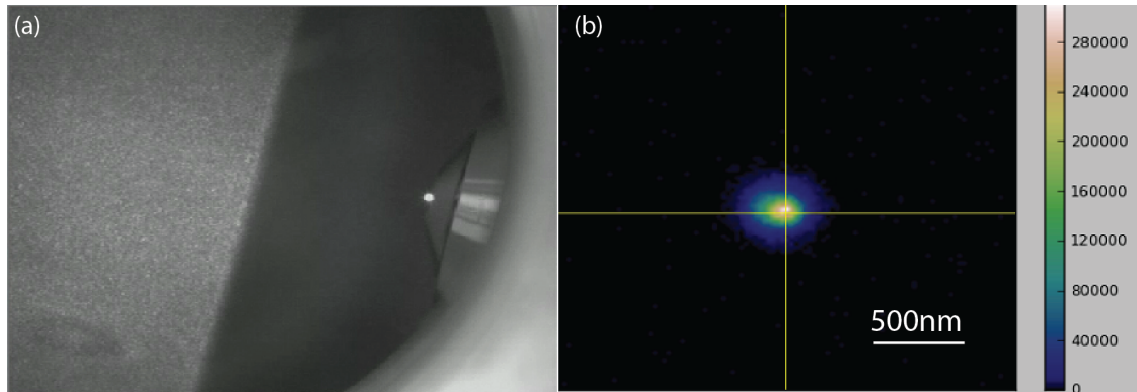


Figure 20: (a) Photo of an optically trapped nanodiamond in atmosphere pressure by 0.9 NA objective lens in the chamber. (b) The Photoluminescence image of the NV centers in the trapped diamond. The optics are optimized for 1064 nm laser focus, the effective NA of green illumination and photoluminescence collection path is smaller than 0.9, which explains the larger size of the diamond on the image compared to the diffraction limit of 0.9 NA.

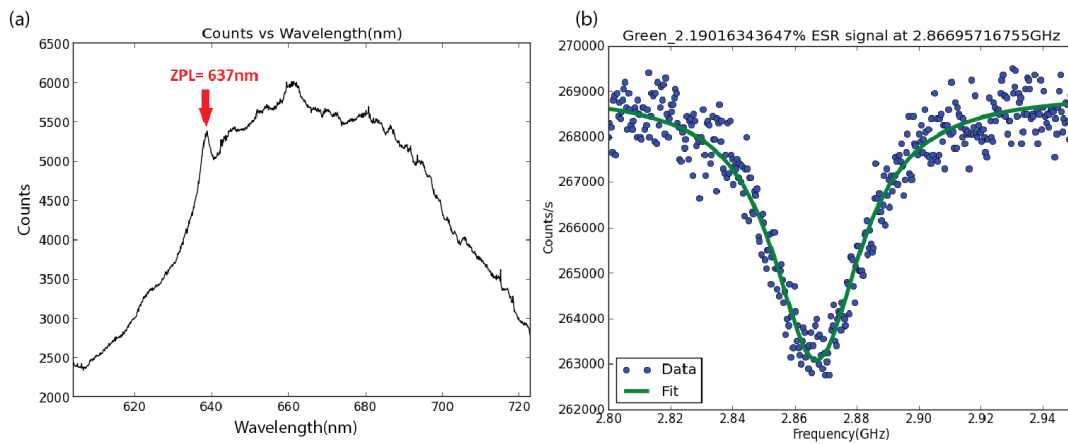


Figure 21: (a) The Photoluminescence spectrum from NV centers detected from a trapped diamond. The fingerprint is the zero-phonon-line of 637 nm. (b) Detected ODMR signal from NV centers in the trapped diamond without an external magnetic field.

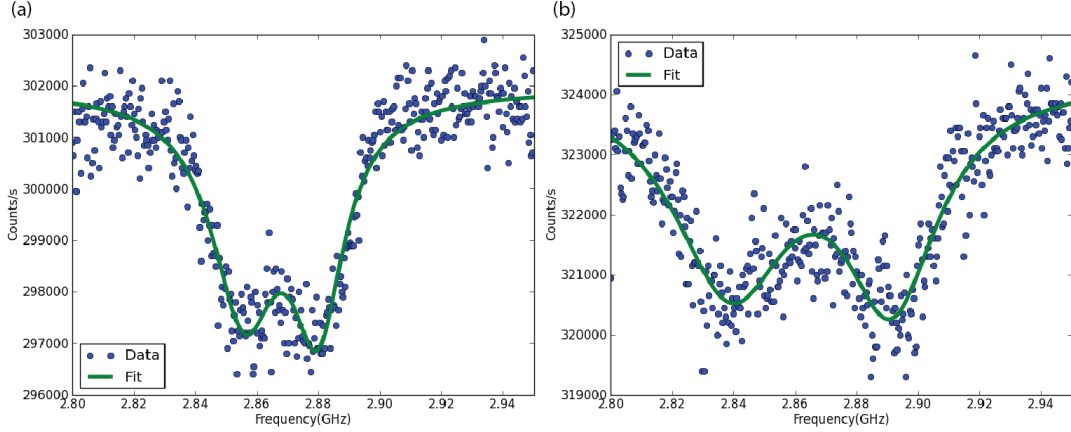


Figure 22: (a)The detected ODMR signal splits when a magnet is placed close to it. (b)Magnet moved closer to the trapped diamond.

3.4.4 Temperature Measurement Using NV Centers in Trapped Diamonds

The zero-field splitting is about 2.870 GHz for NV centers in diamond at room temperature. The shift of ODMR signal is explained by the temperature dependence theory of NV ground state spin splitting. Theory indicates a Zero-Field-Splitting(ZFS) of the NV ground state spin is related to the lattice constant of the diamond. The thermal expansion of the lattice at different temperature takes responsibility for a thermally dependent $D(T)$ [58]. Later experiment points out the temperature relation is well described by [75]:

$$D(T) = a_0 + a_1T + a_2T^2 + a_3T^3 \quad (3.15)$$

T is the temperature of the diamond in Kelvin. From reference [75], $a_0 = 2.8697 \pm 0.0009GHz$, $a_1 = (9.7 \pm 0.6) \times 10^{-5}GHz/K$, $a_2 = (-3.7 \pm 0.1) \times 10^{-7}GHz/K^2$, $a_3 = (1.7 \pm 0.1) \times 10^{-10}GHz/K^3$. This yields a shift as $dD/dT = (-7.9 \pm 0.9) \times 10^{-5}GHz/K$ at 300 K. By Lorentz line shape fitting, we abstract the location of ODMR dip in Figure 21(b) at $2.8669 \pm 0.0002GHz$. From the location of our ODMR dip, we can estimate a temperature of 336 ± 12 K on the trapped diamond. We believe this heating effect is induced by trapping laser (100 mW used in power).

3.5 OPTICAL TRAPPING OF DIAMOND IN VACUUM

3.5.1 Our Results

Our next step in the experiment is to create a vacuum environment. Currently, the ND stays trapped till 1×10^{-1} torr. The reason that we lose the ND during the pumping can be complicated. We first thought about the air flow in the procedure of pumping. We ruled out that possibility by slowing down the pumping procedure with a controlled valve. Another group has reported that they successfully trapped silica beads of the similar size and pump down to 10^{-9} torr with no problem [62]. So in principle, based on the refractive index and transparency of diamond, the trapping of diamond by gradient force should be even stronger.

Considering the heating effect from trapping laser in air, another possible reason is the nano-diamonds themselves are heated up and vaporized or graphitized due to high laser power and diamond impurities. These impurities can be introduced when the NDs were synthesized and milled. Different from surface residue such as graphite, the acid cleaning procedure usually could not remove these impurities. Also, much higher absorption may occur when many defects like NV centers exist in the NDs. Therefore, the temperature of the diamond could be extremely high in vacuum and the diamond could escape or graphitize due to heating.

3.5.2 Estimation of the Temperature in High Vacuum

We try to calculate the temperature of the trapped diamond in high vacuum and to analyze whether it is possible to trap a diamond in high vacuum with laser heating. From the temperature measured under air condition, we can deduce the temperature of a trapped diamond in high vacuum. Under thermal equilibrium condition, the heat power absorbed by the trapped diamond should be the same as the heat power dissipated:

$$P_{absorb} = P_{dissipate} = P_{thermal-conduct} + P_{radiation} \quad (3.16)$$

where $P_{thermal-conduct}$ and $P_{radiation}$ are the heat dissipations through thermal contact with media and thermal radiation:

$$P_{absorb} = P_{laser} \frac{A_{ND}}{A_{spot}} \alpha_{absorb} d_{ND} \quad (3.17)$$

$$P_{thermal-conduct} = -k_{air} \nabla T(r) \cdot \mathbf{S}(r) \quad (3.18)$$

$$P_{radiation} = A_{surface} \sigma \varepsilon (T_{ND}^4 - T_0^4) \quad (3.19)$$

where $P_{laser} = 1.0 \times 10^{-1} W$ is the power of laser beam with a spot size $A_{spot} = 8.5 \times 10^{-14} m^2$ (Gaussian beam waist focused by a 0.9NA objective); the diamond has a diameter(thickness) $d_{ND} = 4.0 \times 10^{-8} m$ and a cross section $A_{ND} = 1.3 \times 10^{-15} m^2$; α_{absorb} denotes the absorption coefficient of the diamond. $k_{air} = 2.4 \times 10^{-2} W/(m \cdot K)$ is the thermal conductivity of the air at ambient condition, which is proportional to the environment pressure. Assuming the thermal dissipation is isotropic in air and the diamond is the center of the heat source, $\nabla T(r)$ is the gradient of temperature and $\mathbf{S}(r)$ is a enclosure surface area at distance r from the center. $A_{surface} = 5.0 \times 10^{-15} m^2$ is the surface area of the diamond; $\sigma = 5.7 \times 10^{-8} W \cdot m^{-2} \cdot K^{-4}$ is the Stefan-Boltzmann constant and we assume $\varepsilon = 1$ is the emissivity; T_{ND} is the surface temperature of the trapped diamond and $T_0 = 295 K$ is the environment temperature for the radiation.

Assuming the heat equation still holds when the particle size is comparable with the mean free path (See Appendix 3.7.1 for our justification), the temperature distribution can be obtained by solving the steady state of a heat equation in spherical coordinate:

$$\frac{\partial T}{\partial t} - \beta \nabla^2 T = 0 \quad (3.20)$$

where $\beta = 1.9 \times 10^{-5} m^2/s$ is the thermal diffusivity of the media, which does not affect the steady temperature distribution. Considering the spherical symmetry of the isotropic environment and assuming a spherical shape of the diamond, we can get:

$$T(r) = T_0 + \frac{(T_{ND} - T_0) d_{ND}}{2r} \quad (3.21)$$

where the boundary conditions are the surface temperature of the diamond T_{ND} and the room temperature at infinity $T_0 = 295 K$. Substitute (3.21) into (3.18) and together with

(3.16)-(3.19), we can reversely calculate the absorption coefficient $\alpha_{absorb} = 42cm^{-1}$ for the trapped diamond using the measured $T_{ND} = 336K$ at ambient pressure. This result is 5 orders larger than the value for a CVD bulk diamond, where $\alpha_{absorb} = 3.0 \times 10^{-3}cm^{-1}$. In high vacuum, only the radiation term matters. The internal temperature of diamond is calculated as $T_{ND} = 5.4 \times 10^4K$. Diamond cannot reach this temperature before it is completely graphitized ($\sim 2200K$ [76]) and therefore the current diamond sample cannot survive in high vacuum.

3.5.3 Review of Peer's Work at the Same Time

Right after we saw ODMR signal and began to organize our discovery for a publication, we found several concurrent publications from other groups reported similar results and problems for optical trapping nanodiamond in the vacuum. Major results come from the following three papers:

1. Neukirch, etc. [77] reports the observation of single NV photoluminescence and ODMR signal in air for a trapped nanodiamond.
2. Hoang, etc. [78] reports the ODMR signal dependence as the vacuum pressure goes down to single millibar regime.
3. Rahman, etc. [79] reports the burning and graphitization of commercially available nanodiamond with oxygen or vacuum condition.

So far no one has reported a successful levitation of nanodiamond in a better vacuum than our result. And they also attributed the problem to the laser heating effect due to the high power and poor diamond purity.

3.5.4 Key Parameters to Develop Optical Trapping of Diamond System

For a spin-mechanical coupling open quantum system, cooperativity $C = \frac{\lambda^2}{\Gamma_s \Gamma_{th}}$ is signifying quantum operation regime when $C > 1$ as introduced in Chapter 1. λ is the coupling strength and $\Gamma_s = \frac{2\pi}{T_2 N^s}$ is the spin decoherence rate, where T_2 is the coherence time of a single NV center; N is the number of dynamical decoupling cycles and $s=1$ is the efficiency

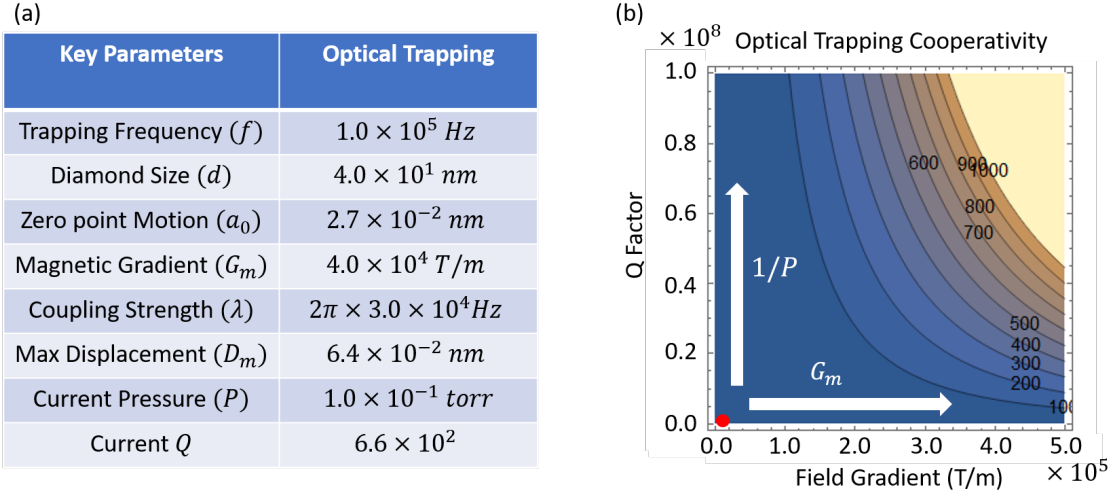
of a cycle in ideal case [80, 81]. $\Gamma_{th} = \frac{\bar{n}_{th}\omega_m}{Q}$ is the mechanical decoherence rate, where the quantum number $\bar{n}_{th} = \frac{1}{e^{\hbar\omega_m/k_B T} - 1}$ follows Bose-Einstein relation at temperature T ; Q is the mechanical energy dissipation factor for the oscillator. Together with scheme introduced from Chapter 2, the key parameters for our current optical trapping are calculated in Figure 23(a). The magnetic gradient can be introduced by a nearby magnetic tip and the values used in Figure 23(a) comes from a moderate selection in reference [11]. If we can improve the diamond quality and trap it in high vacuum, the threshold for $C = 1$ can be achieved when the pressure lowers down to 10^{-5} torr using the values in Figure 23(a). Assuming we can pump down to 10^{-8} torr, the corresponding cooperativity is calculated in Figure 23(b). The magnetic gradient range is based on a reported 10^6 T/m generated by a magnetic tip [13]. And the vacuum range selection is based on the reported 10^{-8} mBar created for a trapped silica sphere [12]. We can see a higher Q is the key to achieve $C \gg 1$, the strong coupling regime. The major limitation for the Q factor is pressure [19] at this moment, and they are related by the damping rate of the oscillator:

$$Q = \frac{\omega_m}{\Gamma_0} \quad (3.22)$$

where the Γ_0 is the damping induced by the collision from gas molecules (viscosity damping), which is proportional to the environmental pressure:

$$\Gamma_0 = \frac{8}{\pi} \frac{P}{rv\rho} \quad (3.23)$$

where P is the pressure in a unit of Pascal; r, ρ are the radius and density of the trapped diamond; $v = \sqrt{3RT/M_{air}} = 508$ m/s is the speed of air molecule at room temperature $T = T_0$. When the environment can be pumped down to ultra-high vacuum, other damping mechanisms could contribute to the limit of Q . For example, we did not consider the damping rate induced by trapping laser's radiation pressure [82, 12] in calculations since we are still far away from ultra-high vacuum regime in an optical trapping experiment.



3.6 CONCLUSION

Because of we cannot optically trap a diamond in high vacuum, probably due to impurities in the diamond samples, we move to a newly developed magneto-gravitational trapping technique, which does not need high power trapping laser. This trapping technique for a micron-sized particle is pioneered by our collaborator Dr.D'Urso and have been demonstrated for holding the diamond in high vacuum [14].

3.7 APPENDIX

3.7.1 Appendix: Justification of Thermal Dissipation Model

The mean free path of the gas molecule can be calculated as

$$\bar{l} = \frac{k_B T}{\sqrt{2}\pi d^2 P} \quad (3.24)$$

where \bar{l} is the mean free path; d is the diameter of the gas molecule; P is the pressure and T is the temperature of the gas. We got $\bar{l} \cdot P = 6.7 \times 10^{-3}$ at temperature of 273.15 K from reference [83]. We can therefore calculate the average diameter for an air molecule is 3.56×10^{-10} m. Then we got the mean free path of air at different pressures in Table 3.

To justify our model for temperature distribution, we tested our model on measured temperature from a trapped $10\mu\text{m}$ diamond under roughing vacuum by Paul trapping technique in reference [1]. Similarly, we first calculated the absorption coefficient for their diamond using the temperature under 0.9 mBar. The temperature is about 328 K in Figure 24(b). Then we use the thermal conductivity of air at different pressure (reported by [2] in Figure 24(a)) and our model to estimate the internal temperature of the trapped diamond as the pressure goes down in Table 4. It shows a reasonable agreement with the experimental data reported by reference [1] in Figure 24(b). It worth to notice that the mean free path at these pressures are larger than the diamond size (1.0×10^{-5} m). Therefore, considering our

Pressure(torr)	\bar{l} (m)
7.6×10^2	7.1×10^{-8}
1.0×10^2	5.4×10^{-7}
1.0×10^1	5.4×10^{-6}
1.0×10^0	5.4×10^{-5}
1.0×10^{-1}	5.4×10^{-4}
1.0×10^{-2}	5.4×10^{-3}
1.0×10^{-3}	5.4×10^{-2}
1.0×10^{-4}	5.4×10^{-1}
1.0×10^{-5}	5.4×10^0

Table 3: Mean free path of air at 295 K

nanodiamond size (4.0×10^{-8} m) is similarly comparable with the mean free path of air at atmospheric pressure, we think our model is reasonable for an estimation purpose.

On the other hand, reference [78] provide a another model when the mean free path is larger than the size of diamond. The relation is simply $\Delta T \propto 1/P$ due to the air collision. If we apply this model to the measured results in Figure 24(b) calibrate again at 0.9 mBar, the temperature at 0.2 mBar will be 443 K, much more different form the result by our model. Overall, we believe our model using heat equation when the size of the diamond is comparable with the mean free path, is still reasonable for an estimation and it tends to underestimate the real temperature on the diamond.

3.7.2 Appendix: Trapping Diamond with Graphene

A novel method we introduce here was not successful but may still be worth pursuing under different conditions. It will enable the selective optical trapping of nano-diamond. We got

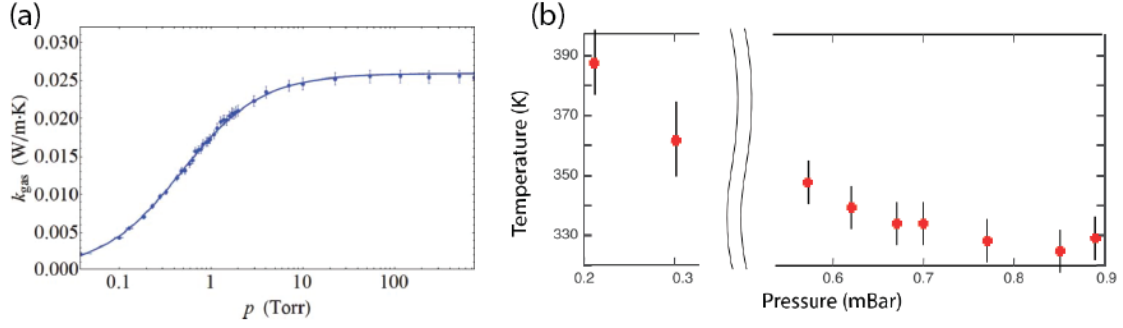


Figure 24: (a) Thermal conductivity from Figure 4 in reference [2]. We use the fit parameters in this figure and equation (10) in their paper to calculate the thermal conductivity from 0.2 to 0.9 mBar pressure as in reference [1]. (b) The measured internal temperature of a Paul trapped diamond using the ODMR technique from NV centers in the diamond. The measured pressures ranged from 0.2 to 0.9 mBar (Figure 3(b) in reference [1]). Figures are reprinted with permissions from References [2, 1]

Pressure(mBar)	Pressure(torr)	\bar{l} (m)	Calculated Temperature (K)
0.9	0.68	8.0×10^{-5}	328 (calibration)
0.8	0.60	9.0×10^{-5}	330
0.7	0.53	1.0×10^{-4}	332
0.6	0.45	1.2×10^{-4}	335
0.3	0.23	2.4×10^{-4}	353
0.2	0.15	3.6×10^{-4}	374

Table 4: Mean free path of air in pressure ranged from 0.2 to 0.9 mBar, as the measured range in reference [1]. And the calculated temperatures are based on our model and the parameters from [2]. The temperature is calibrated for 0.9 mBar and same parameters are used to predict temperature for the rest of the pressures down to 0.2 mBar.

graphene grown on a super flat copper substrate from our collaborator. Then we deposit nanodiamonds on top of it. FeCl_3 solution is then used to etch out the copper. The graphene with diamond will float on the surface of the solution. Then we use Transmission Electron Microscope (TEM) grid to lift the graphene layer beneath the solution. Finally, we got a graphene layer covering the TEM grid with nanodiamond on top of it. We then focus the trapping laser onto one of the selected diamond on the graphene, burning the graphene and catching the diamond by the trapping laser. Figure 25 shows the schematic diagram of this burning and catching technique on a TEM grid.

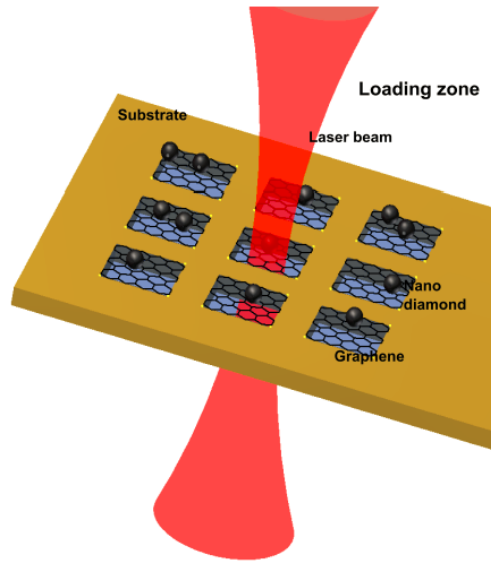


Figure 25: The schematic of our laser trapping technique on the TEM grid

Using graphene as a suspended media has several advantages. First, the monolayer graphene is least gas (CO_2) producer we can think of during the burning. With the control of oxygen concentration by adjusting background pressure, we can manipulate the rate of gas generation. Second, when an asymmetric burning happens, the monolayer graphene minimize the possible tensions that compete with the trapping force. Another concern is the burning may complete before trapping power is achieved as well as the asymmetric burning tension will drag the diamond out of trapping volume soon before the power is on. An estimated calculation shows these procedures can happen within 100 ns based on

the oscillating frequency of the nano-diamond graphene system. So an acoustic-optical-modulator(AOM) is necessary for us to fast turn on the trapping laser within 10 ns rise time.

With all the preparation above, we repeated burning and capturing procedure. The results were in two cases: one is the diamond is indeed pulled away by the burned and curved graphene around. Another one is the diamond drops with large piece unburned graphene beneath it, which the laser cannot trap. There is one time out of hundreds of attempts that a diamond seemed to be trapped but last only for 2 seconds and was never repeatable after.

4.0 MAGNETO-GRAVITATIONAL TRAPPING OF MICRODIAMONDS

Magneto-Gravitational(MG) trapping is an alternative technique in high vacuum to levitate a diamond with NV centers. To develop the hybrid quantum system with the mechanical oscillation of a trapped diamond and NV spins in it, one important step is to detect the spin signal from NV centers in a trapped diamond. In this chapter, we demonstrate our effort in exploring ODMR signal from such a diamond in high vacuum. We show and compare our results of two samples from different companies and demonstrate our preliminary data of a possible ODMR signal detected from one of the samples.

4.1 INTRODUCTION

The magnetic potential energy of an object with susceptibility χ in a magnetic field can be written as:

$$U_B \approx -\frac{\chi|\mathbf{B}(x, y, z)|^2V}{2\mu_0} \quad (4.1)$$

where $\mathbf{B}(x, y, z)$ is the magnetic field at the position of the object (x, y, z) ; V is the volume of the object and μ_0 is the vacuum permeability. The approximation in (4.1) comes from the assumption that the object is small enough where the magnetic field is uniform inside the object and can be represented by $\mathbf{B}(x, y, z)$. Then the magnetic force on the object follows:

$$\mathbf{F}_B \propto \chi \nabla |\mathbf{B}(x, y, z)|^2 \quad (4.2)$$

Diamagnetic materials have a negative susceptibility. Therefore if there is only a magnetic force exerted on a diamagnetic particle, it tends to bring the particle to lowest magnetic field

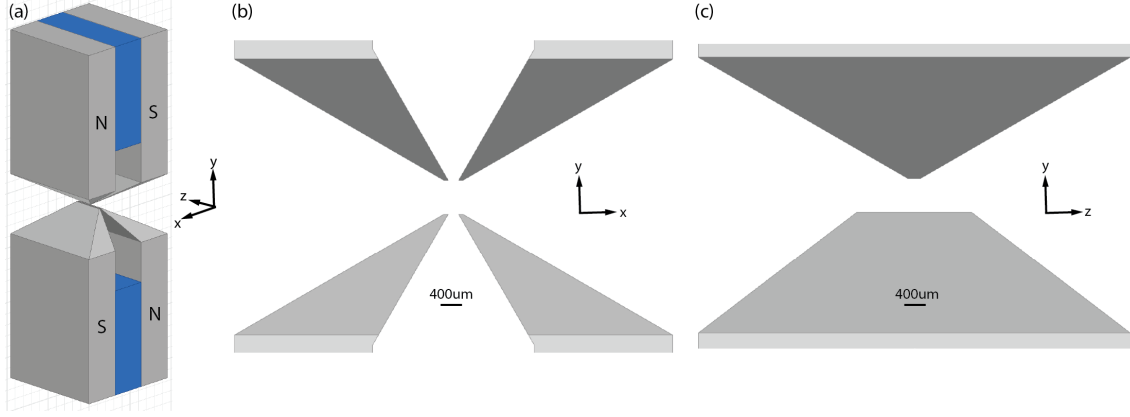


Figure 26: Geometry of our experimental Magneto-Gravitational trap. (a) Outline of the trap (b) X-Y plane projection (c) Y-Z plane projection.

region. If the gradient of the magnetic field is large enough to balance the gravity in the vertical direction, then the particle can be levitated. To trap a diamagnetic particle such as a diamond with tiny susceptibility $\chi = -2.2 \times 10^{-5}$, a quadrupole asymmetric configuration of magnets and ferromagnetic pole pieces are used. Figure 26 shows the geometry of such a Magnetic-Gravitational(MG) trap looking from different directions in our experiments. To obtain sufficient magnetic gradient, the magnetic flux from the magnets (blue) are conducted and focused with a ferromagnetic material (Hiperco 50A, High Saturation at 2.4 T) to hundreds of micron region. In first order approximation, the particle oscillates harmonically for small displacements with respect to the equilibrium position [16].

4.2 MAGNETIC FIELD DISTRIBUTION AT THE TRAP REGION

4.2.1 Coordinates and Origin

We use Cartesian coordinate for the calculation below. The $\hat{x}, \hat{y}, \hat{z}$ directions are named as “Transverse”, “Vertical” and “Axial” directions separately. The origin has been chosen

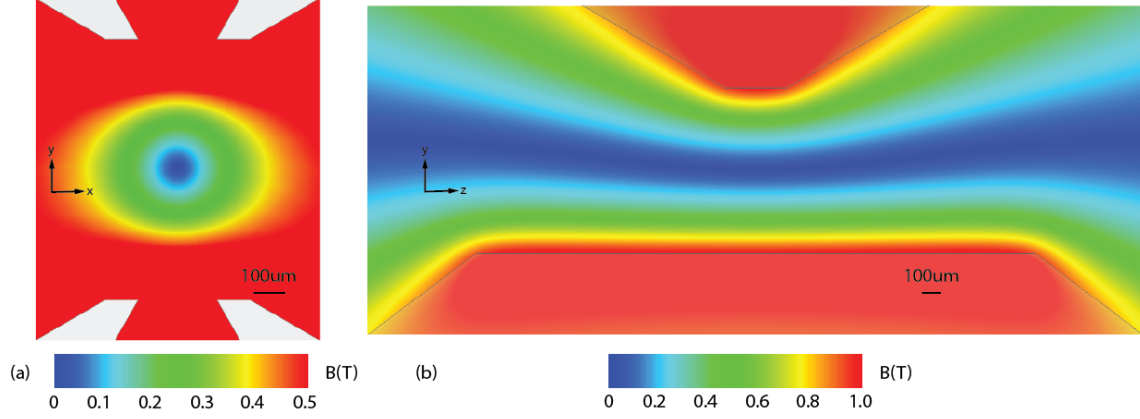


Figure 27: Magnitude of the B-field distribution in our magneto-gravitational(MG) trap. We set a upper limit threshold of 0.5 T (or 1 T) on the color map for a better contrast (a)X-Y plane, $z=0$. (b)Y-Z plane, $x=0$.

naturally as the center of the gap on X-Y plane and the midpoint along \hat{z} direction.

4.2.2 Magnetic Field and Potential Energy in the Trap

The magnetic field distribution in the trap is a static magnetic problem with certain boundary condition(See Appendix 4.7.1 for parameters). We simulate the field distribution with finite element method using commercial software(Ansys EM suite). Figure 27 shows a color map of the magnitude of magnetic field on different planes, which qualitatively shows a zero field pathway through the trapping region. The vertical gap is 740 μm , and the transverse gap is 220 μm in the simulation. In Figure 28, we compared the magnetic potential energy U_B and the total potential energy $U = U_B + U_g$ (where $U_g = mgy$, m is the mass of the diamond) of a 15 μm diamond in the trapping region. Clearly, the gravity plays a key role in trapping the diamond on the axial direction (\hat{z}).

A quantitatively study of the magnetic field components on the cross lines through origin along three directions is shown in Figure 29(a)(c)(e). The total potential energy $U = U_B + U_g$ is shown in Figure 29(b)(e)(f). A couple of results can be seen from these calculations:

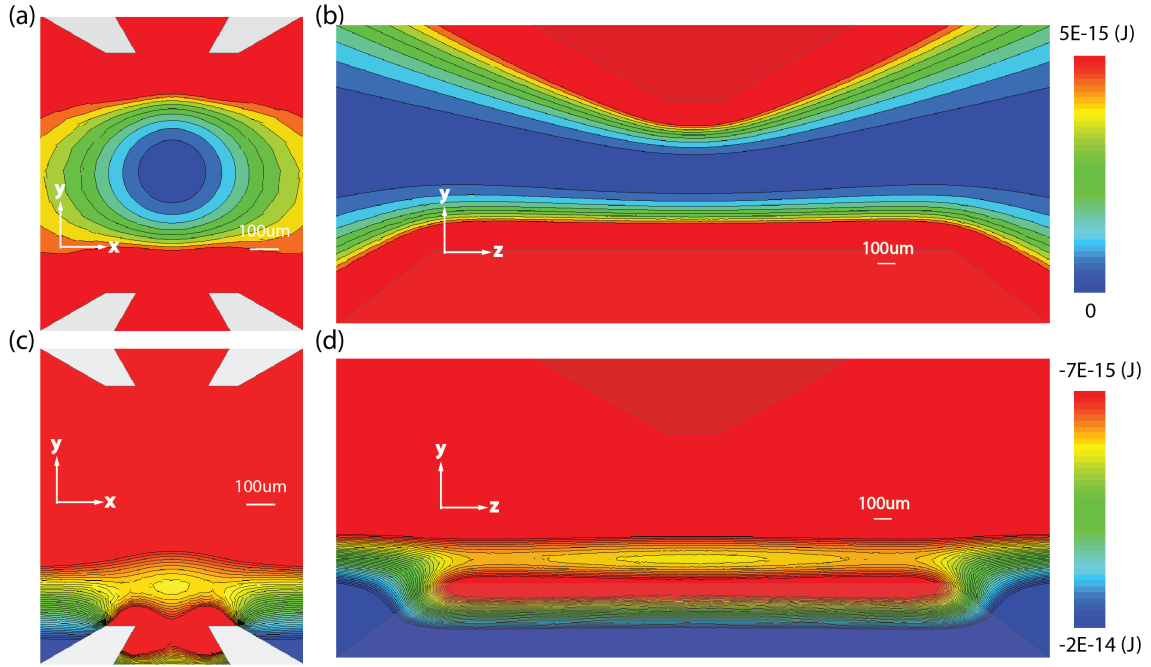


Figure 28: Comparison of the magnetic potential energy U_B and the total potential energy $U = U_B + U_g$ of a $15 \mu m$ diamond in the trapping region. Black lines are equal potential energy boundaries for different colors. (a) U_B on the X-Y plane, $z=0$, shows an enclosed energy minimum on this plane (b) U_B on the Y-Z plane, $x=0$, shows no enclosed energy minimum on this plane (c) U on the X-Y plane, $z=0$, shows an enclosed energy minimum on this plane also shows an enclosed energy minimum on this plane close to the bottom pole pieces. (d) U on the Y-Z plane, $x=0$, also shows an enclosed energy minimum on this plane close to the bottom pole pieces.

1. There are 1D potential wells on all three directions.
2. The potential energy minimum shifts on \hat{y} direction due to the gravity, the minimum potential energy on vertical direction, or the equilibrium position on vertical direction is located at $y_{eq} = -256.8 \mu m$.
3. The zero field pathway does not go through the origin we choose.
4. The maximum gradients from this configuration are similar on vertical and transverse direction, which are about 20 Gauss/ μm .

Since we have field data all through the trapping region, we find out that magnetic potential energy is minimized at $(0, 5.0 \mu m, 0)$ along with a vertical cross line through the origin. This means the zero field pathway shifts $y_{zf} = 5.0 \mu m$ upwards respect to the origin in our trap on vertical direction due to the asymmetry of pole pieces. More simulations indicate the zero field point along the vertical direction of a trap is geometry-dependent.

Considering the trapping region is free of current source $\mathbf{J} = 0$, the Maxwell's equations can be reduced to a Laplace's equation for a scalar magnetic potential:

$$\nabla^2 \Phi_M = 0 \quad (4.3)$$

The magnetic scalar potential can be expressed using multipole expansion in spherical coordinate:

$$\nabla^2 \Phi_M(r, \theta, \phi) = \sum_{l=0}^{\infty} \sum_{m=-l}^l (A_l r^l + B_l r^{-l-1}) Y_l^m(\theta, \phi) \quad (4.4)$$

Reference [16] justified their multi-pole selections based on the symmetry argument and the numerical simulation results:

$$\begin{aligned} \Phi_M(x, y, z) = & \left(\frac{a_2 y_0}{2}\right) \left(\frac{1}{y_0}\right)^2 r^2 RY_{2,-2}(x, y, z) \\ & + \left(\frac{a_4 y_0}{4}\right) \left(\frac{1}{y_0}\right)^4 r^4 RY_{4,-4}(x, y, z) \\ & + \left(\frac{a_3 y_0}{3}\right) \left(\frac{1}{y_0}\right)^3 r^3 RY_{3,1}(x, y, z) \end{aligned} \quad (4.5)$$

where a_2, a_3, a_4 are fitted by the experimental trapping frequencies and y_0 is related to the vertical gap size between the top and bottom pole pieces; $RY_{l,m}(x, y, z)$ are the spherical

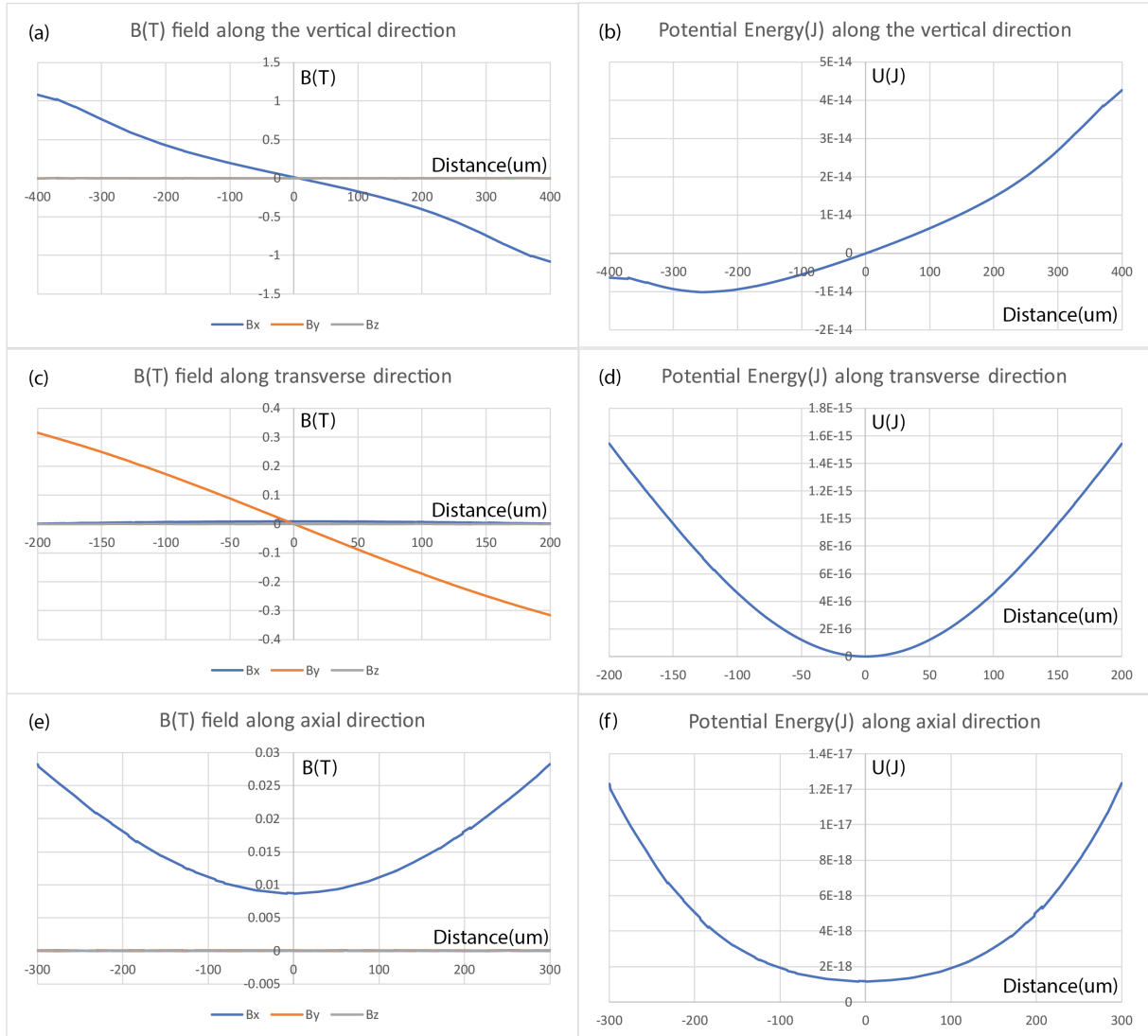


Figure 29: B-field components and total potential energy of a $15 \mu\text{m}$ diamond in the Magneto-Gravitational (MG) trap. (a)(b) B-field and potential energy along a vertical (\hat{y}) cross line through the origin. (c)(d) B-field and potential energy along a transverse (\hat{x}) cross line through the origin. (e)(f) B-field and potential energy along an axial (\hat{z}) cross line through the origin.

harmonic functions in the rectangular coordinate(Cartesian); r is the distance from the origin. It worth to notice the origin (expansion center) in this method has been chosen as zero field point ($(0, y_{zf}, 0)$ in our coordinate). However, the zero field position is a trap geometry-dependent value based on our simulations. In our experiment, it is important to know the absolute position of the zero field point respect to the trap geometry. Therefore, we directly apply the numerical simulation to obtain the field information.

4.3 EXPERIMENTAL SETUP

4.3.1 Optical Setup

The optical setup for collecting the photoluminescence(PL) from NV centers in a trapped diamond is modified from the optical trapping experiment. The objective for collecting the photoluminescence and scattering light from a diamond is a lower NA(0.28) one outside the vacuum chamber. The NA is limited by both the geometry of the trap and working distance from the chamber's window to the trapped diamond. Placing the objective outside is convenient to control the relative position between the objective and the trap; the ultra-high vacuum requirement in the future also prevents us from placing a commercial objective(usually contains out-gassing adhesive and paint) inside the chamber. The chamber is placed on a translation stage which is used for the relative motion between the optical path and trap. We found a focused beam from the objective tends to repel the particle out of focus due to the scattering force. Therefore, we choose the side illumination with large beam diameter (1.5mm) which yields a relatively uniform light field distribution across the trapped diamond. The green laser now is a collimated beam illuminating from axial(\hat{z}) direction of the trap. The green laser will only induce a constant shift of the trapped diamond along the axial direction. The green laser also excites the NV centers in diamond at the same time. A weak red 670nm diode laser is used in a control experiment as a fake photoluminescence (Figure 30).

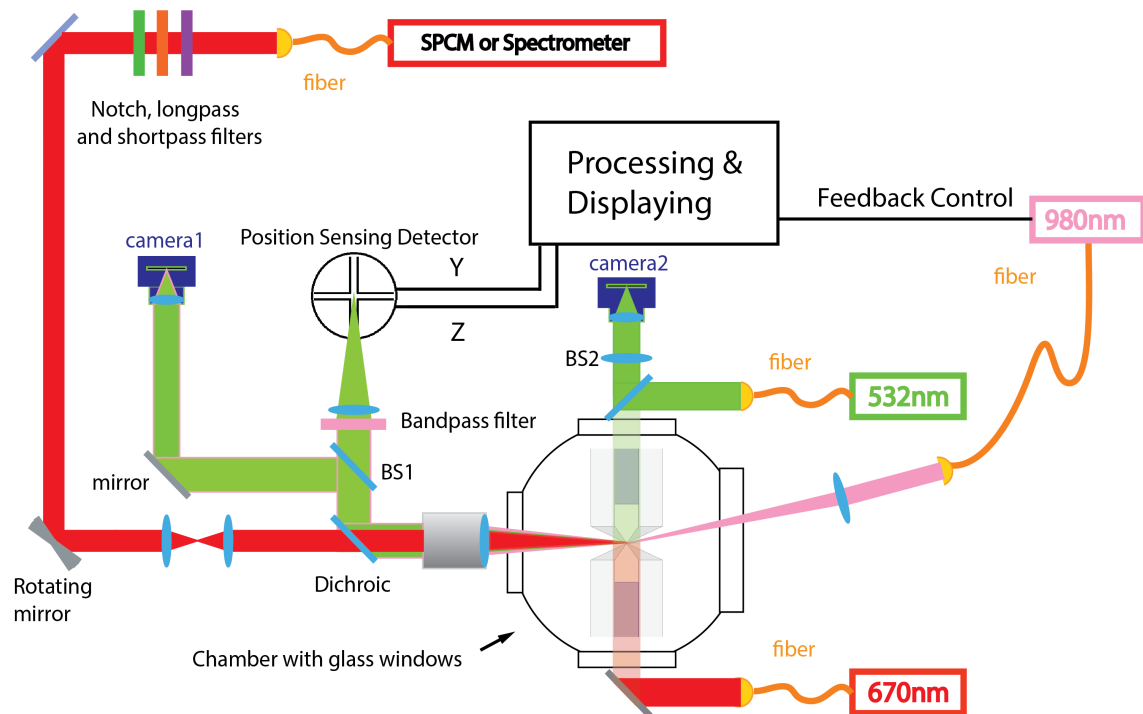


Figure 30: Optical setup for MG trapping experiments. The trap is placed in a vacuum chamber, and an objective lens is placed outside to collect the PI and scattering light from the trapped diamond. The green laser illuminates along with the axial direction. The photoluminescence is collected along the transverse direction and conducted to a Single Photon Counting Module (SPCM) or a Spectrometer. The rotating mirror is for scanning the photoluminescence image of the trapped diamond in free space. The scattering of the green laser can be monitored on camera 1 and camera 2 toward transverse and axial directions. The scattering laser spot is also projected on a Position Sensitive Detector (PSD), which mainly tells the position of the diamond on axial and vertical directions in our experiment. The position signal will be displayed on a computer and processed to control the feedback laser force from a 980nm diode laser.

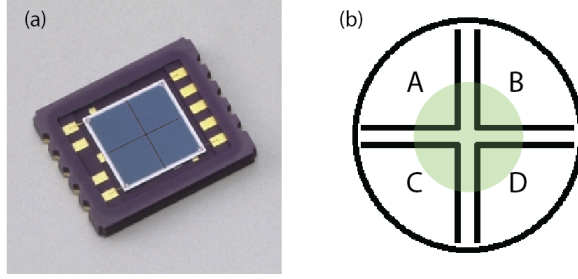


Figure 31: (a) PSD chip from Hamamatsu model s5980. Black lines are fake color $30 \mu\text{m}$ gaps in between the four elements. (b) The principle of position detection: Photo-current induced by the scattered laser beam (light green color) tells the positions of the trapped diamond. $(I_A + I_B) - (I_C + I_D)$ tells the vertical position of the diamond respect to the equilibrium position. $(I_A + I_C) - (I_B + I_D)$ tells the axial position of the diamond respect to the equilibrium position. $(I_A + I_B + I_C + I_D)$ should tell the transverse position of the diamond respect to the equilibrium position when the diamond is in and out of the focus. External circuits are used to convert the current to voltage signals.

Another branch for detecting the position of a trapped diamond has been integrated into the photoluminescence collection system. The scattering green laser from a trapped diamond can be seen from a front(transverse, camera 1) and a side(axial, camera 2) cameras in Figure 30. The scattering green laser spot is also projected onto a Position Sensitive Detector(PSD) with a 25 times optical magnification factor. With calibration, the PSD will tell the position of the particle relative to the equilibrium point (Figure 31) and feedback the signal to a diode laser controller. The controller then drives a 980 nm laser which is focused at an angle onto the diamond. Then the scattering force will have components in all three directions on the diamond. Under vacuum, when the air damping is heavily reduced, the motion of the diamond shows harmonic behavior on the PSD. If the harmonic motion signals from the three directions can be detected separately in frequencies, the output of the 980 nm laser can be driven at the three different resonance frequencies simultaneously with a modulated intensity based on the motion amplitude. A proper phase shift with respect to the motion signal can result in an damping effect of the motion (section 4.4.3.3). Therefore,

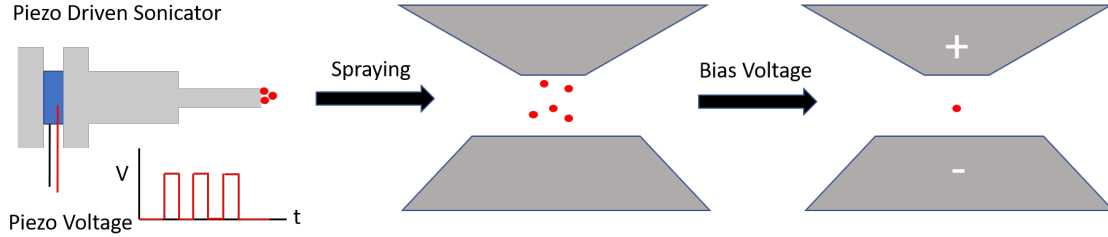


Figure 32: A diagram of depicting the procedure of loading diamonds into a magneto-gravitational trap.

the kinetic energy will be gradually removed from the trapped diamond, and the center of mass (CM) motion is cooled. In our experiments, we followed the same cooling circuit designs as in reference [16] and build them in our lab (Details of the feedback circuit designs can be found in Appendix 4.7.9). In our system, due to the low NA fact, our motion detection on transverse direction (signals sum channel) is not efficient to tell the position changes in and out of focus. We will only report the cooling results detected from axial and vertical channels for a trapped diamond with calibration (section 4.4.3.5).

4.3.2 Microdiamond Samples and Loading Method

We used two samples in this project. One is the sample from our collaborator Columbus Nanoworks (CNW), which we used at first. The size of this sample is in a big range from submicron to single microns. Another one is commercially available Adamas 15 μm micron-sized diamond which shows up later on the market. The Adamas diamond is better controlled in size, and the photoluminescence rate from NV centers in it is at least 50 times higher than the CNW diamond. In the magneto-gravitational trap, we load the diamond directly as dry powders. Typically a few powders are deposited on the tip of the ultrasonicator. The vibration of the sonicator will spray out the powder into the trapping region, and multiple diamonds can be trapped simultaneously. These diamonds are usually not neutral. Therefore, we can apply a bias voltage across top-bottom pole pieces to get rid of most

of the trapped diamond (e.g.let them bump the pole pieces) and left just one in the trap (Figure 32).

4.4 RESULTS FROM CNW DIAMOND SAMPLE

4.4.1 Probing the Spin Signals in the Magneto-Gravitational Trap

In Chapter 2, we have introduced that the position of NV ODMR signal is sensitive to the magnitude of an aligned magnetic field. When the NV direction is not aligned with a strong external magnetic field, the ODMR contrast is also reported to be transverse-field dependent [15, 56] (see Appendix 4.7.2 for the model). Figure 4(a) in reference [56] shows a single NV ODMR contrast decreases as the transverse magnetic field component increases in their report. Therefore, to optimize the ODMR contrast in our experiment, we need to either align our NV centers axis to the local magnetic field, or find the weak magnetic field region in the trap.

Because we are using an ensemble of NVs in experiments and there are four possible orientations in the diamond crystal, misalignment of NV and magnetic field happens for most of our NV centers. Therefore, we can only search for the weak field region around the zero-field point in the trap to optimize the ODMR contrast. Besides, the NV centers' distribution in the gradient magnetic field will also lead to the averaging of ODMR signal, which further reduces the contrast. Therefore, we first used a probe with a selected CNW diamond on it and put it in the trapping region to check if we can see any ODMR signals with the same experimental configuration as for a trapped diamond (including the illumination power, microwave delivery method, etc).

The probe is mounted on an automated stage with $1\ \mu m$ resolution. Then we program to move the probe around the center of the trap to search for weak field region and ODMR signal. Experimentally, when the vertical gap size is smaller than $500\ \mu m$, we never successfully observed ODMR signal from the diamond on the probe in the trap. When the gap size is larger than $500\ \mu m$, we start seeing ODMR signals on some selected diamonds with $1\ \mu m$

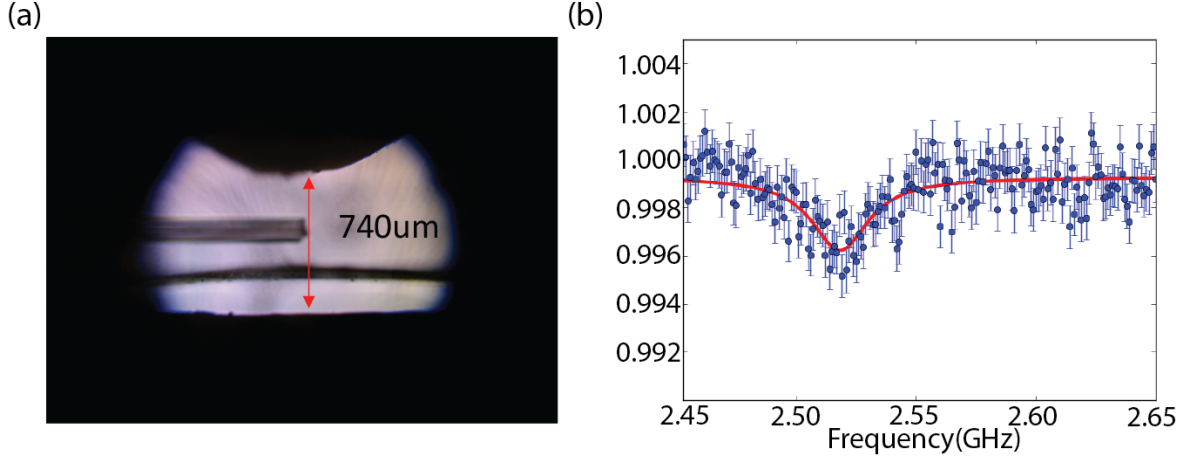


Figure 33: (a) Probe coated with diamonds is inserted into the trapping region. The black strip is the copper deposited kapton film which delivers the MW to the trapping region. (b) The best ODMR we observed from a selected diamond on the probe with same illumination method for a trapped diamond.

step resolution. When the gap becomes even larger, it is easier to find the ODMR signals. Figure 33(a)(b) shows the ODMR signal detected in a $740 \mu m$ vertical gap size MG trap with a selected CNW diamond on a probe. The transverse gap at this moment is $220 \mu m$. It worth to mention here we could not observe ODMR from most of the diamonds on the probe. Also, the selected diamond in Figure 33(b) has an ODMR contrast over 6% when there is no magnetic field outside the trap. So it is clear that the misaligned magnetic field reduces the spin contrast easily by a factor of 10 in the trapping region.

4.4.2 Electro-Static Force Assisted Magneto-Gravitational Trap

We enlarged the gaps observing an ODMR signal like Figure 33(b). However, levitation of a diamond becomes difficult with pure diamagnetic force when the gaps are enlarged. Although the simulation shows the minimum potential energy still exists when gaps are enlarged (Figure 29(b)), experimentally, the diamond cannot be levitated with pure diamagnetic force against its gravity at gap size larger than $\sim 400 \mu m$. Therefore, we charged the diamond and

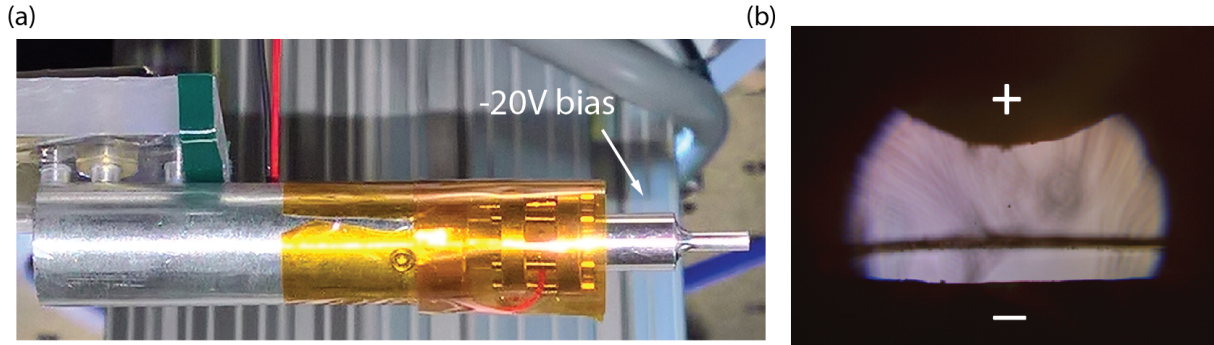


Figure 34: (a)The ultrasonicator is biased with -20 V voltage to negatively charge diamonds on it before spraying (b)The Enlarged MG trap levitating a negatively charged diamond with the help of electrostatic force from biased pole pieces.

biased the pole pieces, using the electrostatic force to balance part of the gravitational force. Then the trapping of the diamond is experimentally achievable again (Figure 34). Different from the procedure in Figure 32, the sonicator has a bias voltage on it at loading and the trapping relies on the bias voltage on the pole pieces all the time. There are two advantages of using electrostatic force:

1. The electrostatic force helps to balance the gravity and make it possible to levitate diamonds in an enlarged gap size magneto-gravitational trap.
2. The electrostatic force enables movement of the diamond in X-Y plane.

The charging process depends on the size of a diamond, the contact area between the diamond and the ultrasonicator, surface condition of the diamond and the bias voltage on the sonicator, etc. Therefore, even we optimized and fixed the sonicator voltage and bias voltage on the pole pieces, the loading of diamond powder is still a random process. We believe that the charge to mass ratio of the diamond should fall into a range where the vertical electric force balances part of the gravity. In our current trap, our recipe is -20 V bias voltage on the sonicator and around 15 V on bias voltage on the pole pieces (Figure 34). The loading efficiency is on average 1/50. However, because the CNW diamond has very

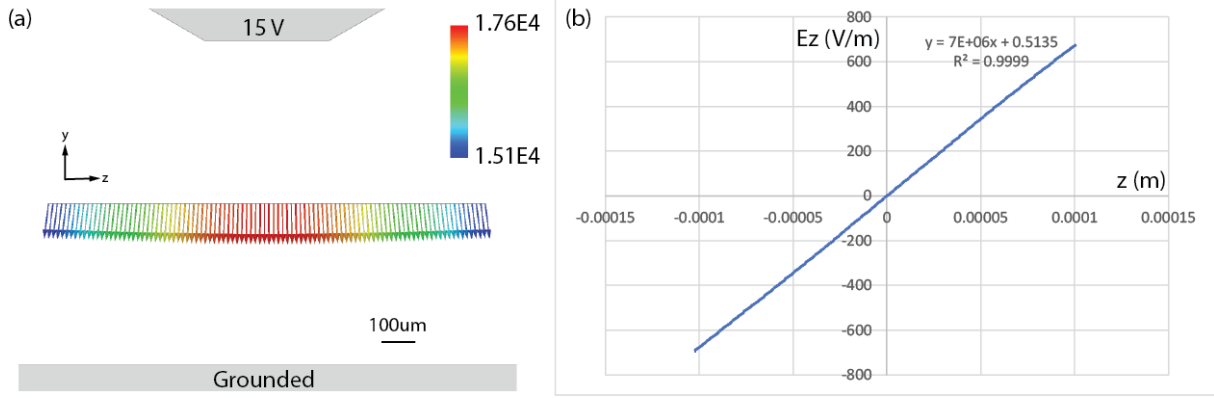


Figure 35: Electric field distribution in the trap region when a 15 V voltage is applied on top pole pieces and the bottom ones are grounded (a)The field vector along the axial direction through the origin (b)The numerical result of the E_z component of electric field along axial direction in (a) with a linear fit.

low photoluminescence rate in our optical system, it is usually difficult to find a trapped diamond with enough photoluminescence to do our experiment. Then we need to repeat the loading procedure until we find one.

After trapping the diamond, assuming we've moved the diamond to the zero field point, the gravity should be balanced completely with the vertical electrostatic force since magnetic force becomes zero from equation (4.2):

$$\frac{|q|}{m} = \frac{g}{E_y} \quad (4.6)$$

where $|q|$ is the magnitude of charge on the diamond. However, this brings a problem to the trap since we have demonstrated in Figure 28 that the gravity played a key role in confining the diamond along axial direction. It is contradicting to the fact that we've successfully trapped the diamond using this method. Therefore, we analyze the electric field inside our trap and figure out it is the electrostatic force that traps the diamond on the axial direction. We use the same software (Ansys EM Suite) to analyze the electrostatic problem (parameters and boundary conditions can also be found in Appendix 4.7.1). With the same coordinate

and origin defined in section 4.2.1, we shows the electrical field on the axial (\hat{z}) direction through origin in Figure 35(a). We see the electric field has an axial component as shown in Figure 35(b). Because our diamond is negatively charged, the electrostatic force serves as a restoring force when the diamond moves away from our origin along axial direction. Based on the extracted E_y around the origin in simulation we can estimate the charge on the diamond by equation (4.6). The electric field gradient $G_e = 7.0 \times 10^6 \text{ V/m}^2$ can also be fitted from Figure 35(b) for E_z . Finally, we got:

$$-|q|E_z = -|q|G_e\Delta z = -k\Delta z \quad (4.7)$$

where $k = |q|G_e$ is the spring constant and Δz is the displacement away from our origin on \hat{z} direction. The diameter of diamond we used here is $15 \mu\text{m}$; the density of diamond is 3510 kg/m^3 ; $g = -9.8 \text{ m/s}^2$; $E_y = -17589.5 \text{ V/m}$. With these parameters, we can calculate that $|q| = 3.5 \times 10^{-15} \text{ C}$ and $k = 2.4 \times 10^{-8} \text{ N/m}$. The corresponding trapping frequency is about 9.9 Hz , which is in a good agreement with our measured trapping frequency along axial direction (section 4.4.3.5). We also analyzed the electrical field effects for the other two directions and the magnetic forces are still the dominating restoring forces at the origin of current trap geometry.

The help from the electrostatic force is limited. Further enlarging the gaps will cause extremely low loading efficiency. Moreover, since we increase the gap, the stiffness of the trap is much lower on vertical and transverse direction. It is easier for air flow to kick off the trapped diamond during the pumping procedure. Therefore, we stay with the parameters that $740 \mu\text{m}$ vertical gap and $220 \mu\text{m}$ transverse gap to ensure trapping and survival of a trapped diamond during the pumping down procedure.

4.4.3 Motion Properties of A Trapped Diamond in Vacuum

Before we explored the ODMR signal from a trapped diamond, another important step is to obtain stable photoluminescence counts from a trapped diamond. This is hard to achieve if the diamond is moving with large amplitude. Therefore, we try to stabilize the motion of the trapped diamond by the feedback cooling method mentioned in section 4.3.1. In this section,

we describe the motion properties and the cooling results of a trapped CNW diamond in the Enlarged MG trap under vacuum.

4.4.3.1 Thermalized Motion of the Trapped Diamond If we ignore the internal freedom of motion in the trapped diamond and treat it as a large gas molecule, the collision between the diamond and other gas molecules surrounding it will bring its center of mass motion to thermal equilibrium. Considering the diamond's motion along z-direction (Figure 26) for example, the probability of finding the diamond at location z follows Boltzmann distribution [16](Details of derivation are in Appendix 4.7.3):

$$P(z) = \frac{N}{\pi\sqrt{S_0}} e^{-\frac{z^2}{\pi S_0}} \quad (4.8)$$

where N is the total occurrence number (total camera picture taken) in experiment; $S_0 = \frac{k_B T_{CM}}{2m f_0^2 \pi^3}$ where k_B is Boltzmann constant; T_{CM} is the temperature representing the center of mass motion of the trapped diamond, which equals to the environment temperature under the equilibrium condition; m, f_0 are the mass and oscillation frequency of the trapped diamond. Using the reciprocal of equation (3.23), we can estimate the time required for thermalization with surrounding air molecule, which is environmental pressure dependent. We measured the thermalization motion of the trapped diamond at 2.0×10^{-2} torr vacuum, our diamond has a diameter on the order of $10 \mu m$. The estimated thermalization time is ~ 1.3 s. Figure 36 shows the position distributions of a trapped diamond over 150000 camera images sampled at 20 Hz. We can extract the root-mean-square (RMS) amplitude as $z_{rms} = 800 \pm 4$ nm, $y_{rms} = 496 \pm 2$ nm from the standard deviation of the Gaussian distribution.

4.4.3.2 Power Spectrum of the Motion The motion equation of a one dimensional harmonic oscillator can be written as:

$$\ddot{z}(t) + \Gamma_0 \dot{z}(t) + \omega_0^2 z(t) = \frac{1}{m} \xi(t) \quad (4.9)$$

where we assume the random force $\xi(t)$ performs as a white noise ($\langle \xi(t) \rangle = 0$ and $\langle \xi(t) \xi(t') \rangle = g \delta(t - t')$, g is a constant). ω_0 is the resonance angular frequency; Γ_0 is the damping rate

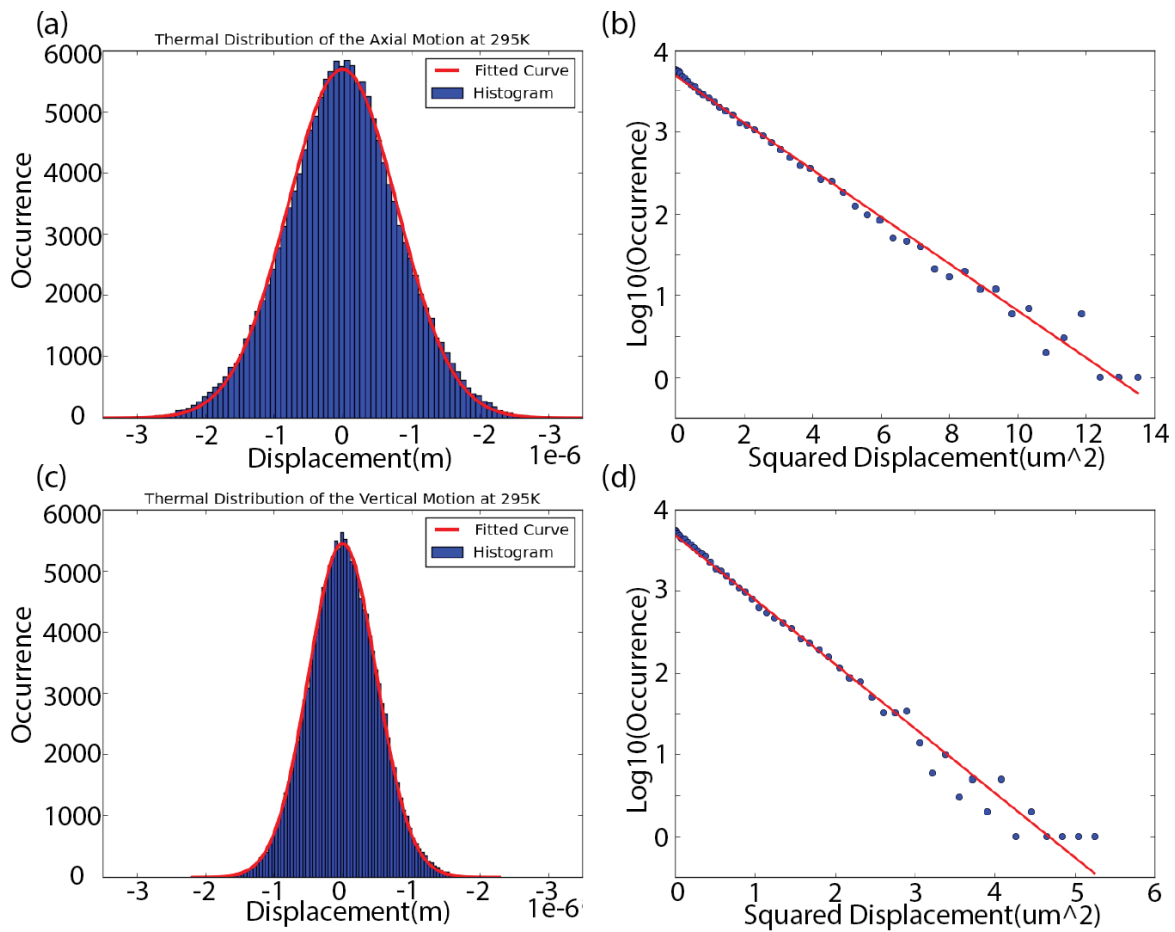


Figure 36: Thermalized motions of the trapped diamond at 2.0×10^{-2} torr vacuum (a)The occurrence histogram and Gaussian fit (red) of axial position (b)The linear fit(red line) of axial position on the log scale (c)The occurrence histogram and the Gaussian fit (red) of vertical motion (d)The linear fit (red line) on the log scale of vertical motion.

in unit of rad/s; m is the mass of the oscillator. The power spectrum for a series position measurement $z(t)$ over a time period t_{msr} is defined as:

$$S(\omega) = \frac{2|\tilde{z}(\omega)|^2}{t_{msr}}, \omega > 0 \quad (4.10)$$

where $\tilde{z}(\omega)$ is the Fourier Transform (FT) of $z(t)$. Substituting the inverse FT into both sides of (4.9) and doing ensemble averaging on (4.10), the power spectrum can be written as [16]:

$$\langle S(f) \rangle = S_0 \frac{f_0^2 \Gamma_{f_0}}{(f_0^2 - f^2)^2 + f_0^2 \Gamma_{f_0}^2} \quad (4.11)$$

where the equipartition theorem is applied to obtain the constant factor g (Derivation in Appendix 4.7.3). S_0 is the same parameter in equation (4.8); $\Gamma_{f_0} = \frac{\Gamma_0}{2\pi}$ is the damping rate in the unit of Hz; f_0 is the resonance trapping frequency. Let $f = f_0$ in equation (4.11), it's not hard to realize that S_0 represents the area under the resonance trapping frequency with a linewidth Γ_{f_0} on the the power spectrum (linear scale). T_{CM} is proportional to the mean-square position of the diamond based on the equipartition theorem $\frac{1}{2}k_B T_{CM} = \frac{1}{2}m\omega_0^2 z_{rms}^2$; where $\omega_0 = 2\pi f_0$; m is the mass of the trapped diamond. Since S_0 is proportional to T_{CM} , S_0 is also proportional to the mean-square position of the diamond. In our experiment, the time-varying positions of the diamond are recorded by a Position Sensitive Detector (PSD). They are then translated to the power spectrum by Fast Fourier Transform.

4.4.3.3 Cooling of the Diamond in Vacuum We use scattering force from a 980 nm diode laser to damp the motion of the trapped diamond in the vacuum. As described before, we scattered 980 nm laser beam at the direction where the scattering force has all three components along axial(\hat{z}), vertical(\hat{y}) and transverse(\hat{x}) axis of the trap. We used 180 μW power and a 100 μm beam diameter. Taking the axial motion for example, when the scattering force acting on the diamond π radian out of phase with the velocity ($F_{ext} = -\gamma_c \dot{z}(t)$), the motion equation for the forced harmonic oscillator can be written as [16]:

$$m\ddot{z}(t) + (\gamma_0 + \gamma_c)\dot{z}(t) + m\omega_0^2 z(t) = 0 \quad (4.12)$$

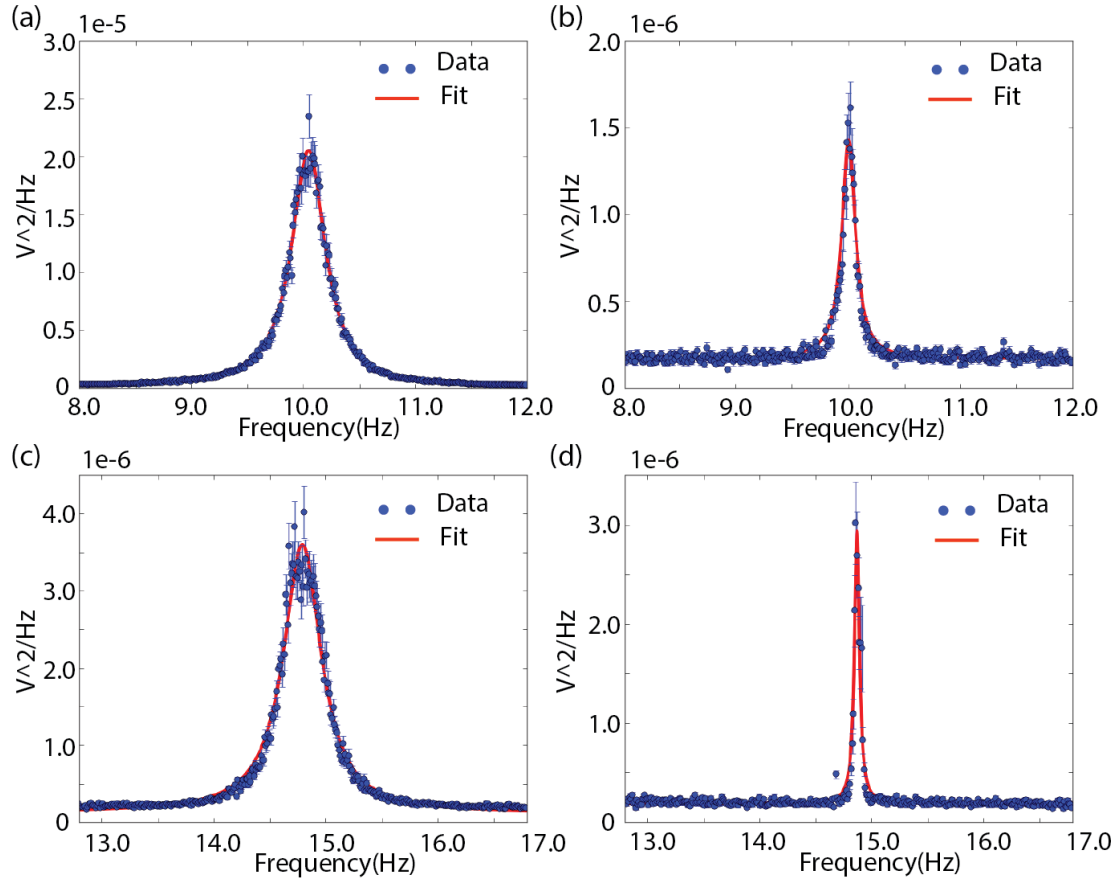


Figure 37: The power spectrum from the motion of a trapped diamond before and after the cooling is applied in linear scale (a)Thermalized motion on axial(\hat{z}) direction 2.0×10^{-2} torr vacuum (b)Cooled motion on axial(\hat{z}) direction 1.0×10^{-5} torr vacuum (c)Thermalized motion on vertical(\hat{y}) direction 2.0×10^{-2} torr vacuum (d)Cooled motion on vertical(\hat{y}) direction 1.0×10^{-5} torr vacuum

where m is the mass of the diamond; $\gamma_0 = m\Gamma_0$; ω_0 is the resonance angular frequency of the trap; Equation (4.12) results in an extra damping term with damping rate γ_c . A large γ_c compared to natural damping rate γ_0 is the key for a strong cooling. Phase mismatching is another factor to affect the cooling efficiency. Assuming the motion takes the form $z = \cos(\omega_0 t)$ and the scattering force is acting as $F_{ext} = -\gamma_c \sin(\omega_0 t + \phi)$, the resulting motion equation is

$$m\ddot{z}(t) + (\gamma_0 + \gamma_c \cos(\phi))\dot{z}(t) + (m\omega_0^2 + \gamma_c \sin(\phi))z(t) = 0 \quad (4.13)$$

Equation (4.13) indicates that if the phase of a feedback force is not π radian out of the phase of velocity, it will end up with a feedback damping rate less than γ_c and result in a resonance frequency shift at the same time. Therefore, phase matching is another key for an efficient cooling. Figure 37 shows the power spectrum before and after cooling for the trapped CNW diamond under vacuum. The cooled amplitude can be calculated by the ratio of the areas under the resonance peaks before and after cooling. So we do not need to carry on an absolute calibration between the voltage collected from PSD and the real displacement. The unit of our power spectrum is V^2/Hz instead. However, we still need to validate the linearity of the PSD response when the signal changes.

4.4.3.4 Linearity of the PSD Signal To prove the linearity of the PSD response, we use a commercial Galvo mirror to reflect the laser onto the PSD, simulating the motion of diamond in harmonic behavior. Figure 38(a) shows the linearity of the time domain position amplitude versus the Galvo mirror rotating amplitude at fixed laser power. The diamond trapped each time may differ in size and therefore scatters different amount of laser. Hence, we also need to check the linearity of PSD response to different laser power. Figure 38(b) shows the linearity of the time domain position amplitude versus the laser power at fixed Galvo scan range.

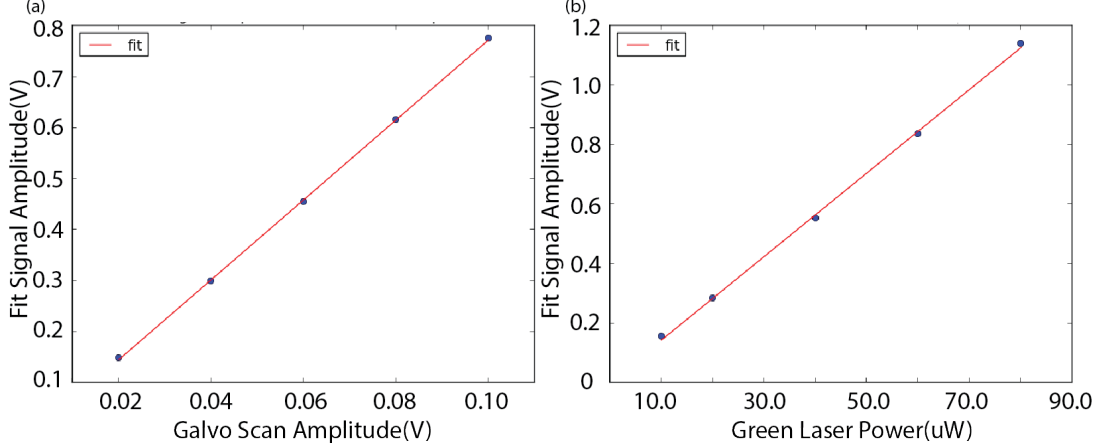


Figure 38: PSD time domain harmonic amplitude linearity calibration, the error is too small to be seen. (a) PSD signal versus galvo amplitude at fixed laser power (b) PSD signal versus laser power at fixed galvo amplitude

4.4.3.5 Cooling Results We fit the data points in Figure 37 with line shape:

$$\langle S(f) \rangle = BKG + S_0 \frac{f_0^2 \Gamma_{f_0}}{(f_0^2 - f^2)^2 + f_0^2 \Gamma_{f_0}^2} \quad (4.14)$$

where we the background is added into the average power spectrum. For thermalized motion under 2.0×10^{-2} torr vacuum, we got the area under resonance peak $f_{0-th-axial} = (1.0051 \pm 0.0001) \times 10^1$ Hz is $S_{0-th-axial} = (7.54 \pm 0.06) \times 10^{-6} V^2$ on axial direction. On vertical direction, $f_{0-th-vertical} = (1.4796 \pm 0.0002) \times 10^1$ Hz, $S_{0-th-vertical} = (1.43 \pm 0.02) \times 10^{-6} V^2$; For cooled motion under 1.0×10^{-5} torr vacuum (See Appendix C for vacuum measurement), we obtain the area under resonance peak $f_{0-cool-axial} = (1.0007 \pm 0.0004) \times 10^1$ Hz is $S_{0-cool-axial} = (1.86 \pm 0.11) \times 10^{-7} V^2$ on axial direction while on vertical direction, $f_{0-cool-vertical} = (1.48717 \pm 0.00005) \times 10^1$ Hz, $S_{0-cool-vertical} = (1.49 \pm 0.03) \times 10^{-7} V^2$; By calculating the ratio

$$\frac{T_{CM-th}}{T_{CM-cool}} = \frac{S_{0-th} f_{0-th}^2}{S_{0-cool} f_{0-cool}^2} \quad (4.15)$$

Assuming $T_{CM-th} = T_0 = 295K$ as room temperature and comparing with the thermalized RMS amplitude recorded by camera 1, we can easily estimate the cooled motion temperature

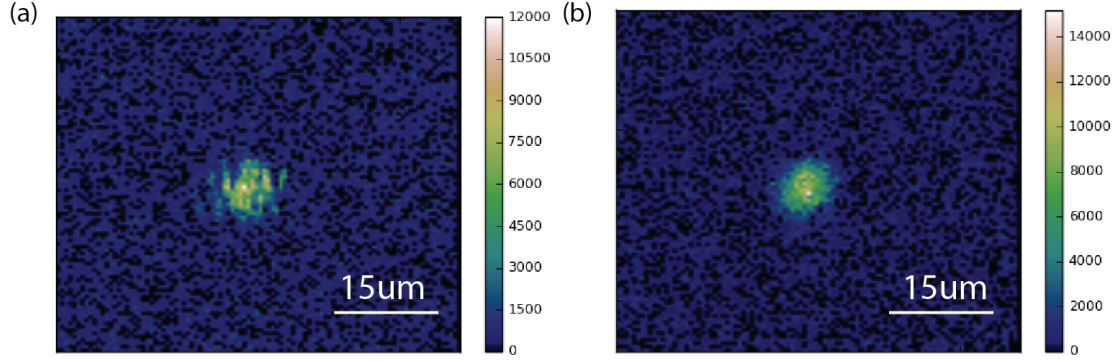


Figure 39: The photoluminescence image from the CNW diamond in the trap (a) not cooled (b) cooled

and RMS amplitude. For axial direction, $z_{rms} = 125 \pm 4$ nm; the equivalent motion temperature is 7.21 ± 0.43 K. For vertical direction, $y_{rms} = 160 \pm 2$ nm, the equivalent motion temperature is 31.1 ± 0.8 K. With all the effort above, we can observe a steady photoluminescence image from NV centers in the trapped diamond. With scanning ability of our optical imaging system, we compared the photoluminescence images of the trapped diamond under high vacuum at a 400 Hz sampling rate for each point (Figure 39). We will further show its stability over ODMR microwave frequency scan latter. At this moment, we start searching ODMR signals following the procedures below.

4.4.4 Procedure to Look for ODMR Signal from A Trapped Diamond

1. Label the relative probe tip position (when we see the ODMR signal with the probe method) on both front view (camera 1 towards transverse) and side view (camera 2 towards axial) images (Figure 30 and Figure 40(a)).
2. Load a diamond into the trap, turn on both green laser and cooling IR laser, adjust the bias voltage and lasers' power to move the trapped diamond to roughly overlapping the position of tip diamond on camera images (Figure 40(b)).
3. Pump down to 10^{-5} torr vacuum, start cooling.

4. Move the diamond carefully by finer adjustment of bias voltage towards the labeled camera pixel under cooling.
5. Run microwave to explore ODMR signals from the trapped diamond.

4.4.5 Possible ODMR Signal from A Trapped CNW Diamond

Following the procedure above and with many tests, we show one set of data which is a possible ODMR demonstration from a cooled diamond in high vacuum. We see our first signal as shown in Figure 41(a). 1 mW green laser is used for illumination. We figure out and label the position of it on camera 1 and move it about 20 μm downward by adjusting bias voltage V1 and V2 (Figure 40) at the same amount. V1-V2 is kept the same to maintain the diamond's position along the transverse direction. At the new position, we run the microwave and obtain data in Figure 41(b). We completely lose the signal with all the same experimental parameters except for the position. Then we try to move back the diamond to the previous labeled position on camera. The same scan partially recovers the signal in Figure 41(c). The slight difference in signal position and amplitude could be explained by the inaccuracy of the position recovery and drift during the long-time signal taking procedure. Because NV is sensitive to the magnetic field and there is a large magnetic gradient in the trap, the change of the NV signals and recovery could be one evidence of an ODMR signal. We also did a control experiment as our second proof. We load a non-florescent diamond in the trap and move it to the same location in the trap. Then we collect the scattering of a 670 nm laser from it as a fake photoluminescence signal of NV centers. The same scan shows no signal compared to the CNW diamond before (Figure 41(d)).

We also estimated how the position shift of a trapped diamond affects the ODMR signals in the gap. There are two types of position changes; one is the oscillation relative to balance position. Considering our diamond size is $\sim 10\mu m$, and our optical limit is $\sim 2\mu m$, the NV centers are already distributed in a field change about 40 Gauss ($20 \text{ Gauss}/\mu m$) if the diamond stays still. The cooled motion amplitude of $\sim 200nm$ is only a small addition to this distribution. Therefore, the oscillation will not contribute much to blur out the observed

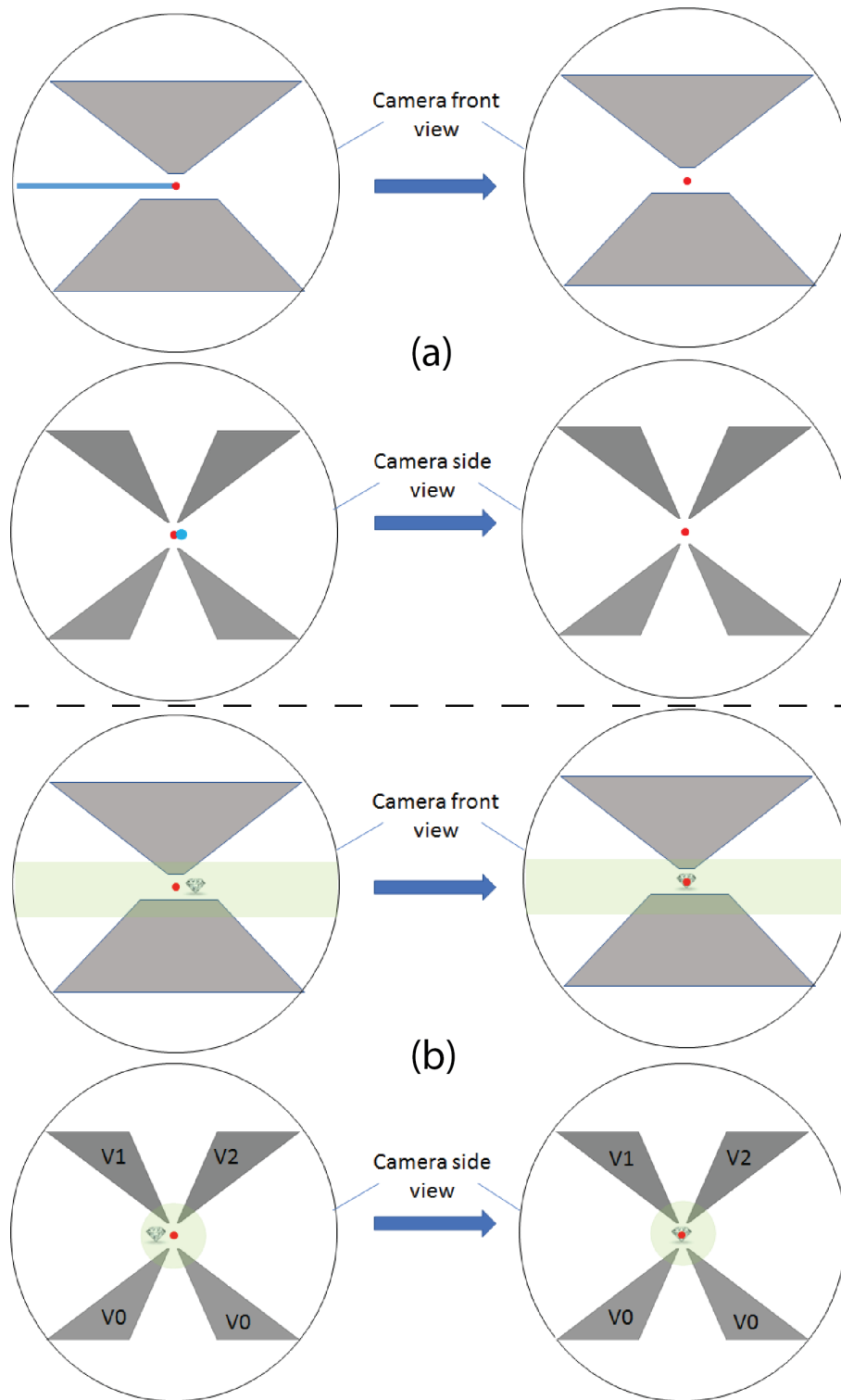


Figure 40: (a) Step 1: label the probe tip on cameras (b) Step 2: move the diamond to overlap the marker on the cameras. High voltages V1 and V2 are on top pole pieces. The bottom pole pieces are grounded. The diamond is negatively charged.

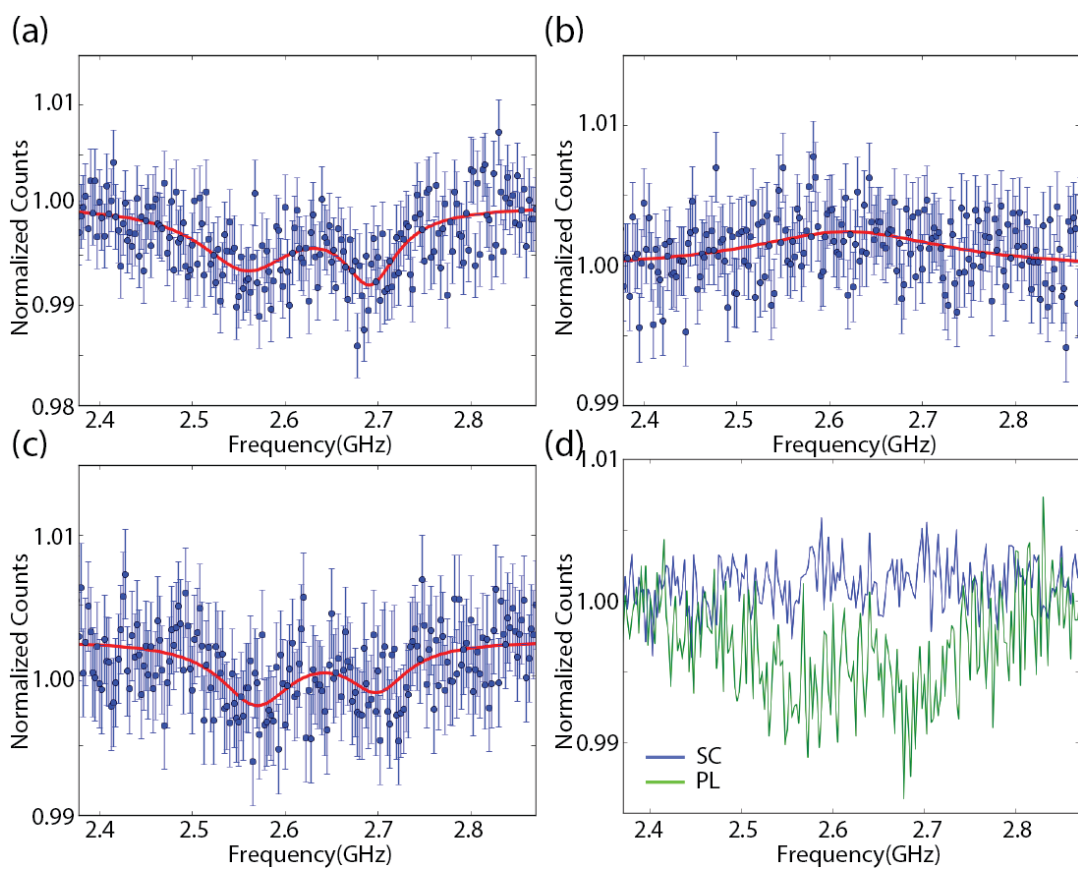


Figure 41: (a)Signal at position $(z=0, y=0)$ on camera 1 (b)Signal at position $(5 \mu m, -18 \mu m)$ on camera 1 (c)Signal at position $(2 \mu m, 0 \mu m)$ on camera 1 (d)The scattering(SC) signal from a non-fluorescence diamond compared to the photoluminescence signal from the CNW diamond in (a).

ODMR signals. On the other hand, the other type of motion is the relative translation to the pole pieces. As we did in our experiment, we moved the diamond $\sim 20 \mu m$ downwards, which corresponds to 400 Gauss field change along the transverse direction. This change will induce a ~ 1.1 GHz (2.8 MHz/Gauss) shift of the dips if all NV centers are aligned with the field direction. Considering NVs have four different orientations in the crystal, this shift could be smaller than expected value due to the different projections on each of the NV orientations. However, the field change is significant enough in most of cases to move the single dips out of our scanned frequency in Figure 41(a)(b). Also, as we mentioned in section 4.4.1 that the misalignment will reduce the ODMR contrast from an NV center as the field increases. Therefore, the change of the dips in an ODMR spectrum due the change of position is not merely a change of frequencies but also reductions of their amplitudes. We believe the position change analysis is not against that our observation is a possible ODMR signal from the trapped diamond.

4.4.6 Limitation of Current Technique

As illustrated in Figure 41, we cannot always move the diamond back to where it was by adjusting the bias voltage across the top-bottom pole pieces. This is because the bottom of the axial potential well is relatively flat and we do not have good control of the diamond position along the axial direction. Diamond could drift over time on this weakly controlled direction.

Drifts are in two categories: 1. Change of the position of the diamond relative to the pole pieces. 2. Change of the position of the trap relative to the optics. The relative drift could exist due to the environmental temperature (e.g., affects the magnetization saturation of the pole pieces) and the bias voltage drifts on pole pieces over time. But it is difficult to evaluate this drift separately due to other displacement mechanisms (optics drift and discharging described later). The drift of the diamond relative to the trap could be responsible for the difference between Figure 41(a) and (c). On the other hand, we can tell the second drift sometimes. After each experiment, we can illuminate the trap with a white light source. Although the corners of the pole pieces are not on focus when the diamond is on focus, we

can still tell the movement of the pole pieces on the optical image (if the movement is large). The movement is not consistent from time to time. Therefore, we believe it is drift due to unstable factors in the current setup such as vibrations from the connecting bellow to the chamber or other mechanical changes. To improve this, we can place the chamber on a stage with large mass and isolate the chamber and optics from the environment with an acoustic enclosure.

We also find that the strong green laser illumination power will cause the diamond moving downwards over time. We believe this is heating-induced electron loss from the charged diamond. We rule out the random drift possibility for this behavior because the movement is directional(keep going downwards). When we swap the sign of the bias voltages on the sonicator and pole pieces, a positively charged diamond will gradually move upwards instead, which support the electron loss reasoning. Increasing the green laser power will increase the speed of moving. Therefore, the illumination power is on average limited around 1 mW, where the downwards-moving is not obvious within two hours.

Also, our method to search the zero magnetic field region with ODMR signal, and position the trapped diamond based on the searching result is not quite efficient. First, we have never seen a real zero field signal with current trap configuration from the probe method, where the dips should concentrate in the vicinity of 2.87 GHz(Strain field may still induce splitting even the magnetic field is 0). Second, when we see a dip like Figure 33(b) at a non-zero field location from one diamond on the probe, we are not necessarily seeing ODMR from another diamond at the same location. This can be explained by the random orientations of these diamond crystals: the field that partially reduces the spin contrast of NVs in one diamond may completely destroy the spin contrast in others. Therefore, for a randomly trapped diamond, only when its NVs orient similarly to the one we labeled on the tip, our procedure (Figure 40) becomes more efficient. Due to these reasons, we are still looking for a recipe that can help to locate the zero field more efficiently.

In current experiments, drifts and discharging of the trapped diamond prevent us from increasing illumination power and taking data for a long time to reduce the random noise. Therefore, it is natural to think about using higher photoluminescence rate diamond in our experiment in the next section.

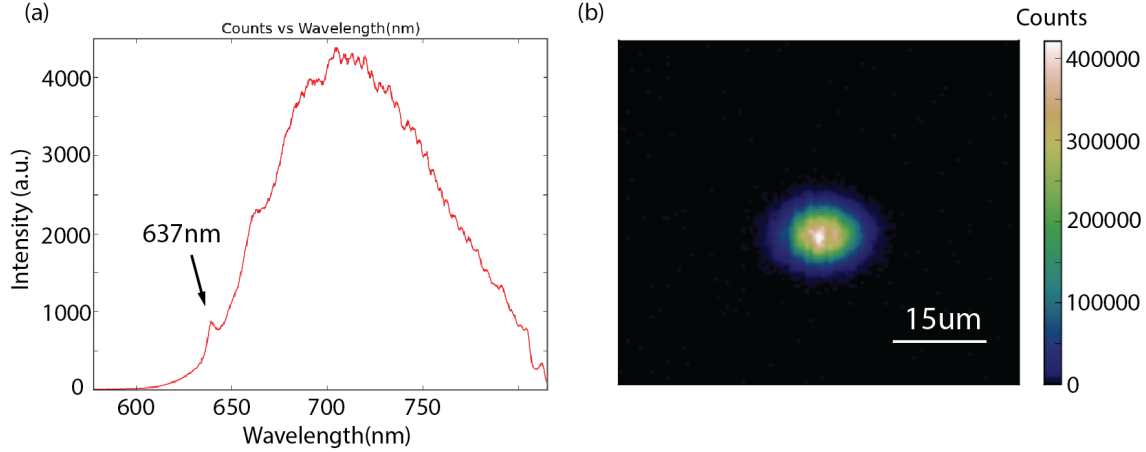


Figure 42: (a)Identify NV centers in trapped diamond with optical spectrum (b)PL image for NVs in a trapped Adamas 15 μm diamond with cooling under 10^{-5} torr vacuum.

4.5 RESULTS FROM ADAMAS DIAMOND SAMPLE

4.5.1 Photoluminescence and Spectrum from A Trapped Diamond

The Adamas 15 μm diamond is much brighter than the CNW diamond. We show the spectrum of NV centers and the photoluminescence image of a trapped Adamas diamond with cooling in high vacuum in Figure 42. 0.2 mW green laser power is used for illumination.

4.5.2 Probing Method Result

With plenty of trials, so far, we did not succeed in observing ODMR signals from an Adamas 15 μm diamond on the probe or trapped in the high vacuum. We use the same parameters for the test with CNW samples. Therefore, We suspect that there could be a difference for the ODMR contrast for these two samples.

4.5.3 Statistic of ODMR Contrast over Samples

We did statistic of the ODMR contrast outside the trap(zero magnetic fields) for both CNW and Adamas 15 μm samples in Figure 43. Because the ODMR spectrum is a result of multiple dips for an ensemble of NV centers, we use the area under the normalized ODMR spectrum to represent the ODMR contrast. On average, the CNW diamond shows three times larger ODMR contrast compared with Adamas 15 μm diamond in the same experimental condition. In the trap, because of the large field gradient and the diffraction limit of our optical setup, we are collecting photoluminescence from NV centers distributed in a different magnetic field. The position of the ODMR signal shifts with B field strength and average ODMR contrast will be reduced. Also, the local field is not necessarily aligned with NV axis, where the transverse field will mix the spin states or even break the symmetry of the defect, which further reduces the ODMR contrast [15]. Therefore, we think the lower contrast and randomness of the Adamas 15 μm diamonds in the trap is responsible for not seeing ODMR signals from this sample.

4.5.4 Thermal Detection from a Trapped Diamond in Vacuum

The high temperature is also a factor to decrease the ODMR contrast. [75, 78]. We conducted temperature measurements on a trapped Adamas 15 μm diamond in a high vacuum using temperature dependent NV photoluminescence technique [84]. Because of the influence of temperature on the electron-phonon coupling, the ZPL intensity over the total emission band intensity $\alpha(T)$ on the NV photoluminescence spectrum follows the relation:

$$\alpha(T) \approx \exp\left[-\int d\omega \rho(\omega) s(\omega) \coth\left(\frac{\hbar\omega}{2k_B T}\right)\right] \quad (4.16)$$

where $s(\omega)$ is the Huang-Rhys factor; $\rho(\omega)$ is the density of phonon modes. Applying Debye approximation to the phonon density, the expression is Debye Waller factor (DWF), which can be written as:

$$DWF = \alpha(T) \approx \exp\left[-\bar{s}\left(1 + \frac{2}{3}\pi^2\left(\frac{T}{\Theta}\right)^2\right)\right] \quad (4.17)$$

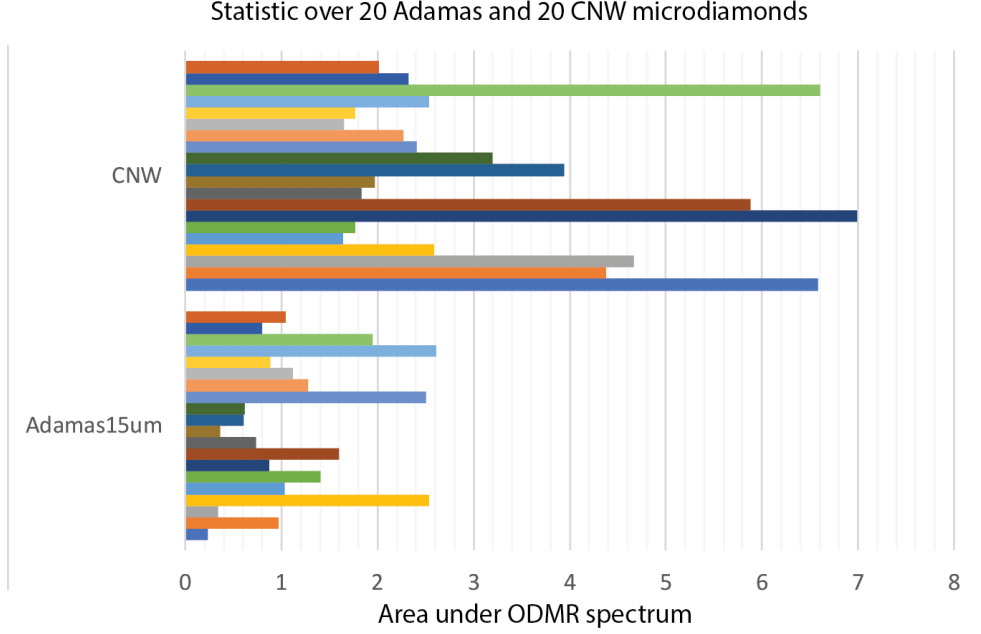


Figure 43: Statistic of ODMR contrast outside the trap from 20 Adamas 15 μm and 20 CNW diamonds. The x axis indicate the area under the (normalized) ODMR spectrum.

where $\bar{s} = \frac{s(\omega)}{\omega}$; Θ is the Debye temperature of diamond sample and $T \ll \Theta$ (2250 K for diamond). To examine the relation, we first did the thermal calibration over ten different Adamas 15 μm diamond, ten measurements for each of the diamond. The diamonds are deposited on a copper wafer which is attached to a ceramic heating element. The temperature is controlled with a PID loop where a thermal coupler is attached to the surface of the copper plate as a sensor. The raw data and error bar shows in Figure 44(a) and the linearity of DWF on log scale is shown in Figure 44(b).

The green laser excitation power in calibration and real measurement are not necessarily the same. It is reported the high illumination intensity will shift the charge state components of NV center in diamond and therefore change the DWF. This laser-induced DWF change should be a constant factor in front of equation (4.16) as long as the laser intensity is fixed on the trapped diamond. To correct the laser intensity induced shifts, we recalibrate the

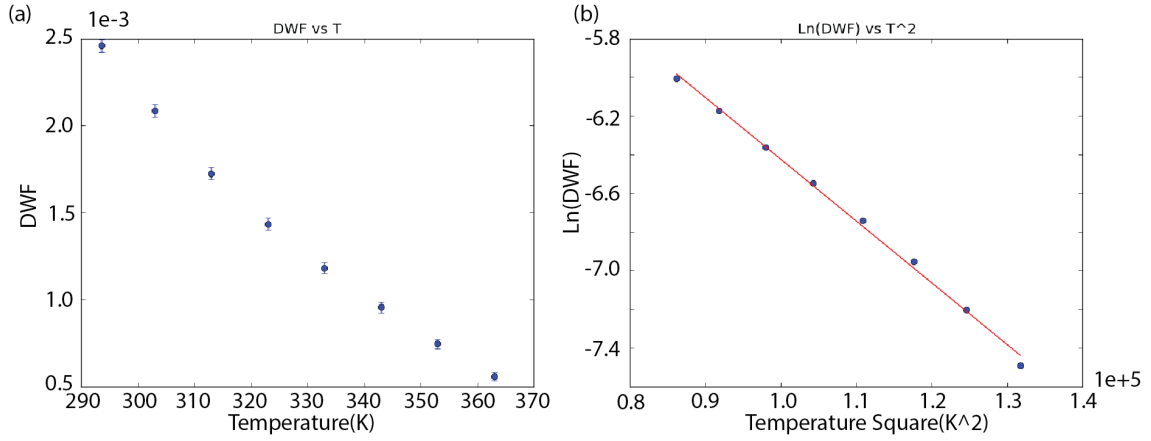


Figure 44: (a)The temperature dependent DWF from 10 different diamonds (10 sampling for each) with error bar (b)The mean DWF on log scale shows its linearity.

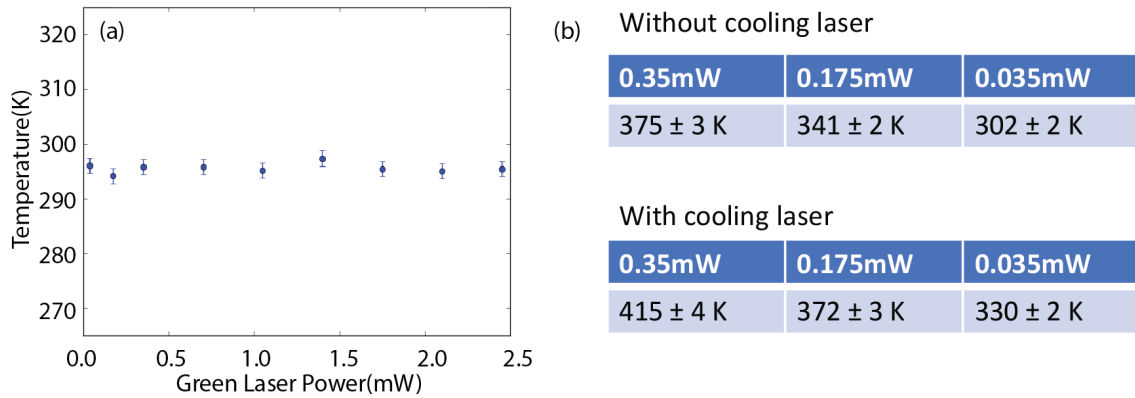


Figure 45: (a) Temperature on a trapped diamond detected at ambient pressure at different green laser powers. (b)With or without cooling IR laser, the temperature of the same trapped diamond is measured under 10^{-5} torr vacuum at different green laser powers.

temperature on the target trapped diamond directly at ambient condition. We believe the diamond temperature at room ambient condition is the same as the environment temperature which is 295 K with lasers on. Figure 45(a) shows our proof of this argument. We simply change the illuminating power by ten times, and no obvious increase in temperature can be observed. We believe the heat dissipation is large enough in the air to avoid the heating effect on a trapped diamond. We also proved with this data that within the green laser power range we used on the trapped diamond, the charge state will not introduce extra changes in DWF. After we obtain the correction factor, we use it for the rest of experiments. Under 10^{-5} torr vacuum, we detected the temperature with different laser conditions in Figure 45(b). The 532 nm excitation laser spot size is 1.5 mm while the laser spot size is $100 \mu\text{m}$ for the 980 nm infrared(IR) cooling laser. When the cooling laser is on, the laser power is set to 0.18 mW. We believe the tendency that the error of this temperature measurement increases with the temperature for the Debye approximation becomes less appropriate. To the best of our knowledge, no one has demonstrated the temperature measurement on a trapped diamond in high vacuum.

4.5.5 Thermal Dependence of ODMR Signals outside the Trap

The highest diamond temperature we detected in the vacuum is 415 K. Based on the experiment and model in reference [75] on a bulk diamond, we should observe $\sim 10\%$ decrease of ODMR signal at this temperature. We did the temperature dependence ODMR contrast tests for both Adamas $15 \mu\text{m}$ and CNW diamonds outside the trap in Figure 46. Our results show a certain agreement with reference [75] for the bulk diamond sample. Our results indicate that at the temperature we measured from a trapped diamond, the ODMR contrast will reduce slightly, but it is not a significant reduction. The reduction of ODMR contrast is not as large as reported in reference [78], which can be explained by the size of our diamond compared to 100 nm in reference [78]. The temperature dependence property for our sample is closer to that of bulk diamond.

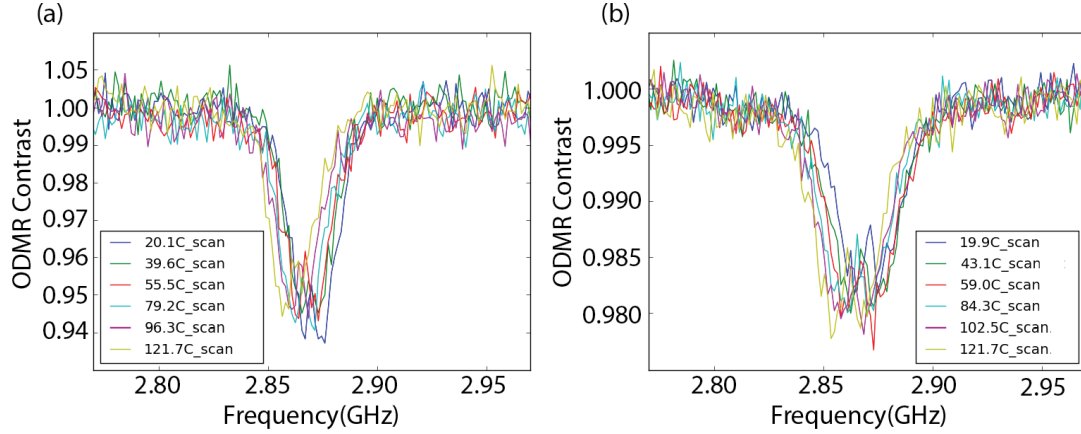


Figure 46: The temperature dependence ODMR signal when the magnetic field is zero outside the trap (a)A CNW sample (b)An Adamas 15 μm sample

4.5.6 Analysis Conclusion

1. The lower ODMR contrast and randomness of the Adamas 15 μm diamonds in the trap takes the main responsibility for not seeing ODMR signals from this sample.
2. The temperature will reduce the contrast of ODMR signal but not significantly at the temperature we measured.

4.6 CONCLUSION AND FUTURE DIRECTIONS

We observed a possible ODMR signal from a CNW diamond. We did not see ODMR signal by using high photoluminescence Adamas diamond, and we analyzed the reasons. Overall, with our current setup, we need sample with high photoluminescence and high quality of ODMR contrast.

Other than the property of the sample, the key problem prevents us from seeing the good ODMR signal is the collection from an ensemble of NVs in a large magnetic gradient. This

(a) Key Parameters	MG Trapping	Enlarged MG Trapping
Trapping Frequency (f)	$1.0 \times 10^2 \text{ Hz}$	$1.0 \times 10^1 \text{ Hz}$
Diamond Size (d)	$1.0 \times 10^3 \text{ nm}$	$1.0 \times 10^4 \text{ nm}$
Zero point Motion (a_0)	$7.0 \times 10^{-3} \text{ nm}$	$6.7 \times 10^{-4} \text{ nm}$
Magnetic Gradient (G_m)	$1 \times 10^4 \text{ T/m}$	$2.0 \times 10^3 \text{ T/m}$
Coupling Strength (λ)	$2\pi \times 1.9 \times 10^3 \text{ Hz}$	$2\pi \times 3.8 \times 10^1 \text{ Hz}$
Max Displacement (D_m)	$1.0 \times 10^0 \text{ nm}$	$2.0 \times 10^{-2} \text{ nm}$
Current Pressure (P)	$5.0 \times 10^{-8} \text{ torr}$	$1.0 \times 10^{-5} \text{ torr}$
Current Q	3.3×10^7	5.4×10^4

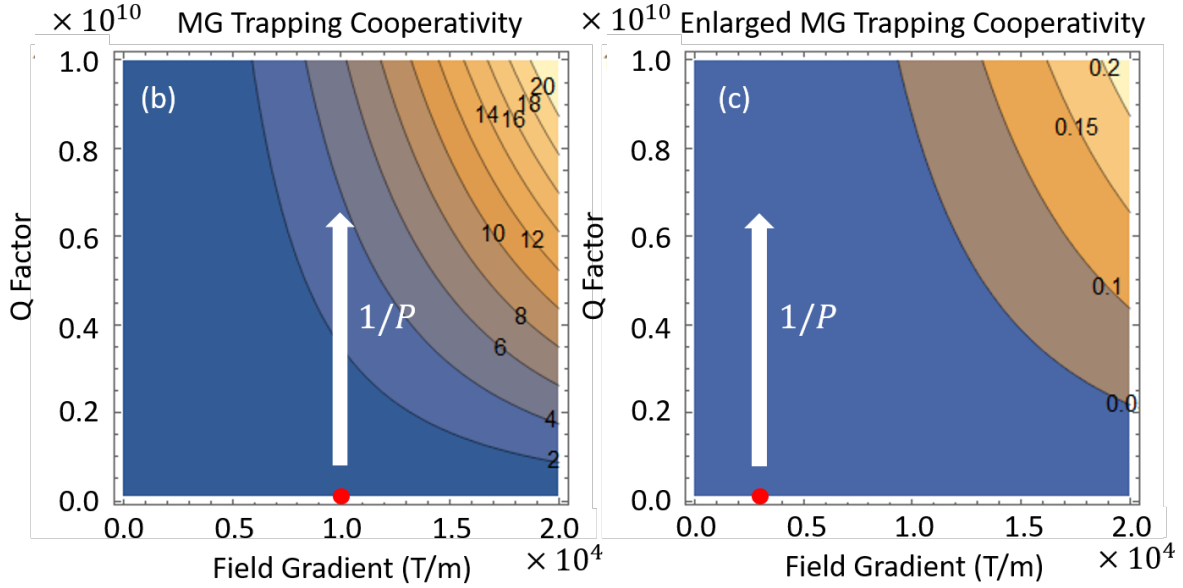


Figure 47: (a)Key parameters in the cat state creation scheme above for the MG trapping [14] and the Enlarged MG trapping with current parameters (b)Cooperativity as a function of Q and magnetic field gradient for MG trapping (c)for Enlarged MG trapping. For cooperativity calculation in (b)(c), $T_2=100 \mu s$, $N=10$, $s=1$, $T=300 \text{ K}$. The magnetic gradient range used for calculation is based on a possible gap size in a MG trap. Current experiments stay on the red spots on the figures.

situation will be improved by loading smaller diamond, where field changes less across the sample. However, loading smaller diamond requires a tighter trap which will again increase the gradient in the trap. To solve this dilemma, we think the future direction should be using diamonds with less NV center in the trap and develop high numerical aperture collection system in the vacuum. The extreme case is a single NV center in the diamond. Then instead of searching for a low field region, we can try to align the NV to the local field direction by polarized light [85]. An alternative method could be to functionalize a non-florescent, irregular shaped material (such as silica pillar, etc) with nanodiamonds: the smaller size of the diamond limits the field changes across the sample while an irregular shape of the media is for the NV-field alignment purpose [85].

Similar to the optical trapping, we calculated the key parameters to implement the "Cat state" creation scheme in chapter 2. In Figure 47(a), we compared the typical parameters and current configurations between a tight Magneto-Gravitational (MG) trap (no electrostatic force) from reference [14] and the Enlarged MG Trap (with electrostatic force) in our experiment. One difference from an optical trapping is the magnetic gradients in these MG traps are fixed, creating by the traps themselves. The gradient can be altered by changing the gap size between the pole pieces. A tighter trap will have larger magnetic gradient and trapping frequency which will increase coupling strength, displacement, and Q factor, etc. The Q factor in our experiment (Enlarged MG Trapping) is calculated from the fitted damping rate in Figure 37(a) for 2×10^{-2} torr vacuum first and then deduced by $1/P$ pressure dependence. The cooperativity for both systems are also calculated in Figure 37(b)(c). A $10^{-9} \sim 10^{-10}$ torr vacuum will create a high Q factor up to 1.0×10^{10} . For the MG trapping, it is possible to step into the quantum regime where the cooperativity $C > 1$. However, the Enlarged MG trapping will be difficult to achieve $C > 1$ with current parameters in calculation. Therefore, we think a tighter trap and levitating diamond with a single NV center is the direction towards the hybrid quantum mechanical system.

We also need to mention that we only considered the air damping rate so far. A recent paper focusing on cooling a trapped silica sphere in a tight MG trap reported a higher damping rate in ultrahigh vacuum than the prediction of equation (3.23) [86]. Although the reference has not determined the source of extra damping, an analogy to cavity optomechanics system

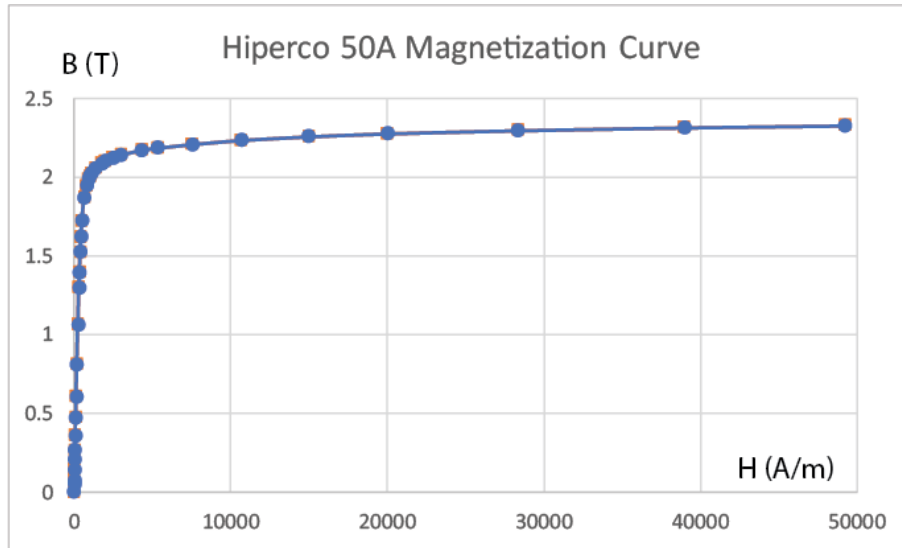


Figure 48: The magnetization curve of soft ferromagnetic material Hiperco 50A.

provides some clues [7]:

1. Fundamental anharmonic effects such as thermoelastic damping and phonon-phonon interactions [87, 88, 89, 90].
2. Materials-induced losses, which are caused by the relaxation of intrinsic or extrinsic defect states in the bulk or surface of the resonator [91, 92, 93, 94, 95]

These extra damping sources may dominate in ultrahigh vacuum and decrease the Q factor further, which makes our calculation of Q factor and cooperativity in Figure 47 an upper limit. Determine the extra damping source is one of the future task for both cooling and coupling purpose of the trapped particle.

4.7 APPENDIX

4.7.1 Appendix: Parameters in Simulations

We describe material parameters and boundary conditions in our finite element simulation for magnetostatic and electrostatic problem using Ansys EM Suite. In section 4.2, we did a the magnetic field simulation inside our MG trap model. The ferromagnetic material Hiperco 50A contains 49% cobalt and 2% vanadium, balance iron, which have the highest magnetic saturation of all soft-magnetic alloys. Its magnetization curve has been shown in Figure 48. The permanent magnets we used are NdFeB(Grade N42), which has a Maximum Energy Product (BH_{Max}) of 42 MGOe and a 13200G Residual Induction ((Br_{Max})). The boundary conditions we used in simulation is defined by Ansys for a magnetostatic problem:

1. Natural boundaries on the interface between objects: the Field is continuous across the boundaries, which satisfies $H_{1\parallel} = H_{2\parallel}, B_{1\perp} = B_{2\perp}$, when there is no current on the boundary in our case.
2. Neumann boundaries on the outer boundaries: the \mathbf{H} Field is tangential to the boundary and flux cannot cross it. This oriented from the fact that all sources has been included in the simulated area.

In section 4.4.2, we did a the electrical field simulation inside our MG trap model. We applied a 15 V voltage on the top pole pieces while the bottom ones are grounded. The specific boundaries conditions in a electrostatic problem are:

1. Natural boundaries on the interface between objects: the normal component of the \mathbf{D} Field at the boundary changes by the amount of surface charge density α on the boundary, which satisfies $D_{2\perp} - D_{1\perp} = \alpha, E_{1\parallel} = E_{2\parallel}$.
2. Neumann boundaries on the outer boundaries: the \mathbf{E} Field is tangential to the boundary and flux cannot cross it.

For outer boundaries in both magnetostatic and electrostatic problem we simulated, we kept the boundaries far away from the region we care about and boundaries at different distances from the center has been tested that would not affect the simulation results in the trapping region.

4.7.2 Appendix: ODMR Contrast Model

When a strong transverse magnetic field exists respect to a single NV axis in diamond, the quantized axis is determined by the applied magnetic field instead. The spin Hamiltonian (2.1) need to be re-diagonalized for a group of new basis. Following the model in reference [15], a seven levels system is considered. Neglecting the strain field induced splitting and the interaction with nearby nuclear spins, there are three levels for the ground state and three for the excited state. Together with the metastable state, there are seven states shown in

The new basis can be written as the linear combination of the old basis:

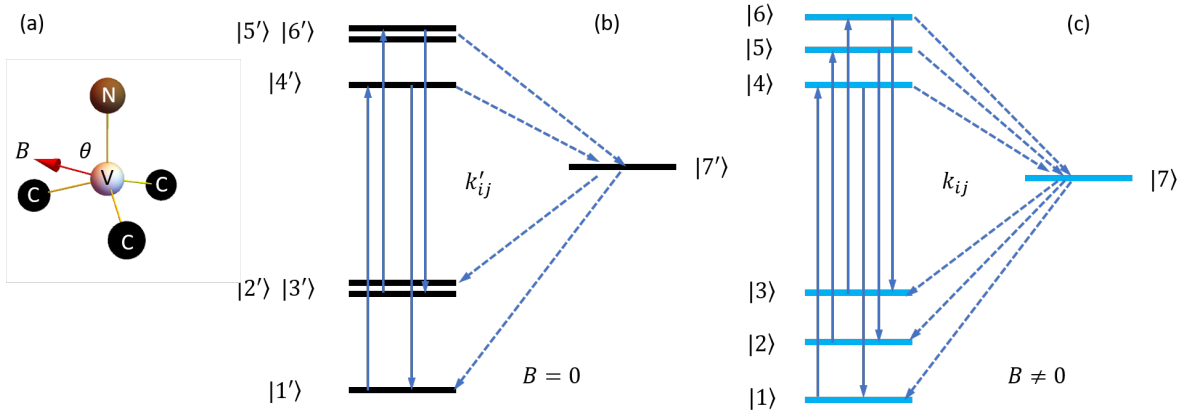


Figure 49: Seven-level model as in reference [15] (a)A single NV with non-aligned magnetic field (b)The seven levels when magnetic field is 0. The transition rates between levels can be written as k'_{ij} . Solid lines are radiative decays while dashed lines are non-radiative decays. (c)The new seven levels when the magnetic field is not 0. The transition rates between levels can be written as k_{ij} . Solid lines are radiative decays while dashed lines are non-radiative decays.

$$|i\rangle = \sum_{j=1}^7 \alpha_{ij} |j'\rangle \quad (4.18)$$

Then the new transition rates are related by:

$$k_{ij} = \sum_{p=1}^7 \sum_{q=1}^7 |\alpha_{ip}|^2 |\alpha_{jq}|^2 k'_{pq} \quad (4.19)$$

The average population of each state \bar{n}_i can be solved by the classical rate equation with steady condition:

$$\frac{dn_i}{dt} = \sum_{j=1}^7 (k_{ji}n_j - k_{ij}n_i) \quad (4.20)$$

The photoluminescence collected from the NV center is proportional to the average populations on the excited state and the related radiative decays:

$$PL \propto \sum_{i=4}^6 \sum_{j=1}^3 \bar{n}_i k_{ij} \quad (4.21)$$

Finally, when the microwave is driving between $|1\rangle$ and $|2\rangle$ (or $|3\rangle$), simply let $k_{12} = k_{21} \neq 0$ (or $k_{13} = k_{31} \neq 0$), the ODMR contrast can be expressed as:

$$Contrast = \frac{PL(k_{12} = 0) - PL(k_{12} \neq 0)}{PL(k_{12} = 0)} \quad (4.22)$$

4.7.3 Appendix: Thermal Distribution and Power Spectrum

Considering a one dimensional harmonic oscillator along axial direction (\hat{z}), the energy of the diamond is

$$E = \frac{1}{2}mv^2 + \frac{1}{2}m\omega_0^2z^2 \quad (4.23)$$

When the diamond's center of mass motion achieves thermal equilibrium with the surrounding air molecule, the possibility to find this diamond with velocity v and at position z follows the Boltzmann distribution:

$$P(v, z) \propto e^{-\frac{E}{k_B T}} \quad (4.24)$$

Integrate out all possible velocity, the possibility to find the diamond at position z is :

$$P(z) = P_0 e^{-\frac{m\omega_0^2}{2k_B T}z^2} = P_0 e^{-\frac{1}{s_0\pi}z^2} \quad (4.25)$$

where P_0 is the normalization factor. $T = T_{CM}$ when the motion of the diamond is thermalized. The integral $\int_{-\infty}^{\infty} dz P(z)$ should be normalized to the total measurement number N , which gives the the final expression as

$$P(z) = \frac{N}{\pi\sqrt{S_0}} e^{-\frac{1}{\pi S_0}z^2} \quad (4.26)$$

The motion equation of a one dimensional harmonic oscillator can be written as:

$$\ddot{z}(t) + \Gamma_0 \dot{z}(t) + \omega_0^2 z(t) = \frac{1}{m} \xi(t) \quad (4.27)$$

where we assume the random force $\xi(t)$ performs as a white noise ($\langle \xi(t) \rangle = 0$ and $\langle \xi(t)\xi(t') \rangle = g\delta(t-t')$, g is a constant). ω_0 is the resonance angular frequency; Γ_0 is the damping rate in unit of rad/s; m is the mass of the oscillator. The inverse Fourier Transform (FT) of frequency domain potions $\tilde{z}(\omega)$ follows

$$z(t) = \frac{1}{2\pi} \int_{-\infty}^{\infty} d\omega \tilde{z}(\omega) e^{i\omega t} \quad (4.28)$$

Substitute the expression of $z(t)$ into the motion equation and we get

$$\tilde{z}(\omega) = \frac{\tilde{\xi}(\omega)}{m} \frac{1}{-\omega^2 + i\omega\Gamma_0 + \omega_0^2} \quad (4.29)$$

$\tilde{\xi}(\omega)$ is the FT of $\xi(t)$. The power spectrum for a series of position measurements $z(t)$ over a time period t_{msr} is defined as:

$$S(\omega) = \frac{2|\tilde{z}(\omega)|^2}{t_{msr}}, \omega > 0 \quad (4.30)$$

Taking ensemble averaging on the power spectrum, it can be written as:

$$\begin{aligned} \langle S(\omega) \rangle &= \frac{2}{m^2 t_{msr}} \frac{1}{(\omega^2 - \omega_0^2)^2 + \omega^2 \Gamma_0^2} \langle |\tilde{\xi}(\omega)|^2 \rangle \\ &= \frac{2}{m^2 t_{msr}} \frac{1}{(\omega^2 - \omega_0^2)^2 + \omega^2 \Gamma_0^2} \left\langle \int_{-\frac{t_{msr}}{2}}^{\frac{t_{msr}}{2}} dt \xi(t) e^{-i\omega t} \int_{-\frac{t_{msr}}{2}}^{\frac{t_{msr}}{2}} dt' \xi(t') e^{i\omega t'} \right\rangle \\ &= \frac{2}{m^2 t_{msr}} \frac{1}{(\omega^2 - \omega_0^2)^2 + \omega^2 \Gamma_0^2} \int_{-\frac{t_{msr}}{2}}^{\frac{t_{msr}}{2}} dt \int_{-\frac{t_{msr}}{2}}^{\frac{t_{msr}}{2}} dt' \langle \xi(t) \xi(t') \rangle e^{i\omega(t-t)} \\ &= \frac{2}{m^2 t_{msr}} \frac{1}{(\omega^2 - \omega_0^2)^2 + \omega^2 \Gamma_0^2} g t_{msr} \end{aligned} \quad (4.31)$$

where whiteness assumption has been applied to simplify the expression. Rewriting the expression with all frequencies in the unit of Hz, we obtain

$$\langle S(f) \rangle = \frac{2g}{(2\pi)^4 m^2} \frac{f_0^2 \Gamma_{f_0}}{(f_0^2 - f^2)^2 + f_0^2 \Gamma_{f_0}^2} \quad (4.32)$$

With Parseval's theorem

$$\int_{-\infty}^{\infty} dt |z(t)|^2 = \frac{1}{2\pi} \int_{-\infty}^{\infty} d\omega |\tilde{z}(\omega)|^2 \quad (4.33)$$

the mean-square z position can be written as

$$\begin{aligned} \langle |z(t)|^2 \rangle &= \frac{1}{t_{msr}} \int_{-\infty}^{\infty} dt |z(t)|^2 \\ &= \frac{1}{2\pi t_{msr}} \int_{-\infty}^{\infty} d\omega |\tilde{z}(\omega)|^2 \\ &= \frac{1}{2\pi} \int_0^{\infty} d\omega \langle S(\omega) \rangle \\ &= \int_{-\infty}^{\infty} df \langle S(f) \rangle, t_{msr} \rightarrow \infty \end{aligned} \quad (4.34)$$

Based on the equipartition theorem, the oscillator has $\frac{1}{2}k_B T$ average energy on each of its motion freedom. So the average potential energy follows

$$\frac{1}{2}m\omega_0^2\langle|z(t)|^2\rangle = \frac{1}{2}k_B T \quad (4.35)$$

Therefore we can solve the expression of constant strength factor g as

$$g = 4\pi k_B T \Gamma_{f_0} m \quad (4.36)$$

Finally, the power spectrum can be expressed as

$$\langle S(f) \rangle = S_0 \frac{f_0^2 \Gamma_{f_0}}{(f_0^2 - f^2)^2 + f_0^2 \Gamma_{f_0}^2} \quad (4.37)$$

where $S_0 = \frac{k_B T_{CM}}{2m f_0^2 \pi^3}$; we use the center of mass motion temperature T_{CM} here to distinguish from the internal temperature symbol T when the particle is not thermalized with environment.

For data collection, we collect N time domain positions $z(k)$ continuously at time spacing δt , and use the python Fast Fourier Transform function to obtain N frequency domain data points. The definition in python is

$$\tilde{z}(n) = \sum_0^{N-1} z(k) e^{-i2\pi \frac{nk}{N}} \quad (4.38)$$

Because there is no δt involved in the expression, we add it in to keep the unit of power spectrum consistent as m^2/Hz

$$S(n) = \frac{2\delta t^2}{t_{msr}} |\tilde{z}(n)|^2 \quad (4.39)$$

4.7.4 Appendix: Vacuum System and Measurement

We describe our vacuum measurement for a Magneto-Gravitational Trapping experiment in Figure 50. The current design of the pumping line is to connect the main chamber in Figure 50(a) with a 1 m bellow to a pump cart. The bellow introduces a vacuum conductance between the pump cart and the chamber. Therefore, we directly measure the pressure on the chamber instead of using the gauges' readings from pump cart. We trust the reading from the hot filament ionization gauge on the chamber for it measures at the lower end of the main chamber. To open the rotating valve (Figure 50(b)) on the pump cart to connect the cart and the chamber with a trapped particle in is always a pain. The particle can escape easily if the opening speed is not slow enough.

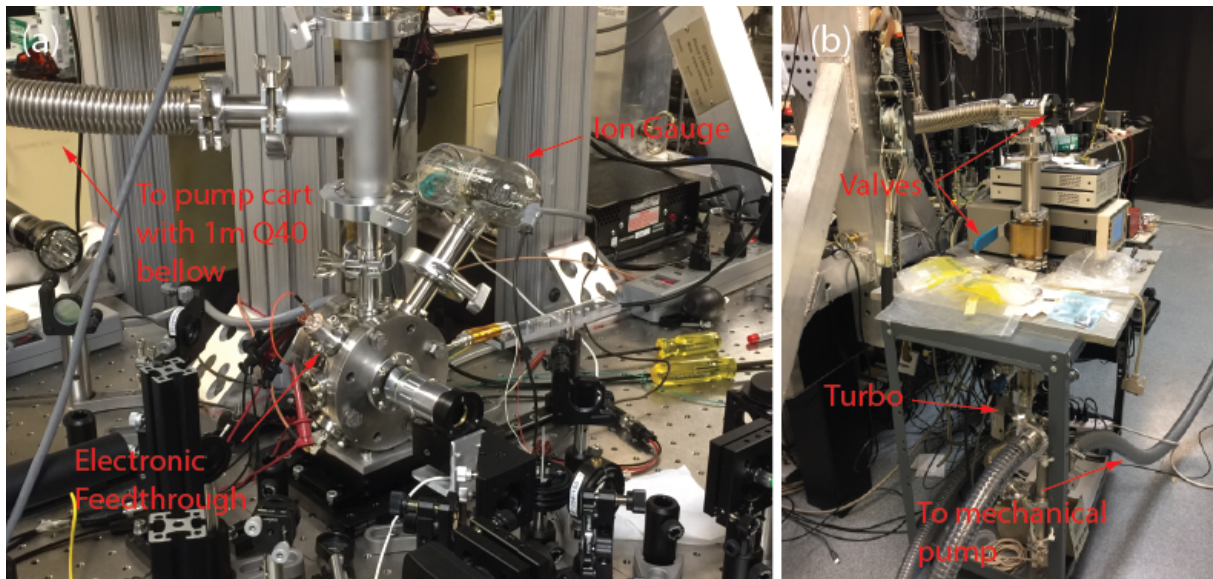


Figure 50: (a) Vacuum chamber, ion gauge and electronic feed through for a MG trapping experiment. (b) The pump cart with a turbo and connected to a mechanical pump in the pump room. The mechanical pump can generate a 10^{-2} torr vacuum while the turbo will create a 10^{-5} torr vacuum in the chamber measured from the ion gauge in (a).

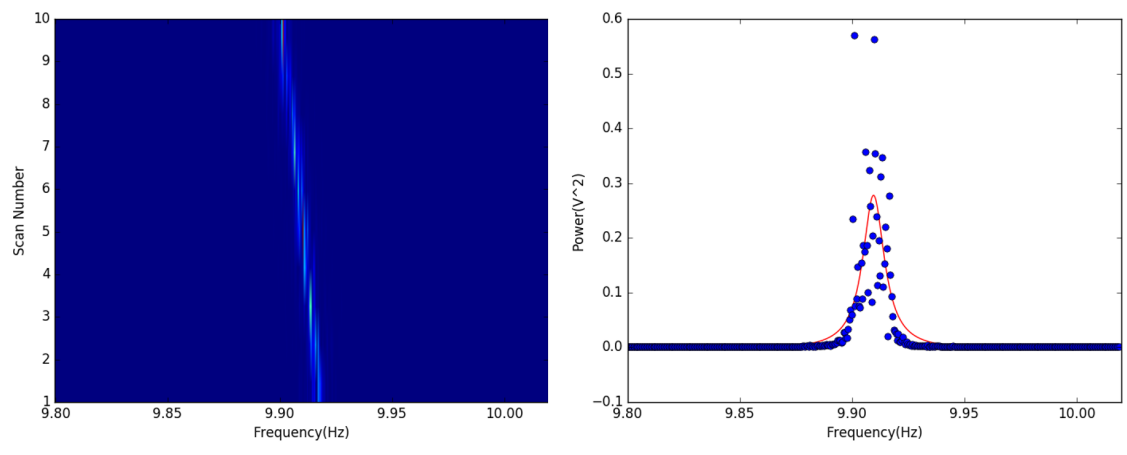


Figure 51: Left: the frequency drift over time. Time lapses with the scan number, which indicates a frequency decrease over time. Right: fitted resonance peak, $Q \approx 846$.

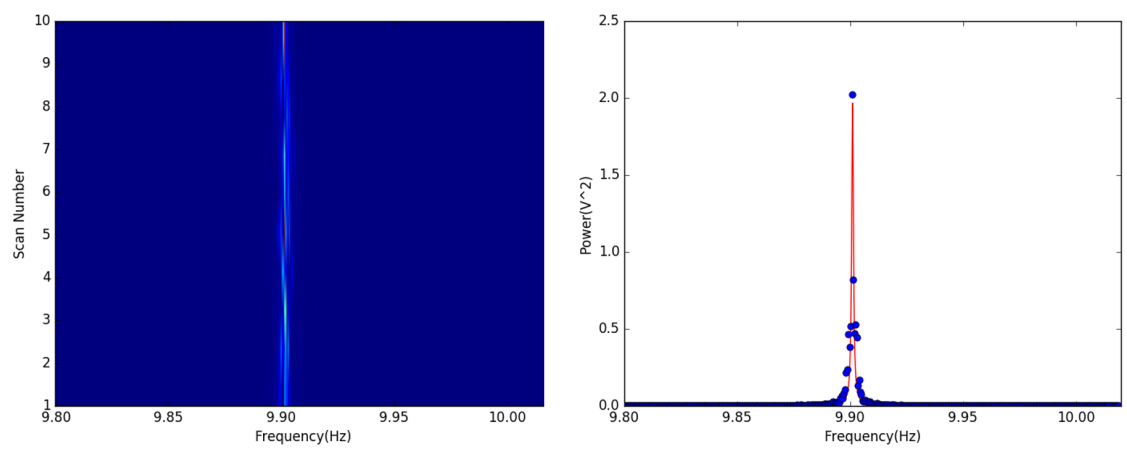


Figure 52: Left: the post-processing shifted frequency map over time. Time lapses with the scan number. Right: fitted resonance peak, $Q \approx 10532$.

4.7.5 Appendix: Q Factor Measurement in High Vacuum

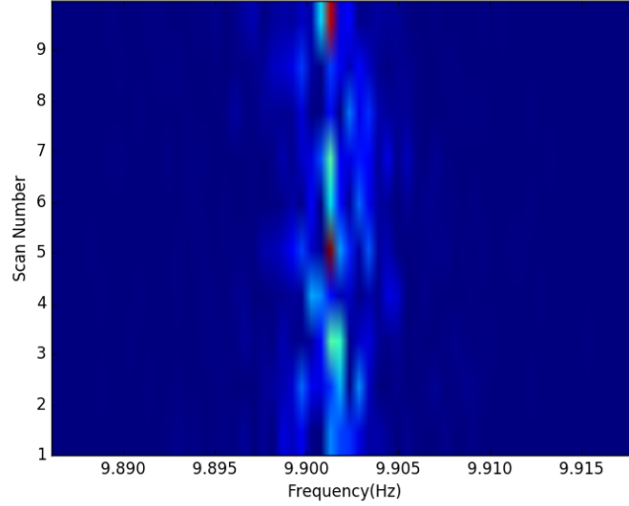


Figure 53: A random frequency diffusion behavior exists

We also try to measure the Q factor directly by the damping fitted from a thermalized motion in high vacuum. One of the formula to predict a viscosity damping of air we listed before is [19]:

$$\Gamma_0 = \frac{8}{\pi} \frac{P}{rv\rho} \quad (4.40)$$

where P is the pressure in a unit of Pascal; r, ρ are the radius and density of the trapped diamond; $v = \sqrt{3RT/M_{air}} = 508$ m/s is the speed of air molecule at room temperature T. Or a similar one from reference [96]:

$$\Gamma_0 = \frac{6\pi\eta r}{m} \frac{0.619}{0.619 + Kn} (1 + c_k) \quad (4.41)$$

where η is the viscosity coefficient of air; r, m are the radius and mass of the trapped diamond; $Kn = \bar{l}/r$, where \bar{l} is the mean free path of air. $c_k = (0.31Kn)/(0.785 + 1.152Kn + Kn^2)$ is a small positive fuction of Kn . With equation (3.22), the first equation predicts $Q = 163348$

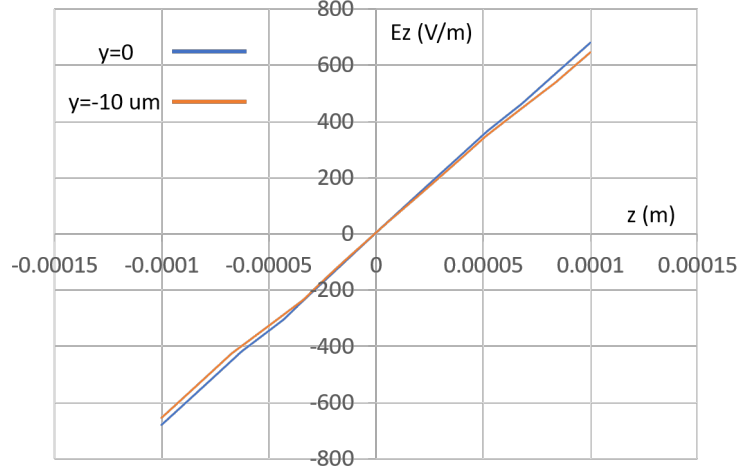


Figure 54: A E field gradient decrease can be seen from a simulation when a diamond drops downwards by $10 \mu m$ along \hat{y} direction.

for a $10 \mu m$ diamond at 10^{-5} torr vacuum (9.9 Hz), while the second formula predicts $Q = 117421$, (9.9 Hz).

We took time domain data for 1920s as one shot and repeat for 10 shots. Then we calculate the power spectrum and do a incoherent averaging over the the 10 shots. We shown our measurement of a trapped diamond in Figure 51 and Figure 52. We see a drift of the resonance frequency over time. With a post processing to realign the central frequency for the linear frequency decreasing behavior, so far we can obtain a $Q = 10532$ at 9.9 Hz. However, we are still limited by the random diffusion of the frequency in Figure 53. Also, we need at least 5 times more frequency resolution (also for beating the thermalization time) for each data taking window and repeat at least 10 averages to reduce the random noise. Therefore, to get a Q factor, we need to take data for more than one day continuously. This is difficult since mechanical and thermal drift in the lab will all matter in this long data taking procedure. We can explain the linear drift as a result of discharging and the diamond moves downwards in the trap. The balance condition gives

$$qE_y + |\mathbf{B}|\nabla_y|\mathbf{B}|\frac{\chi V}{\mu_0} + mg = 0 \quad (4.42)$$

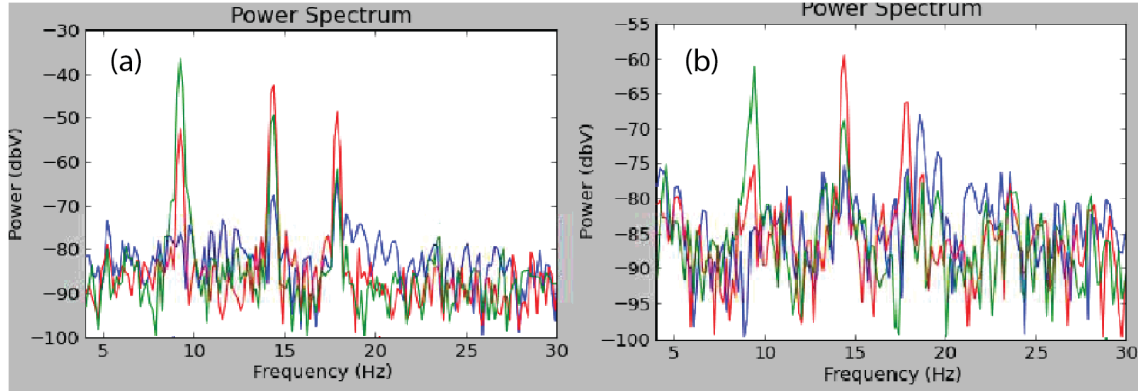


Figure 55: (a) Oscillation frequency peaks detected from a trapped diamond by the PSD (b) Cooling applied for all three peaks. Solid lines corresponds to designed different channels: axial(green), vertical(red), transverse(blue).

Based on our simulation assuming a $15 \mu\text{m}$ diamond moves downwards by $10 \mu\text{m}$, $E_y = -17537.1 \text{ V/m}$. \mathbf{B} and magnetic gradient can be estimated from $20 \text{ Gauss}/\mu\text{m}$ mentioned in section 4.2. Calculation indicates a charge loss of $1.0 \times 10^{-16} \text{ C}$ with these parameters. The simulation also shows a lower electrical field gradient at this new vertical position (Figure 54). Overall, discharging and lower electrical field gradient yield a lower axial trapping stiffness, which agrees with our observation.

4.7.6 Appendix: Cooling of The Motion on Transverse Direction

A general power spectrum we collect from the motion of the trapped diamond looks like Figure 55(a). We can observe three peaks: one maximum from the axial channel (green) of the PSD and two maxima from the vertical channel (red) of the PSD. We think one of the vertical peaks corresponds to the leak from transverse direction even the transverse channel (blue) shows much lower peaks. One of the reasons we suspect could be the misalignment of optics, where the motion along transverse direction shows certain component in the vertical direction. In experiments, due to the higher peaks on vertical direction, we always cool both the vertical and transverse directions based on the feedback signal from vertical channel.

This method results in efficient cooling Figure 55(b) and gives a stable photoluminescence image such as in Figure 39(b) . We could not tell the cooled motion amplitude at present due to the absence of thermal motion calibration on transverse direction. A higher NA side view optical imaging system is required for transverse motion calibration in the future.

4.7.7 Appendix: Possible Improvements of Optics for A Single NV photoluminescence Collection

For a single NV photoluminescence collection, a higher NA photoluminescence collection system needs to be developed beyond the current setup. A 0.5 and a 0.6 NA objective have been used for a single NV photoluminescence collection from a bulk diamond in the reference [97]. Their report shows the possibility that we can further optimize our collection system to observe a single NV center photoluminescence using an objective lens larger than 0.5 NA. One optimization we are considering is imaging the photoluminescence from a single NV onto a deep cooling CCD directly without fiber coupling.

On the other hand, the geometry of the trap restricts an upper limit to increase the collection NA. Also, the geometry requires certain working distance for a high NA objective. So far, a ~ 0.7 NA trap geometry has been tested in an experiment for trapping a micron-sized diamond crystal [14] at a working distance of ~ 4.7 mm. Further increasing the NA of the trap geometry is also possible by making the trap geometry slimmer along the transverse direction supported by simulation but not experimentally tested yet.

With currently tested trap geometry, there are two possibilities to improve our photoluminescence collection system. One is placing a commercial objective (G Plan Apo 50x from Mitutoyo) outside the chamber as well but increase the NA to 0.5 (Working Distance is 13.89 mm). The objective is designed to look through a 3.5 mm glass window and corrected for color aberration. The second strategy is placing an objective lens inside the chamber. This strategy requires special design of the assembly of the objective, which should not include any outgassing materials and can survive through certain baking temperature. We did an investigation among the current commercial vacuum compatible products. The ultrahigh vacuum compatible achromatic objective (LT-APO/LWD/VISIR/0.65) from Attocube sat-

isfies our requirements. It has a 0.65 NA and a 5 mm long working distance and can work at both room temperature and low temperature.

If we make slimmer the transverse dimension of the trap, it gives more choice to increase the collection NA by placing a commercial objective outside the chamber (e.g., Olympus LCPLFN50xLCD, 0.7 NA, 3 mm working distance). Also, meta-lens has been developed recently to replace the traditional lens (Capasso Group at Harvard). The meta-lens is made from a dielectric substrate with subwavelength metallic structures on it. This meta-lens shows its possibility for color aberration correction and high NA feature [98, 99]. Due to the absence of outgassing materials, this opens another possibility to place a meta-lens instead of a traditional objective lens inside a vacuum chamber.

4.7.8 Appendix: Preliminary Result in a Electromagneto-Gravitational Trap

Another strategy to improve the ODMR signal is to use an electromagnet for the trap instead of a permanent one. We can pulse on and off the current in the coil and take the ODMR signals when the current is off. We show in Figure 56 a preliminary test which successfully trapped a particle with such a trap. We are using AWG 32 wire, 500 turns for both two coils attached to the pole pieces. When we run a current of 0.8 A in both coils, we can trap a particle with pure diamagnetic force in Figure 56(b). We see a concave part of the bottom pole pieces which results from the imperfectness of machining. We then wrap the bottom pole piece with the copper deposited Kapton strip and deliver the microwave through the trap. Then we inserted the probe with CNW diamonds(cluster) into the trap (Figure 56(c)). Due to the size of current probe $\sim 120\mu m$, we do not have much space to move around search zero field region. We just placed the probe in a random location and showed the ODMR detection with different currents in Figure 57. It is clear that from 0 A to 0.08 A(1/10 of the trapping current), the ODMR signal not only changes in position but also reduce in contrast. However, it is still promising to use a magnetic field adjustable trap for it will be much easier to locate the zero field region when the current is small and tracking the region as the field increase based on the ODMR signal. The challenge of this strategy so far is to

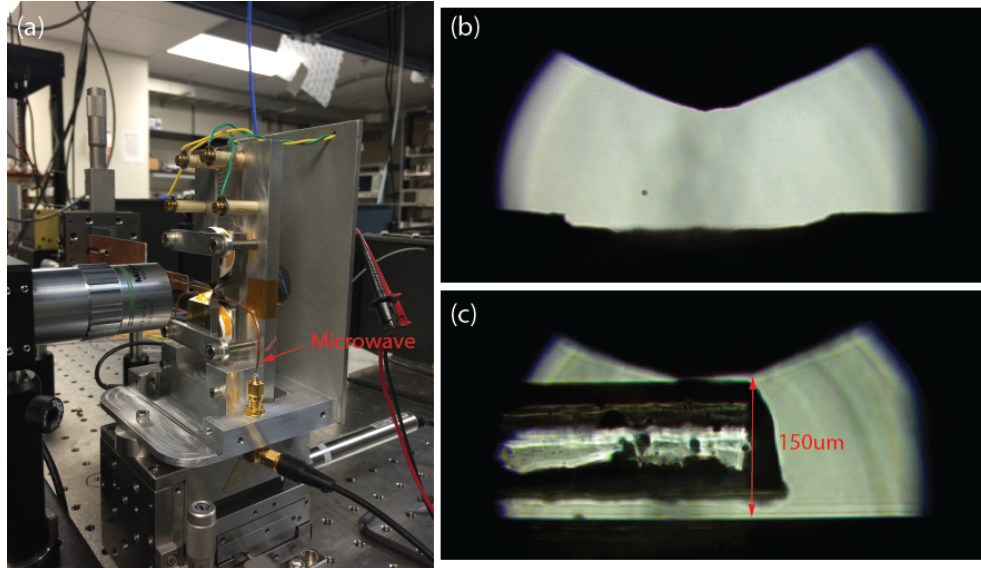


Figure 56: (a)The electromagnet trap, coils are covered under the Teflon(white) (b)A trapped particle in the electromagnet trap. (c)A probe with diamond on it has been inserted into the trapping region to explore the ODMR signal at different currents.

cool the coil in the vacuum chamber. In fact, the trapped particle in Figure 56(b) is slowly moving out of the trap. This is due to current fluctuation when the coil is heated up and the resistance of the coil increase. With 0.8 A current in the coil, the temperature of the trap can reach 100 °C within a couple of minutes. Therefore, a careful design of cooling the trap in the vacuum is required for future development.

4.7.9 Appendix: Designs of Trap, Ultrasonicator and Feedback Circuits

We show the designs of my trap, the ultrasonicator, and feedback circuits from Figure 58 to Figure 63 in this section.

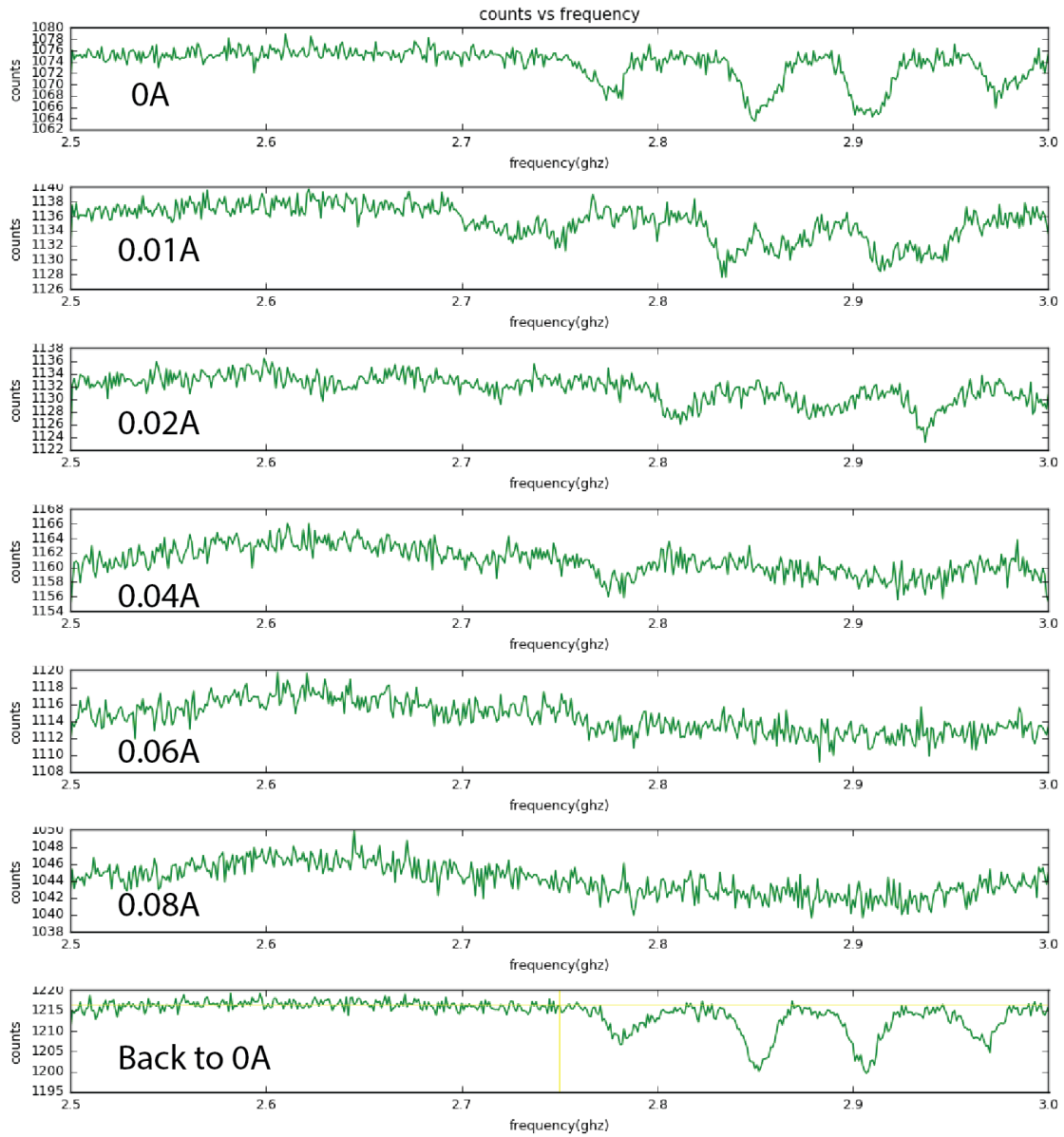


Figure 57: The ODMR detected from CNW diamond sample on the probe in a random location in the Electromagneto-Gravitational trap with different current in the coils. The splitting of ODMR signals at 0 A indicates a non-zero magnetic field at the location of NV centers

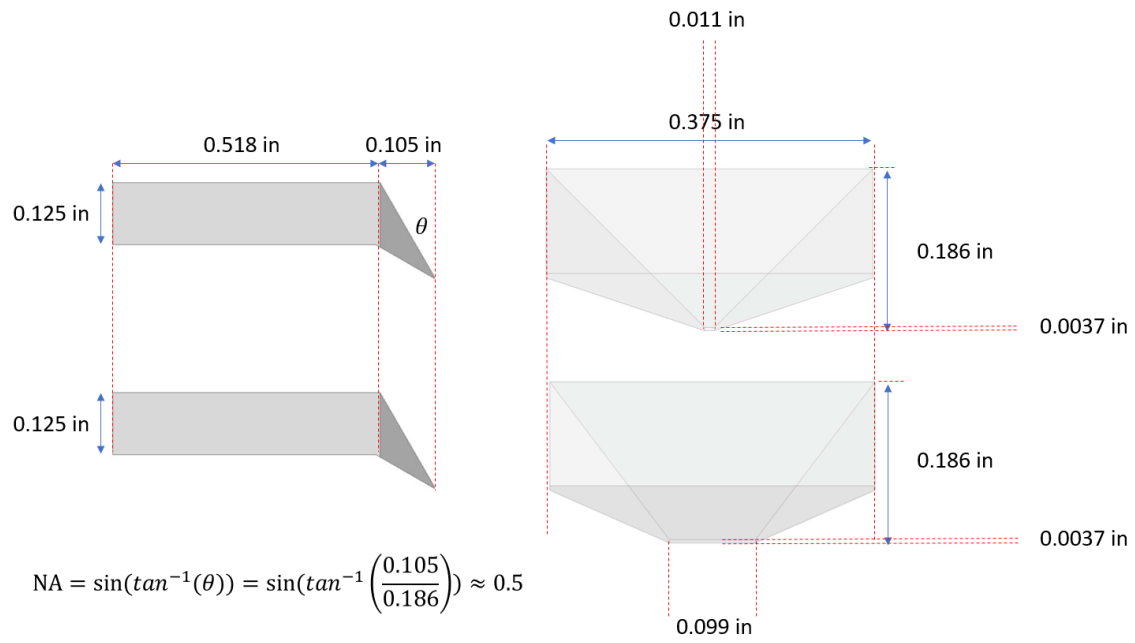


Figure 58: The designed parameters of the Hiperco 50A pole pieces. First row: top pole piece geometry. Second row: bottom pole piece geometry.

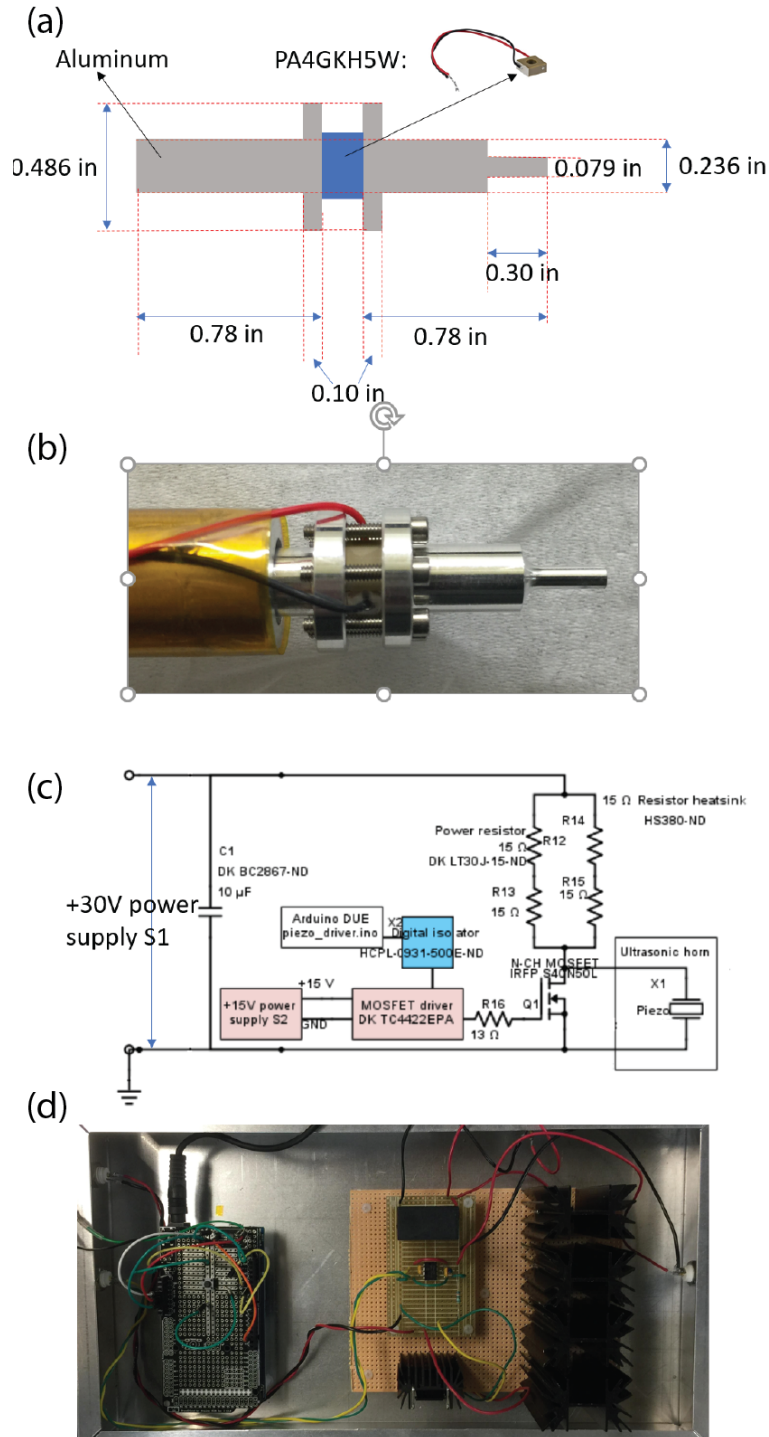


Figure 59: The geometry and driven circuit of for the ultrasonic horn (a)Parameters (b)Photo of the built one in our lab (c)Circuit drawing modified from reference [16] as in our experiment (d)Photo of our built circuit.

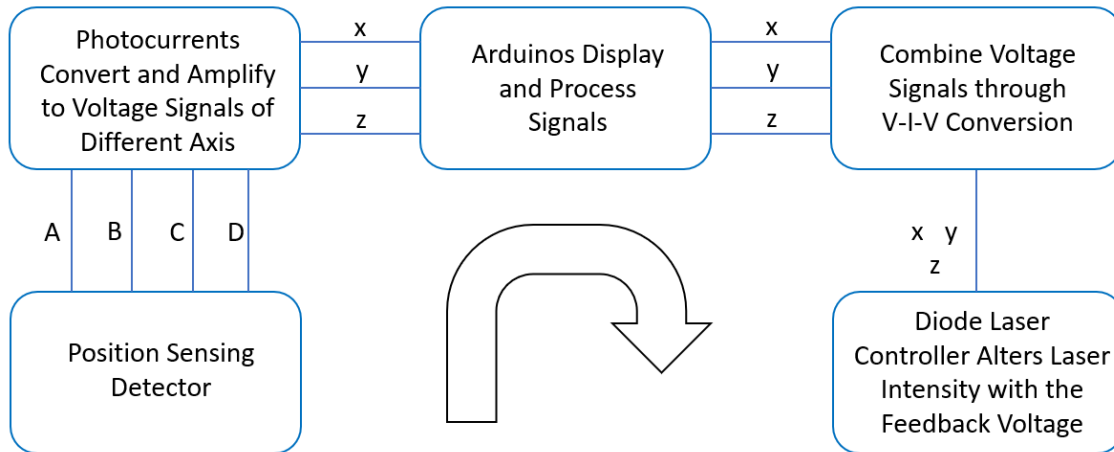


Figure 60: The diagram of the feedback loop. A,B,C,D correspond to the four elements of the position sensing detector in Figure 31. V-I-V indicates a voltage to current to voltage conversion.

4.7.10 Appendix: Other Instruments in the Experiment

In this section, I list other instruments used in our experiment but has not been mentioned in this chapter.

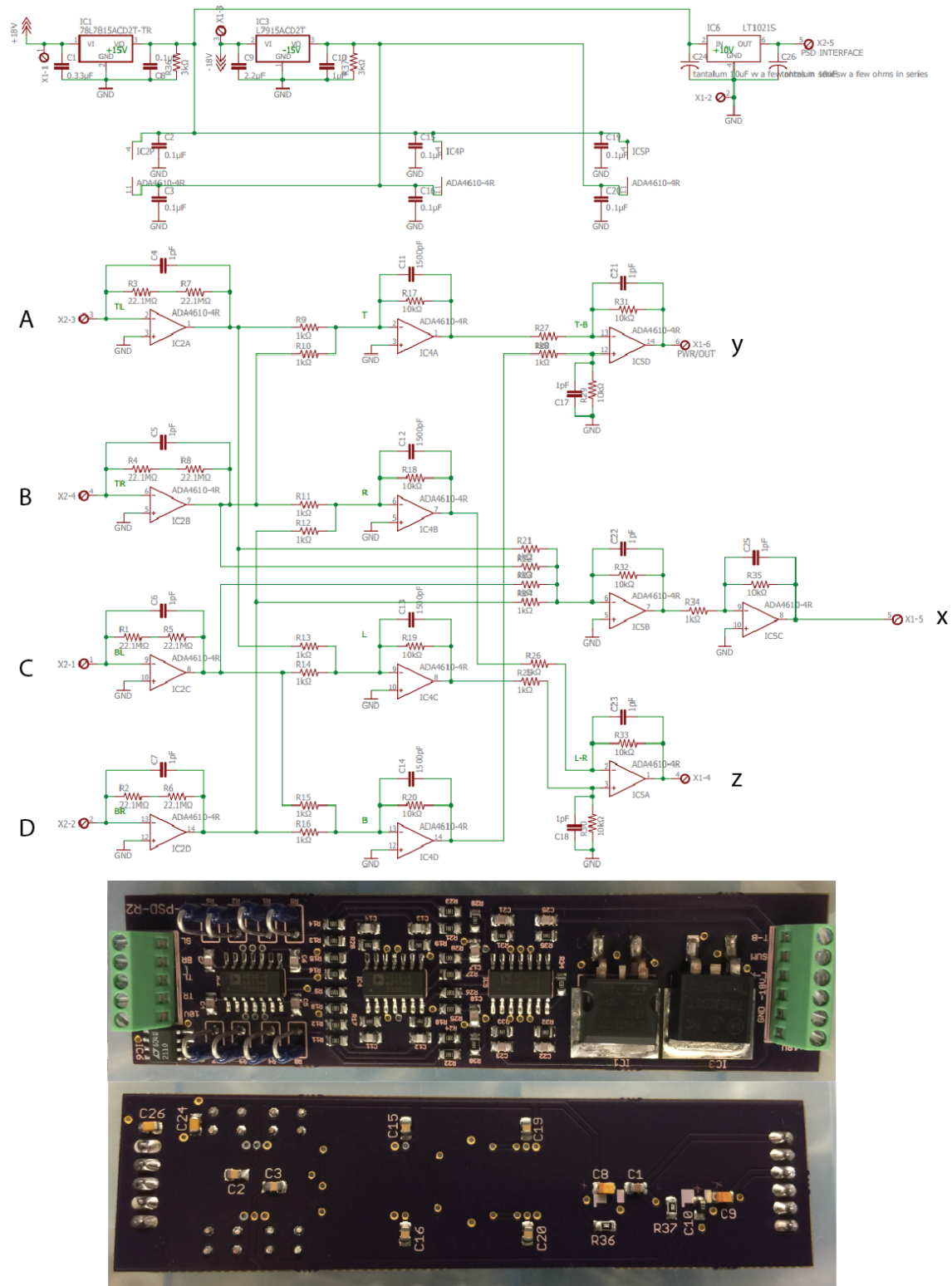


Figure 61: Design of PSD photo currents amplification circuit and the soldered one in our experiment.

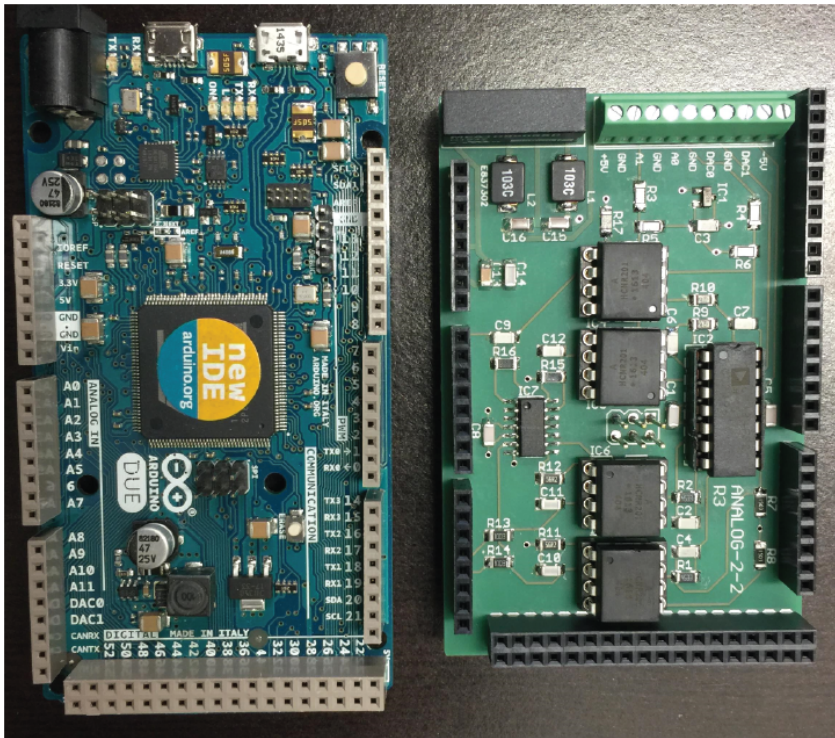


Figure 62: The photo of Arduino Due board and related shield plugging on it. We build the shield based on Dr.D’Urso’s design. There are four set of Arduino used in our experiments. One for displaying the read-in 3 voltages (x,y,z) from the PSD circuit and transfer the values to computer from a serial port. Another three are for processing the PSD circuit voltages and output modulated signals(phase and amplitude) to the feedback circuit.

#	Instrument	Description
1	Coherent Verdi G laser	532 nm, 7 W, for NV excitation and feedback scattering
2	Thorlabs diode laser	670 nm, 4.7 mW, for fake photoluminescence in a control experiment
3	Acopian Y0100MX25	Adjustable floating voltage supply 0-100V, bias voltage on the pole pieces
4	Keithley 2000 Digital Multimeter	Monitor the voltage on the pole pieces
5	Cambridge 06291 Galvo mirror	Scan mirror for the photoluminescence image from a trapped diamond
6	Mitutoyo Plan Apochromat Objective	Scattering and PI collection from the trapped diamond
7	Veeco Ionization Gauge Controller	Monitor the vacuum in the chamber
8	K J Lesker hot filament Ion Gauge	Detect the high vacuum in the chamber
9	Kimball Physics Vacuum Chamber	4.50 inch Spherical Octagon
10	HP 8350B sweep oscillator	Microwave generator for ODMR experiment
11	Agilent 8596E spectrum analyzer	Monitor the transmission power and frequency of the microwave
12	Mini-circuit ZHL-16W-43 Amplifier	Amplify the microwave before delivering to the trapped diamond
13	Amscope MU300 CMOS camera	Monitor the motion of the trapped diamond
14	Pfeiffer THM 261	210 l/s Turbo and Controller, creating the high vacuum in the chamber
15	PerkinElmer Single Photon Counting Module (SPCM)	Detect the photoluminescence photons from the trapped diamond
16	National Instrument DAQMx	PCI-6610, analogue outputs, counters.
17	Andor iDus DU401 CCD	Cooled CCD on a home-made spectrometer

Table 5: List of other instruments used in our experiment

5.0 CHARGE STATE DYNAMICS OF NITROGEN-VACANCY CENTERS IN DIAMOND UNDER 1064 NM LASER EXCITATION

The photophysics and charge state dynamics of the nitrogen-vacancy (NV) center in diamond has been extensively investigated but is still not fully understood. In contrast to previous work, we find that NV^0 converts to NV^- under excitation with low power near-infrared (1064 nm) light, resulting in *increased* photoluminescence from the NV^- state. We used a combination of spectral and time-resolved photoluminescence experiments and rate-equation modeling to conclude that NV^0 converts to NV^- via absorption of 1064 nm photons from the valence band of diamond. We report fast quenching and recovery of the photoluminescence from *both* charge states of the NV center under low power 1064 nm laser excitation, which has not been previously observed. We also find, using optically detected magnetic resonance experiments, that the charge transfer process mediated by the 1064 nm laser is spin-dependent. Same content is published on Phys. Rev. B [100] ©2016 American Physical Society.

5.1 INTRODUCTION

The negatively charged NV defect center (NV^-) in diamond has become prominent for applications in quantum information, nanoscale magnetic and electric field sensing, and fluorescent biological markers [101, 50]. However, the photophysics of the NV^- center, and the dynamics of charge transfer between NV^- and NV^0 defect states, as well as the energy level structure and positions of the defect levels within the diamond bandgap, are still subjects of current research [18, 102, 101]. Improved readout of the spin state via spin-to-

charge conversion [103] is crucially dependent on a better understanding of the photophysics of the NV center. Another exciting recent direction of research is the trapping of diamond nanocrystals for quantum optomechanics [104, 35, 105]. A decrease of photoluminescence was observed from NV centers in the nanodiamonds that were optically trapped by an infrared laser. In 2013, two groups observed fast photoluminescence quenching and recovery under infrared excitation from nanodiamonds on a glass substrate [106, 107]. Explanations for these effects have included heating of diamond [105], multi-photon process [106], charge state transfer [35] and also a dark state within the intrinsic optical transition of the NV center [107]. Although the underlying physics is still not well understood, the infrared laser-induced effect has already been used for NV super-resolution microscopy and the all-optical transistor [108, 106, 107].

In this work, we study the charge state dynamics of the NV center under 1064 nm laser excitation, through a combination of spectral and time-resolved photoluminescence and optically detected magnetic resonance experiments. We report four new findings: (i) the observation of *enhanced* photoluminescence from the NV^- charge state, (ii) fast modulation (quenching and recovery) of the photoluminescence ($\sim ns$) from *both* NV^- and NV^0 charge states, (iii) slow ($\sim \mu s$) charge transfer between NV^- and NV^0 charge states under 1064 nm laser excitation, and (iv) evidence for spin dependent charge state dynamics under 1064 nm laser excitation. Our work brings new physics to light for the NV community, suggesting that NV charge conversion can be induced by the 1064 nm photon, which may help to better understand the photophysics of the NV center and the energy level structure of the NV^0 state.

5.2 EXPERIMENT

5.2.1 Diamond Samples

The electronic grade bulk diamond sample (Element Six, $[N] < 5$ ppb) was nitrogen implanted at 85 KV, with $10^{11}/\text{cm}^2$ dose, followed by annealing at 1000 °C in forming gas

(N₂ and H₂). This procedure creates a 20 nm NV center layer at about 100 nm below the diamond surface with estimated NV area density of 10/ μm^2 . The 100 nm nanodiamonds (Adamas Nanotechnologies, Inc.) used in the experiment contain on average ~ 500 NV centers in each nanodiamond (ND). These diamonds arrived suspended in de-ionized water, and we diluted it with ethanol and deposited it onto clean silicon chips. Figure 74 (c) shows the SEM image of these individual nanocrystals. We observed significant heterogeneity of the count rates from the ND, that could arise from the interplay of the crystal and NV orientation, laser polarization, charge state, and lifetime effects.

5.2.2 Improving Thermal Contact and Drift

Our experimental setup is sketched in Figure 74(a). A confocal microscope is built for imaging the NV centers in diamond samples. We overlap the 532 nm excitation laser (Green) with a continuous wave (CW) 1064 nm laser (IR), and a long focal length lens was placed individually in the 1064 nm laser path to correct the chromatic aberration from the objective lens. The photoluminescence (PL) emitted by NV centers is collected with a high numerical aperture (NA) dry objective (Leica, Apo 0.9 NA). Different bandpass filters are applied for NV⁻ or NV⁰ as described below, and the photoluminescence is fiber-coupled into a Single Photon Counting Module (SPCM) for integrated counts or to a spectrometer. Microwaves are delivered through a 30 μm in diameter gold plated tungsten antenna to the target NV centers to manipulate their ground spin states. The objective and the samples can be enclosed in a cryostat chamber, which enables a low-temperature environment.

Previous studies were carried out with very high peak-power pulsed 1064 nm excitation [106] or moderate CW power [107] and did not mention the thermal drift of the sample caused by laser heating. However, we found in our system that using a substrate with poor thermal conductivity such as cover glass, which was typically used with the earlier ND studies [106, 107], will result in thermal drift of the sample and reducing the collected photoluminescence counts on a time scale of “seconds”. We suspect this is possibly due to the thermal expansion of the substrate when tens of milliwatts of 1064 nm laser are intensely focused on it. This drift can be corrected by re-optimizing the focus on the sample but may

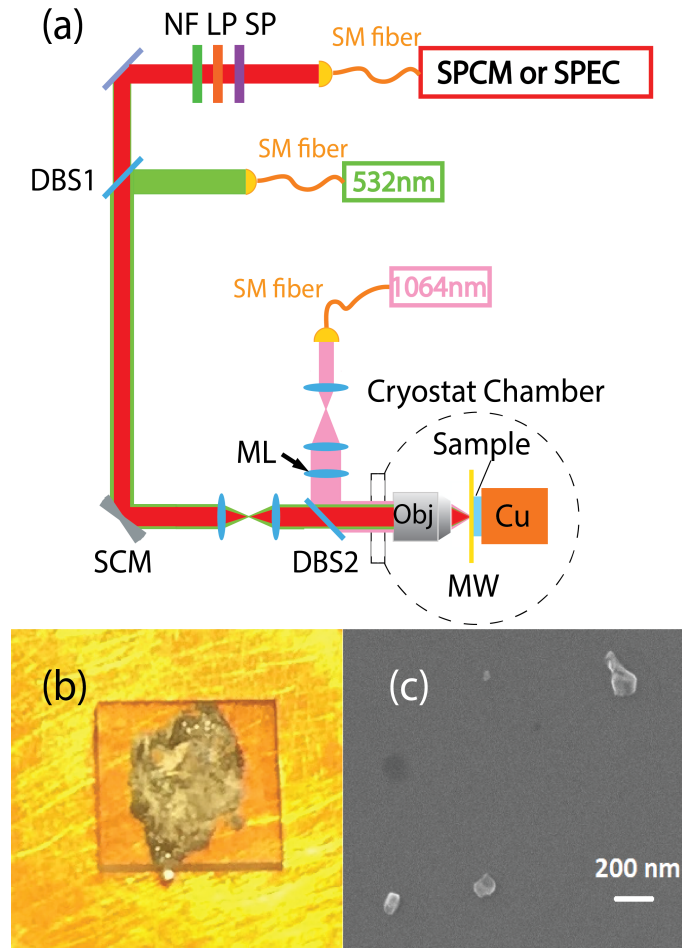


Figure 64: (a) Experimental confocal microscope integrated with 1064 nm CW laser. 532 nm laser, photoluminescence from NV centers and 1064 nm laser are separated by two dichroic beam splitters (DBS1 and DBS2). A moving lens (ML) in 1064 nm laser path helps to correct the chromatic aberration of the high NA Objective (Obj). Scanning mirror (SCM) helps to obtain 2D photoluminescence image. Samples are indium soldered on the cold finger made of copper (Cu), and microwaves are delivered with antenna (MW) to the sample. Notch 532 nm (NF) and different long pass (LP) and short pass (SP) filters are applied for different collection windows (650 nm LP and 800 nm SP for NV^- or 582/75 nm bandpass filter for NV^0). The photoluminescence was coupled into a single mode fiber (SM fiber) and received by Single Photon Counting Module (SPCM) or a spectrometer (SPEC) (b) Optical image of indium soldered bulk diamond on a copper plate (yellow), the indium solder (silver) can be seen through the bulk diamond, which is 3.5*3.5mm for its dimension (c) SEM image of 100 nm commercial nanodiamond deposited on a silicon chip.

interfere with the effects we are interested in. Therefore, we attached our sample to the cryostat cold finger (made of high purity oxygen-free copper), which serves as an excellent heat sink for the sample. The attachment between the sample(or silicon substrate for ND) and a cold finger is by indium soldering. We particularly choose indium soldering because this mechanical bond gives good thermal contact and can survive at low temperature. It also provides a lower photoluminescence background for a transparent sample compared to most optical adhesives. After indium soldering, under tens of milliwatts of 1064 nm laser illumination, we found that the counts were stable under IR excitation, and also found that re-optimizing the focus no longer improved the photoluminescence level, which suggests the thermal drift problem has been eliminated. Figure 74(b) shows the indium soldered bulk diamond sample on a copper plate (part of our cold finger).

5.3 RESULTS AND DISCUSSION

5.3.1 Steady State Photochromism with IR Excitation

We find a marked change in the photoluminescence spectrum when exciting simultaneously with 532/1064 nm CW laser illumination. This phenomenon is robust at both room temperature and low temperature (Figure 65) and is visible in both bulk diamond and diamond nanocrystals.

The photoluminescence in the wavelength range from 550 nm to 625 nm has been identified as originating from NV^0 , while it is usually accepted that the photoluminescence from the NV^- phonon side band (PSB) dominates over that from NV^0 in the wavelength range from 650 nm to 800 nm [109]. Since the photoluminescence change in Figure 65 shows a decrease in the NV^0 band, while there is a corresponding increase at the same time in the NV^- band, we believe the 1064 nm laser has the ability to induce the charge state flipping from NV^0 to NV^- . For the bulk diamond sample at room temperature (295K) in Figure 65(a), we observed obvious photoluminescence decrease at the zero-phonon line (ZPL) of NV^0 centers (575 nm peak), while no marked photoluminescence increase was observed at

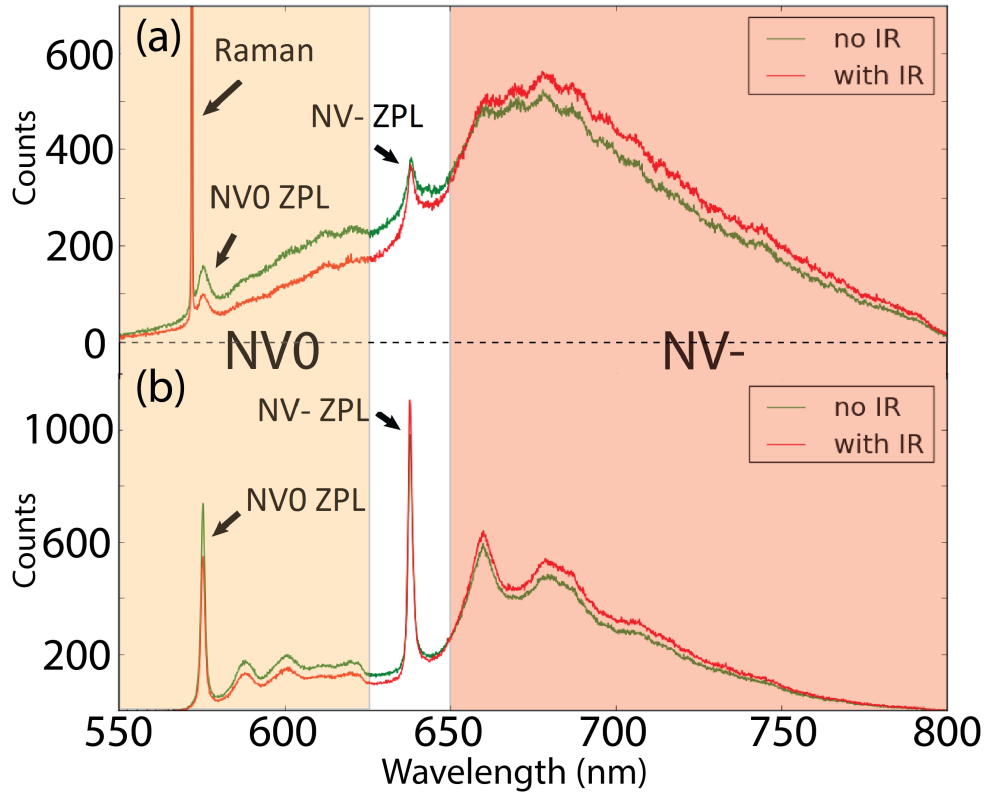


Figure 65: (a) Photochromism behavior of NV centers in bulk diamond at room temperature 295K under 1064 nm laser illumination (120 s exposure). ZPL of NV⁰ and NV⁻ are observed at 575 nm and 638nm; strong Raman peak is observed at 572.8 nm (b) Photochromism behavior of NV centers in 100 nm diamond nanocrystal at 16K under 1064 nm laser illumination (30 s exposure). ZPL of NV⁰ and NV⁻ are observed at 575 nm and 637nm; no obvious Raman peak is observed at 572.8 nm. Shaded ranges indicate NV⁰ (yellow) and NV⁻ (red) photoluminescence collection window, shared with (a) and (b).

the ZPL of NV^- centers (638 nm peak at room temperature and 637nm at low temperature). This is because the PSB of NV^0 center slightly overlap with the NV^- ZPL [18, 110]. We observed similar photoluminescence change under low temperature (16K) from the 100 nm ND sample, as seen in Figure 65(b). One noticeable difference is the absence of a strong Raman line from the ND, which is expected in moving from bulk to nanocrystalline diamond..

In the spectrally-integrated data that we present in the rest of the work, we will refer to photoluminescence collected in the spectral window from 650-800 nm as arising from the NV^- charge state, and to photoluminescence collected in the spectral window from 550 - 625 nm as arising from the NV^0 charge state. This is in good agreement with previous observations, as well as with our data shown in Figure 65.

5.3.2 Time Resolved Photoluminescence

Nanodiamonds that we purchased commercially have large heterogeneity, and therefore we focused on the bulk diamond sample to further study this 1064 nm laser induced effect. Firstly, the confocal images of NV centers in the bulk diamond were taken in Figure 66. We chose randomly a location where both charge states give sufficient counts rate as shown in Figure 66(a) and (b). Then, we turn on and off the IR laser while green excitation is on all the time. The data shown in Figure 66 (c) and (d) are obtained by integrating the counts in the spectral window corresponding to NV^- and NV^0 respectively. The increase (decrease) of the counts in the two spectral regions, modulated by the IR laser, is robust and is the opposite of previous experiments in ND that found only decreased photoluminescence of the NV^- state under IR excitation [106, 107].

We modulated both green and IR lasers on sub-microsecond timescales to time-resolve the photoluminescence from NV^- and NV^0 . We used an acoustic-optic modulator (AOM) in our experiments to realize fast switching of both 532 nm and 1064 nm lasers. The response times of both AOMs are ~ 50 ns. The first experimental pulsed sequence and result are shown in Figure 67. The photoluminescence is collected for both states under the same experimental condition and then normalized to the steady-state photoluminescence separately.

As shown in Figure 67, after the 1064 nm laser was on, we first observed a fast quench

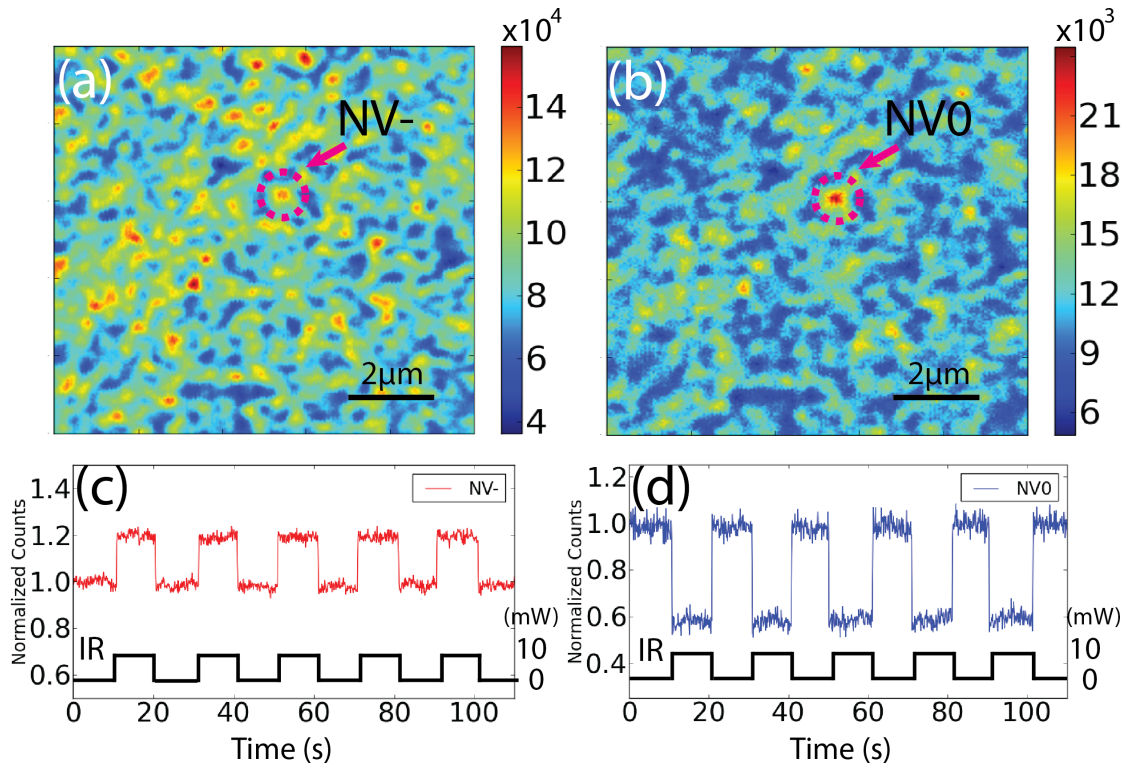


Figure 66: Confocal images of ensemble of NV centers in bulk diamond sample at room temperature under 0.25mW Green excitation (a) NV⁻ photoluminescence data (b) NV⁰ photoluminescence data (c) Time trace of the NV⁻ photoluminescence counts, under IR gating (10 mW), normalized to when IR is off (d) Time trace of the NV⁰ photoluminescence counts, under IR gating (10 mW), normalized to when IR is off.

of photoluminescence counts for both charge states. It was followed by a slow increase for the NV^- state and a slow decrease for NV^0 state separately. Neglecting the fast decrease for the moment, we call the latter effect the “slow effect”. Below, we have developed a simple theoretical model (Figure 68) based on $NV^0 \leftrightarrow NV^-$ charge state transfer which explains quite well the slow effect.

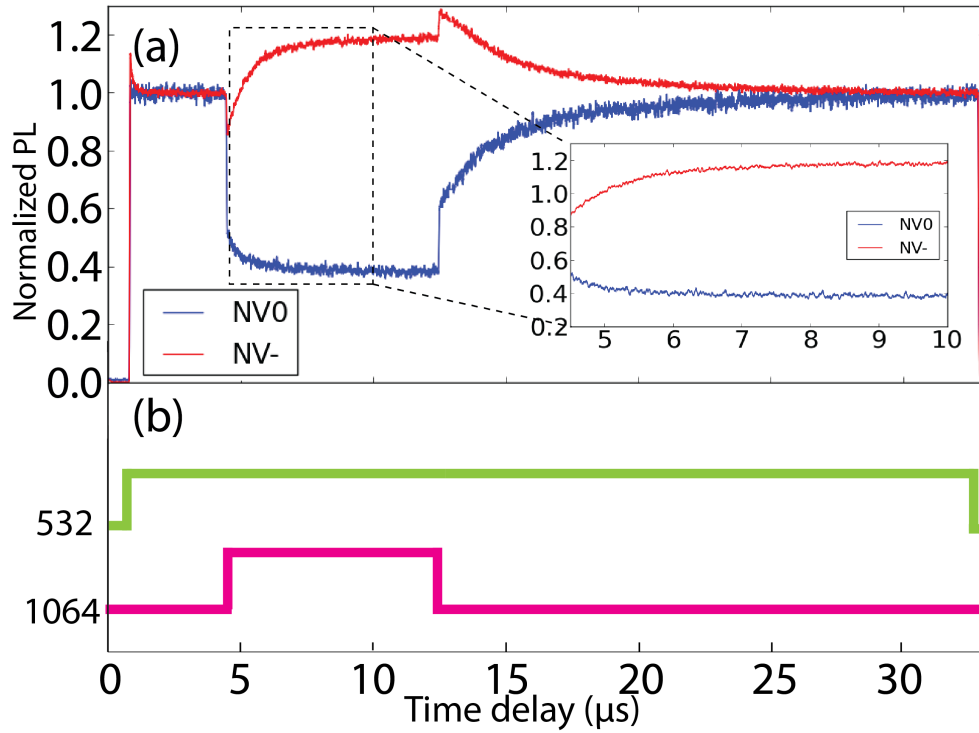


Figure 67: (a) Photoluminescence versus time (Savitzky-Golay filter applied [17]) while fast switching on and off 1064 nm laser applied by AOMs; inner figure: Zoom in of the “slow effect” (b) Optical pulsed sequence used in the experiments for result (a)

5.3.3 Theoretical Model

The relative location of the NV^- charge state to the conduction and valence band of diamond has been established as shown in Figure 68 (following Ref. [18]). The current understanding is that the photo-ionization from NV^- to NV^0 is actually a two-step procedure: one laser photon with energy > 1.95 eV excites the ground state NV^- to the excited state, followed

by another laser photon ionizes it through diamond conduction band, resulting in the NV^0 charge state [111, 112, 113, 18].

Meanwhile, the position of NV^0 energy levels relative to the conduction and valence bands is not well known, and the source of the electron captured by NV^0 to convert it back to NV^- is still under debate. One possible electron donor is the valence band of diamond. Similar to the ionization process, the $NV^0 \rightarrow NV^-$ process was also suggested to be a two-step procedure, which requires one laser photon with energy > 2.15 eV to excite NV^0 to its excited state, followed by another photon that promotes an electron from the valence band, which is captured by NV^0 to form NV^- charge state [102, 113, 18]. This explanation met trouble when experimental detection of $NV^0 \rightarrow NV^-$ process occurred under 593 nm (2.1 eV) laser illumination, in which case the NV^0 charge state should not be excited [18]. The substitutional nitrogen impurity (P1 center) nearby was suggested as another possible source of the electron [114, 18]. In this one-step procedure, NV^0 captures the optically excited electron from a nearby P1 donor through conduction band and is converted to NV^- . However, since the P1 donor level is measured to lie $1.7 \sim 2.2$ eV below the conduction band [115], the 1064 nm laser (energy of 1.165 eV) should not be able to trigger this one-step transformation. Ref. [114, 18] also indicate thresholds as 1.95 eV or 2.03 eV separately to trigger this one-step procedure based on their data. Therefore, we postulate an extension for the two-step $NV^0 \rightarrow NV^-$ model that 1064 nm laser may provide sufficient photon energy to complete the second step, where a 1064 nm laser-excited electron from valence band got captured by an NV^0 to form an NV^- . This extended two-step process competes with the well studied ionization procedure caused by 532 nm laser (converts NV^- to NV^0), forming a new balance of charge states population. We use a simplified two-state (NV^- and NV^0) model to describe the dynamics of charge state flipping. The populations of the charge states can be described as follows:

$$\frac{dP^-}{dt} = -r^{-/0} * P^- + r^{0/-} * P^0 \quad (5.1)$$

$$\frac{dP^0}{dt} = +r^{-/0} * P^- - r^{0/-} * P^0 \quad (5.2)$$

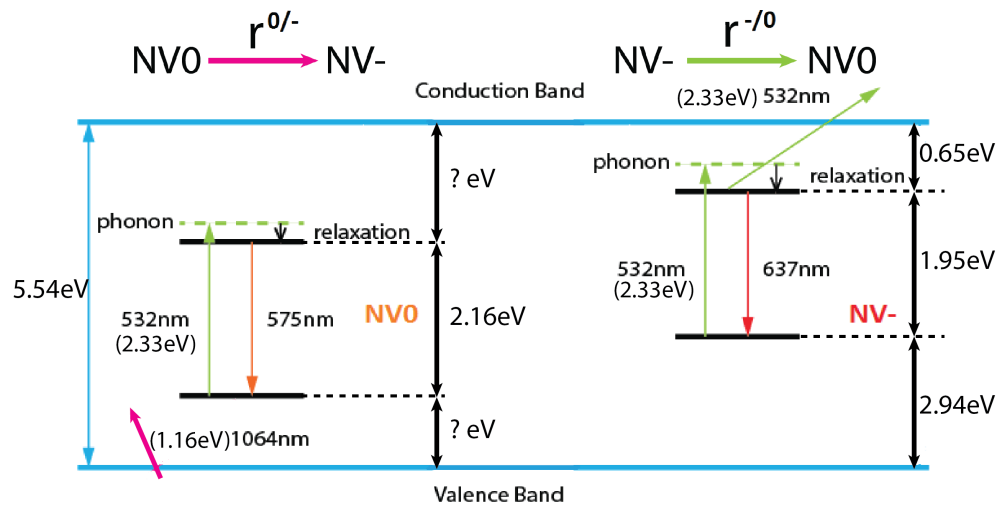


Figure 68: The theoretical model for NV charge state flipping. Left: our postulated model that NV⁰ is excited first by 532 nm laser (green arrow), then it captures an electron promoted by 1064 nm laser from the valence band (pink arrow). This two-step procedure converts NV⁰ to NV⁻. Right: accepted photo-ionization two-step procedure induced by 532 nm laser (green arrows indicate the two steps), which converts NV⁻ to NV⁰ [18] through the conduction band.

where $P^i(t)$ ($i = -$ or 0) are the population of two charge states respectively as a function of time, $r^{-/0}$ is charge flipping rate from negative to neutral state while $r^{0/-}$ is the opposite. The dynamic solution indicates an exponential dependence of populations versus time:

$$P^i(t) \sim \exp(-(r^{-/0} + r^{0/-}) * t) \quad (5.3)$$

We used this result to fit the “slow effect” shown in Figure 67(a) and obtain the dependence of $r = r^{-/0} + r^{0/-}$ on 1064 nm laser power, which is shown in Figure 69.

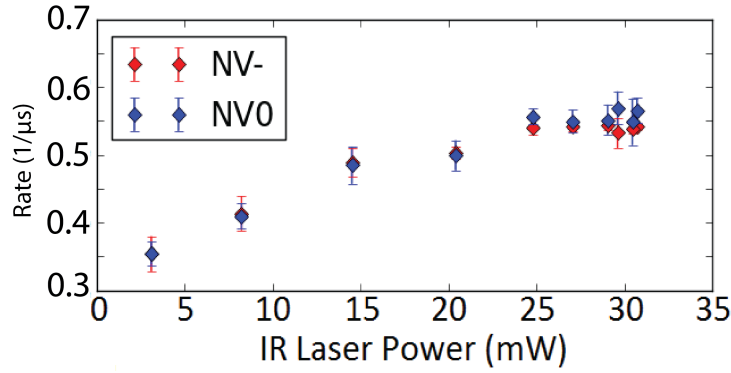


Figure 69: Dependence of the charge-flipping rate $r = r^{-/0} + r^{0/-}$ on the 1064 nm laser power. Green laser excitation is fixed at 0.3 mW.

From Figure 69, firstly, it is clear that the rates of the slow changes in photoluminescence collected from NV^- and NV^0 are synchronized reasonably well, which indicates again that the charge state flipping argument is correct. Secondly, the charge-flipping time constant is on microseconds time scale, which is much slower than the internal optical transitions of NV center [101]. This time scale also agrees with the conclusions in Ref. [18] under IR illumination power we used in experiments. Finally, we found a linear relation between IR power and the sum of flipping rates in Figure 69 when IR power is moderate (<15 mW). We believe the saturation behavior after that is limited by the specific process that happens during electron promotion, such as saturation from weak green excitation and optical pumping.

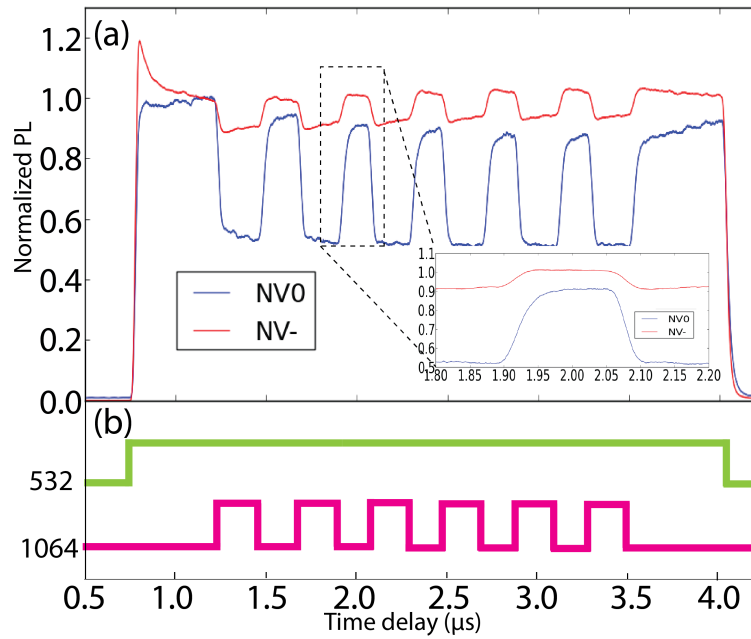


Figure 70: (a) Photoluminescence versus time (SavitzkyGolay filter applied [17]) under fast modulation to examine the rapid quenching behavior; inner figure: Zoom in of the fast edges of photoluminescence counts (b) Optical pulse sequence used for the results in (a)

5.3.4 Fast Modulation of Photoluminescence from Both Charge States

We now return to the rapid quenching and recovery of the photoluminescence which we observed for both charge states in Figure 67. To gain further insight, we applied 1064 nm laser pulses of width 200ns repeated several times, as shown in Figure 70. As seen in the data, the fast decrease and subsequent recovery for both charge states are limited by the response time of our AOM (~ 50 ns).

The first observation of 1064 nm laser induced photoluminescence fast quenching for both charge states were reported by Ref. [106]. In their experiments, a high peak power 1064 nm pulsed laser (4.8 MHz repetition rate, 16 ps pulse duration) was focused by 1.4 NA oil immersion objective onto ND samples. We estimated that the focused peak power density ~ 400 W/ μm^2 from the parameters given in that work. The authors attributed the fast quenching time of hundreds of picoseconds to multiple-photon (MP) related thermal induced change in NV photophysics parameters. However, in Ref. [107], a similar quench was reported on single NV⁻ centers in diamond nanocrystal under very different conditions using a CW IR laser at 1064 nm. In that work, the laser was focused onto ND deposited on cover glass by 1.2 NA oil immersion objective, and we estimated that the focused power density ~ 65 mW/ μm^2 from their parameters. They argued their laser was not powerful enough to trigger MP procedure. The explanation of their data was postulated to be a previously unreported dark state in the optical transitions of the NV⁻ center. However, they did not report that this phenomenon also exists and is even more pronounced for NV⁰ charge state as we show in Figure 70.

Based on the previous results, and our experimental conditions, we believe our data also does not originate from any thermal heating or MP processes. Firstly, we are using a CW laser which is being modulated on much slower timescales in comparison to the pulsed laser in Ref. [106]; secondly, because of the 0.9 NA dry objective we use compared to Ref. [107], our laser-focused intensity is even lower (~ 20 mW/ μm^2 maximum). We also provided a much better thermal contact with a good heat sink material, and in comparison to ND, we used bulk diamond which has extremely high thermal conductivity. Ref. [106] also claimed they did not see an obvious effect by using CW 1064 nm laser, which is the excitation that

we use. Therefore we believe that the fast quenching is not because of the heating or MP processes caused by the 1064 nm laser.

In our model, when low green illumination is used, the excited state of both charge states is populated only weakly. The first possibility is that the IR laser causes transitions from the ground state to one of the metastable electronic levels. However, while the NV^- center has a metastable singlet transition (1A_1 to 1E) at 1042 nm, it is unlikely that a transition will occur at the low excitation powers we use, and further the typical 300 ns singlet relaxation time is much longer than the fast recovery we see. Another possibility is that the IR photon causes a fast deformation of the lattice away from the C_{3v} symmetry via the vibronic coupling, resulting in a dressing of the electronic levels by a Jahn-Teller like splitting and thereby decreasing the dipole matrix elements and the photoluminescence from the electronic levels.

Another explanation for fast quenching suggested by recent experiments [108, 116] is the stimulated emission from the NV excited state to its ground state vibronic side band. However, direct observation of strongly enhanced emission at stimulating wavelength for both NV^- and NV^0 is required before we can attribute the fast quenching effect to stimulated emission.

Finally, it is possible that the IR photon is causing a fast local change in the electric field around the NV centers, for instance through optical rectification (a χ^2 process) or altering the band-bending at the surface of the diamond which is ~ 100 nm away, which also will affect the dipole matrix elements. We are not aware of previous literature where such effects have been explicitly identified. The origin of this fast modulation is an important subject for future research.

5.3.5 Optically Detected Magnetic Resonance (ODMR) Signal under 1064 nm Laser Illumination

We found that the charge state flipping of NV centers, especially with IR illumination, has rarely been studied with optically detected magnetic resonance (ODMR) before. Therefore, we decided to carry out ODMR at the confocal spots where we had already observed charge flipping (sample shown in Figure 66).

The first interesting finding is 1064 nm laser enhances NV^- ODMR contrast under low 532 nm laser excitation power. In this experiment, we used 30 mW 1064 nm laser power and 0.013 mW 532 nm laser power for excitation, which was carefully optimized to improve the contrast. The CW ODMR experimental result for NV^- collection window (650-800 nm) is shown in Figure 71(a). It is very clear that the participation of 1064 nm laser increased the overall photoluminescence counts by a factor of 1.9; meanwhile, the ODMR contrast at 2.87 GHz has also been enhanced by a factor of 1.7. This enhancement effect is robust through the sample, although the amount of this increase is different from one location to another. Because the four orientations of NV centers within the laser spot could be randomly distributed, the effective laser power used in charge flipping dynamics could be different from one location to another. Therefore, it is reasonable that the final populations are different from one location to another.

The thermally-induced ODMR peak shift has been well studied [117, 59]. We did not see any shift of the ODMR peak away from 2.87 GHz during repetitive tests, within our signal to noise limit. The absence of this shift indicates again that our observations are unlikely to be due to temperature shifts.

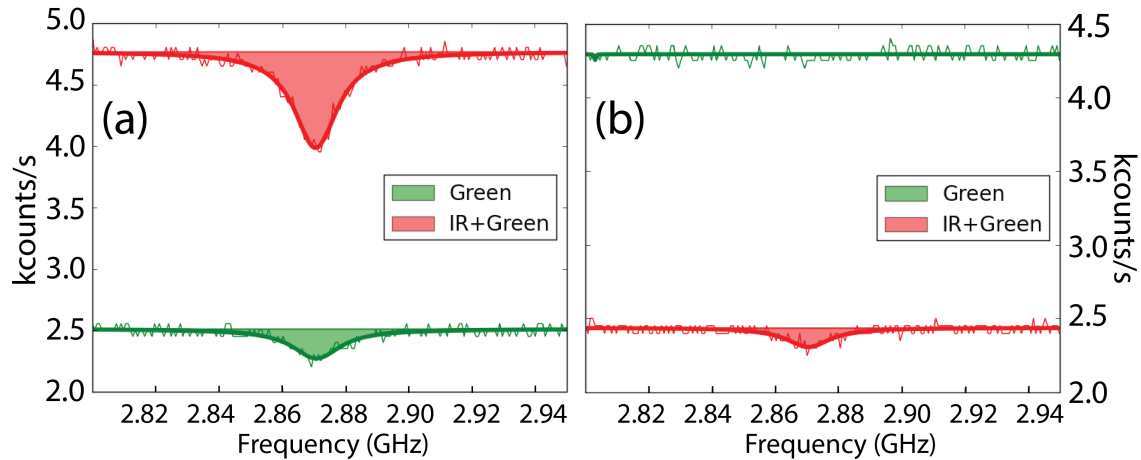


Figure 71: ODMR signals comparison with IR and no IR for (a) NV^- charge state (b) NV^0 charge state

Another interesting finding appears when we switch to NV^0 collection window (550-625

nm). We set 20 mW 1064 nm laser with 0.1 mW excitation 532 nm laser for optimizing the effect. The overall background counts decrease, opposite to NV^- window, consistent to the result in Figure 65 (a) and (b). However, we observe an unexpected ODMR signal around 2.87GHz from the NV^0 collection window in Figure 71(b) when the IR laser excitation is used.

Since we have not applied a magnetic field during this experiment, and due to spin 1/2 nature of NV^0 , we postulated that the charge state flipping procedure under IR excitation is spin dependent. It tends to flip more NV^0 to NV^- when NV^- is populated in the $|m_s = \pm 1\rangle$ state.

To further examine this effect, we attempted a pulsed experiment which is designed to show the spin dependence property of $NV^0 \rightarrow NV^-$ charge state dynamics. The pulse sequences are shown in Figure 72(b). We start the sequence with initialization green laser pulse, followed with a microwave π pulse after switching off the green laser. We independently can measure Rabi oscillations to calibrate our π pulse (data not shown) by using just the green laser and following standard time-resolved counting techniques for NV center [118, 119]. Thus, this procedure populates the NV^- mostly to its $|m_s = \pm 1\rangle$ state with the π pulse. Then the green laser was switched on again 100 ns after the π pulse, and the IR laser was switched on 50 ns after the green laser. We try to compare the behavior after IR laser was on for the cases when microwave π pulse is switched on or not. Normalized results are shown in Figure 72(a). As we expected, mapping NV^- to its spin-1 state by the π pulse seems to enhance the charge state flipping $NV^0 \rightarrow NV^-$ rate and therefore less photoluminescence counts are collected from NV^0 window. A zoom in figure (i) shows the photoluminescence difference between the two cases. Although the contrast is small, this difference is robust from one run to another. We exponentially fitted the photoluminescence contrast in figure (ii), which indicates a 1900 ns decay time before the contrast disappeared.

This decay time may seem long considering the measured ~ 300 ns spin polarization time from the $m_s = \pm 1$ to $m_s = 0$ state of the NV^- center. However, we note that given the excitation power of the green laser which is well below saturation, the rate of spin-polarization by optical pumping will be decreased. While we have not carried out detailed calculations, it seems reasonable given the data that the contrast and the time-scale

shown in Figure 72 arises from optically mediated spin polarization under our experimental conditions. The main feature we are reporting on this work is that there appears to be a spin-dependent component to the charge transfer, as confirmed by the fact that we see ODMR signal when collecting photoluminescence from the NV^0 window under IR excitation, and the time-resolved experiment with and without a microwave π pulse shows a contrast when the IR laser is turned on.

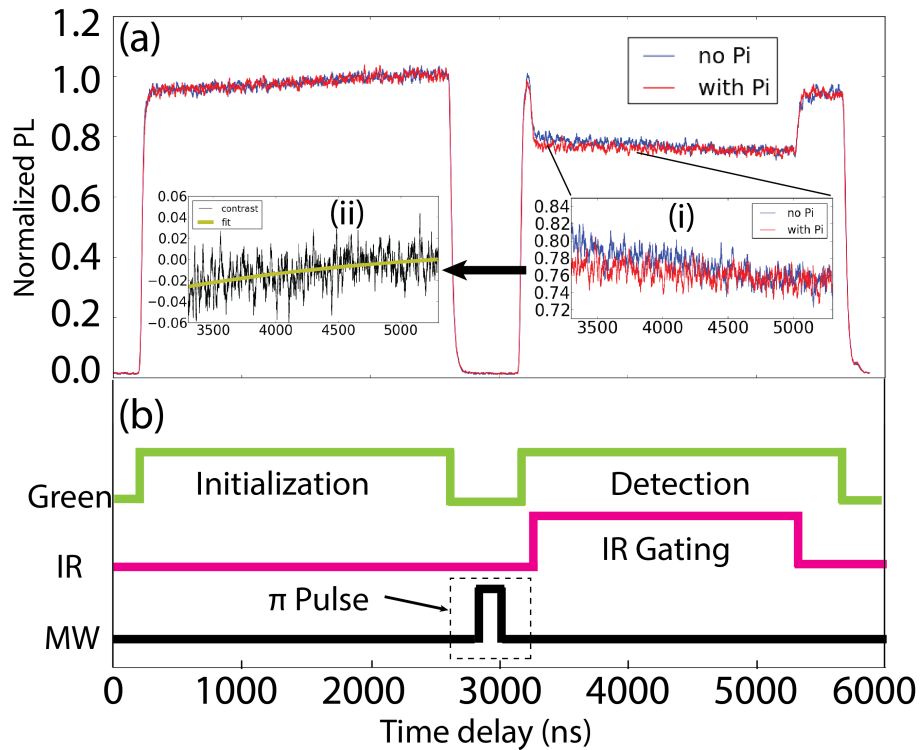


Figure 72: (a) Spin dependence of NV^0 photoluminescence counts (SavitzkyGolay filter applied [17], normalized to steady state) through charge state flipping after switching on 1064 nm laser (i) Zoom in of photoluminescence contrast (ii) Exponentially fit of the photoluminescence contrast decay time (b) Corresponding pulsed sequence: start with green laser initialization pulse for 2300 ns, followed with a 2.87GHz π pulse to flip the spin after green was off. A green detection pulse was applied 100 ns after the Pi pulse, and IR gating pulse was 50 ns after that.

5.3.6 Conclusion

In conclusion, we report the observation of a CW 1064 nm laser induced charge state flipping from NV^0 to NV^- in small ensembles of NV centers, under a wide variety of samples and experimental conditions. A faster (50 ns, limited by our AOMs) photoluminescence quenching and recovery effect for both charge states have been observed but is still not fully understood. We analyzed the charge state flipping model, which indicates 1064 nm laser photon could be sufficient to promote an electron from the valence band, captured by NV^0 to convert to NV^- state, and found good agreement with the slow ($\sim \mu s$) photoluminescence dynamics. This observation could help constrain the positions of the NV^0 energy levels which are hitherto unknown. We also found preliminary evidence that the charge state flipping induced by the 1064 nm laser is spin dependent.

Complementary to previous work on optical transistor using NV centers [107], our observations and analysis unravel the behavior of both NV^0 and NV^- charge state under CW 1064 nm laser illumination. Through careful control of thermal effects, in contrast to Ref. [107], we have identified charge conversion procedure induced by the CW 1064 nm laser. Further, the time-resolved results suggest that an improved version of optical transistor could be realized by using the neutral NV^0 state instead of the negatively charged NV^- state. Our findings may also be important for many exciting applications such as spin readout, super-resolution microscopy, and recently emerging experiments on optical trapping of diamond crystals.

Varying the wavelength of the infrared laser, using excitation wavelengths that predominantly excite only one charge state (e.g., 593 nm laser), as well as performing statistical studies on single NV centers could be potentially useful future directions to investigate this effect. Another fruitful area might be to measure the electron capture and ionization rates ($r^{-/0}$ and $r^{0/-}$ in our work) as a function of temperature and apply principles of detailed balance to try and measure the energy separation between the charge states.

6.0 MULTIPLE-PHOTON PHOTOLUMINESCENCE EXCITATION OF NV CENTERS IN DIAMOND

We report the first observation of multi-photon photoluminescence excitation (PLE) below the resonant energies of nitrogen-vacancy (NV) centers in diamond. The quadratic and cubic dependence of the integrated fluorescence intensity as a function of excitation power indicate a two-photon excitation pathway for the NV^- charge state and a three-photon process involved for the neutral NV^0 charge state respectively. Comparing the total multi-photon energy with its single-photon equivalent, the PLE spectra follow the absorption spectrum of single-photon excitation. We also observed that the efficiency of photoluminescence for different charge states, as well as the decay time constant, was dependent on the excitation wavelength and power. A portion of this content is published on Phys. Rev. B [120] ©2018 American Physical Society.

6.1 INTRODUCTION

The demonstration of single photon generation [121] and optical preparation and readout out of spin [118] in diamond nitrogen-vacancy centers (NV), coupled with its unique combination of features such as biocompatibility, stability, sensitivity to magneto-electric fields and long spin coherence, has launched diamond to prominence with regards to applications for nanoscale biological sensing and carbon-based quantum technology [101, 50]. Due to an efficient absorption in the visible region, around 450 nm to 575 nm for both the NV^0 and NV^- states [101], the electronic states of the electrons trapped in the NV defect centers are often prepared by non-resonantly exciting diamond with single photons using green light

(520-540 nm). Resonant excitation of NV^- zero-phonon line (ZPL) at 638 nm (1.945 eV) to photo-ionize an electron and convert the NV to its neutral charged state via absorption of two photons followed by an Auger process has also been reported [102]. Below resonance excitation at 1064 nm, half the energy of the usual green light excitation, has been used to study nonlinear photo-physical processes [122] and charge state dynamics [123, 124]. An interesting feature observed in these works was the spin-dependent signal that is emitted when simultaneously exciting with near infra-red and visible light, a phenomenon that is not well understood. To the best of our knowledge, there has not been a systematic wavelength-dependent multi-photon photoluminescence excitation (PLE) experiment to investigate multi-photon absorption and its corresponding fluorescence. It is important to note that multiple-photon excitation is extremely advantageous for biological imaging and quantum information processing as it widely separates the signal fluorescence from excitation.

In this project, we did a first PLE measurement of NV photoluminescence using multi-photon excitation with pulsed light in the near-infrared range (0.95~1.18 eV or 1050 to 1300 nm). We discuss the different photoluminescence yields of NV at these excitation wavelengths. We also compare the time-resolved fluorescence decay of the NV excited states at various excitation energies and pump powers to shed light on the important features of the defect states.

6.2 BACKGROUND

The multiphoton process was first predicted in 1931 by Maria Goeppert Mayer and realized in 1961 by Wolfgang Kaiser. Instead of absorbing one photon whose energy is equal or larger than the energy gap between the ground state and excited state, a defect can be excited by simultaneously absorbing multiphoton whose energy is much lower than the energy gap. "simultaneously" here means a typical time interval in the order of 10^{-18} s between photons. Figure 73(a) shows one-photon, two-photon and three-photon equivalents to excite a defect on resonance (not shown) or off resonance to the excited state related vibronic band. The photoluminescence (PL) emission is the intrinsic property of the defect and should be the

same for all three cases. The essence of multiphoton processes can be represented in quantum perturbation theory. A rigorous derivation can be found in reference [125], where the rate of multiphoton transitions can be evaluated with wave function corrections to different orders. To simply estimate the order of the transition rate (photons absorbed in unit time), for example, an intermediate virtual state model can be assumed for a Two-Photon absorption (2PA) process in 73(b). The 2PA absorption cross section σ_2 , which is defined by the transition rate divided by the total incident photon numbers in unit time, can be written as [126]:

$$\sigma_2 = \sigma_{gi}\sigma_{ie}\tau_i \quad (6.1)$$

where σ_{gi}, σ_{ie} are the absorption cross section from ground state to the intermediate state and from the intermediate state to excited state; $\tau_i \approx 10^{-15} \sim 10^{-16}s$ for a visible frequency assumption. The One-Photon absorption (1PA) can be calculated from Fermi Golden rule directly. Reference [126] points out for a fluorescent molecule, 1PA cross section is typically in the order of $\sigma_1 \approx 10^{-17}cm^2$. Therefore, in this case, a typical 2PA cross section is estimated as $\sigma_2 \approx 10^{-50}cm^4 \cdot s/photon$.

Experimentally, the 2PA cross section is related to the observed photoluminescence counts by a photon detector [126]:

$$F \approx 1.28\phi C\eta\sigma_2 n \frac{\lambda P^2}{f\tau} \quad (6.2)$$

where F is in unit of *photon/s*; ϕ is the photoluminescence collection efficiency of the experimental system; η is the quantum yield of the defect; C is the density of the defects, λ is the excitation wavelength in vacuum; n is the refractive index of the media; P is the average laser power; τ is the pulse duration and f is the repetition rate; 2PA cross section here is in unit of GM , where $1GM = 10^{-50}cm^4 \cdot s/photon$. Absolute measurement of multiphoton absorption cross section requires accurate knowledge of the experimental system, which is difficult in many situations (such as the density is not uniform in the sample and the collection efficiency is also an estimation, etc.). An effective way to measure the 2PA cross-section

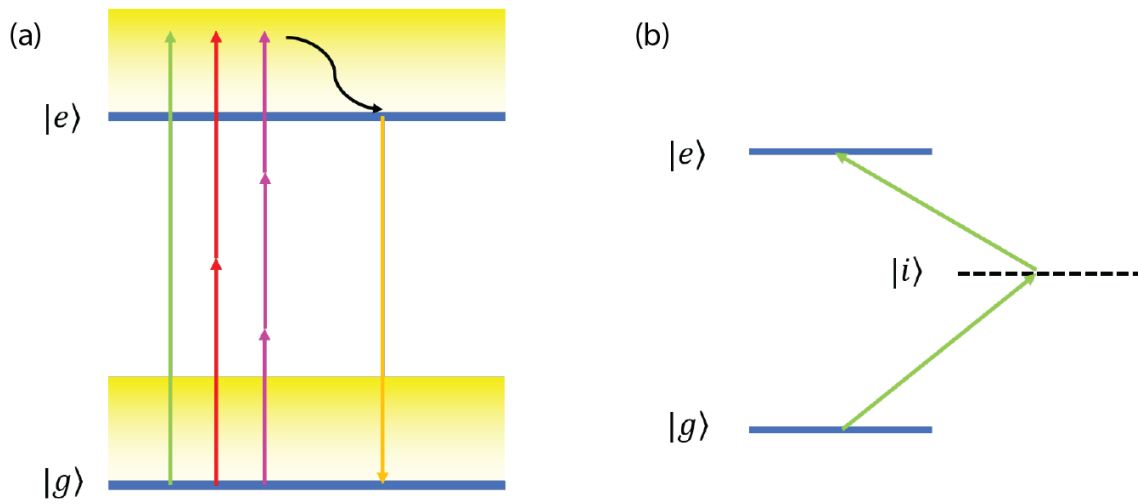


Figure 73: (a) Multiphoton excitation (Green, Red, Pink arrows) and emission processes (Orange arrow) of a defect. The yellow continuum indicates ground and excited state related vibronic band. The black curved arrow represents the phonon relaxation process. (b) Intermediate state (dash line) model for a Two-Photon excitation process.

of an unknown defect is to compare with some known cross section from another defect. The unknown defect 2PA cross section can be calculated as:

$$\sigma_{2new} = \frac{\phi_{cal}\eta_{cal}C_{cal}P_{cal}^2n_{cal}\lambda_{cal}F_{new}}{\phi_{new}\eta_{new}C_{new}P_{new}^2n_{new}\lambda_{new}F_{cal}} \cdot \frac{f_{new}\tau_{new}}{f_{cal}\tau_{cal}} \cdot \sigma_{2cal} \quad (6.3)$$

where the parameters with a subscript "cal" are used in a 2PA cross-section calibration experiment while the parameters with a subscript "new" are used for the unknown 2PA cross-section experiment. It is clear that if we have pre-knowledge of the calibration 2PA cross section σ_{cal} , we can calculate the unknown 2PA cross section σ_{new} of the other defect by comparing the experimental condition differences.

6.3 EXPERIMENTAL SETUP

The NV ensembles investigated in these experiments are implanted within micro-diamond crystals (10-100 μm sizes from Columbus Nanoworks) with 100 ppm nitrogen density. A laser pump, illuminating about 1 μm spot size on these crystals, yields sufficient fluorescence signal to noise ratio despite an inherently low multi-photon excitation efficiency. An Optical Parametric Amplifier (Coherent OPA 9400) pumped by an amplified Ti: Sapphire laser system is used to provide 200 ps pulses, about 30 nm FWHM bandwidth at 250 kHz repetition rate, in the wavelength range used for the experiments. The "signal output of the OPA can be tuned from 500 to 700 nm for non-resonant single-photon excitation while the "idler covers the excitation wavelengths between 1000 to 2000 nm. A 0.8NA objective is used to both focus the pump beam onto the sample and collects the diamond fluorescence. The samples were glued onto a translation stage, and the fluorescence from the NV centers was collected by either a spectrometer for time-averaged spectroscopy or a Single Photon Counting Module (SPCM) for time correlated measurements. The trigger of the single photon counter was sourced from the 250 kHz repetition rate of the OPA pump and counts were recorded by a (PicoHarp 300) dual-channel counter. A 582/75 nm bandpass filter and 650 nm long pass filter placed along the collection path when distinguishing between the NV⁰ and NV⁻ photoluminescence respectively.

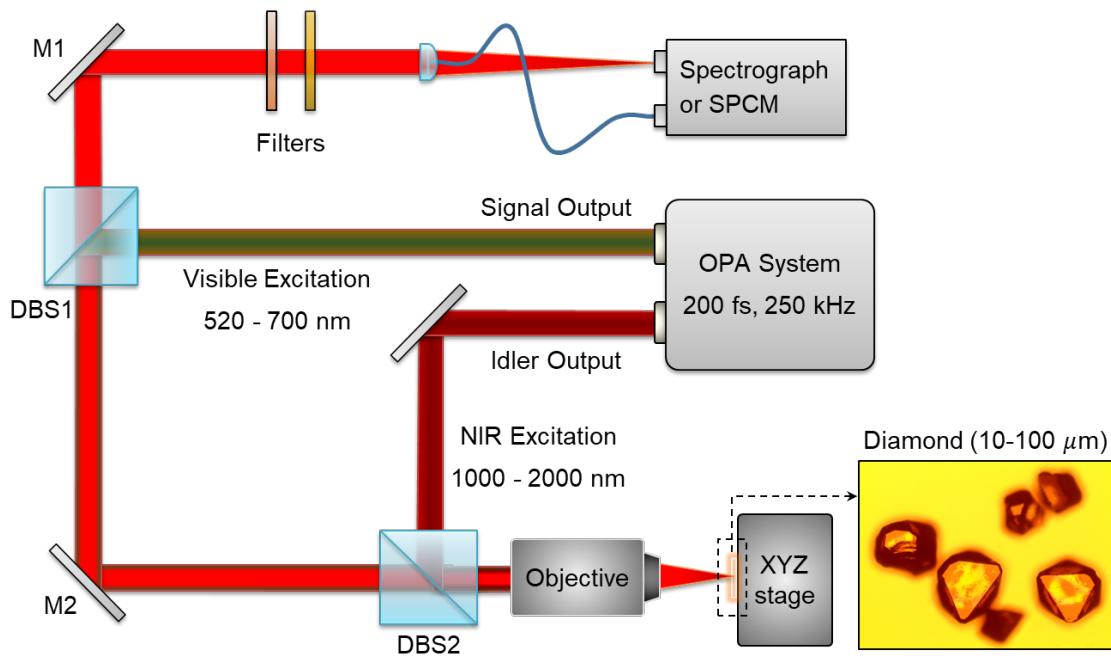


Figure 74: An OPA system served as a tunable light source, providing 200 ps excitation pulses at 250 kHz repetition rate. The “signal and “idler outputs of the OPA were directed onto the sample optical path using dichroic beam splitters (DBS1 and DBS2). Additional bandpass filters and longpass filters were placed along the “signal and idler paths respectively to get rid of any light leaking from the OPAs pump source (800 nm). Laser paths for the different wavelength regions were blocked or opened as needed in the experiments. The photoluminescence can be directed unto a spectrometer or a Single Photon Counting Module (SPCM) for lifetime measurements.

6.4 RESULTS

6.4.1 Power Dependence

To identify multi-photon excitation generated photoluminescence from NV centers, we compared the power dependence of collected photoluminescence with pulsed excitation centered at 535 nm with excitation centered at 1276 nm, half the NV^- ZPL energy in Figure 75(a) and (b). The integrated counts from the spectrally resolved fluorescence for NV^0 (550-620 nm) and NV^- (650-800 nm) as a function of power are fitted with a power law to the n^{th} power. The emission intensity from the 535 nm excitation as a function of pump power yields a clear linear dependence as shown in Figure 75(a). The NV^- fluorescence follows mainly a quadratic dependence $n=2\pm 0.18$ while the NV^0 fits a cubic power law $n=3\pm 0.34$ for 1276 nm excitation. The uncertainty δn of the n^{th} power is the standard deviation of several trials for the corresponding excitation wavelength.

Figure 76 looks at how the near-infrared excitation affects the spectral profile of the NV system. A couple of representative fluorescence in a series of excitation powers and their corresponding NV^- to NV^0 ratio is shown for 1060 nm and 1210 nm. At 1060 nm excitation, two photons have enough energy to excite both the NV^- and NV^0 charge states, while past 1150 nm, e.g., 1210 nm, an additional photon is needed to reach the excited state of NV^0 . Figure 76(a),(b) shows an increase in NV^0 component, or equivalently a decrease in NV^- to NV^0 ratio, with increasing excitation power. Longer excitation wavelengths past 1210 nm show more NV^- than NV^0 . It is clear that irrespective of excitation wavelength, the NV^0 component increases with pump power, e.g., Figure 76(c), albeit at lesser rates for longer wavelengths. This indicates a higher ionization rate from NV^- to NV^0 due to much larger illumination power used for multiple-photon excitation [18]

6.4.2 Spectrum and Lifetime

Following the same diamond centers, we look at the wavelength dependence of the spectral profile. Figure 77(a) shows representative room temperature fluorescence spectra of the NV

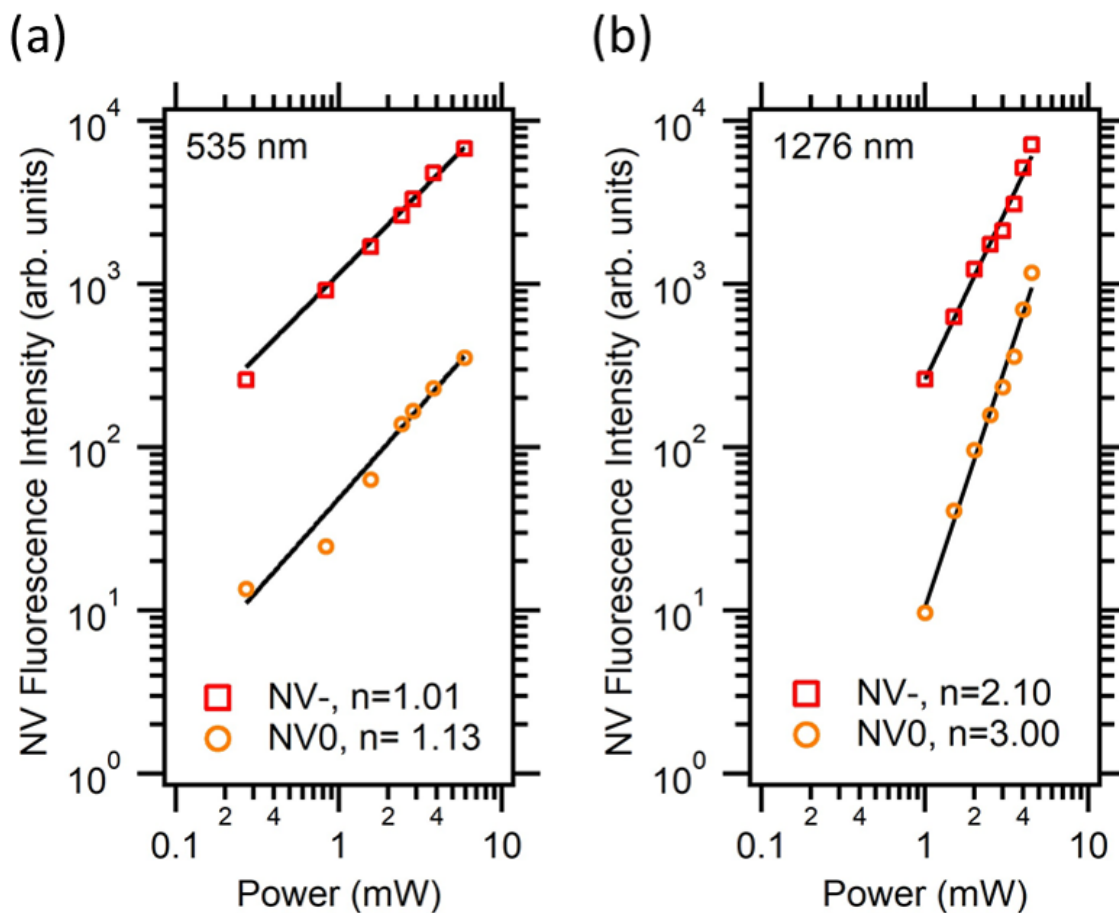


Figure 75: Power dependence of NV^0 and NV^- fluorescence intensities at (a) 535nm and (b) 1276nm excitation wavelengths. The solid lines are power-law fits with n as the power parameter.

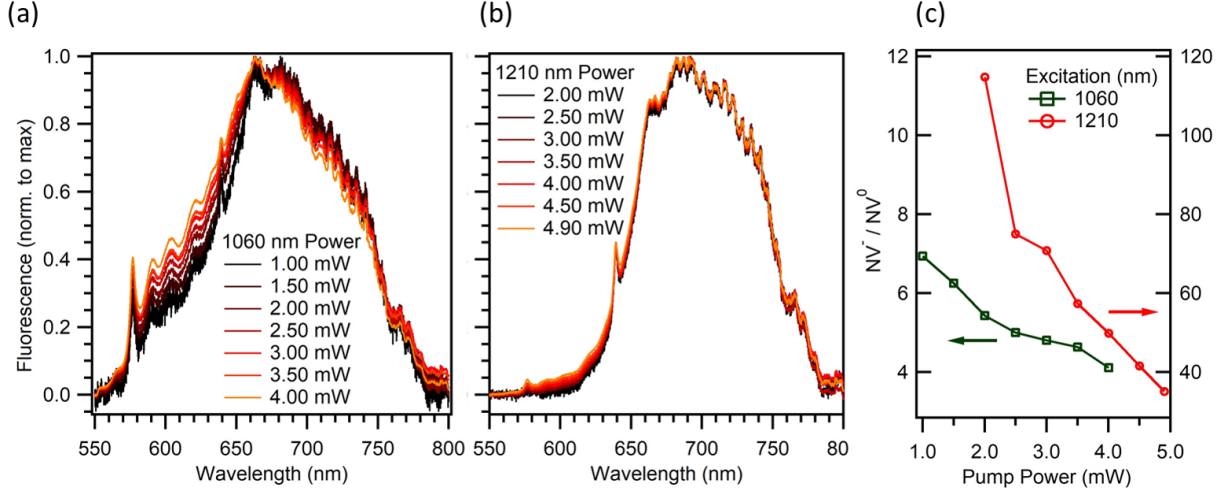


Figure 76: Fluorescence of NV diamond at various pump powers for (a) 1060 nm excitation, (b) 1210 nm excitation and their corresponding NV^- to NV^0 ratio (c).

centers at various excitation wavelengths. Our results indicate that NV centers can be excited continuously from 1030 nm to 1310 nm with varying efficiency for each of the different charged states. Using appropriate bandpass filters, we collect the integrated fluorescence intensity of the NV^- charge state (750-800 nm) and the NV^0 charge state (550-620 nm) separately as a function of pulsed excitation wavelength. The integrated intensity for each charge state and the ratio between them is shown in Figure 77(b). If an energy equivalent of two excitation photons is assumed, the emission intensity at these excitation wavelengths is consistent with the characteristic absorption cross sections or photoluminescence (PLE) spectra of NV^- with conventional single-photon excitation [127]. For example, in our data the intensity in fluorescence emission peaks at around 1070 nm corresponding to twice the wavelength where single photon absorption peaks (535 nm) in diamond NV [113]. The inefficient pumping of the NV^0 charge state with wavelengths longer than the ZPL of the NV^0 (575 nm), is reflected in the decrease in fluorescence intensity as a function of pump wavelength across 1150 nm towards longer wavelengths shown in Figure 77(b). The fluorescence intensity of the NV^0 charge state ensemble goes down as well but remains non-zero. A notable feature is the increase in intensity ratio (NV^-/NV^0) of the charged states toward longer wavelengths. The

NV^- emission and excitation is much more efficient at wavelengths beyond 1150 nm.

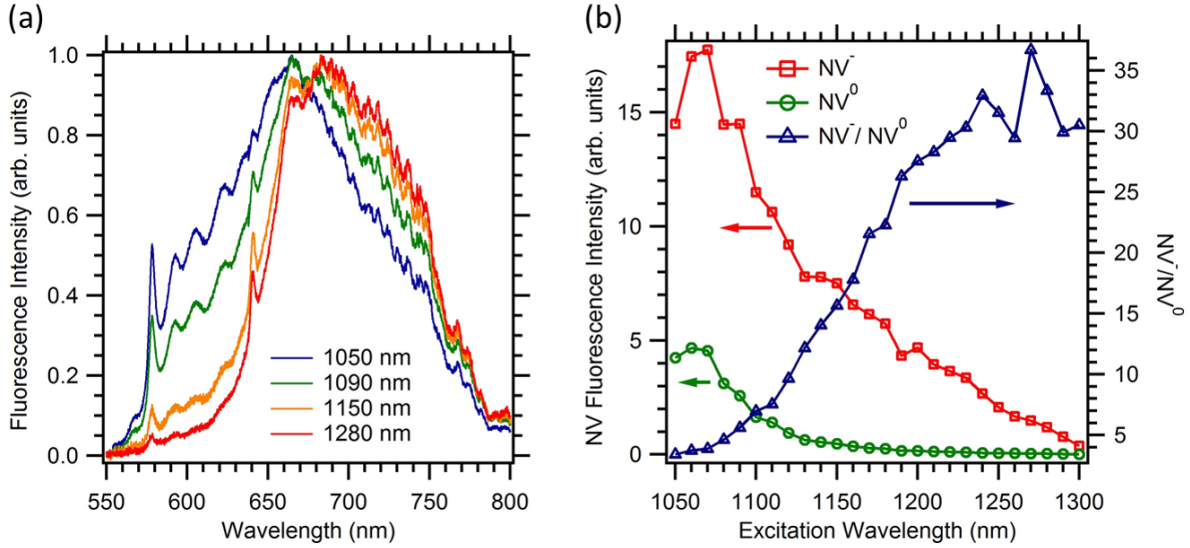


Figure 77: (a) Representative PLE spectra of NV centers at 1050 nm, 1090 nm, 1150, and 1280 nm. The fluorescence spectra are normalized to maximum intensity. (b) Integrated intensity of NV^0 (550-620 nm) and NV^- (750-800 nm) from spectra, e.g. Figure 77(a), versus excitation wavelength. The ratio between NV^- and NV^0 intensities is also shown in the graph.

We also compared the NV ratio between single photon (510 nm, 550 nm) and two-photon excitation (1060 nm) as shown in Figure 78(a). Due to the laser lights proximity to the fluorescence region, a long pass filter with a cut-off at 600 nm is placed in the collection path to filter out the laser reflections from the sample when exciting at 550 nm. The effect of the laser filter is manifested in the loss of fluorescence information below 600 nm for 550 nm excitation. Nonetheless, the reduction of NV^0 with respect to NV^- is qualitatively apparent compared to 510 nm or 1060 nm excitation. Within the single-photon excitation range, longer wavelength yields increasing NV^- intensity with respect to NV^0 as seen when comparing 510 nm excitation with a 550 nm excitation which is consistent with the absorption spectra of the charged states [113]. Also, one can clearly see from Figure 78(a) that near-IR excitation contains relatively more NV^0 component than NV^- .

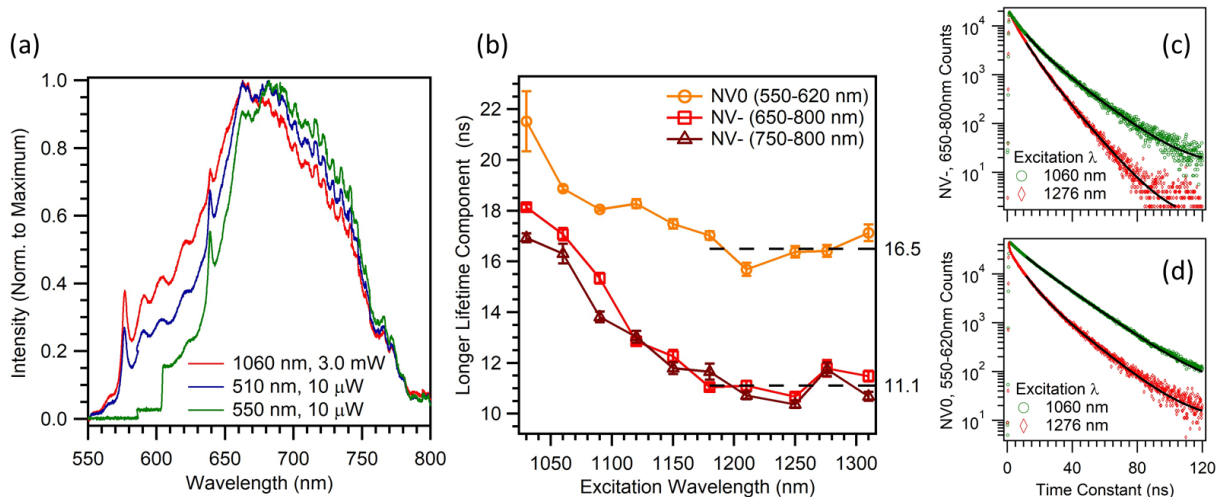


Figure 78: (a) Fluorescence comparison of single-photon excitation (510 nm and 550 nm) with multi-photon excitation (1060 nm). In graph (b), the NV⁻ fluorescence is taken at two wavelength windows for comparison. The fluorescence decay at 1 mW pump power is fitted with a bi-exponential function. The longer lifetime or slower decay component is plotted for various excitation wavelength. The shorter lifetime or faster decay component is consistent at 6.9 ± 1.7 ns. Representative decay plots and bi-exponential fits for (c) NV⁰ and (d) NV⁻ fluorescence comparing shorter, 1060 nm, versus longer, 1276 nm, excitation wavelength are also shown above.

The decay of the fluorescence is also recorded at various wavelengths and fitted with a bi-exponential decay function. The slower decay component is plotted in Figure 78(b). The faster decay component has a lifetime of 6.9 ± 1.7 ns for both charge states which does not vary much with excitation wavelength. For the component with slower decay, there is a noticeable change in the lifetime from shorter to longer excitation wavelength which eventually flattens beyond 1150 nm excitation. The NV^- fluorescence is taken at two wavelength windows for comparison, one in the 650-800 nm interval and the other at 750-800 nm interval. The consistently higher time constant for NV^- 650-800 nm fluorescence, below 1150 nm excitation is indicative of some NV^0 fluorescence leaking into the NV^- collection window. Beyond 1150 nm, the NV^0 is less excited by a two-photon process and minimizing the effect of leakage. We can take the time constant beyond this excitation wavelength to be the NV^0 lifetime 16.5 ± 0.6 ns and NV^- lifetime 11.1 ± 0.4 ns, which are within the range reported by other groups. A two-lifetime component can be justified by radiative lifetime from other traps nearby in the diamond lattice or a non-radiative decay path such as NV^0 and NV^- photoluminescence quenching due to substitutional nitrogen defects [128]. The change in NV center lifetime with excitation wavelength is a feature not yet reported would need to be explored in future work. It is possible that the variation of the longer lifetime component is an effect of other defects that are populated initially at certain wavelengths and gradually feeds back both the NV charge state populations later.

6.5 ANALYSIS

The NV^- 2PA cross section $\sigma_2(\lambda)$ from 1050nm to 1280nm excitation can be estimated from our PLE data. Considering our laser linewidth is ~ 30 nm, we use the measured 2PA cross section at 1064nm from reference [122] as our calibration for the 1060nm excitation such that $\sigma_2(1060) \approx 0.45 \pm 0.23GM$. Assuming the experimental conditions remained fixed during the PLE measurement as the excitation wavelength is changed, then the 2PA cross section

$\sigma_2(\lambda)$ can be simplified to:

$$\sigma_2(\lambda) = \frac{1060}{\lambda} \frac{F(\lambda)}{F(1060)} \sigma_2(1060) \quad (6.4)$$

Figure 79 shows our estimation of 2PA cross section for NV^- center at different excitation wavelength based on our PLE measurement. The 2PA cross section agrees with the reported one-photon absorption(1PA) by reference [113] at room temperature. The missing resonance at 1150nm is possibly due to the our broad laser linewidth. Low temperature experiment and narrower laser linewidth will help to explore the resonance in the future.

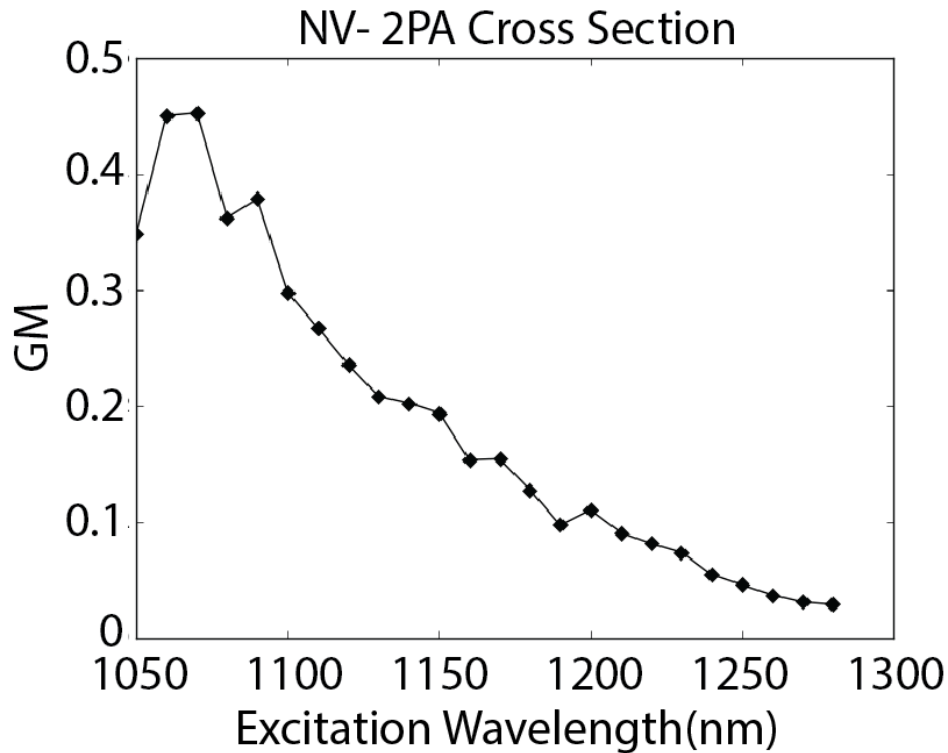


Figure 79: Two-photon absorption cross section calculated based on our PLE data

The schematic of the negative and neutral state shown in Figure 80 maps our understanding of the behavior of the system. The energy level of the states and band offsets follows reference [113] which is the most consistent with our results. From the schematic, we can see that an excited negatively charged state NV^{*-} could absorb another photon, 0.65 eV

or higher, to raise the electron out to the conduction band. Hence, if an NV^- state absorbs three photons, each photon at half the energy of the NV^- ZPL, it can be converted into the excited state of NV^0 . If the total transition energy is attained, a direct three-photon absorption of an NV^0 electron from the ground state will also get the system to its excited state (NV^{0*}).

The power dependence of the NV^- and NV^0 charged states with 1276 nm excitation provides evidence for a multi-photon procedure or a series of pathways for the NV electronic transitions. For the negatively charged state, a two-photon excitation or absorption is the most straightforward interpretation based on its quadratic power dependence. The cubic dependence of the NV^0 photoluminescence intensity, on the other hand, may have two possibilities. The mechanism for these is illustrated in Figure 80. The first is a direct absorption of three photons 1276 nm photons to reach the excited state. Note that three times the energy of a 1276 nm photon, for a total of 2.92 eV, is more than enough to reach the 2.16 eV needed to excite the NV^0 . The second possible explanation is an NV^- to NV^0 conversion. One such conversion mechanism was proposed by Beha et al. [113] and Shiyushev et al. [102] whereby an excited NV^- state absorbs another photon into the conduction band followed by an Auger process that releases enough energy to remove the defect charge. Later work, e.g., [113], on photo-induced ionization dynamics did not invoke the Auger process. The NV^- ionization energy was concluded, per Ref. [113], to be only 2.6 eV. We point out that the three 1276 nm photons have more than enough energy required for an NV^- electron to reach the conduction band from the NV^- ground state.

We also point out that the two-photon process is more efficient in excitation of NV^0 other than NV^- at the Single photon equivalent energy (Figure 78(a)). This is probably induced by the much higher charge state conversion rate from NV^- to NV^0 due to the high peak laser power. Green laser and 650nm long pass filter are commonly used for NV^- related experiment in single-photon excitation case. This strategy is less efficient to filter out NV^0 emission as we demonstrated in Figure 78(b). A longer wavelength long pass filter is required to reduce the overlapping between the two charge states, or, we suggest using excitation wavelength longer than 1150nm to increase NV^- ratio in collection.

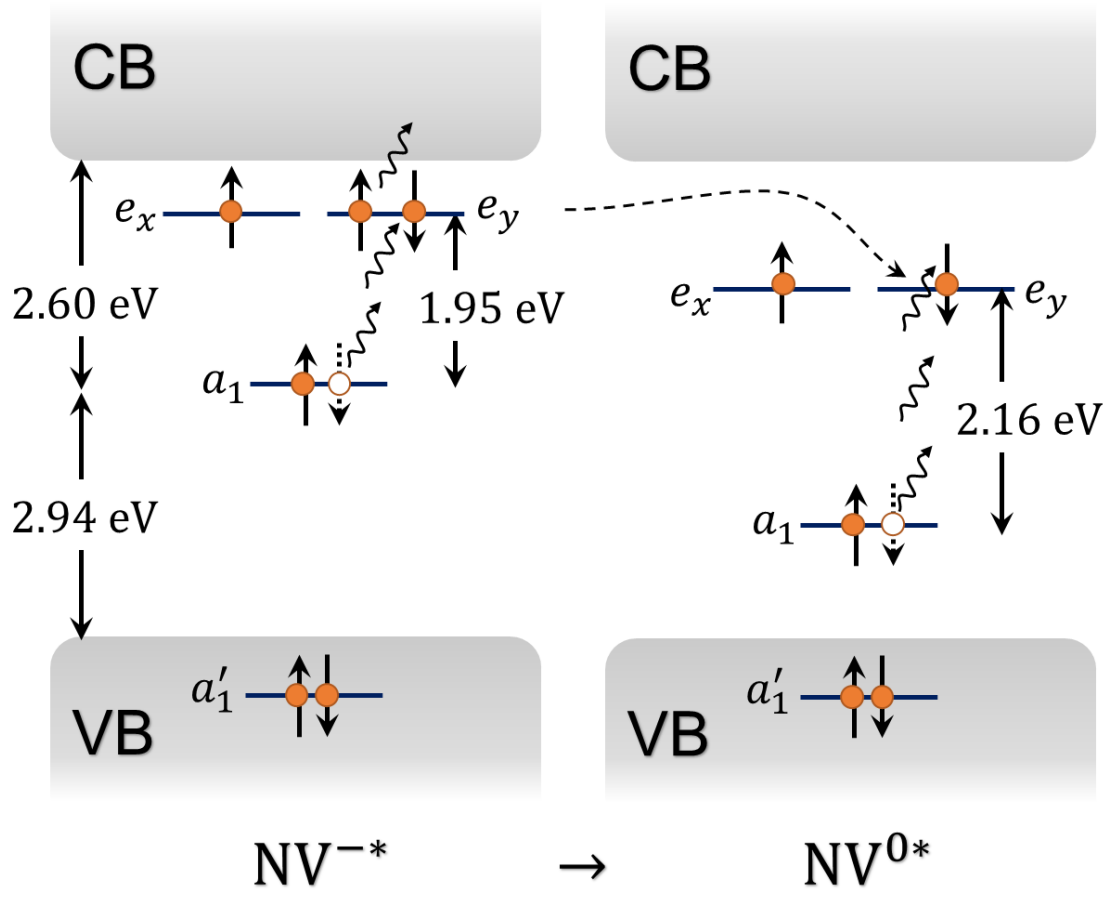


Figure 80: A two-photon, three-photon excitation of NV^- and NV^0 respectively leaving them in their excited states (*). An excited negatively charged state NV^{-*} could absorb another photon to raise the electron out to the conduction band. If an NV^- state absorbs three photons with a total energy of 2.60 eV, it is converted into the excited state of NV^0 . A direct three-photon absorption of an NV^0 electron from the ground state will leave it in its excited state (NV^{0*}) if the total photon energy is greater than or equal to 2.16 eV.

The NV^- 's slower decay component, Figure 78(b), has apparently a shorter lifetime when excited at wavelengths beyond 1150 nm than when excited at wavelengths below 1150 nm. In part, this can be attributed to the likelihood of the NV^0 fluorescence significantly leaking into the NV^- collection window. The leakage effect is supported by a consistently longer time constant for NV^- fluorescence collected at 650-800 nm as compared to a 750-800 nm collection window. The effect can also explain the leveling of the time constant at >1150 nm pumping due to an inefficient two-photon excitation of NV^0 at these wavelengths. Less NV^0 leaks into the NV^- collection window unless the pump power is increased whereby 3-photon processes starts to dominate and NV^0 population recovers.

The longer lifetime component for NV^0 decay for excitation wavelengths shorter than 1150 nm is indicative of multiple processes feeding into NV^0 population. Diamond fluorescence in a series of excitation powers and wavelengths and their corresponding NV^- to NV^0 ratio also shows that there is a significant number of carriers feeding into the NV^0 states at higher powers and for wavelengths shorter than 1150nm (half the energy of NV^0 ZPL). It is possible that this may be due to conversions from NV^- to NV^0 , excitation of other defects in the vicinity. The dependence of the lifetime with wavelength would be better understood using a streak camera which is within the purview of future work.

6.6 CONCLUSION

We have shown that near-IR excitation of NV centers, resonant at half the energies of the NV states and wavelengths within the vicinity (1050 to 1300 nm) is allowed through a multi-photon process. A preferential population of NV^- or NV^0 is achieved by tuning to an appropriate wavelength or excitation power. In general, longer wavelength and lower power are required to have the more NV^- population and vice versa for populating NV^0 . We note that excitation at low energy is extremely useful for biomedical imaging applications since infrared light can penetrate deep into biological tissues with little scattering or damage [129]. Also, the current generation of single photons is limited by spectral jumps and diffusion of emission lines caused by simultaneously exciting impurities in diamond [114].

Near-IR excitation may suppress photo-ionization of surrounding impurities potentially allowing spectrally-stable, indistinguishable single photon generation required for linear optical quantum computing [130]. Another important application is in spin-photon entanglement experiments. NV centers can be prepared in an entangled state between a single photon and the $m_s = \pm 1$ electronic spin of an NV center [131]. Following selective resonant excitation to the A2 state, the system decays into one of the spin states, simultaneously emitting a circularized polarized photon which is orthogonal to the photon emitted when an electron decays to an opposite spin state. Isolating this photon emission is significantly challenging due to the difficulty in extinguishing the resonant excitation pulse back into the detector. A near-IR excitation would widely separate the excitation and emission wavelength, thereby increasing signal contrast for the entangled photon emission.

7.0 CONCLUSION

7.1 DEVELOPING A QUANTUM HYBRID MECHANICAL SYSTEM WITH A TRAPPED DIAMOND AND A SPIN QUBIT

7.1.1 Hypothesis

In this project, we try to experimentally develop a quantum hybrid mechanical system using trapping of diamond techniques with NV spins in the diamond. The trapped diamond size can range from nanometers to tens of microns. Creating a non-classical mechanical state (e.g., Cat state, etc.) for the trapped diamond is our long-term goal, which will help to test quantum theories on a macroscopic object. As a first step to this goal, this dissertation focused on engineering and evaluation of such a system using different trapping techniques. The initial hypothesis is the optical trapping (or Magneto-Gravitational trapping) of diamond with NV centers is a suitable platform to develop the quantum hybrid mechanical system towards creating non-classical motional state purpose.

7.1.2 Accomplishment

We started our experiments on optical trapping platform first. We succeed in loading 40 nm diamond crystals with high efficiency and observed the photoluminescence (PL) spectrum and spin signals from the trapped diamond. We also successfully pump the environmental pressure to a 0.1 torr vacuum before we lost the diamond. These results were novel findings at the time of our experiment. We also used the spin property of NV centers in the trapped diamond as a thermal sensor and measured the temperature of diamond under the illumination of trapping laser and excitation laser in the air. The increased temperature indicates

a higher purity of diamond sample than those commercially available today is required to lower the environmental pressure further to high vacuum.

We proceed with the Magneto-Gravitational trapping technique which could be an alternative to optical trapping in high vacuum towards our long-term goal. We are the first to explore the spin signal from a trapped diamond with NV centers in a strong magnetic gradient after its center of mass motion has been cooled in a high vacuum. We demonstrate a possible ODMR signal detected from a CNW diamond. Using the NV photoluminescence as a thermal detector, we are first to report the internal temperature of a trapped diamond in a high vacuum. To the best of our knowledge, these results are new to the field in the high vacuum regime. Based on our calculation, although the Magneto-Gravitational trapping cannot give as high cooperativity as the optical trapping technique, it still has a chance to enter the strong coupling regime (Section 4.6).

7.1.3 Conclusion

For optical trapping, the developing of the hybrid system requires a high vacuum environment. Therefore, our experimental result is against our hypothesis. Our conclusion is the optical trapping of diamond with NV centers is not a suitable platform for developing the hybrid quantum system at present without improving the purity of the diamond sample.

For MG trapping, the system has been brought to the high vacuum regime. The possible observation of the spin signal and the internal temperature detected on the trapped diamond both support our hypothesis. Therefore, our conclusion is the Magneto-Gravitational trapping platform is more suitable to develop the hybrid quantum system than the optical platform.

7.1.4 Outlook

A common improvement required for both trapping techniques is the quality of diamond. The diamond samples used for trapping in this dissertation are all made from high pressure high temperature method which includes a lot of defects at production. These defects may not be all radiative but many of the them can absorb laser power, which heats up the

sample easily. A better method to create ultra-pure quality sample is the chemical vapor deposition (CVD) technique. The grown diamond can be irradiated with nitrogen ions under well controlled dose, allowing us to control the number of NV centers. Milling the diamond into micron size has been realized. Therefore, fabricating samples using CVD diamond is one promising direction. For MG trapping, to get better ODMR signal, using a diamond with fewer NV centers is necessary. This also requires a better design of both the vacuum chamber and optical system to improve the photon collection efficiency. Also, based on our calculation, we need ultra-high vacuum to enter the quantum regime for the MG trapping technique. Therefore, an ultra-high vacuum design of the vacuum system is also a future task.

Our engineering and experiments of spin detection are the pioneering works to develop a better quantum hybrid mechanical system. The system can be used for fundamental quantum physics study on a macroscopic object by creating its non-classical motional state. The created quantum states can be used to study variety of quantum effects on massive objects beyond atoms and molecules. The trapped diamond system can also be used as ultra-sensitive force sensor to measure the gravity constant with better accuracy.

7.2 CHARGE DYNAMICS OF NV CENTERS UNDER NEAR-IR LASER ILLUMINATION

7.2.1 Hypothesis

In this project, we observed the change of photoluminescence of NV centers under a 1064 nm CW laser illumination. We hypothesize that the intensity change is due to the charge state flipping from neutral charge state NV centers (NV^0) to negatively charged NV centers (NV^-). We also suspect the charge state dynamic depends on the NV^- spin states.

7.2.2 Accomplishment

We showed evidence of a CW 1064 nm laser induced charge state flipping from NV^0 to NV^- in small ensembles of NV centers under a wide variety of samples and experimental conditions. A faster (50 ns, limited by our AOMs) photoluminescence quenching and recovery effect for both charge states has been observed but is still not fully understood. We analyzed the charge state flipping model, which indicates 1064 nm laser photon could be sufficient to promote an electron from the valence band, captured by NV^0 to convert to NV^- state, and found good agreement with the slow ($\sim \mu s$) photoluminescence dynamics. This observation could help constrain the positions of the NV^0 energy levels which are hitherto unknown. We also found preliminary evidence that the charge state flipping induced by the 1064 nm laser is spin dependent. We are the first to explore the IR laser assisted charge dynamics of NV centers.

7.2.3 Conclusion

We verified our hypothesis that the change of photoluminescence of NV centers under a 1064 nm CW laser illumination is due to the charge state flipping from neutral charge state NV centers (NV^0) to negatively charged NV centers (NV^-). And the charge state dynamic depends on the NV^- spin states.

7.2.4 Outlook

Varying the wavelength of the infrared laser, using excitation wavelengths that predominantly excite only one charge state (e.g., 593 nm laser), as well as performing statistical studies on single NV centers could be potentially useful future directions to investigate this effect.

7.3 MULTI-PHOTON PHOTOLUMINESCENCE EXCITATION OF NV CENTERS

7.3.1 Hypothesis

Our hypothesis is the photoluminescence emission efficiency is excitation wavelength dependent. We also expect to see photoluminescence peaks at multi-photon resonances corresponding to the zero-phonon lines of NV centers (575 nm for NV^0 and 638 nm for NV^-).

7.3.2 Accomplishment

We first demonstrate the PLE spectrum of NV centers using multi-photon excitation technique between 1050 nm to 1300 nm. We observed excitation wavelength dependent photoluminescence. We demonstrate the charge state dynamics of NV centers in a multi-photon process agrees with the dynamics in a single-photon process. However, the high illumination peak power of pulsed laser results in a higher ionization rate from NV^- to NV^0 . We point out a higher NV^- to NV^0 ratio can be achieved by using the excitation wavelength in between 1150 nm to 1276 nm. We also measure the lifetime of NV centers as a function of excitation wavelength. Surprisingly, we detected an excitation wavelength dependent lifetime of both NV charge states. We found a longer lifetime at higher energy excitation. We can also excite NV centers on resonance at 1150 nm and 1276 nm. However, photoluminescence peaks are absent at these two wavelengths.

7.3.3 Conclusion

We verified our hypothesis that the photoluminescence emission efficiency is excitation wavelength dependent. We could not see photoluminescence peaks at multi-photon resonances corresponding to the zero-phonon lines of NV centers (575 nm for NV^0 and 638 nm for NV^-).

7.3.4 Outlook

The excitation wavelength dependent lifetime indicates other processes exist in the vicinity of NV centers simultaneously which increased the NV excited state populations even after the pumping process. This discovery requires future exploration and theoretical explanation which may end up with new model of NV dynamics. The absence of emission resonance peaks could be the result of energy level broadening at room temperature. It is worthwhile to try the experiments again at low temperature using narrow linewidth laser to search for the resonance peaks, which has been reported in a single-photon PLE experiment. The spin dynamic is another possible direction to continue with since a multi-photon process can follow completely different selection rules compared with a single-photon process.

7.4 PUBLICATIONS

- Charge state dynamics of the nitrogen vacancy center in diamond under 1064-nm laser excitation. Peng Ji, M. V. Gurudev Dutt. Phys. Rev. B 94, 024101(2016)
- Cooling the motion of diamond nanocrystals in a magneto-gravitational trap in high vacuum. J.-F. Hsu, Peng Ji, C. W. Lewandowski, and B. D'Urso. Scientific Reports, vol. 6, 30125, Jul (2016)
- Multiple-photon excitation of nitrogen vacancy center in diamond. Peng Ji, R. B. Balili, J. Beaumariage, S. Mukherjee, D. W. Snoke, M. V. Gurudev Dutt. Phys. Rev. B 97, 134112(2018)

BIBLIOGRAPHY

- [1] T. Delord, L. Nicolas, M. Bodini, and G. Htet. Diamonds levitating in a paul trap under vacuum: Measurements of laser-induced heating via nv center thermometry. *Applied Physics Letters*, 111(1):013101, 2017.
- [2] D. Ganta, E. B. Dale, J. P. Rezac, and A. T. Rosenberger. Optical method for measuring thermal accommodation coefficients using a whispering-gallery microresonator. *The Journal of Chemical Physics*, 135(8):084313, 2011.
- [3] A. D. O’Connell, M. Hofheinz, M. Ansmann, Radoslaw C. Bialczak, M. Lenander, Erik Lucero, M. Neeley, D. Sank, H. Wang, M. Weides, J. Wenner, John M. Martinis, and A. N. Cleland. Quantum ground state and single-phonon control of a mechanical resonator. *Nature*, 464:697 EP –, Mar 2010. Article.
- [4] Yiwen Chu, Prashanta Kharel, William H. Renninger, Luke D. Burkhardt, Luigi Frunzio, Peter T. Rakich, and Robert J. Schoelkopf. Quantum acoustics with superconducting qubits. *Science*, 2017.
- [5] D. Rugar, R. Budakian, H. J. Mamin, and B. W. Chui. Single spin detection by magnetic resonance force microscopy. *Nature*, 430:329 EP –, Jul 2004.
- [6] P. Rabl, P. Cappellaro, M. V. Gurudev Dutt, L. Jiang, J. R. Maze, and M. D. Lukin. Strong magnetic coupling between an electronic spin qubit and a mechanical resonator. *Phys. Rev. B*, 79:041302, Jan 2009.
- [7] Markus Aspelmeyer, Tobias J. Kippenberg, and Florian Marquardt. Cavity optomechanics. *Rev. Mod. Phys.*, 86:1391–1452, Dec 2014.
- [8] Jasper Chan, T. P. Mayer Alegre, Amir H. Safavi-Naeini, Jeff T. Hill, Alex Krause, Simon Gröblacher, Markus Aspelmeyer, and Oskar Painter. Laser cooling of a nanomechanical oscillator into its quantum ground state. *Nature*, 478:89 EP –, Oct 2011.
- [9] Naufer Mohamed Nusran. Application of phase estimation algorithms to improve diamond spin magnetometry. *Theses*, 2014.

- [10] A. Dréau, M. Lesik, L. Rondin, P. Spinicelli, O. Arcizet, J.-F. Roch, and V. Jacques. Avoiding power broadening in optically detected magnetic resonance of single nv defects for enhanced dc magnetic field sensitivity. *Phys. Rev. B*, 84:195204, Nov 2011.
- [11] Zhang-qi Yin, Tongcang Li, Xiang Zhang, and L. M. Duan. Large quantum superpositions of a levitated nanodiamond through spin-optomechanical coupling. *Phys. Rev. A*, 88:033614, Sep 2013.
- [12] Vijay Jain, Jan Gieseler, Clemens Moritz, Christoph Dellago, Romain Quidant, and Lukas Novotny. Direct measurement of photon recoil from a levitated nanoparticle. *Phys. Rev. Lett.*, 116:243601, Jun 2016.
- [13] H. J. Mamin, M. Poggio, C. L. Degen, and D. Rugar. Nuclear magnetic resonance imaging with 90-nm resolution. *Nature Nanotechnology*, 2:301 EP –, Apr 2007. Article.
- [14] Jen-Feng Hsu, Peng Ji, Charles W. Lewandowski, and Brian D’Urso. Cooling the motion of diamond nanocrystals in a magneto-gravitational trap in high vacuum. *Scientific Reports*, 6:30125 EP –, Jul 2016. Article.
- [15] J-P Tetienne, L Rondin, P Spinicelli, M Chipaux, T Debuisschert, J-F Roch, and V Jacques. Magnetic-field-dependent photodynamics of single nv defects in diamond: an application to qualitative all-optical magnetic imaging. *New Journal of Physics*, 14(10):103033, 2012.
- [16] Jen-Feng Hsu. Cooling the center-of-mass motion of a diamond nanocrystal in a magneto-gravitational trap. *Theses*, 2016.
- [17] Abraham. Savitzky and M. J. E. Golay. Smoothing and differentiation of data by simplified least squares procedures. *Analytical Chemistry*, 36(8):1627–1639, 1964.
- [18] N Aslam, G Waldherr, P Neumann, F Jelezko, and J Wrachtrup. Photo-induced ionization dynamics of the nitrogen vacancy defect in diamond investigated by single-shot charge state detection. *New Journal of Physics*, 15(1):013064, 2013.
- [19] D. E. Chang, C. A. Regal, S. B. Papp, D. J. Wilson, J. Ye, O. Painter, H. J. Kimble, and P. Zoller. Cavity opto-mechanics using an optically levitated nanosphere. *Proceedings of the National Academy of Sciences*, 107(3):1005–1010, 2010.
- [20] O. Arcizet, V. Jacques, A. Siria, P. Poncharal, P. Vincent, and S. Seidelin. A single nitrogen-vacancy defect coupled to a nanomechanical oscillator. *Nature Physics*, 7:879 EP –, Sep 2011. Article.
- [21] Shimon Kolkowitz, Ania C. Bleszynski Jayich, Quirin P. Unterreithmeier, Steven D. Bennett, Peter Rabl, J. G. E. Harris, and Mikhail D. Lukin. Coherent sensing of a mechanical resonator with a single-spin qubit. *Science*, 335(6076):1603–1606, 2012.
- [22] I. Wilson-Rae, P. Zoller, and A. Imamoglu. Laser cooling of a nanomechanical resonator mode to its quantum ground state. *Phys. Rev. Lett.*, 92:075507, Feb 2004.

- [23] David Hunger, Stephan Camerer, Theodor W. Hänsch, Daniel König, Jörg P. Kotthaus, Jakob Reichel, and Philipp Treutlein. Resonant coupling of a bose-einstein condensate to a micromechanical oscillator. *Phys. Rev. Lett.*, 104:143002, Apr 2010.
- [24] Philipp Treutlein, David Hunger, Stephan Camerer, Theodor W. Hänsch, and Jakob Reichel. Bose-einstein condensate coupled to a nanomechanical resonator on an atom chip. *Phys. Rev. Lett.*, 99:140403, Oct 2007.
- [25] Ying-Ju Wang, Matthew Eardley, Svenja Knappe, John Moreland, Leo Hollberg, and John Kitching. Magnetic resonance in an atomic vapor excited by a mechanical resonator. *Phys. Rev. Lett.*, 97:227602, Dec 2006.
- [26] Stephan Camerer, Maria Korppi, Andreas Jöckel, David Hunger, Theodor W. Hänsch, and Philipp Treutlein. Realization of an optomechanical interface between ultracold atoms and a membrane. *Phys. Rev. Lett.*, 107:223001, Nov 2011.
- [27] Philipp Treutlein, Claudiu Genes, Klemens Hammerer, Martino Poggio, and Peter Rabl. *Hybrid Mechanical Systems*, pages 327–351. Springer Berlin Heidelberg, Berlin, Heidelberg, 2014.
- [28] K. Hammerer, M. Aspelmeyer, E. S. Polzik, and P. Zoller. Establishing einstein-poldosky-rosen channels between nanomechanics and atomic ensembles. *Phys. Rev. Lett.*, 102:020501, Jan 2009.
- [29] M. Wallquist, K. Hammerer, P. Zoller, C. Genes, M. Ludwig, F. Marquardt, P. Treutlein, J. Ye, and H. J. Kimble. Single-atom cavity qed and optomechanics. *Phys. Rev. A*, 81:023816, Feb 2010.
- [30] Tobias J Editors Florian Marquardt Aspelmeyer, Markus Kippenberg. Cavity optomechanics: Nano- and micromechanical resonators interacting with light. *Springer Book*, Chapter 14, 2014.
- [31] S. Bose, K. Jacobs, and P. L. Knight. Preparation of nonclassical states in cavities with a moving mirror. *Phys. Rev. A*, 56:4175–4186, Nov 1997.
- [32] William Marshall, Christoph Simon, Roger Penrose, and Dik Bouwmeester. Towards quantum superpositions of a mirror. *Phys. Rev. Lett.*, 91:130401, Sep 2003.
- [33] D. Vitali, S. Gigan, A. Ferreira, H. R. Böhm, P. Tombesi, A. Guerreiro, V. Vedral, A. Zeilinger, and M. Aspelmeyer. Optomechanical entanglement between a movable mirror and a cavity field. *Phys. Rev. Lett.*, 98:030405, Jan 2007.
- [34] A A Clerk, F Marquardt, and K Jacobs. Back-action evasion and squeezing of a mechanical resonator using a cavity detector. *New Journal of Physics*, 10(9):095010, 2008.

- [35] Levi P. Neukirch, Jan Gieseler, Romain Quidant, Lukas Novotny, and A. Nick Vamivakas. Observation of nitrogen vacancy photoluminescence from an optically levitated nanodiamond. *Opt. Lett.*, 38(16):2976–2979, Aug 2013.
- [36] B. D. Cuthbertson, M. E. Tobar, E. N. Ivanov, and D. G. Blair. Parametric backaction effects in a high-q cyrogenic sapphire transducer. *Review of Scientific Instruments*, 67(7):2435–2442, 1996.
- [37] O. Arcizet, P.-F. Cohadon, T. Briant, M. Pinard, and A. Heidmann. Radiation-pressure cooling and optomechanical instability of a micromirror. *Nature*, 444:71 EP –, Nov 2006.
- [38] J. D. Thompson, B. M. Zwickl, A. M. Jayich, Florian Marquardt, S. M. Girvin, and J. G. E. Harris. Strong dispersive coupling of a high-finesse cavity to a micromechanical membrane. *Nature*, 452:72 EP –, Mar 2008.
- [39] Kater W. Murch, Kevin L. Moore, Subhadeep Gupta, and Dan M. Stamper-Kurn. Observation of quantum-measurement backaction with an ultracold atomic gas. *Nature Physics*, 4:561 EP –, May 2008. Article.
- [40] Simon Gröblacher, Klemens Hammerer, Michael R. Vanner, and Markus Aspelmeyer. Observation of strong coupling between a micromechanical resonator and an optical cavity field. *Nature*, 460:724 EP –, Aug 2009.
- [41] J. D. Teufel, T. Donner, Dale Li, J. W. Harlow, M. S. Allman, K. Cicak, A. J. Sirois, J. D. Whittaker, K. W. Lehnert, and R. W. Simmonds. Sideband cooling of micromechanical motion to the quantum ground state. *Nature*, 475:359 EP –, Jul 2011.
- [42] Dustin Kleckner, Brian Pepper, Evan Jeffrey, Petro Sonin, Susanna M. Thon, and Dirk Bouwmeester. Optomechanical trampoline resonators. *Opt. Express*, 19(20):19708–19716, Sep 2011.
- [43] E. Verhagen, S. Deléglise, S. Weis, A. Schliesser, and T. J. Kippenberg. Quantum-coherent coupling of a mechanical oscillator to an optical cavity mode. *Nature*, 482:63 EP –, Feb 2012.
- [44] B L Hu. Gravitational decoherence, alternative quantum theories and semiclassical gravity. *Journal of Physics: Conference Series*, 504(1):012021, 2014.
- [45] Yanbei Chen. Macroscopic quantum mechanics: theory and experimental concepts of optomechanics. *Journal of Physics B: Atomic, Molecular and Optical Physics*, 46(10):104001, may 2013.
- [46] Lajos Diósi. Gravity-related wave function collapse: mass density resolution. *Journal of Physics: Conference Series*, 442(1):012001, 2013.
- [47] L. Diósi. Gravitation and quantum-mechanical localization of macro-objects. *Physics Letters A*, 105(4-5):199–202, oct 1984.

- [48] André Großardt, James Bateman, Hendrik Ulbricht, and Angelo Bassi. Optomechanical test of the schrödinger-newton equation. *Phys. Rev. D*, 93:096003, May 2016.
- [49] R S Balmer, J R Brandon, S L Clewes, H K Dhillon, J M Dodson, I Friel, P N Inglis, T D Madgwick, M L Markham, T P Mollart, N Perkins, G A Scarsbrook, D J Twitchen, A J Whitehead, J J Wilman, and S M Woollard. Chemical vapour deposition synthetic diamond: materials, technology and applications. *Journal of Physics: Condensed Matter*, 21(36):364221, 2009.
- [50] Romana Schirhagl, Kevin Chang, Michael Loretz, and Christian L. Degen. Nitrogen-vacancy centers in diamond: Nanoscale sensors for physics and biology. *Annual Review of Physical Chemistry*, 65(1):83–105, 2014. PMID: 24274702.
- [51] Vadym N. Mochalin, Olga Shenderova, Dean Ho, and Yury Gogotsi. The properties and applications of nanodiamonds. *Nature Nanotechnology*, 7:11 EP –, Dec 2011. Review Article.
- [52] J H N Loubser and J A van Wyk. Electron spin resonance in the study of diamond. *Reports on Progress in Physics*, 41(8):1201, 1978.
- [53] Marcus W. Doherty, Neil B. Manson, Paul Delaney, Fedor Jelezko, Jrg Wrachtrup, and Lloyd C.L. Hollenberg. The nitrogen-vacancy colour centre in diamond. *Physics Reports*, 528(1):1 – 45, 2013. The nitrogen-vacancy colour centre in diamond.
- [54] P. Siyushev, H. Pinto, M. Vörös, A. Gali, F. Jelezko, and J. Wrachtrup. Optically controlled switching of the charge state of a single nitrogen-vacancy center in diamond at cryogenic temperatures. *Phys. Rev. Lett.*, 110:167402, Apr 2013.
- [55] M. Steiner, P. Neumann, J. Beck, F. Jelezko, and J. Wrachtrup. Universal enhancement of the optical readout fidelity of single electron spins at nitrogen-vacancy centers in diamond. *Phys. Rev. B*, 81:035205, Jan 2010.
- [56] L Rondin, J-P Tetienne, T Hingant, J-F Roch, P Maletinsky, and V Jacques. Magnetometry with nitrogen-vacancy defects in diamond. *Reports on Progress in Physics*, 77(5):056503, 2014.
- [57] K. Jensen, V. M. Acosta, A. Jarmola, and D. Budker. Light narrowing of magnetic resonances in ensembles of nitrogen-vacancy centers in diamond. *Phys. Rev. B*, 87:014115, Jan 2013.
- [58] V. M. Acosta, E. Bauch, M. P. Ledbetter, A. Waxman, L.-S. Bouchard, and D. Budker. Temperature dependence of the nitrogen-vacancy magnetic resonance in diamond. *Phys. Rev. Lett.*, 104:070801, Feb 2010.
- [59] G. Kucsko, P. C. Maurer, N. Y. Yao, M. Kubo, H. J. Noh, P. K. Lo, H. Park, and M. D. Lukin. Nanometre-scale thermometry in a living cell. *Nature*, 500(7460):54–58, Aug 2013. Letter.

- [60] Menno Poot and Herre S.J. van der Zant. Mechanical systems in the quantum regime. *Physics Reports*, 511(5):273 – 335, 2012. Mechanical systems in the quantum regime.
- [61] O. Romero-Isart, A. C. Pflanzner, M. L. Juan, R. Quidant, N. Kiesel, M. Aspelmeyer, and J. I. Cirac. Optically levitating dielectrics in the quantum regime: Theory and protocols. *Phys. Rev. A*, 83:013803, Jan 2011.
- [62] Jan Gieseler, Bradley Deutsch, Romain Quidant, and Lukas Novotny. Subkelvin parametric feedback cooling of a laser-trapped nanoparticle. *Phys. Rev. Lett.*, 109:103603, Sep 2012.
- [63] Tongcang Li, Simon Kheifets, and Mark G. Raizen. Millikelvin cooling of an optically trapped microsphere in vacuum. *Nat Phys*, 7(7):527–530, Jul 2011.
- [64] A. Ashkin and J. M. Dziedzic. Optical levitation by radiation pressure. *Applied Physics Letters*, 19(8):283–285, 1971.
- [65] Ryota Omori, Tamiki Kobayashi, and Atsuyuki Suzuki. Observation of a single-beam gradient-force optical trap for dielectric particles in air. *Opt. Lett.*, 22(11):816–818, Jun 1997.
- [66] Keir C. Neuman and Steven M. Block. Optical trapping. *Review of Scientific Instruments*, 75(9):2787–2809, 2004.
- [67] A. Ashkin and J. M. Dziedzic. Optical levitation in high vacuum. *Applied Physics Letters*, 28(6):333–335, 1976.
- [68] Timo A. Nieminen, Gregor Knner, Norman R. Heckenberg, and Halina Rubinsztein Dunlop. Physics of optical tweezers. 82(Supplement C):207 – 236, 2007.
- [69] Mike.Wrdemann. Structured light fields: Applications in optical trapping, manipulation, and organisation. *Springer Theses*, Chapter2, 2012.
- [70] Yasuhiro Harada and Toshimitsu Asakura. Radiation forces on a dielectric sphere in the rayleigh scattering regime. *Optics Communications*, 124(5):529 – 541, 1996.
- [71] K Svoboda, , and S M Block. Biological applications of optical forces. *Annual Review of Biophysics and Biomolecular Structure*, 23(1):247–285, 1994. PMID: 7919782.
- [72] Tongcang.Li. Fundamental tests of physics with optically trapped microspheres. *Springer Theses*, Chapter2, 2013.
- [73] Timo A Nieminen, Vincent L Y Loke, Alexander B Stilgoe, Gregor Knner, Agata M Braczyk, Norman R Heckenberg, and Halina Rubinsztein-Dunlop. Optical tweezers computational toolbox. *Journal of Optics A: Pure and Applied Optics*, 9(8):S196, 2007.

- [74] Lukas Novotny, Randy X. Bian, and X. Sunney Xie. Theory of nanometric optical tweezers. *Phys. Rev. Lett.*, 79:645–648, Jul 1997.
- [75] D. M. Toyli, D. J. Christle, A. Alkauskas, B. B. Buckley, C. G. Van de Walle, and D. D. Awschalom. Measurement and control of single nitrogen-vacancy center spins above 600 k. *Phys. Rev. X*, 2:031001, Jul 2012.
- [76] V R Howes. The graphitization of diamond. *Proceedings of the Physical Society*, 80(3):648, 1962.
- [77] Levi P. Neukirch, Eva von Haartman, Jessica M. Rosenholm, and Nick VamivakasA. Multi-dimensional single-spin nano-optomechanics with a levitated nanodiamond. *Nat Photon*, 9(10):653–657, Oct 2015. Letter.
- [78] Thai M. Hoang, Jonghoon Ahn, Jaehoon Bang, and Tongcang Li. Electron spin control of optically levitated nanodiamonds in vacuum. *Nature Communications*, 7:12250 EP –, Jul 2016. Article.
- [79] A. T. M. A. Rahman, A. C. Frangeskou, M. S. Kim, S. Bose, G. W. Morley, and P. F. Barker. Burning and graphitization of optically levitated nanodiamonds in vacuum. *Scientific Reports*, 6:21633 EP –, Feb 2016. Article.
- [80] G. de Lange, D. Ristè, V. V. Dobrovitski, and R. Hanson. Single-spin magnetometry with multipulse sensing sequences. *Phys. Rev. Lett.*, 106:080802, Feb 2011.
- [81] Shlomi Kotler, Nitzan Akerman, Yinnon Glickman, Anna Keselman, and Roei Ozeri. Single-ion quantum lock-in amplifier. *Nature*, 473:61 EP –, May 2011.
- [82] K. Karrai, I. Favero, and C. Metzger. Doppler optomechanics of a photonic crystal. *Phys. Rev. Lett.*, 100:240801, Jun 2008.
- [83] Karl Jousten. Mean free path. <https://www.pfeiffer-vacuum.com/en/know-how/introduction-to-vacuum-technology/fundamentals/mean-free-path/>.
- [84] Taras Plakhotnik, Marcus W. Doherty, Jared H. Cole, Robert Chapman, and Neil B. Manson. All-optical thermometry and thermal properties of the optically detected spin resonances of the nv-center in nanodiamond. *Nano Letters*, 14(9):4989–4996, Sep 2014.
- [85] Michael Geiselmann, Mathieu L. Juan, Jan Renger, Jana M. Say, Louise J. Brown, F. Javier García de Abajo, Frank Koppens, and Romain Quidant. Three-dimensional optical manipulation of a single electron spin. *Nature Nanotechnology*, 8:175 EP –, Feb 2013.
- [86] Jen-Feng Hsu Brian D’Urso Bradley R. Slezak, Charles W. Lewandowski. Cooling the motion of a silica microsphere in a magneto-gravitational trap in ultra-high vacuum. *arXiv:1802.03424*, 2017.

- [87] Clarence Zener. Internal friction in solids ii. general theory of thermoelastic internal friction. *Phys. Rev.*, 53:90–99, Jan 1938.
- [88] Ron Lifshitz and M. L. Roukes. Thermoelastic damping in micro- and nanomechanical systems. *Phys. Rev. B*, 61:5600–5609, Feb 2000.
- [89] A. Duwel, R. N. Candler, T. W. Kenny, and M. Varghese. Engineering mems resonators with low thermoelastic damping. *Journal of Microelectromechanical Systems*, 15(6):1437–1445, Dec 2006.
- [90] A. A. Kiselev and G. J. Iafrate. Phonon dynamics and phonon assisted losses in euler-bernoulli nanobeams. *Phys. Rev. B*, 77:205436, May 2008.
- [91] K. Y. Yasumura, T. D. Stowe, E. M. Chow, T. Pfafman, T. W. Kenny, B. C. Stipe, and D. Rugar. Quality factors in micron- and submicron-thick cantilevers. *Journal of Microelectromechanical Systems*, 9(1):117–125, March 2000.
- [92] P. Mohanty, D. A. Harrington, K. L. Ekinci, Y. T. Yang, M. J. Murphy, and M. L. Roukes. Intrinsic dissipation in high-frequency micromechanical resonators. *Phys. Rev. B*, 66:085416, Aug 2002.
- [93] D. R. Southworth, R. A. Barton, S. S. Verbridge, B. Ilic, A. D. Fefferman, H. G. Craighead, and J. M. Parpia. Stress and silicon nitride: A crack in the universal dissipation of glasses. *Phys. Rev. Lett.*, 102:225503, Jun 2009.
- [94] Quirin P. Unterreithmeier, Thomas Faust, and Jörg P. Kotthaus. Damping of nanomechanical resonators. *Phys. Rev. Lett.*, 105:027205, Jul 2010.
- [95] A. Venkatesan, K. J. Lulla, M. J. Patton, A. D. Armour, C. J. Mellor, and J. R. Owers-Bradley. Dissipation due to tunneling two-level systems in gold nanomechanical resonators. *Phys. Rev. B*, 81:073410, Feb 2010.
- [96] Jan Gieseler. Dynamics of optically levitated nanoparticles in high vacuum. *Theses*, 2014.
- [97] C. Schreyvogel, V. Polyakov, R. Wunderlich, J. Meijer, and C. E. Nebel. Active charge state control of single nv centres in diamond by in-plane al-schottky junctions. *Scientific Reports*, 5:12160 EP –, Jul 2015. Article.
- [98] Mohammadreza Khorasaninejad, Wei Ting Chen, Robert C. Devlin, Jaewon Oh, Alexander Y. Zhu, and Federico Capasso. Metalenses at visible wavelengths: Diffraction-limited focusing and subwavelength resolution imaging. *Science*, 352(6290):1190–1194, 2016.
- [99] Wei Ting Chen, Alexander Y. Zhu, Vyshakh Sanjeev, Mohammadreza Khorasaninejad, Zhujun Shi, Eric Lee, and Federico Capasso. A broadband achromatic metalens for focusing and imaging in the visible. *Nature Nanotechnology*, 13(3):220–226, 2018.

- [100] Peng Ji and M. V. Gurudev Dutt. Charge state dynamics of the nitrogen vacancy center in diamond under 1064-nm laser excitation. *Phys. Rev. B*, 94:024101, Jul 2016.
- [101] Marcus W. Doherty, Neil B. Manson, Paul Delaney, Fedor Jelezko, Jrg Wrachtrup, and Lloyd C.L. Hollenberg. The nitrogen-vacancy colour centre in diamond. *Physics Reports*, 528(1):1 – 45, 2013. The nitrogen-vacancy colour centre in diamond.
- [102] P. Siyushev, H. Pinto, M. Vörös, A. Gali, F. Jelezko, and J. Wrachtrup. Optically controlled switching of the charge state of a single nitrogen-vacancy center in diamond at cryogenic temperatures. *Phys. Rev. Lett.*, 110:167402, Apr 2013.
- [103] B. J. Shields, Q. P. Unterreithmeier, N. P. de Leon, H. Park, and M. D. Lukin. Efficient readout of a single spin state in diamond via spin-to-charge conversion. *Phys. Rev. Lett.*, 114:136402, Mar 2015.
- [104] Zhang Qi Yin, Tongcang Li, Xiang Zhang, and L. M. Duan. Large quantum superpositions of a levitated nanodiamond through spin-optomechanical coupling. *Phys. Rev. A*, 88:033614, Sep 2013.
- [105] Thai M. Hoang, Jonghoon Ahn, Jaehoon Bang, and Tongcang Li. Observation of vacuum-enhanced electron spin resonance of levitated nanodiamonds. *arXiv:1510.06715*, 2015.
- [106] N D Lai, O Faklaris, D Zheng, V Jacques, H-C Chang, J-F Roch, and F Treussart. Quenching nitrogenvacancy center photoluminescence with an infrared pulsed laser. *New Journal of Physics*, 15(3):033030, 2013.
- [107] Michael Geiselmann, Renaud Marty, F. Javier Garcia de Abajo, and Romain Quidant. Fast optical modulation of the fluorescence from a single nitrogen-vacancy centre. *Nat Phys*, 9(12):785–789, Dec 2013.
- [108] Eva Rittweger, Kyu Young Han, Scott E. Irvine, Christian Eggeling, and Stefan W. Hell. Sted microscopy reveals crystal colour centres with nanometric resolution. *Nat Photon*, 3(3):144–147, Mar 2009.
- [109] T. Gaebel, M. Domhan, C. Wittmann, I. Popa, F. Jelezko, J. Rabeau, A. Greentree, S. Prawer, E. Trajtkov, P.R. Hemmer, and J. Wrachtrup. Photochromism in single nitrogen-vacancy defect in diamond. *Applied Physics B*, 82(2):243–246, 2005.
- [110] L. Rondin, G. Dantelle, A. Slablab, F. Grosshans, F. Treussart, P. Bergonzo, S. Peruchas, T. Gacoin, M. Chaigneau, H.-C. Chang, V. Jacques, and J.-F. Roch. Surface-induced charge state conversion of nitrogen-vacancy defects in nanodiamonds. *Phys. Rev. B*, 82:115449, Sep 2010.
- [111] N.B. Manson and J.P. Harrison. Photo-ionization of the nitrogen-vacancy center in diamond. *Diamond and Related Materials*, 14(10):1705 – 1710, 2005.

- [112] G. Waldherr, J. Beck, M. Steiner, P. Neumann, A. Gali, Th. Frauenheim, F. Jelezko, and J. Wrachtrup. Dark states of single nitrogen-vacancy centers in diamond unraveled by single shot nmr. *Phys. Rev. Lett.*, 106:157601, Apr 2011.
- [113] K. Beha, A. Batalov, N. B. Manson, R. Bratschitsch, and A. Leitenstorfer. Optimum photoluminescence excitation and recharging cycle of single nitrogen-vacancy centers in ultrapure diamond. *Phys. Rev. Lett.*, 109:097404, Aug 2012.
- [114] Lucio Robledo, Hannes Bernien, Ilse van Weperen, and Ronald Hanson. Control and coherence of the optical transition of single nitrogen vacancy centers in diamond. *Phys. Rev. Lett.*, 105:177403, Oct 2010.
- [115] J Walker. Optical absorption and luminescence in diamond. *Reports on Progress in Physics*, 42(10):1605, 1979.
- [116] Jan Jeske, Desmond W. M. Lau, Liam P. McGuinness, Philip Reineck, Brett C. Johnson, Jeffrey C. McCallum, Fedor Jelezko, Thomas Volz, Jared H. Cole, Brant C. Gibson, and Andrew D. Greentree. Stimulated emission from nv centres in diamond. *arXiv:1602.07418*, Feb 2016.
- [117] V. M. Acosta, E. Bauch, M. P. Ledbetter, A. Waxman, L.-S. Bouchard, and D. Budker. Temperature dependence of the nitrogen-vacancy magnetic resonance in diamond. *Phys. Rev. Lett.*, 104:070801, Feb 2010.
- [118] F. Jelezko, T. Gaebel, I. Popa, A. Gruber, and J. Wrachtrup. Observation of coherent oscillations in a single electron spin. *Phys. Rev. Lett.*, 92:076401, Feb 2004.
- [119] L. Childress, M. V. Gurudev Dutt, J. M. Taylor, A. S. Zibrov, F. Jelezko, J. Wrachtrup, P. R. Hemmer, and M. D. Lukin. Coherent dynamics of coupled electron and nuclear spin qubits in diamond. *Science*, 314(5797):281–285, 2006.
- [120] Peng Ji, R. Balili, J. Beaumariage, S. Mukherjee, D. Snoke, and M. V. Gurudev Dutt. Multiple-photon excitation of nitrogen vacancy centers in diamond. *Phys. Rev. B*, 97:134112, Apr 2018.
- [121] A. Gruber, A. Dräbenstedt, C. Tietz, L. Fleury, J. Wrachtrup, and C. von Borczyskowski. Scanning confocal optical microscopy and magnetic resonance on single defect centers. *Science*, 276(5321):2012–2014, 1997.
- [122] Tse-Luen Wee, Yan-Kai Tzeng, Chau-Chung Han, Huan-Cheng Chang, Wunshain Fann, Jui-Hung Hsu, Kuan-Ming Chen, and Yueh-Chung Yu. Two-photon excited fluorescence of nitrogen-vacancy centers in proton-irradiated type Ib diamond. *The Journal of Physical Chemistry A*, 111(38):9379–9386, 2007. PMID: 17705460.
- [123] Peng Ji and M. V. Gurudev Dutt. Charge state dynamics of the nitrogen vacancy center in diamond under 1064-nm laser excitation. *Phys. Rev. B*, 94:024101, Jul 2016.

- [124] David A. Hopper, Richard R. Grote, Annemarie L. Exarhos, and Lee C. Bassett. Near-infrared-assisted charge control and spin readout of the nitrogen-vacancy center in diamond. *Phys. Rev. B*, 94:241201, Dec 2016.
- [125] Farhad H. M. Faisal. Theory of multiphoton processes. *Springer Book*, 1987.
- [126] Chris Xu and Warren R. Zipfel. Multiphoton excitation of fluorescent probes. *Cold Spring Harbor protocols*, 2015 3:250–8, 2015.
- [127] G. Davies and M. F. Hamer. Optical studies of the 1.945 eV vibronic band in diamond. *Proceedings of the Royal Society of London A: Mathematical, Physical and Engineering Sciences*, 348(1653):285–298, 1976.
- [128] G Liaugaudas, G Davies, K Suhling, R U A Khan, and D J F Evans. Luminescence lifetimes of neutral nitrogen-vacancy centres in synthetic diamond containing nitrogen. *Journal of Physics: Condensed Matter*, 24(43):435503, 2012.
- [129] Steven L Jacques. Optical properties of biological tissues: a review. *Physics in Medicine and Biology*, 58(11):R37, 2013.
- [130] E. Knill, R. Laflamme, and G. J. Milburn. A scheme for efficient quantum computation with linear optics. *Nature*, 409(6816):46–52, Jan 2001.
- [131] E. Togan, Y. Chu, A. S. Trifonov, L. Jiang, J. Maze, L. Childress, M. V. G. Dutt, A. S. Sorensen, P. R. Hemmer, A. S. Zibrov, and M. D. Lukin. Quantum entanglement between an optical photon and a solid-state spin qubit. *Nature*, 466(7307):730–734, Aug 2010.